ETP-KA/2023-5

Search for Dark Matter produced in association with a top quark in hadronic and leptonic final states with the CMS experiment

Zur Erlangung des akademischen Grades eines

DOKTORS DER NATURWISSENSCHAFTEN (Dr. rer. nat.)

von der KIT-Fakultät für Physik des
Karlsruher Instituts für Technologie (KIT)
angenommene

DISSERTATION

von M.Sc. Sebastian Wieland

aus Waldenburg

Tag der mündlichen Prüfung: 26.05.2023

Referent:	Prof. Dr. Ulrich Husemann	Institut für Experimentelle Teilchenphysik
Korreferent:	Prof. Dr. Günter Quast	Institut für Experimentelle Teilchenphysik

This document is licensed under a Creative Commons
Attribution-Non Commercial 4.0 International License (CC BY-NC 4.0):
https://creativecommons.org/licenses/by-nc/4.0/deed.en

Erklärung der selbstständigen Anfertigung der Dissertationsschrift
Hiermit erkläre ich, dass ich die Dissertation mit dem Titel

Search for Dark Matter produced in association with a top quark in hadronic and leptonic final states with the CMS experiment

selbstständig angefertigt, alle benutzten Hilfsmittel vollständig und genau angegeben und alles kenntlich gemacht habe, was aus Arbeiten anderer unverändert oder mit Abänderungen entnommen wurde.

Ich versichere außerdem, dass ich die Dissertation nur in diesem und keinem anderen Promotionsverfahren eingereicht habe und dass diesem Promotionsverfahren keine endgültig gescheiterten Promotionsverfahren vorausgegangen sind.

Karlsruhe, 19.04.2023

. . . . . .
(**Sebastian Wieland**)

Contents

1 Introduction **1**

I Foundations **3**

2 Theoretical background **5**
2.1 The Standard Model of particle physics 5
2.2 Physics Beyond the Standard Model (Dark Matter) 9
2.3 Physics at hadron colliders 14
2.4 Event generation and simulation 15

3 Experimental environment **17**
3.1 The Large Hadron Collider 17
3.2 The Compact Muon Solenoid 19
3.3 Reconstruction of physics objects 22
3.4 Experimental searches for Dark Matter 24

4 Introduction to statistical data analysis **29**
4.1 General approach 29
4.2 Parameter estimation 30
4.3 Hypothesis tests 30
4.4 Application to high energy physics 31
4.5 Systematic uncertainties 33
4.6 Goodness of fit tests 33

II Mono-top Analysis **35**

5 General foundations of the mono-top analysis **37**
5.1 Physics of top quarks 37
5.2 Tagging of heavy quarks 39
5.3 The mono-top model 44
5.4 Simulation samples 52
5.5 Corrections for simulations 55
5.6 Recorded data 61
5.7 Object definitions 62
5.8 Systematic uncertainties 80

6 Leptonic mono-top analysis **85**
6.1 Analysis strategy 85
6.2 Event Selection 88
6.3 Validation of the statistical model 91

6.4 Expected results . . . 97
6.5 Observed results . . . 100

7 Hadronic mono-top analysis 105
7.1 Analysis strategy . . . 105
7.2 Event selection . . . 108
7.3 Statistical model . . . 121
7.4 Validation of the statistical model . . . 124
7.5 Expected results . . . 130
7.6 Observed results . . . 133

8 Combined Mono-top Analysis 137
8.1 Statistical model . . . 137
8.2 Expected results . . . 141

9 Conclusion and outlook 143

Acronyms 147

Bibliography 151

Appendix 163
A Electron trigger scale factors . . . 163
B Photon trigger scale factors . . . 165
C B-tagging efficiencies . . . 167
D Naming of nuisance parameters . . . 169
E Control distribution in the leptonic analysis channel . . . 171
F Pulls in control region only fit in leptonic analysis . . . 183
G Pulls and constraints in leptonic analysis . . . 187
H A-posteriori distributions in the leptonic analysis channel . . . 189
I Expected exclusion limits for leptonic analysis . . . 191
J Observed exclusion limits for leptonic analysis . . . 195
K Hadronic control distributions w/o top-tagging . . . 197
L $\not{E}_{\mathrm{T}}$ in hadronic channel with top-tagging . . . 217
M Transfer factors in the hadronic analysis channel . . . 226
N A-posteriori distributions in the hadronic analysis channel . . . 231
O Expected exclusion limits for hadronic analysis . . . 239
P Observed exclusion limits for hadronic analysis . . . 241

Acknowledgements 243

1 Introduction

The essence of high-energy physics is the exploration of the fundamental building blocks of the universe, the elementary particles, and their interactions. The current theoretical description, referred to as the Standard Model of particle physics (SM), has been one of the most successful theories in the history of science. During the last decades, its predictions have been confirmed by numerous experiments to an unprecedented level of precision. Despite this tremendous success, several experimental observations are not in agreement with the SM. Consequently, efforts are being made on the theoretical side to extend the SM by adding new particles and interactions to account for these shortcomings. From an experimental point of view, the Compact Muon Solenoid (CMS) experiment located at European Organization for Nuclear Research (CERN) in Geneva, Switzerland, provides unique opportunities to study these Beyond the Standard Model (BSM) physics phenomena by analyzing data of colliding proton beams at the Large Hadron Collider (LHC). These proton-proton collisions allow probing the smallest length scales currently accessible in a laboratory environment due to the unprecedented center-of-mass energy of the LHC.

One of the most prominent flaws of the SM is the existence of Dark Matter (DM). The presence of DM in the universe is supported experimentally both on astrophysical as well as on cosmological scales. On an astrophysical scale, the presence of DM is inferred, for example, from measurements of the rotation speed of galaxies, which are not in agreement with the expectation based on the observed visible matter. These measurements suggest that DM only interacts very weakly and gravitationally.

An example on cosmological scale is given by measurements of the cosmic microwave background (CMB) radiation which essentially provides a snapshot of the universe roughly 300,000 years after the big bang. Small fluctuations in this spectrum provide a way to measure the energy composition of the universe and suggest that only approximately 5 % of the energy density is due to visible matter and 25 % is due to DM. The remaining 70 % is attributed to a mysterious form of energy, called dark energy, which is responsible for the accelerated expansion of the universe.

In general, there are three experimental ways to search for DM if its production mechanism in the early universe is based on a thermal freeze-out. The first one is to directly detect the DM particles which are supposed to recoil against a nucleus of a target material such as xenon. Alternatively, indirect detection of DM can be achieved by measuring overabundances of positrons or anti-protons in cosmic rays which would occur if DM particles annihilate into these particles.

The third way, which is the subject of this thesis, is to directly produce DM particles via collisions of SM particles in a laboratory environment. A search for DM particles is performed by analyzing proton-proton collisions provided by the LHC with the CMS experiment. Since the DM particles are expected to interact only very weakly, they are not directly detectable. Instead, they lead to a momentum imbalance, referred to as missing transverse energy (MET). In this thesis, a special signature of DM production is targeted, in which the DM particles are produced in association with a single top quark.

This mono-top signature is a very promising way to search for DM since the final state consisting of a top quark and MET is not possible at leading order in the SM. Consequently, any significant deviation from the SM expectation would be a strong indication for the production of DM particles.

From a theoretical point-of-view, the SM is minimally extended by the addition of a new bosonic mediator and fermionic DM particles. The mediator establishes a flavor-changing neutral current (FCNC) interaction between the SM and DM particles and is responsible for the production of DM particles in association with a top quark at leading order. This mono-top model essentially introduces two new parameters, the masses of the mediator and the DM particles. If no signal is observed, the allowed parameter space of the theoretical mono-top model is restricted via exclusion limits.

The top quark is the heaviest known elementary particle in the SM. Due to its short lifetime, it decays almost immediately after its production into a W boson and a bottom quark. Depending on the subsequent decay of the W boson into a lepton and a neutrino or a quark-antiquark pair, either a fully hadronic or leptonic final state of the top quark is realized. Due to these different decay modes, the mono-top signature can be observed in both hadronic and leptonic final states. Consequently, two different analysis channels are considered in this thesis.

In the hadronic analysis channel, the decay products of the top quark are reconstructed as a collimated spray of particles called jets. The top quark is identified by applying state-of-the-art multivariate techniques on these jets, reconstructed with large-radius jet clustering algorithms. In the case of a leptonic final state of the mono-top signature, the DM is signal is discriminated from the SM backgrounds via a kinematic observable, called transverse mass.

This thesis consists of two main parts. The general foundational elements informing this thesis are discussed in Part I. After describing the theoretical principles of the SM and BSM physics with a focus on DM in chapter 2, the experimental environment is summarized in chapter 3. Afterward, an introduction to statistical data analysis is given in chapter 4. Part II is dedicated to the search for DM produced in a mono-top signature. First, general aspects relevant to both analysis channels are discussed in chapter 5. This chapter also contains a more detailed description of the theoretical mono-top model. Subsequently, the leptonic and hadronic analysis channels are described in chapter 6 and chapter 7, respectively, in which details regarding the analysis strategies, event selection and the statistical models are given. Finally, the combination of both analysis channels is presented in chapter 8.

Part I

Foundations

2 Theoretical background

In the following chapter, the basic theoretical foundations needed in the context of this thesis are briefly introduced. After describing the SM, BSM physics with a focus on DM is introduced. Subsequently, specifics of the physics at hadron colliders are described. Finally, a short introduction on event generation and simulation is given. The natural unit system is used exclusively in this thesis, where the speed of light as well as Planck's constant are set to unity. The following sections are based on [1–5].

2.1 The Standard Model of particle physics

The SM is a theory that describes the fundamental particles and their interactions. All currently known particles and their interactions except for gravity are incorporated based on a quantum field theory (QFT) connecting classical field theory with special relativity and quantum mechanics. Consequently, every particle is described by its corresponding field. Interactions between particles are also characterized by the exchange of particles, which are therefore referred to as mediators. The theoretical description of the SM is based on the Euler-Lagrange formalism in four-dimensional Minkowski space. In general, the particle content of the SM can be divided into two groups, fermions and bosons. Fermions carry half-integer spin, whereas bosons carry integer spin. Interactions between particles are mediated by bosons with spin one. The Higgs boson is the only exception; it is a scalar boson with spin zero and does not mediate any interactions but is responsible for the mass of particles via the Brout-Englert-Higgs mechanism [6, 7]. A graphical representation of the SM is shown in figure 2.1. In the following, the fermions and all possible particle interactions in the SM are described in more detail. Subsequently, a brief introduction to the Brout-Englert-Higgs mechanism is given.

2.1.1 Fermions of the Standard Model

In general, the fermions can be grouped into three generations, which differ mostly in their masses. Each generation of particles consists of two particles. The lightest, first-generation, fermions make up the everyday matter we observe in our universe, and they are the building blocks of atoms. According to the possible interactions of the fermions, they are further grouped into leptons and quarks. Contrary to leptons, quarks carry color charge, which enables them to interact via the strong interaction. Each generation of leptons contains an electrically charged lepton with a charge of -1 in units of the elementary charge e and

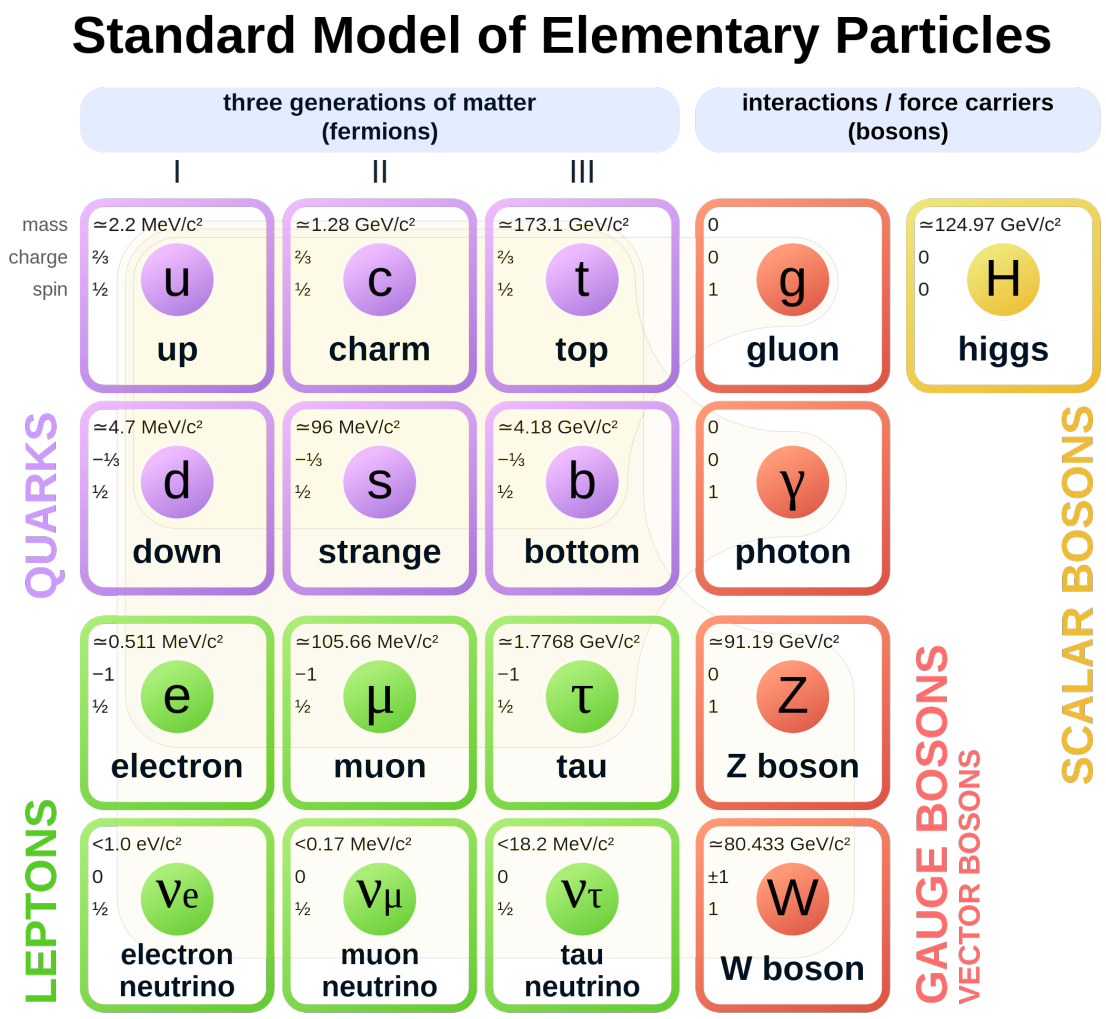

Figure 2.1: Graphical illustration of the Standard Model of particle physics. Taken from [8].

a corresponding electrically neutral neutrino. The constituents of each quark generation are distinguished by their electric charge. Up-type quarks carry an electric charge of 2/3, whereas down-type quarks carry an electric charge of $-1/3$ in units of the elementary charge e. Quarks span a large range of masses, from 2.2 MeV for the up-quark up to 172.5 GeV for the top-quark. Consequently, the up, down and strange quarks are commonly referred to as light-flavor (LF) quarks, whereas the charm, bottom and top quarks are referred to as heavy-flavor (HF) quarks.
In addition to each fermion, a corresponding antifermion is also part of the SM. The antiparticles are related to their corresponding particles via the charge conjugation operator C.

2.1.2 Particle interactions

Currently, four fundamental interactions are known in particle physics: the strong interaction, the electromagnetic interaction, the weak interaction and gravity. The SM is able to describe all interactions except for gravity based on the requirement that the Lagrangian $\mathcal{L}$ must be invariant under local transformations under a symmetry group called gauge group. In order to retain this gauge invariance additional gauge fields are introduced.

2.1.2.1 Strong interaction or Quantum Chromodynamics (QCD)

The theory describing the strong force is quantum chromodynamics (QCD), based on the non-abelian gauge group SU(3) of color transformations [9, 10]. The charge of QCD is called color, where the possible charges are red, blue and green. The corresponding anti-color charges are anti-red, anti-blue and anti-green. The strong interaction is mediated by the exchange of eight massless gluons, which are the gauge bosons of QCD. Gluons have spin one and carry both color and anti-color charges. Since gluons carry color charge themselves, self-interactions are possible. These self-interactions lead to a limited range of QCD interactions. The static strong interaction potential can be described in a semi-classical way via

$$V_{\mathrm{QCD}}(r) = \frac{4}{3}\frac{\alpha_s(r)}{r} + k \cdot r\,. \tag{2.1}$$

Here, r is the distance between two color-charged particles, α_s is the strong coupling constant and k is a constant. For different distances r or, equivalently, different energies, two different regimes can be distinguished. First, for large distances (or low energies), the potential increases linearly with a factor of $k \approx 1\,\mathrm{GeV\,fm}^{-1}$. Ultimately, the potential energy becomes large enough to generate new color-charged particles. Consequently, only color-neutral particles are able to propagate freely. Such color-free particles consist of either quark-antiquark pairs, referred to as mesons, or three and more quarks, referred to as baryons. This feature of QCD is called confinement. The second important aspect is called asymptotic freedom [11, 12]. For small distances (or high energies), the potential decreases, resulting in quasi-free color-charged particles in this regime. This asymptotic freedom offers the possibility to describe the strong interaction in a perturbative way at high enough energies.

2.1.2.2 Electroweak interaction

The electromagnetic and weak interactions are unified in the electroweak (EWK) interaction [13–15]. The gauge group of the EWK interaction is $\mathrm{SU}(2)_L \times \mathrm{U}(1)_Y$. Two charges are relevant for the EWK force. The weak hypercharge corresponds to the $\mathrm{U}(1)_Y$ symmetry, whereas the weak isospin corresponds to the $\mathrm{SU}(2)_L$ symmetry. In this theory, left-handed

fermion doublets are realized acting under the $\mathrm{SU}(2)_L$ symmetry:

$$\begin{pmatrix} \nu_i \\ l_i \end{pmatrix}_L \text{ for leptons, } \begin{pmatrix} u_i \\ d_i' \end{pmatrix}_L \text{ for quarks,} \tag{2.2}$$

where i denotes the generation index and u_i an up-type quark. The flavor-eigenstate of a down-type quark is given by d_i'. Using the Cabibbo-Kobayashi-Maskawa (CKM) matrix V_{ij}, the quark flavor eigenstates can be expressed in terms of the corresponding mass eigenstates d_i [16, 17]:

$$d_i' = \sum_j V_{ij} d_i \,. \tag{2.3}$$

In contrast to the left-handed fermion doublets, the right-handed fermions $d_{i,R}$, $u_{i,R}$ and $l_{i,R}$ transform as singlets under the $\mathrm{SU}(2)_L$ symmetry. In total, four gauge bosons are introduced: three W bosons with a corresponding coupling constant g for the $\mathrm{SU}(2)_L$ symmetry and one B boson with a coupling constant g' for the $\mathrm{U}(1)_Y$ transformation. However, these fundamental gauge bosons are not physically observable. Instead, two electrically charged W bosons are realized in addition to the Z boson and photon γ, both carrying no electric charge, as a superposition of the fundamental gauge bosons. Interestingly, experimental measurements show that the W and Z bosons are massive, whereas the photon is massless. However, due to the symmetry of the SM, no straightforward addition of mass terms to the Lagrangian is possible. This puzzle is solved by the Higgs mechanism, which is discussed in the following section. Due to the large masses of the W and Z boson, the weak interaction is only short-ranged.

2.1.3 Brout-Englert-Higgs mechanism

As mentioned in the previous section, the SM is not able to generate the masses of the W and Z bosons. Instead, the masses are generated via the Higgs-Englert-Brout mechanism via EWK symmetry breaking [6, 7, 18]. Also, the mass generation of fermions can subsequently be explained via Yukawa-type interactions. In the Higgs-Englert-Brout mechanism, an additional left-handed SU(2) doublet Φ_L consisting of an electrically neutral as well as charged component, ϕ^0 and ϕ^+, respectively, is introduced, called Higgs field:

$$\Phi_L = \begin{pmatrix} \phi^+ \\ \phi^0 \end{pmatrix} . \tag{2.4}$$

Being a complex field, four degrees of freedom are realized. The corresponding Higgs Lagrangian is given by

$$\mathcal{L}_{\text{Higgs}} = \left(D_\mu \Phi^\dagger\right)\left(D^\mu \Phi\right) - V(\Phi). \tag{2.5}$$

with the covariant derivative D_μ ensuring the correct gauge invariance and the potential $V(\Phi)$. The potential $V(\Phi)$ is given by

$$V(\Phi) = \mu^2 \left(\Phi^\dagger \Phi\right)^2 + \lambda^2 \left(\Phi^\dagger \Phi\right). \tag{2.6}$$

The first term of equation (2.5) incorporates the kinetic term of the Higgs doublet and its interaction with the EWK gauge bosons W and B. If $\mu^2 < 0$, a non-vanishing vacuum expectation value (VEV) of the Higgs field Φ is realized and the ground state of the doublet takes the form

$$\langle \Phi \rangle = \begin{pmatrix} 0 \\ v \end{pmatrix} \text{ with } v = \sqrt{-\frac{\mu^2}{2\lambda^2}}. \tag{2.7}$$

By expanding the potential around the VEV and choosing the neutral component such that the $U(1)_Y$ symmetry remains unbroken, the field Φ can be expressed as

$$\Phi = \begin{pmatrix} 0 \\ v + H \end{pmatrix}. \tag{2.8}$$

Consequently, by using equation (2.5) three of the four degrees of freedom are absorbed such that the physical EWK bosons gain their masses

$$\begin{aligned} m_W^2 &= \frac{g^2 v^2}{4} \\ m_Z^2 &= \frac{\left(g^2 + g'^2\right) v^2}{4}. \end{aligned} \tag{2.9}$$

The last degree of freedom corresponds to the Higgs boson with a mass of

$$m_H^2 = \sqrt{2\lambda} v. \tag{2.10}$$

Fermion masses are incorporated by adding Yukawa-type interactions to the Lagrangian. In these interactions, the Higgs doublet couples to fermion fields in a gauge invariant way. Consequently, after symmetry breaking, the fermions acquire masses via the VEV of the Higgs field:

$$m_f = \frac{y_f v}{\sqrt{2}}, \tag{2.11}$$

with y_f being the Yukawa coupling strength of fermion f to the Higgs field. In summary, the Brout-Englert-Higgs mechanism generates the masses of the fermions and bosons via EWK symmetry breaking and adds the corresponding Yukawa couplings and the mass of the Higgs boson as free parameters to the SM.

2.2 Physics Beyond the Standard Model (Dark Matter)

Over the last decades, the SM has been successfully tested and confirmed by numerous experiments. However, despite the tremendous success of the SM, there are still several open questions that cannot be explained by the SM. Examples of the shortcomings of the SM are the existence of dark matter and dark energy, the origin of neutrino masses, the hierarchy problem or the missing description of gravity. Consequently, the SM is not the final theory of nature and has to be extended. In the following, aspects of DM are discussed in more detail based on [19, 20].

Evidence for Dark Matter

Already in the 1930s Fritz Zwicky estimated the mass of the Coma Cluster [21, 22] based on the velocity dispersion of the galaxies in the cluster. This mass estimate was much larger than the mass estimated based on the luminous galaxies directly. Hence, a large amount of non-luminous matter (DM) was required to explain the observed velocity dispersion. Similar observations were confirmed on galactic scales later on. One prominent example is the measurement of rotation curves [23–25] pioneered by V. Rubin and J. Ford. In such rotation curves, the rotation velocities of objects inside a galaxy or galaxy cluster are measured as a function of the distance from the center. Such a curve is shown in

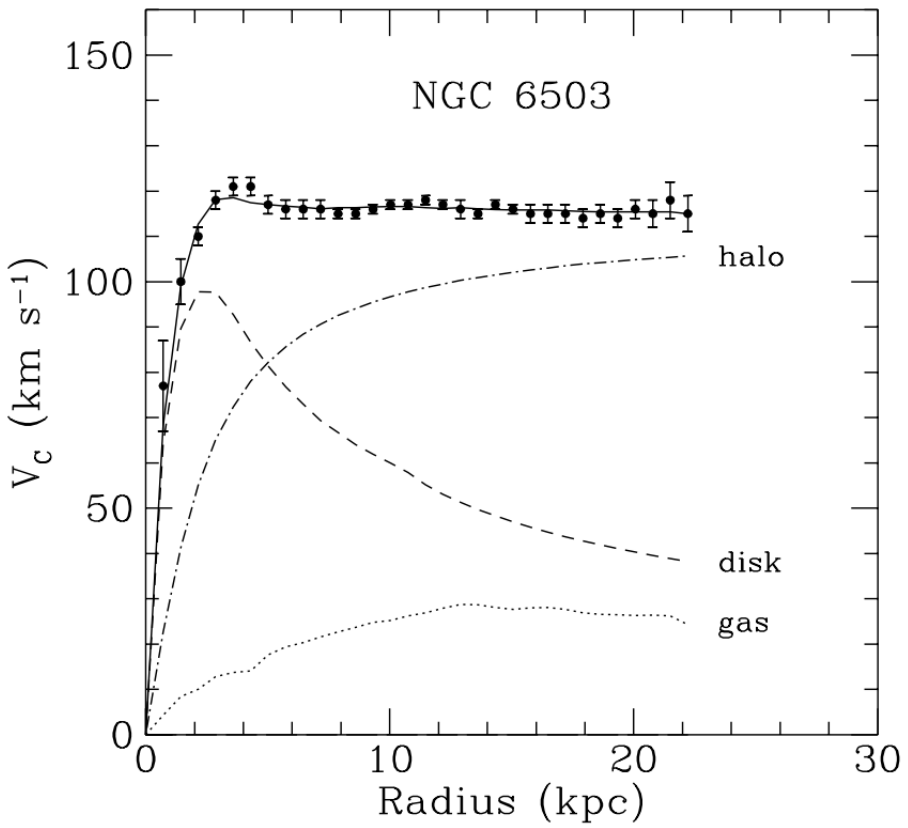

Figure 2.2: Roation curve for the galaxy NGC6503. The measurements are shown as black points. The dashed and dotted curves correspond to the predictions based on the observed masses in the disk of the galaxy as well as gas, respectively. The dot-dash curve illustrates an additional contribution due to a hypothetical DM halo. Taken from [26].

figure 2.2 for the galaxy NGC6503. The velocities are constant with increasing distance from the galactic center. This constant velocity is in contrast to the expected behavior of luminous matter distribution shown as dotted and dashed lines. A possible explanation is the existence of a non-luminous matter component in the galactic halo.

Another piece of evidence on galactical scales is given by gravitational lensing effects [27]. In gravitational lensing, the light of a distant object is bent by the gravitational field of a massive object. Consequently, by analyzing the strength of the lensing effect, the mass of the lensing object can be estimated. This is shown in figure 2.3 for the merger of two sub-clusters within the galaxy cluster 1E0657-558 as green contour lines. The merger in visible light is shown on the left-hand side, whereas the right-hand side corresponds to an X-ray image. The X-rays are emitted from hot gas inside this merger and correspond to the main contribution of baryonic matter. Since these two distributions do not match each other, another form of nonbaryonic matter is required to explain the observed lensing effect. Hence, the existence of DM is supported by the observations of gravitational lensing.

Interestingly, the existence of DM is also supported on cosmological scales. During the evolution of the universe after the Big Bang, the universe cooled down due to expansion. Eventually, the energies were low enough such that stable atoms were formed. During this recombination period, the universe became transparent and the CMB was emitted [29]. These CMB photons are still present today and provide a picture of the

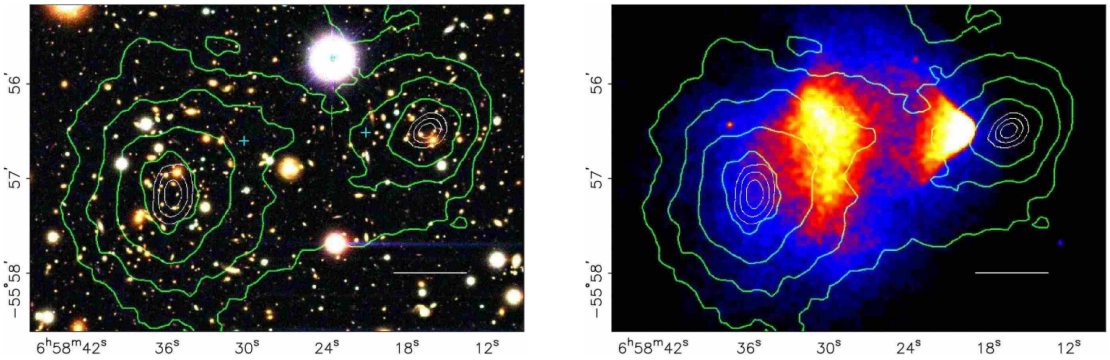

Figure 2.3: Shown is the merger of two sub-clusters within the galaxy cluster 1E0657-558. The left-hand side shows the image obtained from visible light. The right-hand side shows the same image in X-ray light. In both pictures the mass distribution reconstructed based on gravitational lensing is overlaid in green. Taken from [28].

entire universe at an age of about 380,000 years. To first order, the CMB spectrum is essentially a perfect blackbody radiation spectrum with a temperature of 2.725 K. Only very small temperature fluctuations in the order of 10^{-5} are present. By deploying an angular correlation analysis, a power spectrum can be obtained. This power spectrum is shown in figure 2.4 for the latest measurement from the Planck experiment [30]. The measurement is shown as red points, whereas the light blue lines illustrate the best fit to the cosmological model, referred to as ΛCDM model. The lower panel illustrates the difference between the data points and the best-fit model. The different peaks observed in this power spectrum are due to small over- and under-densities of matter at the moment of recombination, leading to acoustic oscillations. Consequently, the peaks can be used to infer information on the energy content in the universe today. The height of the first peak yields the total energy density of the universe, whereas the ratio of baryonic to dark matter energy density can be inferred from the second and third peaks. In summary, measurements of the CMB suggest that the energy content of DM (relic density) in the universe should be approximately five to six times larger than the energy content of the visible matter.

Several different models have been proposed to explain the existence of DM. In the context of particle physics proposed models predict a wide range of masses for DM particles, reaching from $\mathcal{O}$ (µeV) for axions to $\mathcal{O}$ (TeV) for weakly interacting massive particles (WIMPs) as explained in the following.

2.2.1 Thermal freeze-out and weakly interacting massive particles (WIMPs)

As discussed in the previous section, baryonic matter described by the SM is not sufficient to explain the observed matter distribution in the universe. Hence, the existence of DM is required. Under the assumption that DM is made up of particles the observed relic density can be explained by thermal freeze-out. In the early stages of the universe, the temperature was high enough such that the DM particles were created and annihilated in equilibrium. As the universe expanded, the temperature decreased. Eventually, when the interaction rate became smaller than the expansion rate of the universe, this equilibrium was broken and the abundance of DM particles was fixed. Consequently, the relic density is determined by the mean interaction cross section of the DM particles. The relic density is shown in figure 2.5 for different mean interaction cross sections in addition to the measurement of

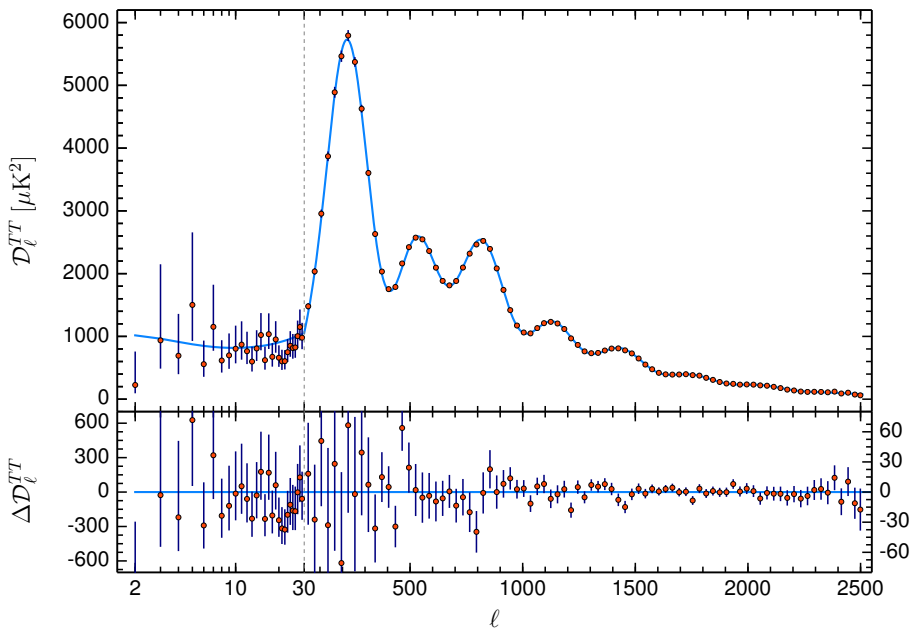

Figure 2.4: Power spectrum of the CMB. Shown is the latest measurement from the Planck satellite as red points. The light blue lines illustrate the best fit to the cosmological model. The lower panel illustrates the difference between the data points and the best-fit model. Taken from [30].

the relic density provided by the Planck experiment. It can be seen that the measured relic density is obtained by assuming a mean interaction cross section corresponding to the interaction strength of the weak force for DM particle masses in the range of $\mathcal{O}\,(10\,\mathrm{GeV})$ to $\mathcal{O}\,(1\,\mathrm{TeV})$. These considerations suggest the existence of a WIMP. Furthermore, the rather large mass of the WIMP leads to a non-relativistic (cold) form of DM which is in agreement with the observed structure formation in the universe [31]. Current state-of-the-art searches for WIMPs are discussed briefly in section 3.4.

2.2.2 Non-thermal production of DM

Contrary to the previously discussed thermal freeze-out, DM particles can also be produced non-thermally [33]. A prime example of such a non-thermally produced DM particle is the axion, or more generally axion-like particles (ALPs) with a very light mass in the range of $\mathcal{O}\,(10^{-5}\,\mathrm{eV})$. From a theoretical point of view, the axion is motivated in the context of solving the strong CP problem [34]. Experimental measurements suggest that the electric dipole moment of the neutron is vanishing small in the order of $10^{-26}\,\mathrm{e}\cdot\mathrm{cm}$ [35]. This small electric dipole moment could be explained by adding a term to the QCD Lagrangian without violating any gauge symmetries by adding a free parameter θ. However, in order to explain the smallness of the electric dipole moment, the parameter θ needs to be very small as well, which leads to an unnatural fine-tuning of the theory. A possible solution to this strong CP problem is given by the introduction of another global $U(1)$ symmetry, called Peccei-Quinn symmetry. This symmetry is spontaneously broken leading to a dynamical parameter $\theta(x)$, referred to as axion field. The smallness of θ is then explained by the fact, that the corresponding potential vanishes in minimum. The mass of the axion is inversely proportional to the breaking scale of the Peccei-Quinn symmetry. Consequently, the axion mass is very small, and the production mechanism of axions is non-thermal. Despite its light mass the axion still provides a candidate for non-relativistic (cold) DM, since it is produced essentially at rest in the early universe.

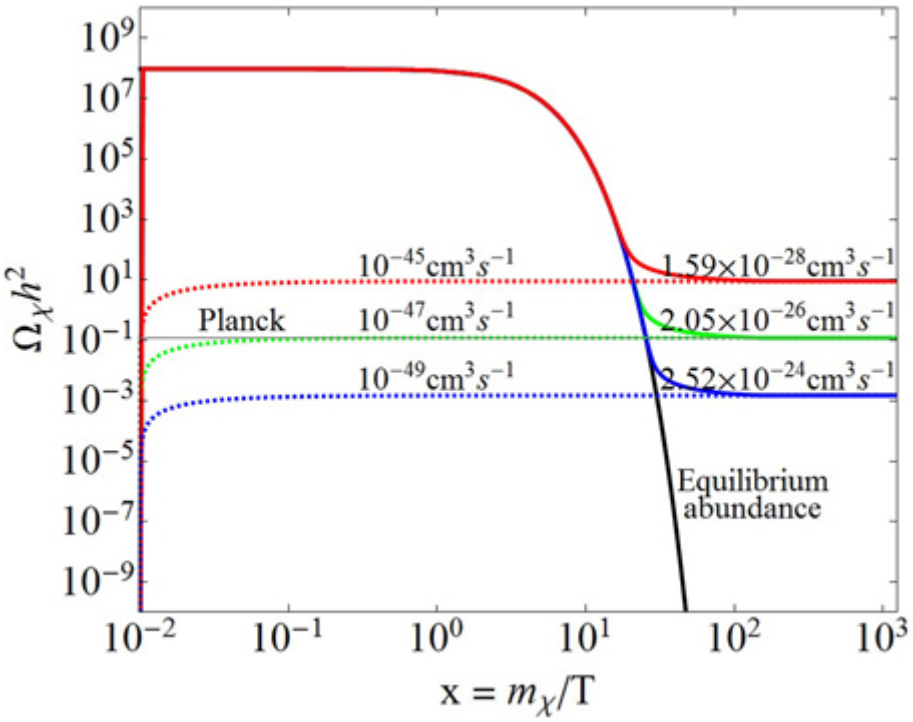

Figure 2.5: Schematic illustration of the thermal freeze-out of DM particles. Shown is the relic DM density as a function of the DM particle mass divided by the temperature T for different mean interaction cross sections in addition to the measurement of the relic density provided by the Planck experiment. Taken from [32].

ALPs are generated similarly to axions, however, with a much higher breaking scale. Consequently, the couplings and masses of ALPs can be even lower than for axions. However, ALPs are not directly able to solve the strong CP problem. From an experimental point of view axions and ALPs can be probed via a potential axion-photon interaction [36].

2.2.3 Simplified models

As made clear by the previous section, extensions to the SM are necessary to explain the observation of DM. However, such extensions need to be designed in a way that the observed confirmations of predictions of the SM are not violated. In general two extremes are possible. On the one hand, the extensions can be designed in a way that the SM is recovered in the limit of low energies. In such effective field theorys (EFTs), the interaction between the SM and DM particles is given by an effective contact interaction. On the other hand, complete BSM theories are possible. In such models, the SM is, again, recovered in the limit of low energies. However, at high energy scales, a full set of new interactions is realized accompanied by a potentially large number of new particles. Accordingly, a potentially large number of new parameters is introduced. Simplified models are situated in between these two extremes [37] and are considered in this thesis. Contrary to effective field theories, simplified models do not assume effective contact interactions. However, only a small number of generic new particles and corresponding interactions are introduced. Usually, two new particles are proposed. One of these particles is a WIMP candidate, whereas the other particle is a mediator particle which enables the interaction between the SM and DM particles. This mediator can either be exchanged in the s-channel or the t-channel. One advantage of these simplified models is that they only introduce a small number of new parameters such as the masses of the two new particles as well as

the coupling strength of the mediator to SM and DM particles. Additionally, since not only effective contact interactions are considered, the models are very suitable in an energy range in which the EFT approach is not yet applicable.

2.3 Physics at hadron colliders

In the following, the most important aspects of physics at hadron colliders are discussed. Two essential parameters of a hadron collider are the center-of-mass energy E_{cm} and the (integrated) luminosity L. The luminosity is used to estimate how many interactions or events N of a given process are expected to be observed in a given time interval Δt via

$$N = \sigma \cdot L = \sigma \cdot \int_{t}^{t+\Delta t} \frac{dL}{dt'} dt'. \tag{2.12}$$

The instantaneous luminosity is given by $\frac{dL}{dt'}$, whereas σ denotes the cross section of the process. While the instantaneous luminosity depends on the parameters of the collider such as the beam intensity or the frequency at which particles collide, the cross section is a property of the process under consideration.

In order to calculate the cross section, one needs to take into account that not elementary particles but rather composite hadrons made up of quarks and gluons are colliding. Hadrons exist due to the confinement property of QCD, i.e. at large values of the strong coupling constant. Hence, it is not possible to describe the interaction of quarks and gluons inside the hadron by perturbation theory. However, these long-range interactions inside the hadron can be separated from the hard interaction of the colliding partons which happens at high energies and hence small distances, where the strong coupling constant is small. This factorization approach allows calculating the hard partonic interaction in a perturbative manner in QCD. The energy scale at which this factorization is valid is called the factorization scale μ_{F}. Consequently, the total cross section of a proton-proton collision into a final state X ($pp \to X$) can be written as

$$\sigma_{pp\to X} = \int dx_1 \mathrm{PDF}_{1,p}\left(x_1, \mu_{\mathrm{F}}^2\right) \int dx_2 \mathrm{PDF}_{2,p}\left(x_2, \mu_{\mathrm{F}}^2\right) \hat{\sigma}\left(x_1 p_1, x_2 p_2, \mu_{\mathrm{F}}^2, \mu_{\mathrm{R}}^2\right). \tag{2.13}$$

In this equation, the momentum of the colliding protons is denoted by p_1 and p_2. The momentum fraction of the interacting partons is given by x_1 and x_2. The probability to find a parton with momentum fraction x inside a proton is parametrized by the parton distribution function (PDF), which is a function of the momentum fraction x and an energy scale which is chosen to be μ_{F} in this case. The subscripts 1 and 2 denote the two partons probed inside the respective protons. The partonic cross section is given by $\hat{\sigma}$. This partonic cross section depends on the momenta of the interacting partons $x_1 p_1$ and $x_2 p_2$, the factorization scale μ_{F} and an additional energy scale, called renormalization scale μ_{R}. This renormalization scale is introduced in the calculation of the partonic cross section to ensure that the perturbative expansion is convergent. It should be noted here, that it is currently not possible to predict the PDFs from first principles purely based on theoretical considerations. Instead, they are obtained by dedicated experimental measurements. However, the evolution of the PDFs to different energy scales can be calculated perturbatively using the Dokshitzer-Gribov-Lipatov-Altarelli-Parisi (DGLAP) evolution equations [38–40]. The PDFs considered in this thesis are derived by the NNPDF collaboration [41]. The hard partonic cross section $\hat{\sigma}$ on the other hand is a purely theoretical input. It is calculated by considering Fermi's golden rule and perturbation theory.

2.4 Event generation and simulation

A common approach in high-energy physics at colliders is to compare the observed data with predictions from theoretical models. In order to ensure comparability between the underlying physics of the hard interaction and the observed data, event simulations are deployed. These simulations rely on Monte Carlo (MC) methods and are therefore often referred to as MC simulations. An overview and more in-depth details can be found in the *Monte Carlo Event Generators* review in [4] and in [42]. The main aspects of MC simulations are briefly discussed in the following.

Hard process

The first step is to generate the hard process, i.e. the interaction of the colliding partons. For this simulation, the aforementioned factorization approach is utilized. Consequently, the PDFs are considered in conjunction with the hard partonic cross section. For the partonic cross section the matrix element is needed together with the final-state phase space integral for the final state considered. The matrix element is calculated based on fixed-order perturbation theory. The integration of the phase space integral, on the other hand, is performed by using MC methods due to its often high dimensionality. These MC methods also allow to directly numerically sample from the PDFs. Software tools such as MadGraph5_aMC@NLO [43, 44] and Powheg [45–47] allow the generation of the hard process in a fully automated way at next-to-leading order (NLO) in QCD perturbation theory for many processes.

Parton shower

Due to the nature of QCD, color-charged final-state particles emit gluons. Since gluons are also color-charged, a cascade of strong interacting particles evolves. This process is called parton shower (PS). Since the energy of the particles in the PS decreases, the perturbative regime ends and the non-perturbative effects are approximated by $1 \to 2$ parton splittings. The stochastic process of the PS is therefore simulated by using MC methods.

Hadronization

Due to the confinement property of QCD, the particles generated in the PS are not able to propagate freely. Instead, color-neutral hadrons are formed. The process of this hadronization is subsequent to the simulation of the PS. Since perturbative QCD is not applicable in this process, phenomenological models, such as the Lund string model [48, 49] are deployed.

Both the simulation of the PS and the hadronization are realized by using software tools such as Pythia 8.2 [50–52].

Underlying event

The underlying event describes the interactions of additional partons present in the colliding protons. Since the hard process removes one parton from the proton, the remaining proton remnant is not color-neutral anymore. Consequently, the remaining partons are subject to additional interactions with subsequent hadronization. These multiple parton-parton interactions (MPI) lead to additional hadronic activity in an event and are referred to as underlying event. Since the MPI can happen at various energy scales, a perturbative approach is considered for high-momenta interactions, whereas phenomenological models are used for low-momentum interactions. These phenomenological models are tuned to match the observations in data.

3 Experimental environment

The experimental environment used to collect the experimental data considered in this thesis is described in the following. First, the LHC introduced in section 3.1. The LHC is a storage ring capable of producing proton-proton collisions with a center of mass energy of up to 14 TeV. Several experiments are situated at collision points of the LHC, including the CMS experiment, which is described in section 3.2. Following the introduction of the CMS experiment, the reconstruction of physics objects in the CMS detector is discussed. Finally, general aspects of DM searches at hadron colliders are discussed.

3.1 The Large Hadron Collider

The LHC is a particle collider situated at CERN. Being the last stage of a accelerator complex, the LHC is the largest and most powerful particle collider ever built, achieving a center of mass energy of up to 14 TeV for proton-proton collisions. In the following, the main aspects of the accelerator complex as well as the LHC itself are described, based on [53–56].

In order to achieve such unprecedented energy, a whole chain of particle accelerators is needed. Figure 3.1 shows a schematic of the accelerator complex at CERN.

First, electrons are removed from hydrogen atoms via a strong electric field, creating protons. These protons are then injected into a Linear Accelarator (LINAC) called LINAC2/4, increasing the proton energy up to 50 MeV. Three circular accelerators are used to further accelerate the protons before injecting them into the LHC. The first circular accelerator is the Proton Synchrotron Booster (PBS), which brings the energy of the protons up to 1.4 GeV and splits the continuous proton beam into bunches. Subsequently, the Proton Synchrotron (PS) and the Super Proton Synchrotron (SPS) are used to achieve energies of up to 25 GeV and 450 GeV, respectively. The LHC is the last stage of the accelerator complex and is used to achieve the final energy of currently 13.6 TeV.

Being a circular collider, strong magnetic fields are needed to keep the protons on the desired trajectory. Dipole magnets are used to deflect the protons. In order to keep the protons in a circular orbit, the dipole magnets achieve a field strength of around 8 T. Such high field strengths are possible due to the use of superconducting magnets, which are cooled down to a temperature of 2 K via superfluid helium. In addition, quadrupole and higher-order magnets are used to focus and stabilize the proton beams.

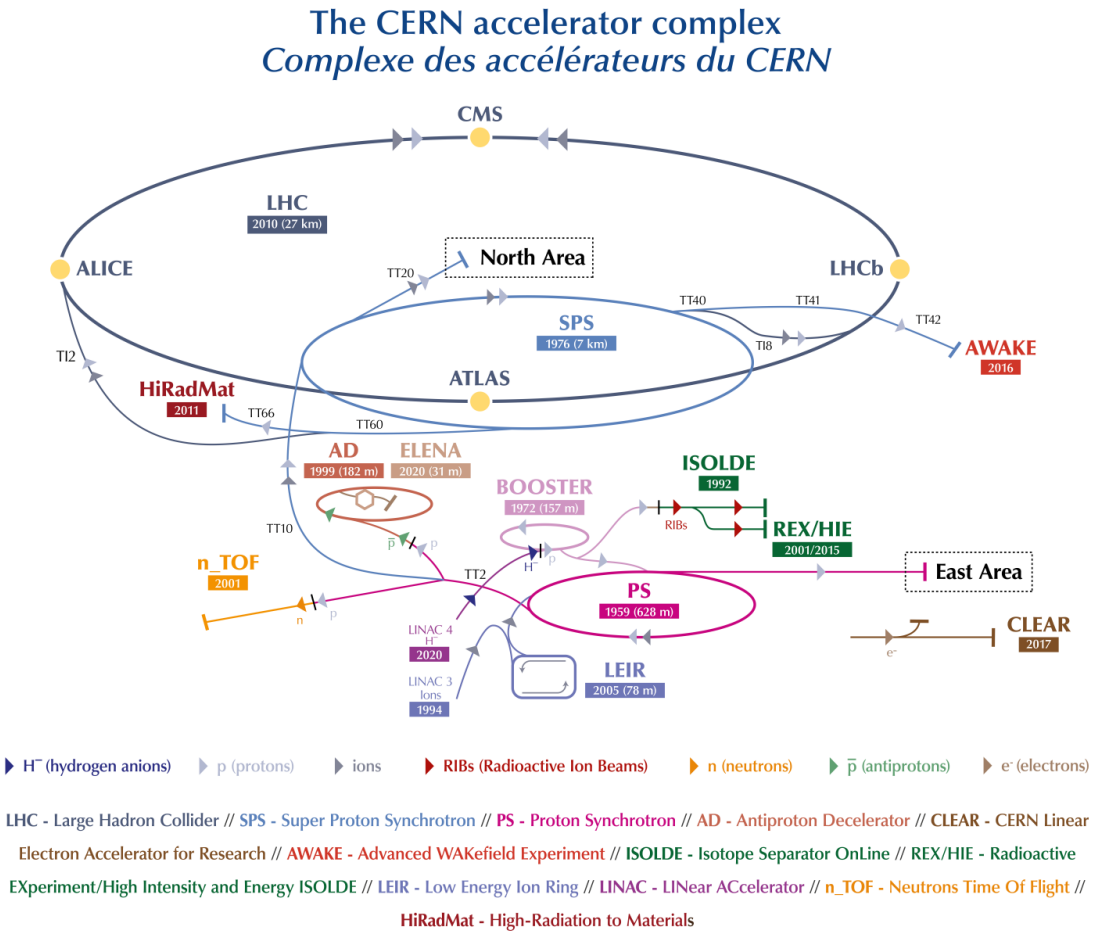

Figure 3.1: Layout of the LHC accelerator complex. Taken from [57].

The actual acceleration of the protons is achieved by using radio-frequency cavities. In these cavities, electromagnetic waves with a frequency of 400 MHz are established, accelerating the proton bunches and replenishing the energy lost due to the synchrotron radiation.

After achieving the final energy, the protons are brought to collision at several interaction points. At these interaction points, specialized detectors are situated.

3.2 The Compact Muon Solenoid

The CMS detector can be used to study a wide range of physics topics due to being designed as a general-purpose detector. These studies include precise measurements of SM processes as well as BSM physics. The analysis of this thesis considers data taken with the CMS detector in the years from 2016 to 2018. Figure 3.2 shows a schematic of the CMS detector.

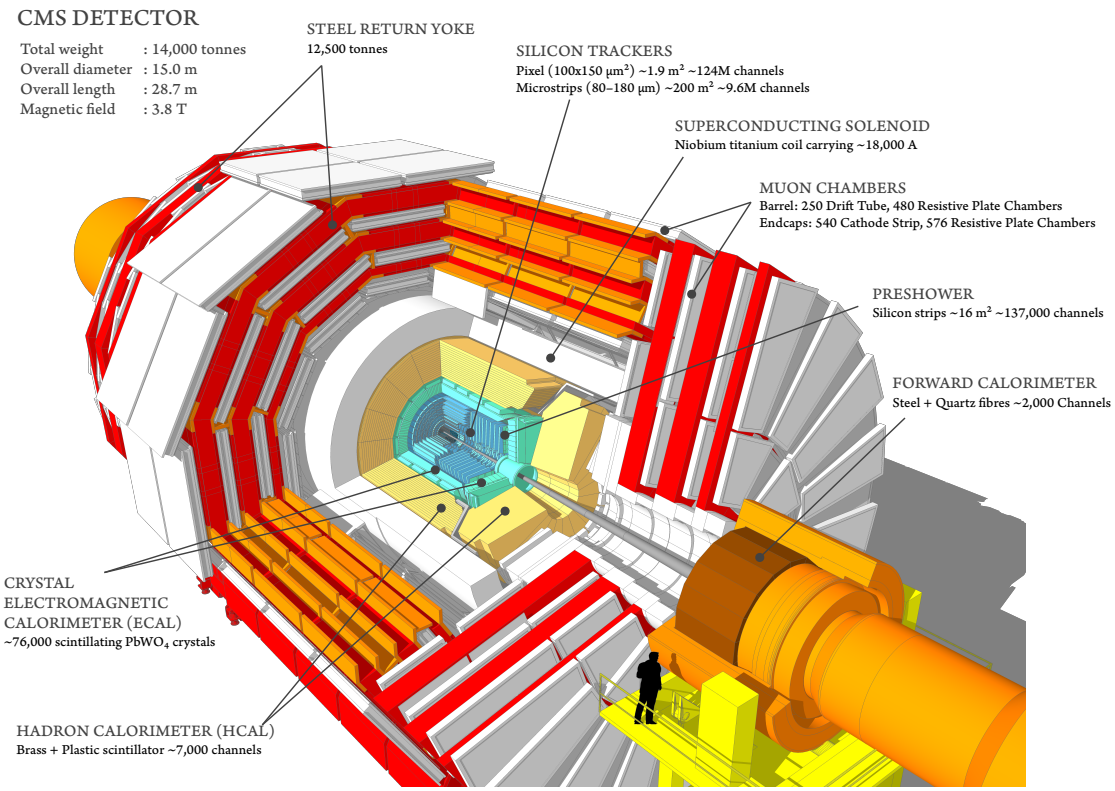

Figure 3.2: Schematic of the CMS detector. Taken from [58].

The detector consists of several subdetectors constructed in an onion-like structure around the interaction point. Each of these subdetectors serves a particular purpose. The most essential subdetectors will be introduced in the following based on [59] where more details can be found.

3.2.1 Coordinate system and conventions

A right-handed Cartesian coordinate system is used with the origin at the interaction point and the x-axis pointing towards the center of the LHC. Consequently, the y-axis points vertically upwards and the z-axis points along the beamline in clockwise direction.

The momentum of the protons perpendicular to the z-axis is negligible. Since not the protons themselves but rather their constituents, the partons, are interacting in a collision, their momentum in the transverse plane is also negligible. However, since the initial

momentum component along the z-axis is unknown, observables invariant under Lorentz-transformations along this direction are of special interest.

The transverse momentum is defined as

$$\vec{p}_{\mathrm{T}} = (p_x, p_y, 0)\,,\ p_{\mathrm{T}} = |\vec{p}_{\mathrm{T}}| = \sqrt{p_x^2 + p_y^2}. \tag{3.1}$$

The rapidity is a function of the energy E as well as the z-component p_z of the momentum of a particle:

$$y = \frac{1}{2} \ln \frac{E + p_z}{E - p_z}. \tag{3.2}$$

For high-energy particles, the rapidity is approximately equal to the pseudo-rapidity η

$$\eta = -\ln \tan \frac{\theta}{2} \tag{3.3}$$

with the polar angle θ, which can directly be measured by the detector.

The spatial distance ΔR between two particles in the plane of the azimuthal angle ϕ and the pseudo-rapidity η is defined as

$$\Delta R = \sqrt{\Delta\eta^2 + \Delta\phi^2}, \tag{3.4}$$

where $\Delta\eta$ and $\Delta\phi$ denote the difference in pseudo-rapidity and azimuthal angle of two particles, respectively.

3.2.2 Tracking detectors

The innermost part of the CMS detector consists of the silicon tracking detectors. These detectors aim at reconstructing the trajectories of charged particles. The working principle of a silicon tracker is based on a diode in reverse bias direction. If a charged particle traverses the depletion zone, free charge carriers are created. These charges induce a voltage that can be measured by dedicated readout electronics. More details on silicon tracking detectors can be found in [60]. By layering such silicon detectors, the trajectories, as well as primary and secondary interaction vertices of charged particles, can be reconstructed. The magnetic field of 3.8 T provided by the superconducting solenoid covers the whole tracking system. Since the trajectory of a charged particle is bent within a magnetic field depending on its momentum, it is possible to infer the sign of the electric charge as well as the momentum of the reconstructed particles by measuring the curvature of the trajectory.

The tracking system is further split into two parts, both arranged in a cylindrical (barrel region) as well as disk-like (endcap region) structure. The innermost part consists of pixel detectors. These pixel detectors provide the advantage of a 2D position measurement with high granularity. In 2017 an upgrade was performed, where a new four-layer pixel detector was installed. This upgrade significantly improved the tracking performance [61]. After the pixel detectors, the silicon strip detectors are situated. Although only providing a 1D position measurement in general, the setup of several stereo layers effectively yields 2D information. The lower granularity of the strip detectors is sufficient due to the lower flux of particles.

Considering the cross section for inelastic proton-proton scattering as well as the luminosity of the LHC in Run 2, approximately 34 interactions per bunch crossing are expected on average. The primary vertex is defined as the one with the largest sum of squared momenta $\sum p_{\mathrm{T}}^2$, whereas the remaining ones are referred to as pileup (PU). Due to the excellent resolution of the tracking detector, also secondary vertices arising for example from B-hadron decays, are measurable. The tracking system plays a crucial role in identifying the primary vertex and, therefore, in reconstructing the physics objects of interest.

More in-depth information on the CMS tracking system can be found in [62, 63].

3.2.3 Calorimeters

Calorimeters are used to measure the energy of particles. Since the material interaction is different for electromagnetic interacting particles, such as electrons/positrons and photons, and hadronically interacting particles such as pions and kaons, the calorimeters are split into two parts.

First, the electromagnetic calorimeter (ECAL) is used to measure the energy of mainly electrons and photons. The three main interactions of charged particles and photons in matter are ionization, bremsstrahlung and pair production, where the latter two dominate for high energies. If an energetic photon interacts with the material, it can produce an electron-positron pair. These electrons/positrons will again interact with the material and emit bremsstrahlung, creating a photon in turn. Consequently, a cascade of secondary particles is produced. This results in an electromagnetic shower in the ECAL. The energy of the particle can be inferred by measuring the energy deposited by the secondary particles. In CMS, a $PbWO_4$ crystal calorimeter is used, providing a large energy loss due to its high density. Additionally, $PbWO_4$ provides a detection mechanism of the energy lost by the secondary particles due to its scintillation properties. As the energy of the secondary particles in the electromagnetic shower gets lower, ionization becomes the dominant interaction process. The ionized atoms emit light (scintillation), which is detected. The energy of the primary particle can be inferred by measuring the amount of scintillation light emitted since the number of scintillation photons is directly proportional to the number of secondary particles. Further details can be found in [64–67].

The working principle of the CMS hadron calorimeter (HCAL) is similar to the ECAL. However, since the hadronic interaction length is much larger than the electromagnetic interaction length a technically impractical large calorimeter would be required. By alternating absorber and scintillator layers, the calorimeter size can be significantly reduced. Such calorimeter setups are referred to as sampling calorimeters. In CMS brass is used as absorber material providing a high nuclear interaction cross section due to its high density. An incoming hadron will interact with the brass nuclei, creating a cascade of secondary particles. By layering sections of the absorber with pla the energy loss and, thus, the energy of the primary hadron can be measured. Further details including performance numbers can be found in [68–72].

3.2.4 Muon System

Due to the high absorption of the HCAL, only very few particles should penetrate the calorimeters. However, muons only interact very weakly in material and thus can pass the calorimeters as the only visible particles without depositing all their energy. Muon chambers are situated outside the calorimeters within the iron return yoke to provide improved detection and measurement of mouns. Similar to the silicon tracker, the muon chambers can measure the position of a traversing muon with high precision and are therefore utilized to reconstruct the trajectories of muons as well as their momentum. However, contrary to silicon detectors, the muon chambers consist of gaseous detectors, where different technologies, such as drift tube chambers, cathode drift chambers, and resistive plate chambers, are deployed in CMS. Further details can be found in [73, 74].

3.2.5 Trigger System

Due to the bunch crossing frequency of 40 MHz of the LHC, resulting in proton-proton collisions every 25 ns, it is currently technically impossible to save the full information of all proton-proton collisions, referred to as events. Therefore, a trigger system [75] is deployed

to select events that might be of interest. The CMS trigger system is split into two parts, the level 1 (L1) trigger and the high-level trigger (HLT).

Custom electronics are deployed in the L1 trigger. These specialized electronics are able to perform a crude but fast reconstruction of signatures compatible with being electrons, photons, muons, τ leptons, jets or missing transverse momentum. In order to do this, information on the calorimeters as well as the muon system is considered and processed such that a decision to keep or reject an event is made within 4 µs. If the L1 trigger accepts an event, the event is kept, and the detector data is passed to the HLT. The L1 trigger is capable of reducing the rate from 40 MHz to 100 kHz. Further details can be found in [76, 77].

The second stage of the CMS trigger system is the HLT. The L1 trigger reduces the data rate enough in order to perform a more detailed object reconstruction utilizing information from all the subdetectors. This event reconstruction utilizes more complex algorithms, which are the same as in the offline event processing, and is therefore run on a dedicated computer farm. These reconstruction techniques will be briefly introduced in section 3.3. The HLT offers a classification of events based on so-called trigger paths. These trigger paths are defined based on the presence of a certain object or a certain kinematic signature. If no HLT path is passed, the event is rejected. This way, the HLT is capable of reducing the event rate further to the order of 100–1000 Hz. More technical details can be found in [76, 77].

3.3 Reconstruction of physics objects

The reconstruction of physics objects is the process of reconstructing the kinematic properties of the particles in an event and combining them to the objects, which are used in data analysis. Since this reconstruction is crucial for the analysis of the data as well as the HLT, the most important aspects will be discussed in the following.

3.3.1 Particle-flow algorithm

The foundation of the reconstruction of all physics objects in CMS is the particle-flow (PF) algorithm [78]. By combining information from the different subdetectors, the full strength of the CMS detector is utilized. The algorithm is capable of reconstructing all final-state particles in an event. In the following, the reconstruction of the most important particles is described.

3.3.2 Muon reconstruction

The main subdetectors used for the reconstruction of muons are the muon chambers and the slicon tracker. The PF algorithm considers three types of muons based on requirements concerning the associated tracker reconstruction. Standalone muons only consider tracks based on information from the muon chambers. Global muons are required to match their tracks reconstructed in the silicon tracker with the tracks reconstructed in the muon chambers. If these two tracks are compatible, a new track is reconstructed, considering both the hits in the silicon tracks as well as in the muon chambers. The third type of muons are tracker muons. For these muons, silicon tracks are extrapolated to the muon chambers. If at least one muon segment matches the extrapolated track, the muon is considered a tracker muon. Subsequently to this muon classification, additional requirements are applied before considering a muon as a PF muon. These additional requirements aim at distinguishing between isolated muons originating from the hard process and non-isolated muons originating from hadron decays.

3.3.3 Electron reconstruction

For the reconstruction of electrons, mainly the information from the ECAL as well as the tracker is used. The PF algorithm considers different reconstruction algorithms for isolated and non-isolated electrons. For isolated electrons, the PF algorithm considers the ECAL energy deposits as a seed, where an extrapolation back to the hits in the inner tracker is performed. Similar to the processes inside the ECAL, electrons passing through the tracker might emit photons due to bremsstrahlung. Therefore, ECAL entries within a specific cone (supercluster) are considered in order to account for the radiated energy. The matching of the ECAL clusters to the inner track is not possible for non-isolated electrons occurring inside jets due to the presence of additional ECAL clusters originating from other charged particles. Consequently, the reconstruction of non-isolated electrons is seeded by the inner tracker, where an iterative tracking algorithm is deployed. Afterward, both electron collections are subject to further additional selection and identification criteria to yield the final reconstructed electrons. Since the two different seeding methods differ, additional corrections are applied.

3.3.4 Photon reconstruction

Photons are expected to deposit their energy in ECAL. The corresponding energy is reconstructed via superclusters similar to electrons. Contrary to electrons, photons do not carry electric charge and are not expected to leave a track in the inner tracker. However, a photon might convert into an electron-positron pair inside the tracker material, leaving tracks. Such conversions are accounted for by the PF algorithm. Finally, a photon candidate needs to be isolated from other tracks and its energy deposit in the ECAL and HCAL needs to be compatible with an electromagnetic shower.

3.3.5 Hadron and jet reconstruction

The last reconstruction step of the PF algorithm is to reconstruct charged and neutral hadrons as well as non-isolated photons, which can arise from π^0 decays. Energy clusters in the calorimeters give rise to neutral hadrons and photons if they are not linked to any track. Here, ECAL clusters are attributed to photons and HCAL clusters are used to identify neutral hadrons. This procedure is justified by the fact that neutral hadrons only deposit about 3% of their energy in the ECAL. On the contrary, if a cluster is linked to a track, the energy is attributed to a charged hadron. However, outside the tracker acceptance, the distinction between charged and neutral hadrons is no longer possible due to the lack of track reconstruction. Therefore, linked ECAL and HCAL clusters are attributed to the same hadron, whereas standalone ECAL clusters are still identified as photons.

Due to the confinement property of QCD, color-charged particles are subject to hadronization, which will lead to a stream of particles in the detector. Such streams of articles are called jets and are reconstructed using jet clustering algorithms. In this thesis, only jets based on the Anti-k_T (AK) algorithm [79] are considered. This algorithm has the advantage of being collinear and infrared safe, meaning that the jet does not change due to low energy radiation or collinear gluon splitting. The algorithm defines the following distance metrics:

$$d_{ij} = \min\left(p_{\mathrm{T,i}}^{-2}, p_{\mathrm{T,j}}^{-2}\right)\frac{\Delta R_{ij}^2}{R^2} \tag{3.5}$$

$$d_{iB} = p_{\mathrm{T,i}}^{-2} \tag{3.6}$$

Here $p_{\mathrm{T,i,j}}$ is the transverse momentum of particle i and j and ΔR_{ij} denoted the distance between the ith and jth particle as defined in equation (3.4). The distance of object i to the

beamline is denoted by d_{iB}, and R denotes a radius parameter. Based on these metrics, the AK algorithm sequentially combines neighboring particles. By using the inverse of the jet transverse momenta in equation (3.5) particles with high momenta are combined first with neighboring low momentum particles. If the minimum distance between particles is d_{iB}, the algorithm stops, and the resulting object is declared as a jet. The algorithm also has the property of producing jets with an almost conical shape in the plane of the azimuthal angle ϕ and the pseudo rapidity η, with the radius parameter R as an appropriate measure of the jet cone size.

As mentioned earlier, multiple proton-proton interactions per bunch crossing are expected besides the primary interaction. Since this additional activity also gets clustered into the jets, dedicated PU removal algorithms are deployed. By utilizing the tracking information, charged particles from pileup vertices are identified and removed from the collection of particles prior to the jet clustering. This process is called charged hadron subtraction (CHS) [80]. Another PU removal method is called pileup per particle identification (PUPPI) [81]. Here, a weight gets assigned to each particle to rescale its four-momentum, characterizing its probability of originating from the primary vertex (weight close to one) or a PU vertex (weight close to zero).

Two kinds of jets are considered in this thesis. On the one hand, jets with a radius parameter of $R = 0.4$ are referred to as AK4 jets. For AK4 jets, the recommended PU mitigation algorithm is CHS. On the other hand, jets with $R = 1.5$ are referred to as AK15 jets. Due to the larger radius parameter, these jets are also referred to as fatjets. The larger jet size renders the fatjets especially sensitive to PU contributions. Therefore, the more advanced PUPPI algorithm is deployed for AK15 jets.

3.3.6 Missing transverse energy reconstruction

The transverse momentum of the colliding protons is negligible. Therefore, if all decay products of the proton-proton interaction are reconstructed, the sum of their transverse momenta measured should vanish. However, some particle species, such as neutrinos or potentially DM particles, do not interact with the detector and therefore escape the detector unreconstructed. This leads to a non-vanishing transverse momentum sum. The negative of this sum is called missing transverse momentum or MET. It is calculated as

$$\vec{\not{E}}_{\mathrm{T}} = -\sum_{i=\text{reconstructed particles}} \vec{p_{\mathrm{T,i}}} = \sum_{i=\text{not reconstructed particles}} \vec{p_{\mathrm{T,i}}}. \tag{3.7}$$

Often the magnitude of MET $\not{E}_{\mathrm{T}} = |\vec{\not{E}}_{\mathrm{T}}|$ is used instead of the full vector.

3.4 Experimental searches for Dark Matter

In the following, concepts for experimental searches for DM are introduced under the assumption that DM consists of WIMPs. All current experimental searches for DM rely on the assumption that interactions between DM and SM particles exist. Based on this assumption, the searches can be classified into three categories as depicted in figure 3.3.

3.4.1 Direct detection

The first category is direct detection. Since the earth is supposedly moving through a halo of DM particles, the direct detection searches for the scattering of such a DM particle with a nucleus (SM particle). The recoil of the nucleus is then detected in experiments. Several detection mechanisms, such as phonon signals, ionization or scintillation, are used.

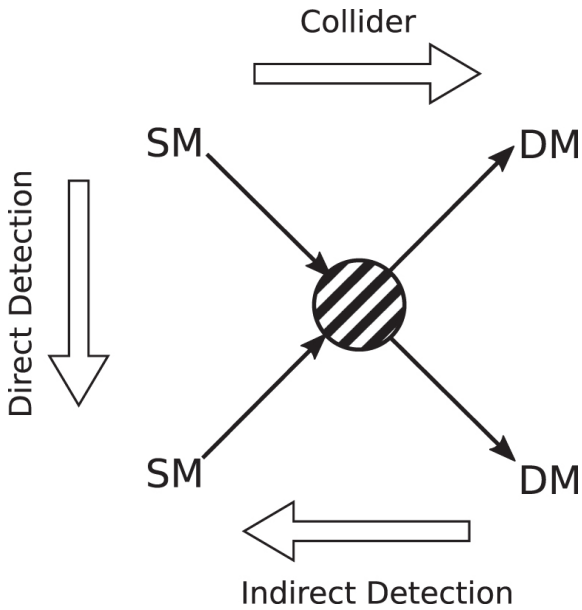

Figure 3.3: Schematic of the three possible search methods for DM. Taken from [82].

The combination of multiple detection mechanisms can be used to suppress backgrounds. Direct detection searches are performed, for example, at the CRESST I/II/III [83], EDELWEISS [84], LUX [85], LZ [86], XENON 10/100/1T [87] or XENON nT [88] experiments. A detailed review of direct detection of DM can be found in [89]. Figure 3.4 shows the latest results obtained by the LZ and XENON nT experiments [90, 91], providing the most stringent limits on the WIMP-nucleon interaction cross section as a function of the WIMP mass to date at 90 % confidence level. These experiments are able to probe WIMP masses in the range of a few GeV up to a few TeV for interaction cross sections in the order of $10^{-46}\,\mathrm{cm}^2$ by deploying liquid xenon as a target material. These unprecedented sensitivities are achieved by measuring the recoil energy of the nucleus both via an ionization as well as a scintillation signal. This combination of two detection mechanisms allows a powerful suppression of backgrounds originating for example from cosmic rays or radioactive decays inside the detector material, rendering the DM searches essentially background-free. Lower WIMP masses are not possible to probe in such liquid noble gas detectors due to limited energy resolution in the order of a few keV. Experiments such as CRESST I/II or EDELWEISS deploy solid-state targets such as germanium and measure the recoil energy via small temperature increases.
An overview of exclusion limits is shown in figure 3.5, where the latest measurements by the LZ, XENON nT as shown in figure 3.4 are not included.

3.4.2 Indirect detection

The second method is indirect detection. Here, the detection relies on the annihilation of DM particles into SM particles such as photons, electrons and positrons, neutrinos, or protons and antiprotons. Due to these potential annihilation processes, an increased flux of SM particles is expected, originating from regions of high DM density in the universe. This potentially increased flux is studied by gamma-ray telescopes, such as Fermi-LAT[93], H.E.S.S.[94] or MAGIC[95], or neutrino detectors, such as IceCube[96], ANTARES[97] or KM3NeT[98]. Furthermore, cosmic radiation experiments such as AMS-02 or PAMELA are able to search for a possible signal. Despite being a promising method to search for DM, the estimation of potential background sources from an astroparticle point of view is challenging. For instance, the intergalactic flux of particles needs to be known

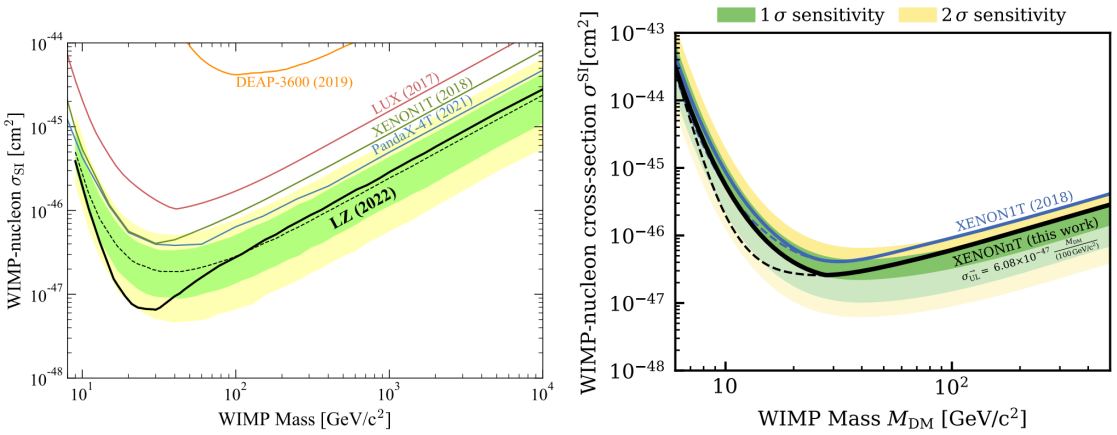

Figure 3.4: Exclusion limits for WIMP production as a function of WIMP mass and spin-independant (SI) WIMP-nucleon interaction cross section obtained by the LZ (left) and XENON nT (right) experiments. Taken from [90] and [91], respectively.

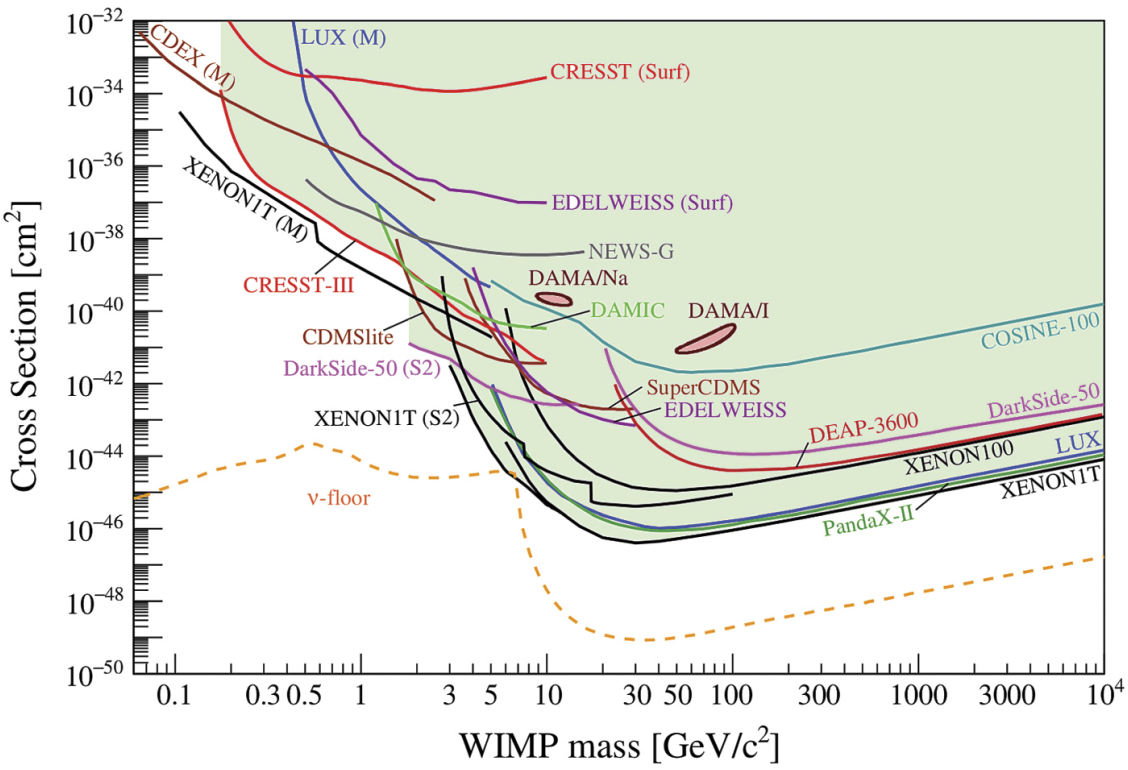

Figure 3.5: Overview of exclusion limits for WIMP searches as a function of WIMP mass and WIMP-nucleon interaction cross section. Taken from [92]

to high precision, which involves detailed understanding of the astrophysical processes in the universe. Consequently, indirect detection searches are subject to sizable model dependencies.

A detailed review of indirect detection of DM can be found in [99].

3.4.3 Collider searches

The third method is the potential production of DM at colliders, which is the focus of this thesis. Again, this method relies on the assumption that an interaction between SM and DM particles exists at all. If the center-of-mass energy of the collider is high enough, the DM particles can potentially be produced in proton-proton collisions. However, potential DM particles are expected to interact only very weakly, if at all, with the detector itself. Therefore, the DM particles are expected to escape the detector without being directly detected. In conjunction with the assumption that the transverse momentum of the colliding particles is negligible, the potential production of DM particles leads to a significant amount of MET. The conservation of the transverse momentum, however, dictates that a large amount of MET also means that another particle is produced, which recoils against the MET. This particle is expected to be an SM particle, such as a quark, a photon or a charged lepton, depending on the theoretical model. The distinctive signature of DM production at a collider is a large amount of MET in conjunction with a reconstructed particle often referred to as MET+X or mono-X signature. The search in this thesis aims at signatures containing a top quark in addition to MET in the final state (mono-top signature). More details on this specific theoretical model can be found in section 5.3.

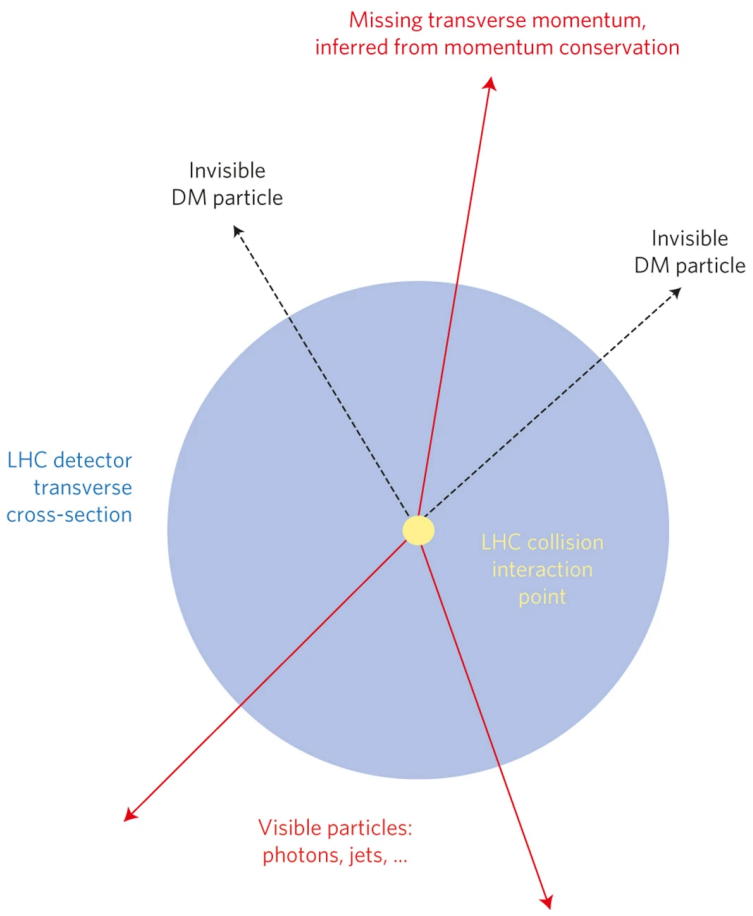

Figure 3.6: Illustration of a mono-X signature. Taken from [100].

4 Introduction to statistical data analysis

In the following, the concepts of statistical data analysis used within this thesis are introduced. After introducing general concepts, such as frequentist and Bayesian statistics, probability functions are introduced. A high-energy physics analysis aims to estimate a parameter of an underlying theory or test a given hypothesis based on the measured data. Therefore, the procedure for estimating such parameters in statistical data analyses is discussed afterward. Finally, the incorporation of systematic uncertainties into the parameter estimation is described in addition to goodness-of-fit (GoF) tests. The explanations in this chapter are based on [101, 102] as well as the *Statistics* review article in [4].

4.1 General approach

Two approaches are commonly used in statistical data analysis: frequentist and Bayesian statistics. In frequentist statistics, the probability of an event is defined as the relative frequency of a specific outcome in several independent trials:

$$P(\text{event}) = \frac{\text{number of times event occurs}}{\text{number of trials}} \tag{4.1}$$

However, it is not possible to define the probability of a hypothesis or for a specific value of a parameter.

The second approach is Bayesian statistics. In this approach, a subjective probability is introduced, which allows evaluating ones *degree of belief* in a hypothesis. Bayesian probabilities can be expressed using Bayes' theorem:

$$P(A|B) = \frac{P(B|A) \cdot P(A)}{P(B)} \tag{4.2}$$

Here, $P(A|B)$ is the probability of outcome A given outcome B and $P(B|A)$ vice-versa. The general probabilities are denoted by $P(A)$ and $P(B)$ and are often referred to as priors. Therefore, the Bayesian approach offers a direct way to incorporate prior knowledge to the analysis. This prior knowledge can be based on auxiliary independent measurements or theoretical considerations. An important concept in statistics is the probability density function (p.d.f.), which is a function that describes the probability of finding a continuous variable x within the range $[x, x + dx]$.

In typical high-energy physics analyses, data is often represented as histograms. In histograms, events are sorted into intervals $[a, b)$ of a continuous variable, where each interval can be interpreted as an independent measurement. This approach allows the approximation of a continuous p.d.f.. This approximation is improved by increasing the number of bins and thus decreasing the size of the bin intervals. However, an increasing number of measurements is needed as well.

4.2 Parameter estimation

As mentioned earlier, one of the main aspects of a high-energy physics analysis is to measure a parameter of an underlying theory or to test a given hypothesis. A method for parameter estimation considered often in literature is the bias-free and numerically stable maximum likelihood method. In this method, the quantity $\mathcal{L}(H)$ is defined as the probability for hypothesis H given the data $\mathbf{x}$. Often, the hypothesis H is characterized by a set of continuous parameters $\boldsymbol{\theta}$.

Having defined the likelihood function, an estimation of the parameters $\boldsymbol{\theta}$ can be performed via a frequentist approach by maximizing the likelihood function and thus retrieving the maximum likelihood estimators (MLEs) $\hat{\boldsymbol{\theta}}$. This maximization is performed by solving

$$\frac{\partial \ln \mathcal{L}(\boldsymbol{\theta})}{\partial \theta} = 0 \tag{4.3}$$

for all parameters of the hypothesis. By using Wilks' theorem [103] confidence intervals on these parameters can be calculated. More details on this confidence interval estimation are provided later in section 4.4. The pull of a given parameter θ is defined as

$$\text{pull}(\theta) = \frac{\hat{\theta} - \theta_0}{\sigma_\theta}, \tag{4.4}$$

where θ_0 is the initial value of parameter θ with prior uncertainty σ_θ. The prior uncertainty is often estimated via the aforementioned auxiliary measurements or theoretical considerations. The MLEs $\hat{\boldsymbol{\theta}}$ are the values of θ that maximize the likelihood function. The pull of a parameter is a measure of how far the MLEs is from the initial value.

4.3 Hypothesis tests

The hypothesis test is a statistical procedure to determine if a given hypothesis is preferred by the data with respect to another one. As described earlier, the two main hypotheses to be tested are the signal+background (H_1) hypothesis as well as the background-only (H_0) one. The test is based on defining a critical region w such that the probability of a given outcome under the hypothesis is equal to the significance level α. Often, a test statistic t is defined as a measure of compatibility between the data and the hypothesis. The Neyman-Pearson lemma [104] is used to define a likelihood ratio to maximize the power of the test:

$$t = \frac{\mathcal{L}\left(\mathbf{x}|H_1\right)}{\mathcal{L}\left(\mathbf{x}|H_0\right)} \tag{4.5}$$

For testing only a single hypothesis a p-value can be calculated utilizing the p.d.f. $f\left(t|H\right)$ imposed by hypothesis H:

$$p = \int_{t_{\text{obs}}}^{\infty} f\left(t|H\right)\, \mathrm{d}t. \tag{4.6}$$

This p-value corresponds to the probability of observing a test statistic t as large as the observed one t_{obs} or larger under the assumption that the hypothesis H is true. Due to being a function of data, the p-value is a random variable itself. Such single hypothesis tests are often called GoF or significance tests. More details on the application of GoF tests in this thesis are given in section 4.6.

4.4 Application to high energy physics

As mentioned earlier, data in high-energy physics is often represented as histograms. The data within each bin can be described via a Poisson probability. Consequently, if the contents of the bins are independent of one another, the likelihood function can be written as a product of Poisson probabilities:

$$\mathcal{L}(\mathbf{n}, \boldsymbol{\theta}) = \prod_{i=1}^{N} \frac{\lambda_i^{n_i}}{n_i!} \exp\left(-\lambda_i\right) \tag{4.7}$$

Here, n_i denotes the content of bin i, and the expectated number of events in a bin is given by λ_i, which is a function of the parameters of the hypothesis $\boldsymbol{\theta}$. To be more precise, the expected number of events λ_i is defined as

$$\lambda_i = \lambda_i(\mu, \boldsymbol{\theta}) = \mu \cdot s_i(\boldsymbol{\theta}) + b_i(\boldsymbol{\theta}), \tag{4.8}$$

where the expectation of events is split into the signal and background contributions s and b, respectively. Another free parameter μ referred to as signal strength modifier is introduced. This parameter is able to scale the signal contribution directly and therefore allows the construction of both a background-only ($\mu = 0$) as well as a signal-plus-background ($\mu > 0$) hypothesis. The set of parameters $\boldsymbol{\theta}$ adds more degrees of freedom which might be needed to cope with possible differences between the expectation and the observed data and are often referred to as the nuisance parameters. This additional freedom often arises from the fact that the measurements are subject to systematic effects, which need to be taken into account. Since prior knowledge about the systematic effects is often available, constraint terms are added to the likelihood function in equation (4.7). These constraint terms are often referred to as *penalties* and characterize the degree of belief $\rho(\theta_j|\tilde{\theta}_j)$ of the true values $\tilde{\boldsymbol{\theta}}$. By using Bayes' theorem, this penalty can be written as

$$\rho(\theta|\tilde{\theta}) = p(\tilde{\theta}|\theta) \cdot \pi(\theta), \tag{4.9}$$

where $\pi(\theta)$ is a flat prior and $p(\tilde{\theta}|\theta)$ corresponds to the prior knowledge about the systematic effect. More specifics on these penalty terms are provided in section 4.5. Consequently, the likelihood function can be written as

$$\mathcal{L}(\mu, \boldsymbol{\theta}) = \prod_{i=1}^{N} \frac{\mu \cdot s_i + b_i}{n_i!} \exp\left(-\mu \cdot s_i + b_i\right) \cdot \rho(\theta|\tilde{\theta}). \tag{4.10}$$

By expressing the nuisance parameters $\boldsymbol{\theta}$ as a function of μ

$$\mathcal{L}(\mu, \boldsymbol{\theta}) = \mathcal{L}(\mathbf{n}, \boldsymbol{\theta}(\mu)) \tag{4.11}$$

a profile likelihood is constructed. According to the Neyman-Pearson lemma [104] the test statistic

$$\tilde{q}_\mu = -2 \ln \left(\frac{\mathcal{L}\left(\mu, \hat{\boldsymbol{\theta}}_\mu\right)}{\mathcal{L}\left(\hat{\mu}, \hat{\boldsymbol{\theta}}_\mu\right)} \right) \tag{4.12}$$

can be defined as a likelihood ratio maximizing the statistical power. Here, $\hat{\mu}$ and $\hat{\boldsymbol{\theta}}_\mu$ denote the values maximizing $\mathcal{L}$ and thus minimizing the test statistic $\tilde{q}_\mu$. If the limit of large samples is fulfilled, Wilks' theorem [103] states that the test statistic $\tilde{q}_\mu$ allows to construct confidence intervals corresponding to Gaussian standard deviations s via

$$\tilde{q}_\mu(s) = \tilde{q}_\mu^{\min} + s^2. \tag{4.13}$$

Having defined the test statistic, p-values for the background-only and signal-plus-background hypothesis can be calculated:

$$p_\mu = P\left(\tilde{q}_\mu \geq \tilde{q}_\mu^{\text{obs}} | \mu \cdot \text{signal+background}\right) = \int_{\tilde{q}_\mu^{\text{obs}}}^{\infty} f\left(\tilde{q}_\mu | \mu, \hat{\boldsymbol{\theta}}_\mu^{\text{obs}}\right) \tag{4.14}$$

$$1 - p_b = P\left(\tilde{q}_\mu \geq \tilde{q}_\mu^{\text{obs}} | \text{background-only}\right) = \int_{\tilde{q}_\mu^{\text{obs}}}^{\infty} f\left(\tilde{q}_0 | 0, \hat{\boldsymbol{\theta}}_0^{\text{obs}}\right). \tag{4.15}$$

In these equations, $\tilde{q}_\mu^{\text{obs}}$ is the minimum value of the test statistic observed in the data. The p.d.f.s of the test statistic under the respective hypotheses are denoted by $f\left(\tilde{q}_\mu | \mu, \hat{\boldsymbol{\theta}}_\mu^{\text{obs}}\right)$ and $f\left(\tilde{q}_0 | 0, \hat{\boldsymbol{\theta}}_0^{\text{obs}}\right)$. Stating it differently, the p-value for the background only hypothesis reflects the compatibility of the observed data with the background-only hypothesis. Therefore, it can be used to reject the null hypothesis and consequently claim the presence of a signal. The p.d.f.s needed for this calculation are derived by creating pseudo-datasets around the best estimators $\hat{\boldsymbol{\theta}}$ considering the posterior probability distribution of the test statistic for a given hypothesis as well as all systematic and statistical uncertainties. A single pseudo-dataset is often referred to as a toy. The process of constructing such pseudo-datasets requires a large amount of computing power. Consequently, the p-values are often approximated by exploiting the asymptotic behavior of the likelihood test statistic $\tilde{q}_0$ using Wilk's theorem. The p-value then becomes

$$p^{\text{estimate}} = \frac{1}{2}\left[1 - \text{erf}\left(\frac{\tilde{q}_0^{\text{obs}}}{2}\right)\right] \tag{4.16}$$

which is an analytical function involving the Gaussian error function "erf" and is used throughout this thesis. The p-value can be converted into a Gaussian significance Z by considering a one-sided Gaussian tail

$$p = \int_Z^{\infty} \frac{1}{\sqrt{2\pi}} \exp\left(-\frac{x^2}{2}\right) dx = \frac{1}{2} P_{\chi_1^2}\left(Z^2\right) \tag{4.17}$$

where $P_{\chi_1^2}$ is the survival function of χ^2 for one degree of freedom. In high-energy physics, two levels of significance are agreed upon. The Z-scores are given in terms of Gaussian standard deviations σ. If an excess is found with a significance of $Z > 3$ it is considered evidence, whereas a significance of $Z > 5$ is required to claim a discovery. If the significance level is below these thresholds, the null hypothesis is not rejected, and a possible excess is compatible with a statistical fluctuation. In this case, exclusion limits based on a specific confidence level (CL) are calculated. For this, the two p-values are combined into a CL_s value via

$$\text{CL}_s(\mu) = \frac{p_\mu}{1 - p_b}. \tag{4.18}$$

This CL_s can be used to exclude the signal+background hypothesis at a $(1-\alpha)\,\%$ CL_s CL. By adjusting μ such that $\mathrm{CL}_s = 1-\alpha$, an $(1-\alpha)\,\%$ CL upper limit $\mu_{\mathrm{UL}}^{(1-\alpha)\,\%}$ is obtained. Since the observed data is used here, the obtained results are called observed limits.

Furthermore, it is possible to assess how sensitive an analysis is to a specific signal by calculating expected limits. Again, a large number of toys are constructed under the background-only hypothesis. Then, for each toy, CL_s and the corresponding exclusion limits are calculated by estimating the p.d.f. via another set of toy datasets. The expected limit is then the median of the resulting distribution of exclusion limits. Furthermore, this procedure enables the calculation of uncertainties on the expected limit. The $\pm 1(2)\sigma$ uncertainty is calculated by considering the $16(2.5)\,\%$ and $84(97.5)\,\%$ quantiles of the distribution of exclusion limits. Again, this calculation is computationally expensive. Therefore, due to large datasets, asymptotic approximations are used throughout this thesis [101].

4.5 Systematic uncertainties

As mentioned previously, systematic effects are incorporated into the statistical procedures via nuisance parameters $\boldsymbol{\theta}$. The degree of belief of where the true value of these parameters should lie is considered in the likelihood function via penalty terms $\rho\left(\theta|\tilde{\theta}\right)$. Depending on the expected effect on the predictions, different penalty terms are chosen. In the scope of this thesis, two different cases are of special interest.

The first one aims at parameterizing an overall change in the yield of the histograms. A log-normal p.d.f. is chosen as a penalty term in this case:

$$\rho\left(\theta|\tilde{\theta}\right) = \frac{1}{\sqrt{2\pi}\ln(\kappa)} \exp\left(-\frac{\left(\ln\left(\theta/\tilde{\theta}\right)\right)^2}{2\ln^2(\kappa)}\right)\frac{1}{\theta} \tag{4.19}$$

In this p.d.f., the parameter κ controls the width of the p.d.f. and therefore corresponds to the prior uncertainty ϵ via $\kappa = 1+\epsilon$. For example, a flat normalization uncertainty of $10\,\%$ is encoded in this p.d.f. by choosing $\kappa = 1.10$. From a technical standpoint, the log-normal p.d.f. is implemented via a standard Gaussian p.d.f. by parameterizing the variation of an observable A with a best estimate $\hat{A}$ via $A = \hat{A}\cdot\kappa_A^{\theta}$. The Gaussian p.d.f. is given by

$$g\left(\theta|\tilde{\theta}\right) = \frac{1}{\sqrt{2\pi}\sigma} \exp\left(-\frac{\left(\theta-\tilde{\theta}\right)^2}{2\sigma^2}\right), \tag{4.20}$$

where $\sigma = 1$ and $\tilde{\theta} = 0$ is chosen.

The second case considers a systematic effect that may change the yield and the actual shape of a (binned) distribution. The change of yield is again modeled via a log-normal p.d.f. as described above. However, the change of shape is considered via dedicated histograms parameterizing the effect of varying the uncertainty source by one standard deviation σ up or down. Within this $\pm 1\sigma$ band, an interpolation via spline functions is used to model the shape effect, whereas, outside this band, a linear extrapolation is deployed. The associated penalty term is modeled via a Gaussian distribution as written in equation (4.20).

4.6 Goodness of fit tests

As mentioned in section 4.3, single hypothesis tests are often referred to as GoF tests. One important statistical test is the compatibility of a given model with the measured data. A

possible test to assess this compatibility is the *saturated model* test [105] as a generalization of the χ^2 test. For a χ^2 test, the test statistic is defined as

$$\chi^2 = \sum_i \frac{(d_i - f_i)^2}{\sigma_i^2}, \tag{4.21}$$

where d_i corresponds to a measurement point with its known true uncertainty σ_i and f_i is the prediction of the model. If the true uncertainty σ_i is not known, it is replaced with d_i as an estimate. If only the compatibility between the data and a specific hypothesis is of interest, an alternative hypothesis can be artificially constructed so that all f_i are equal to d_i. Such models are referred to as saturated models. If the data follows a Gaussian distribution, the likelihood function of the saturated model is given by

$$\mathcal{L} = \prod_i \frac{1}{\sqrt{2\pi\sigma_i^2}}. \tag{4.22}$$

Consequently, the likelihood ratio λ, considered as test statistics, is given by

$$\lambda = \prod_i \exp\left(-(d_i - f_i)^2/2\sigma_i^2\right), \tag{4.23}$$

which can be set in relation to the χ^2 test statistic via

$$\chi^2 = -2\ln\lambda. \tag{4.24}$$

The p.d.f. of the test statistic λ is obtained via toy datasets. This p.d.f. is then used to calculate a p-value using the value of the test statistic for observed data. A lower threshold on the p-value commonly considered in high energy physics data analysis to indicate that the model is compatible with the data is 5 %.

Part II

Mono-top Analysis

5 General foundations of the mono-top analysis

In the following, the general foundations of the mono-top analysis are presented. First, general aspects of top quark physics and tagging of heavy quarks physics will be discussed. Afterward, an introduction to the theoretical mono-top model is given. Subsequently, the simulation samples considered in this thesis as well as the corrections applied to these samples are described. Finally, the physics object definitions are given.

5.1 Physics of top quarks

The main aspects of top quarks physics based on the *Top Quark* review article in [4] are discussed in this section. Top quarks carry an electric charge of $q = 2/3e$, where e is the negative of the elementary charge of an electron. The lifetime of a top quark is very short with $\tau_{\text{top}} \approx 10^{-25}\,\text{s}$. The reason for this lies in its very high mass of approximately 173 GeV as well as the fact that the CKM matrix element $|V_{tb}|$ is much larger than $|V_{td}|$ and $|V_{ts}|$ [16, 17]. Since this lifetime is shorter than the mean QCD hadronization timescale $\Lambda_{\text{QCD}}^{-1} \approx 10^{-23}\,\text{s}$, the top quark decays before it hadronizes [106]. Top quarks decay almost exclusively via the weak interaction into a W boson and a bottom quark. Due to the special properties of B-hadrons, it is possible to distinguish jets originating from a bottom quark decay from other jets. This is called b-tagging and is further discussed in section 5.2.1. Since the W boson is also not stable, two different decay modes are possible. The W boson can decay into a quark-antiquark pair with different flavors (hadronic decay) or a charged lepton and its corresponding neutrino (leptonic decay). The branching fractions for this W boson decay are given in the *Gauge and Higgs bosons* summary table in [4]:

$$\begin{aligned} &\mathrm{W}^{\pm} \to \mathrm{q\bar{q}} : 67.41\,\% \\ &\left.\begin{aligned} \mathrm{W}^{+} &\to \ell^{+}\nu_{\ell} : 10.86\,\% \\ \mathrm{W}^{-} &\to \ell^{-}\bar{\nu}_{\ell} : 10.86\,\% \end{aligned}\right\} \text{ for a single lepton flavor } \ell. \end{aligned}$$

Consequently, from an experimental point of view, the signature of a hadronically decaying top quark consists of three jets in the detector. In contrast, a leptonically decaying top quark is characterized by a jet, a charged lepton, and some amount of MET due to the (anti-)neutrino escaping the detector. Similar to the tagging of bottom quarks, hadronically decaying top quarks can be tagged if the decay products are collimated and reconstructed

as a single jet. More specifics on top-tagging are provided in section 5.2.2. However, it should be noted that a potentially produced τ-lepton can also decay into quarks and, therefore, also can produce a hadronic signature in the detector. The primary production mechanism of top quarks at hadron colliders is top quark-antiquark pair production via the strong interaction. The subdominant production mechanism is the production of a single top quark via the weak interaction. Figure 5.1 shows the corresponding leading order Feynman diagrams.

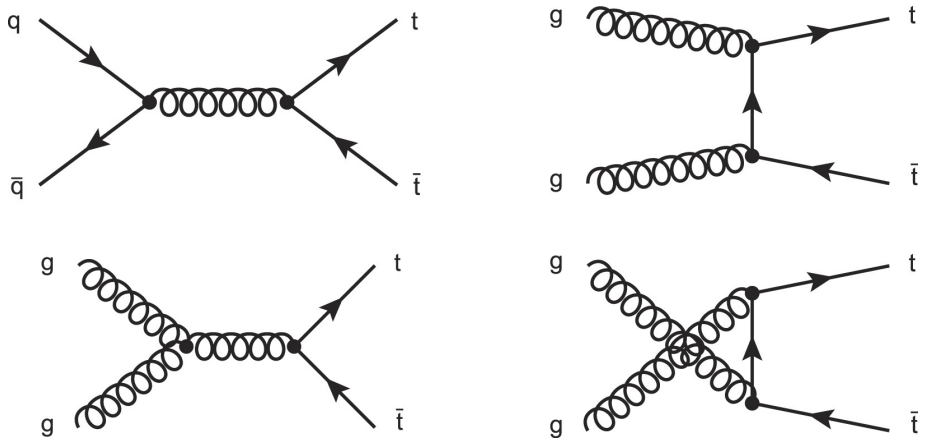

(a) Top quark-antiquark pair production.

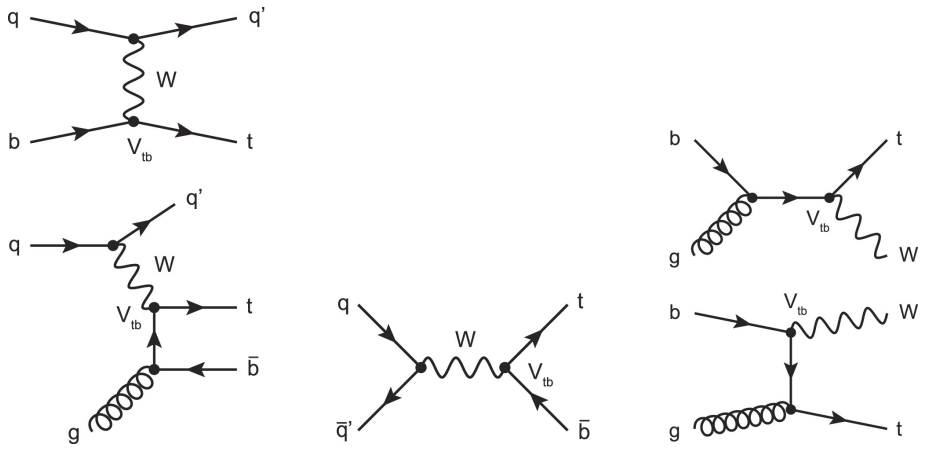

(b) Single top quark production.

Figure 5.1: Leading order Feynman diagrams for the production of a top quark-antiquark pair (top) and a single top quark (bottom). Taken from [107]

.

For more insights into the physics of top quarks, see e.g. [107, 108].

5.2 Tagging of heavy quarks

Due to the unique properties of heavy quarks and, therefore, their hadronization into jets, distinguishing such jets from jets originating from light quarks offers a powerful tool to enrich the recorded datasets with physic processes of interest. In the scope of this thesis, the tagging of jets arising from bottom as well as top quarks are relevant and will be discussed in the following.

5.2.1 Tagging of bottom quarks

The following general aspects of b-tagging are based on [109, 110], where also further information can be found. The tagging of bottom quarks is based on the fact that B-hadrons are relatively long-lived with proper lifetimes of the order of 1.5 ps. Due to the excellent tracking capabilities of the CMS detector, a secondary vertex (SV) can be reconstructed, corresponding to the decay of the B-hadron. The displacement of the SV from the primary vertex, characterized by the impact parameter (IP) of displaced tracks originating from the SV, is a good measure for the probability that the jet originates from a B-hadron. Additionally, due to the large mass of bottom quarks and the harder fragmentation, compared to light quarks or gluons, the decay products of a B-hadron have a larger p_{T} relative to the jet axis. Since a B-hadron decays into an electron or muon in approximately 10 % of the cases, the presence of such a charged lepton inside the jet can also be used for discrimination. Figure 5.2 shows a schematic representation of a b-jet, where the SV, the IP of a displaced track as well as the charged leptons are illustrated.

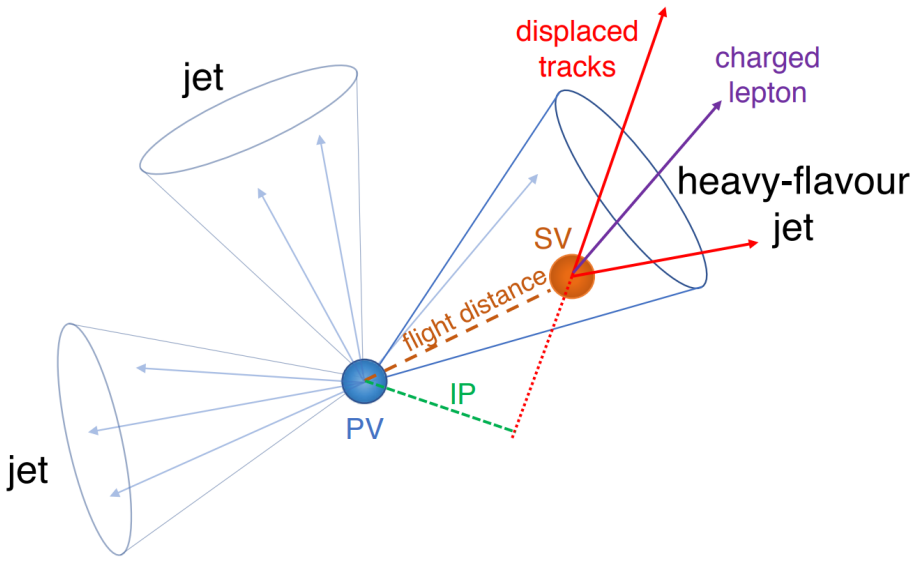

Figure 5.2: Schematic representation of a heavy flavor jet and the corresponding SV. Taken from [109].

In order to utilize the aforementioned properties optimally, a sophisticated multivariate algorithm based on neural networks is deployed (`DeepJet` tagger) [111, 112]. This algorithm combines information of approximately 650 input variables in order to obtain probabilities of a jet originating from a special flavor. These input variables consist of information of charged and neutral PF candidates, the SVs, as well as global features considering the information of the whole jet. Figure 5.3 shows an overview of the neural network architecture of the `DeepJet` tagger.

These four types of input variables undergo different branches of the network. All features except the global ones are subject to an automatic feature engineering step via convolutional

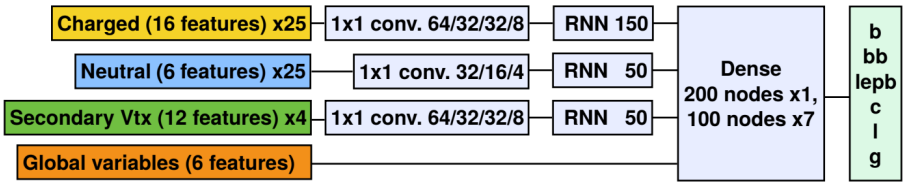

Figure 5.3: Layout of the `DeepJet` neural network architecture. Taken from [111].

layers [113] with filter sizes of 1×1. Following these convolutional layers, recurrent layers of type long short-term memory (LSTM) are deployed [114]. Treating the constituents as sequences, these LSTM layers are especially suited here since they can handle an arbitrary number of elements that naturally arise in jet physics. As a last step, the information of all four branches is combined in fully connected layers performing the final classification. In order to define signal and background classes for this discrimination the jet origin needs to be known. This is accomplished by setting the four-momenta of B and C-hadrons to a very small value and subsequently re-clustering the jet. This approach ensures that the four-momentum of the jet doesn't change. However, after this so-called ghost hadron clustering, the jet hadron flavor can be identified based on the hadron inside the jet. By considering ghost partons instead of hadrons, the jet parton flavor is defined[115]. The `DeepJet` tagger discriminates between six jet classes:

- b: Jet contains hadronically decaying B-hadron.
- bb: Jet contains two B-hadrons.
- lepb: Jet contains a leptonically decaying B-hadron.
- c: Jet contains at least one C-hadron and no B-hadrons.
- l: Jet contains neither B-hadrons nor C-hadrons, but the hardest parton is matched to a LF (u,d,s) quark.
- g: Jet contains neither B-hadrons nor C-hadrons, but the hardest parton is matched to a gluon.

By using the softmax aggregation function [116] the probabilities of a jet being of a particular class are obtained. The CMS collaboration recommends using the sum of the probabilities corresponding to the classes containing B-hadrons as a final b-tagging discriminant:

$$d_{\texttt{DeepJet}} = P(\mathrm{b}) + P(\mathrm{bb}) + P(\mathrm{lepb}). \tag{5.1}$$

If the value of the discriminant is larger than a certain threshold, the jet is considered b-tagged. This threshold is also referred to as working point (WP) and is based on the rate of misidentifying a specific rate of misidentifying a LF jet as a b-jet accepted for the analysis. Two WPs are considered in this thesis. The medium WP corresponds to a misidentification rate of 1 %, whereas the loose WP corresponds to a misidentification rate of 10 % [112]. Using the loose WP has the advantage of increased efficiency of approximately 95 % compared to the medium WP with an efficiency of approximately 85 %.

5.2.2 Tagging of top quarks

From an experimental point of view, a hadronically decaying top quark usually results in three well-seperated jets in the detector. However, if the momentum of the top quark is much larger than its rest mass ($p \gg m$), the decay products of the top quark get collimated

due to the large Lorentz boost. If this boost of the top quark is large enough, the three jets may be merged into a single large-radius jet, referred to as fatjet, as illustrated in figure 5.4. The distance between the decay products can be approximated for a two-body decay via

$$\Delta R \approx \frac{2m}{p_{\mathrm{T}}}, \tag{5.2}$$

where ΔR is the spatial distance in the transverse plane between the decay products. The mass and transverse momentum of the mother particle is denoted by m and p_{T}, respectively.

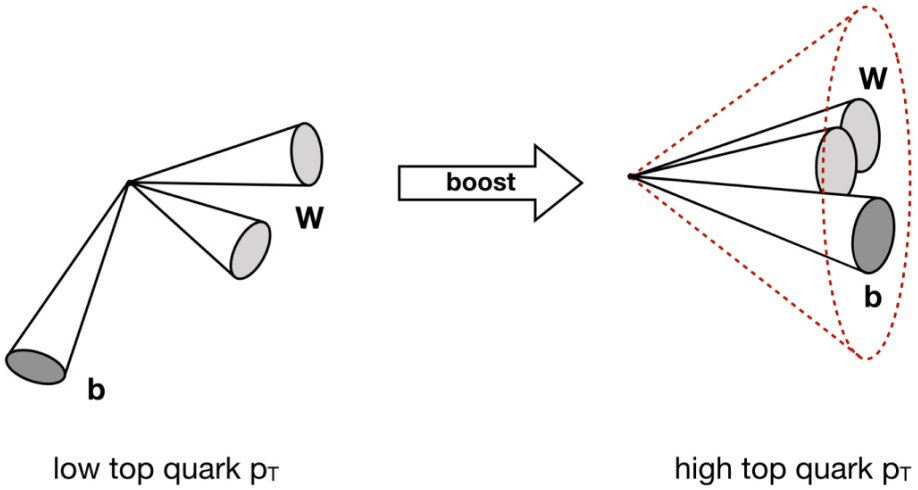

Figure 5.4: Illustration of a boosted top quark. Taken from [82].

However, not only hadronic top quark decays can result in a fatjet but also, for example, jets originating from light quarks or gluons, referred to as QCD jets. Additionally, hadronically decaying heavy resonances such as W/Z or Higgs bosons can also result in fatjets.

In order to discriminate between fatjets originating from top quarks and from other processes, modern approaches via multivariate algorithms based on neural networks have been developed. The tagger deployed in this thesis is called `ParticleNet` [117]. Contrary to image-based approaches, such as the `DeepAK` tagger [118], the `ParticleNet` tagger deploys a graph-based approach. In this approach, all jet constituents are represented via an unordered, permutation invariant set, called graph, similar to the representation of 3D objects in computer vision. The previous success of image-based approaches, as used in the `DeepAK` tagger, is based on convolutional layers [113]. These layers allow the exploitation of spatial information of the input image. This input image can, for example, be based on the calorimeter entries in the η-ϕ plane of the detector. Additionally, stacking such convolutional layers allows the construction of deep networks, enabling the algorithm to learn global features. A similar approach is used in the `ParticleNet` tagger by adapting the convolutional layers to the point cloud-like representation of the jet constituents. This modified version of a convolutional layer is called edge convolution (`edgeConv`) [119]. The inputs considered by the `ParticleNet` tagger are information of up to 100 PF candidates, such as their four-momenta or spatial coordinates. Information regarding the SVs, such as the impact parameter, is also considered. For the `edgeConv` block, the point cloud is represented as a graph, where the edges are the connections between the points and their k nearest neighbors. An edge feature can be calculated for each connection by defining a distance metric. These features are then piped through three layers of multilayer perceptrons (MLPs) consisting of a linear transformation, followed by a batch normalization [120] and a rectified linear unit (ReLU) activation function [121]. These MLPs are characterized by their number of channels C. Additionally, a bypass is implemented to consider each input

feature of the `edgeConv` block without the linear transformations. Figure 5.5a shows an overview of the `edgeConv` block.

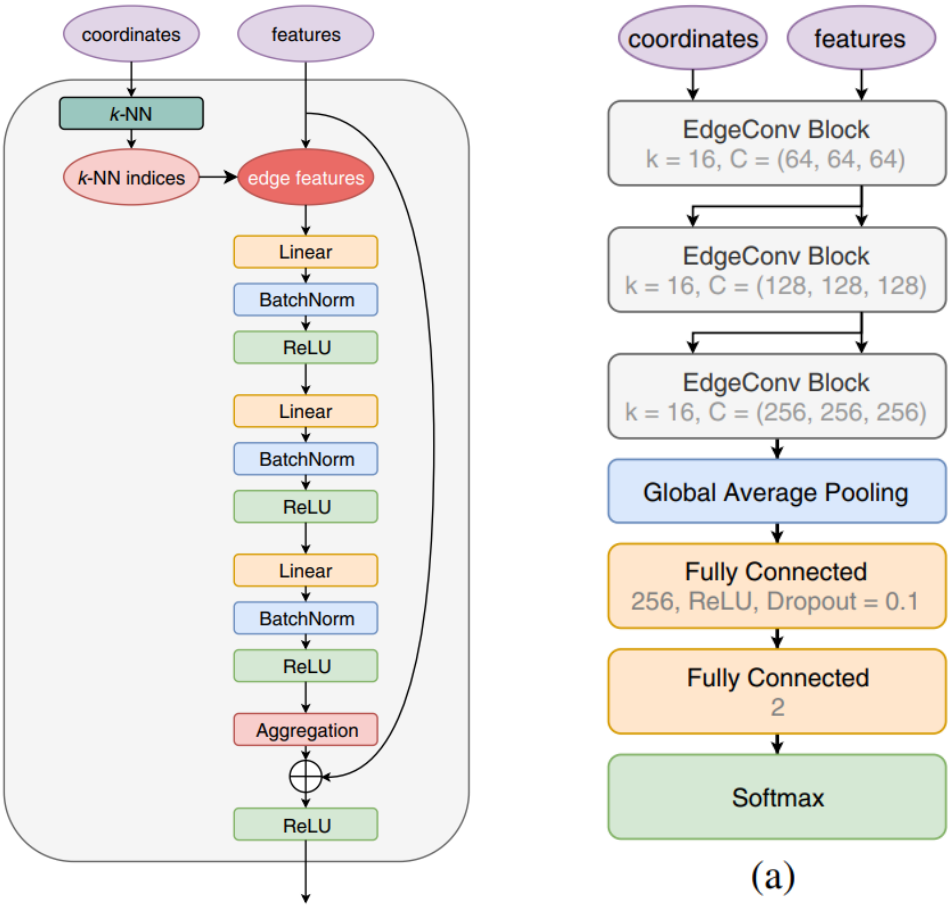

(a) `edgeConv` block (b) `ParticleNet` architecture

Figure 5.5: Illustration of the `edgeConv` block (left) and the `ParticleNet` architecture (right). Taken from [117]

.

By stacking several `edgeConv` blocks, a hierarchical network structure is realized enabling the ability to learn global features. After a pooling layer [122], which reduces the dimensionality of the latent space, fully connected layers are deployed. The output of these fully connected layers is transformed into a probability-like score via a softmax [116] function. Like the `DeepJet` tagger, the `ParticleNet` tagger is trained to discriminate between several classes. The output classes are defined by considering generator-level information and matching a parton within a distance of $\Delta R = 0.8$ to the jet axis. In the scope of this thesis, the discrimination of top quark and QCD jets is relevant. The classes relevant for top jets are the following, where exactly one bottom quark needs to originate from a top quark decay:

- Tbqq: exactly one bottom quark from a top decay and exactly two LF quarks originating from a W boson decay
- Tbcq: exactly one bottom quark from a top decay in addition to one LF and one c quark originating from a W boson decay

The QCD jet classes are defined as follows, where at least one quark or gluon is present and is not stemming from a W/Z or Higgs decay:

- b: Exactly one bottom quark and no charm quark is matched.

- bb: Exactly two bottom quarks and no charm quark are matched.
- c: Exactly one charm quark and no bottom quark is matched.
- cc: Exactly two charm quarks and no bottom quark are matched.
- other: all remaining cases

By using these classes, a powerful discriminant between top quark and QCD jets is obtained:

$$d_{\texttt{ParticleNet}}\,(\text{TvsQCD}) = \frac{P(\text{top})}{P(\text{top}) + P(\text{QCD})}. \tag{5.3}$$

Here, $P(\text{top})$ corresponds to the sum of the probabilities of the classes Tbqq and Tbcq, whereas $P(\text{QCD})$ corresponds to the sum of the probabilities of the classes bb, b, cc, c and other.

Figure 5.6 shows the background versus signal efficiency for the `ParticleNet` as well as the `DeepAK` tagger evaluated on AK jets with a radius parameter of $R = 0.8$ (AK8 jets). In this comparison the signal (top quark initiated jet) and background classes (QCD jet) are defined by only considering a generator-level p_{T} between 500 GeV and 1000 GeV and a pseudorapidity of $|\eta| < 2.4$. Furthermore, a requirement on the SoftDrop (SD) mass [123] is applied, such that only jets with an SD mass between 105 GeV and 210 GeV are considered. It can be observed that the `ParticleNet` tagger yields a higher background rejection for a given signal efficiency than the `DeepAK` tagger.

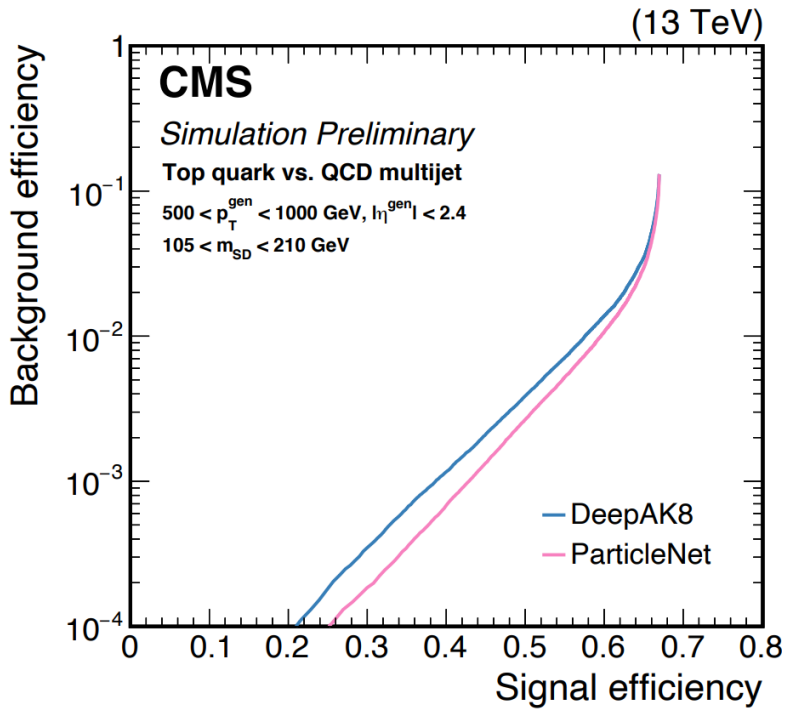

Figure 5.6: Performance of the `ParticleNet` tagger. Shown is the background versus signal efficiency for the `ParticleNet` as well the `DeepAK` tagger. Taken from [124].

5.3 The mono-top model

As explained in section 3.4,mono-X signatures offer a powerful method to search for DM at hadron colliders such as the LHC. This thesis focuses on the production of a single top quark in conjunction with MET. In the SM, such a final state is only possible via higher-order effects in perturbation theory. A Feynman diagram of such a process in the SM is shown in figure 5.7a. Two aspects lead to strong suppression of such a process in the SM. First, a loop of a W boson and two strange quarks is realized. Second, additional suppression arises due to the Glashow–Iliopoulos–Maiani (GIM) [125] mechanism.

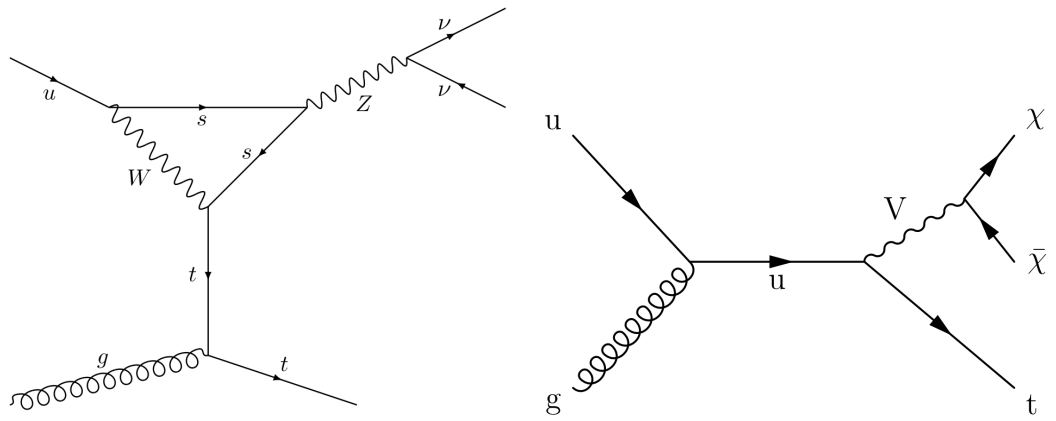

(a) SM (b) tree-level FCNC

Figure 5.7: Feynman diagram of a mono-top signature in the SM on the left-hand side and a production via an FCNC at tree level on the right-hand side. Taken from [126].

The theoretical mono-top model extends the SM in a way to allow for mono-top signatures at tree level. In the following, the theoretical background of the mono-top model is explained based on [127–129]. In this simplified model (see section 2.2.3), a new bosonic mediator is introduced. Two new interactions with this mediator are possible. First, the mediator can be produced in the s-channel. Such a resonant mono-top process would enable baryon number violation at tree level. However, this directly contradicts the observation that no signs of baryon number violation have been observed so far.

Therefore, this thesis focuses on the second process, corresponding to the non-resonant mono-top model. Here, the mono-top signature is realized via an FCNC between two up-type quarks from different generations via the new mediator. Depending on the spin of the mediator, two different interactions are possible in the non-resonant mono-top model. A scalar interaction is realized in the case of a spin-0 mediator, whereas a vector mediator corresponds to the case of a spin-1 mediator.

5.3.1 Scalar mediator

For the case of a scalar mediator, both right-handed, as well as left-handed couplings to quarks are allowed. In order to make this possible, the scalar field needs to be a doublet with a charged and a neutral component similar to the Higgs field before electroweak symmetry breaking. Consequently, this scalar mediator would carry the same quantum numbers as the Higgs field resulting in a mixing of both. Furthermore, the DM candidate would also be a doublet containing a charged and a neutral component. Further information can be found in [129]. In order to keep the model as minimal as necessary, the scalar mediator case is not considered further in this thesis.

5.3.2 Vector mediator

By only considering a vector mediator, the mono-top model can be simplified substantially and the desired MET+X final state is realized. In this case, the mediator is a singlet. A leading order Feynman diagram of a mono-top process via a FCNC is shown in figure 5.7b. The interactions of the mono-top model with a spin-1 mediator V are incorporated into the Lagrangian:

$$\begin{aligned}\mathcal{L} &= \mathcal{L}_{\text{kin}}(\text{V}) + \mathcal{L}_{\text{vector}}(\text{V}) + \text{h.c.} \\ &= \mathcal{L}_{\text{kin}}(\text{V}) \\ &+ \text{V}_\mu \bar{u}\left(a^1\gamma^\mu + b^1\gamma^\mu\gamma_5\right) u + \text{V}_\mu \bar{d}\left(a^1\gamma^\mu + b^1\gamma^\mu\gamma_5\right) d + \text{h.c.}\end{aligned} \tag{5.4}$$

Here, $\mathcal{L}_{\text{kin}}$ is the kinetic part of the Lagrangian, characterizing the kinetic, mass and gauge interactions terms of the new mediator. The vector of up-type (u,c,t) quarks is represented by u, whereas the down-type (d,s,b) quarks are denoted by d. Color indices are implied. The interaction strength between the quarks and the mediator is given by the flavor matrices a^1 and b^1 for the vector mediator. It can be observed that, both a vector as well as an axial-vector interaction is possible. The couplings are chosen such that only quarks of the first and third generation interact since these production modes are preferred by the PDFs at the LHC. Explicitly, the only non-zero couplings are given by:

$$a_{13}^{0/1}, a_{31}^{0/1} \neq 0 \tag{5.5}$$

$$b_{13}^{0/1}, b_{31}^{0/1} \neq 0 \tag{5.6}$$

Consequently, the following decay modes of the mediator into SM particles are possible:

$$\begin{aligned}&\text{V} \to \text{t}\bar{\text{u}} \\ &\text{V} \to \bar{\text{t}}\text{u} \\ &\text{V} \to \text{d}\bar{\text{b}} \\ &\text{V} \to \bar{\text{d}}\text{b}\,.\end{aligned}$$

As shown, also mono-bottom signatures are possible in addition to the targeted mono-top final state. Such mono-bottom signatures are considered in the model and influence the predicted branching ratios (BRs) and cross sections. However, during the event generation, only mono-top final states are realized. In addition, the newly introduced mediator is assumed to decay into a pair of invisible, fermionic DM candidates χ with a significant branching fraction. The latter requirement ensures the desired MET+X final state.

Assuming a Dirac DM candidate χ being a singlet under all SM interactions, the decay term in the Lagrangian is given by

$$\mathcal{L}_{\text{V}\to\chi\bar{\chi}} = \mathcal{L}_{\text{kin}} + \text{V}_\mu \bar{\chi}\gamma^\mu \left(g_{\text{V}}^{\chi} + g_A^{\chi}\gamma^5\right)\chi. \tag{5.7}$$

The kinetic term $\mathcal{L}_{\text{kin}}$ of the Lagrangian contains the kinetic as well as mass terms for the DM candidate χ. The axial and vector coupling strengths of the mediator to the DM particles are given by g_A^{χ} and g_{V}^{χ}, respectively. Consequently, two different benchmark coupling scenarios are considered in the scope of this thesis. The nominal scenario involves a purely vectorial coupling with

$$(g_{\text{V}}^{\text{u}})_{13} = (g_{\text{V}}^{\text{u}})_{31} = (g_{\text{V}}^{\text{d}})_{13} = (g_{\text{V}}^{\text{d}})_{31} = 0.25 \tag{5.8a}$$

$$g_{\text{V}}^{\chi} = 1 \tag{5.8b}$$

$$(g_{\text{A}}^{\text{u}})_{13} = (g_{\text{A}}^{\text{u}})_{31} = (g_{\text{A}}^{\text{d}})_{13} = (g_{\text{A}}^{\text{d}})_{31} = 0 \tag{5.8c}$$

$$g_{\text{A}}^{\chi} = 0\,. \tag{5.8d}$$

The second scenario involves a purely axial coupling with

$$(g_V^u)_{13} = (g_V^u)_{31} = (g_V^d)_{13} = (g_V^d)_{31} = 0 \tag{5.9a}$$
$$g_V^\chi = 0 \tag{5.9b}$$
$$(g_A^u)_{13} = (g_A^u)_{31} = (g_A^d)_{13} = (g_A^d)_{31} = 0.25 \tag{5.9c}$$
$$g_A^\chi = 1\,. \tag{5.9d}$$

The superscripts u and d denote the coupling to both up-type and down-type quarks and antiquarks, respectively. As mentioned above, couplings to left-handed down-type quarks will lead to mono-bottom signatures. The exact coupling values are chosen such that the invisible decay mode is dominant, as it will be shown in the following. Furthermore, they follow the recommendation of the LHC DM working group, ensuring comparability between different searches and experiments [37].

Depending on the mass hierarchy of the mediator and the top quark different phenomenological features are realized.

5.3.2.1 Mediator lighter than top quark

If the mediator is lighter than the top quark mass, the decay into a top quark and a light up-type quark is kinematically forbidden. Therefore, only a decay via a virtual top quark is possible:

$$\mathrm{V} \to \mathrm{u}\bar{\mathrm{b}}\mathrm{W}^- \tag{5.10}$$
$$\mathrm{V} \to \bar{\mathrm{u}}\mathrm{b}\mathrm{W}^+ \tag{5.11}$$

If the mass of the mediator is below the W boson mass, the W boson is virtual as well. In this mass regime, loop-induced processes need to be considered. For example, a W triangle loop generates a coupling to a pair of down-type quarks, resulting in a new dijet decay channel. Since such loop-induced processes are suppressed, the lifetime of the mediator gets enhanced. Therefore, it might not be necessary to consider a decay into DM candidate particles. However, it can be shown that the lifetime would still be too short to have a reasonable coupling allowing for observation at collider experiments. For more details on this, see [129].

Furthermore, this mass hierarchy opens up a new decay channel of the top quark $\mathrm{t} \to \mathrm{uV}$. This additional decay channel allows constraining the model by measurements of the top quark decay width and searches for FCNC decays of the top quark for example. However, such measurements disfavor light mediators. More details on this can be found in [129].

Consequently, an invisible decay channel is necessary. However, the model needs to be able to predict the correct DM relic density observed in the universe, see section 2.2.1. In the $m_V < m_t$ case, the main annihilation process $\chi\chi \to \mathrm{V} \to \mathrm{t}\bar{\mathrm{u}}/\bar{\mathrm{t}}\mathrm{u}$ is kinematically forbidden. Therefore, mainly loop-induced processes contribute to the annihilation cross section. Since such processes are heavily suppressed, an overabundance of DM would be the consequence. Consequently, the mass regime, in which the mediator is lighter than the top quark mass is already excluded.

5.3.2.2 Mediator heaver than top quark

If the mediator is heavier than the sum of top quark and bottom quark mass, a decay into a top quark and a bottom quark is kinematically allowed. Therefore, the mediator itself

cannot be long-lived. Consequently, the mono-top signature can only be accomplished if the branching fraction of the mediator into a pair of DM candidates is the dominant one. This is the case if the coupling of the mediator to SM particles is much weaker than to the DM particles, which motivates the chosen coupling values of the nominal benchmark couplings as given in equation (5.8) and equation (5.9). Figure 5.8 shows the BRs of the mediator into a pair of DM candidates as a function of the mediator and DM candidate mass m_{V} and m_{χ}, respectively. In general, all BRs are above 50 %, indicating that the invisible decay mode is dominant. If the DM candidate mass is close to the kinematically allowed boundary of $m_{\mathrm{V}} = 2 \times m_{\chi}$, the invisible BR decreases. This behavior can be attributed to the fact that the available phase space for the invisible decay mode decreases.

5.3.2.3 Cross sections

Figure 5.9 shows the predicted cross sections for the vector and axial-vector mono-top model as a function of the mediator and DM candidate masses $\mathrm{M_V}$ and M_{χ} at NLO perturbation theory in QCD. A sharp decline in the cross section as a function of the mediator mass is observed. As a consequence, the cross sections are expected to be below 0.1 pb for mediator masses above 1.8 TeV. Correspondingly, very small signal yields are expected in this high-mass regime, motivating the need for sophisticated analysis methods and large datasets in order to probe this region.

5.3.2.4 Constraints from Dark Matter relic density

Constraints based on the relic DM abundance can be considered in order to further constrain the mono-top model. The relic DM abundance is determined by the annihilation cross section of the DM candidate into a pair of SM particles

$$\chi\overline{\chi} \rightarrow \mathrm{V} \rightarrow \mathrm{t}\overline{\mathrm{u}} \text{ or } \overline{\mathrm{t}}\mathrm{u}. \tag{5.12}$$

The relic abundance is given by

$$\Omega_{\mathrm{DM}} h^2 = \frac{1.04 \times 10^9}{M_{\mathrm{Pl}}} \frac{x_F}{\sqrt{g*}} \frac{1}{\langle \sigma v \rangle}, \tag{5.13}$$

where M_{Pl} is the Planck mass, x_F is the freeze-out fraction m_{χ}/T_F with the freeze-out temperature $T_F \approx 25\,\mathrm{GeV}$, $g* = 92$ is the effective number of relativistic degrees of freedom at the freeze-out and $\langle \sigma v \rangle$ is the mean annihilation cross section. The most distinctive feature of this equation is the inverse dependency of the relic abundance on the annihilation cross section. More information on the calculation of the relic abundance can be found in [131].

By using MadDM [132, 133], an extension of the MadGraph5_aMC@NLO [43, 44] generator, the relic abundance for the mono-top model as a function of the DM candidate and mediator mass m_{χ} and m_{V}, respectively, is calculated. This is shown in figure 5.10 for the two benchmark scenarios considered, pure vector and pure axial couplings.

The predicted relic abundance is strongly suppressed for a mediator mass close to the production threshold of the two DM candidates ($m_V \approx 2 \cdot m_{\chi}$). Since the annihilation cross section increases when approaching the on-shell production of the mediator, the relic abundance decreases due to its inverse proportionality to the annihilation cross section. The structural pattern in this threshold region is an artifact due to the limited number of mass hypotheses considered in this study. Further constraints on the mono-top model can be made by considering the measured value of the relic density in the universe [30] of $\Omega_{\mathrm{DM}} h^2 = 0.12 \pm 0.001$. This value is shown as a black contour in figure 5.10. If the

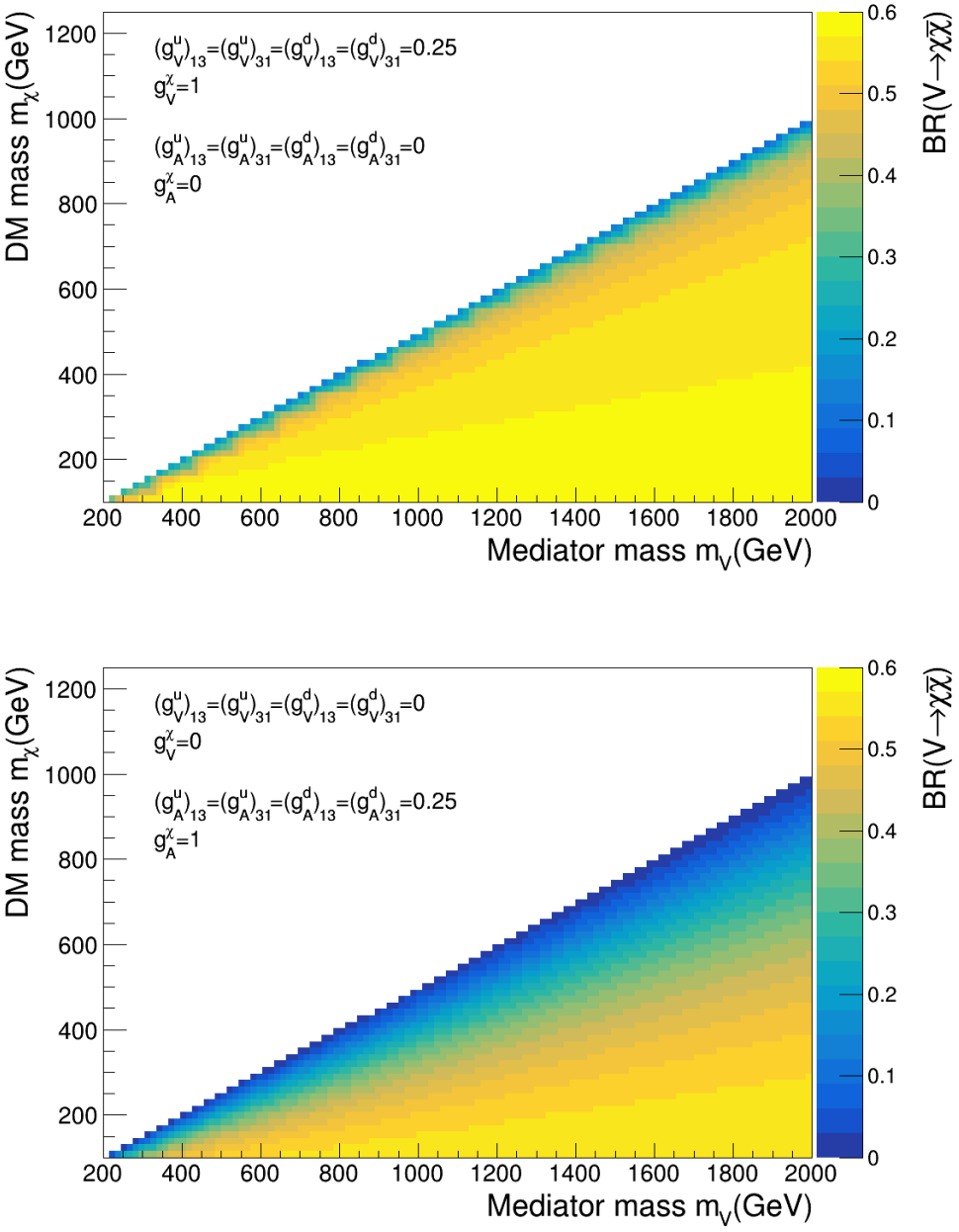

Figure 5.8: Branching ratios of the mediator into pair of DM candidates as a function of the mediator and DM candidate mass m_V and m_χ, respectively. The nominal pure vectorial coupling scenario is considered for the upper plot, whereas the pure axial model is deployed in the lower plot.

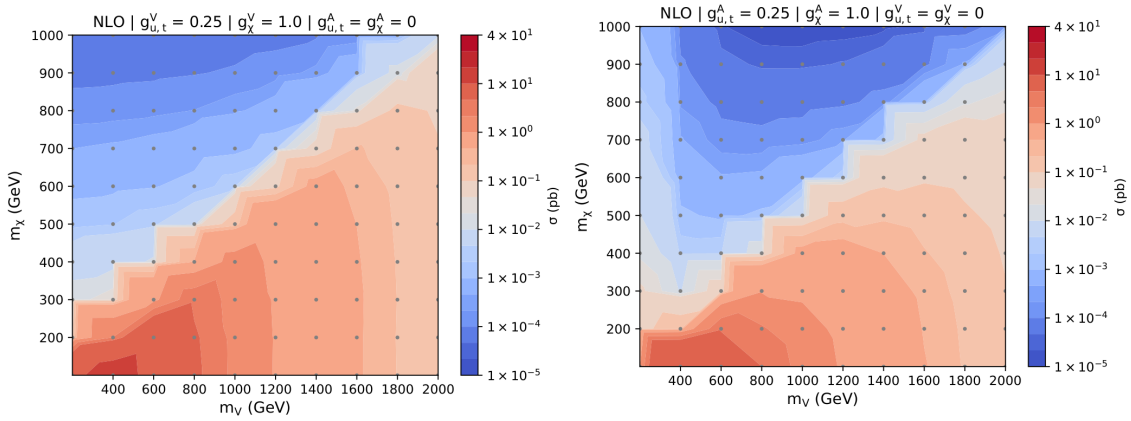

Figure 5.9: Cross sections as a function of the mediator and DM candidate masses M_V and M_χ for the vector (left) and axial-vector (right) mono-top model at NLO perturbation theory in QCD. Taken from [130].

assumption of a minimal DM model is made, i.e., there are no additional mediators and DM particles and the DM candidate χ is stable on cosmological time scales, only mass values on this line are allowed. However, if this assumption is not made, the parameter space of the mono-top model below the black line is excluded, since the predicted relic abundance would be too small. In the case of a pure axial-vector coupling also the parameter region enclosed by the black line in the regime of $m_V < 2 \times m_\chi$ is excluded. Two interesting features are observed when comparing the two benchmark scenarios. First, the relic density is not falling as sharply when approaching the production threshold of $m_V = 2 \times m_\chi$, for the pure axial-vector coupling scenario. This is due to the fact that the annihilation cross section is helicity-suppressed for the pure axial-vector coupling scenario and thus increasing the predicted relic abundance. Second, there is an additional region of allowed mass hypotheses, where $m_V < 2 \times m_\chi$. This parameter space can be attributed to a kinematic region in which a decay of the mediator into a pair of mediators is kinematically allowed. In principle, this decay channel is also possible for the pure vectorial coupling scenario. However, this regime is only relevant for the pure axial-vector coupling due to the increase of predicted relic abundance. Consequently, strong bounds on the mono-top model can be made already based on cosmological constraints.

5.3.2.5 Branching ratios and partial decay widths

In the case of a vector mediator, the partial decay widths of the mediator into the DM candidates and quarks can be used to calculate the BR of the mediator into DM candidates. Details on the following calculations can be found in [37, 129]. For the calculation of partial widths, all masses except for the top quark, DM candidate and mediator masses are neglected. The partial decay width into a first-generation down-type quark (antiquark) and a third-generation down-type antiquark (quark) is given by

$$\Gamma_d = \frac{m_V}{4\pi} g_q^2, \tag{5.14}$$

since only couplings between the first and third generations are considered. In this equation, the mass of the hypothetical mediator is denoted by m_V. The coupling strength g_q between this mediator and the SM quarks is given by either $g_{V,q}$ in the case of a pure vectorial coupling or $g_{A,q}$ for the axial-vector coupling scenario. Analogously, the partial width into a first-generation up-type quark and a third-generation up-type quark (top quark) is given

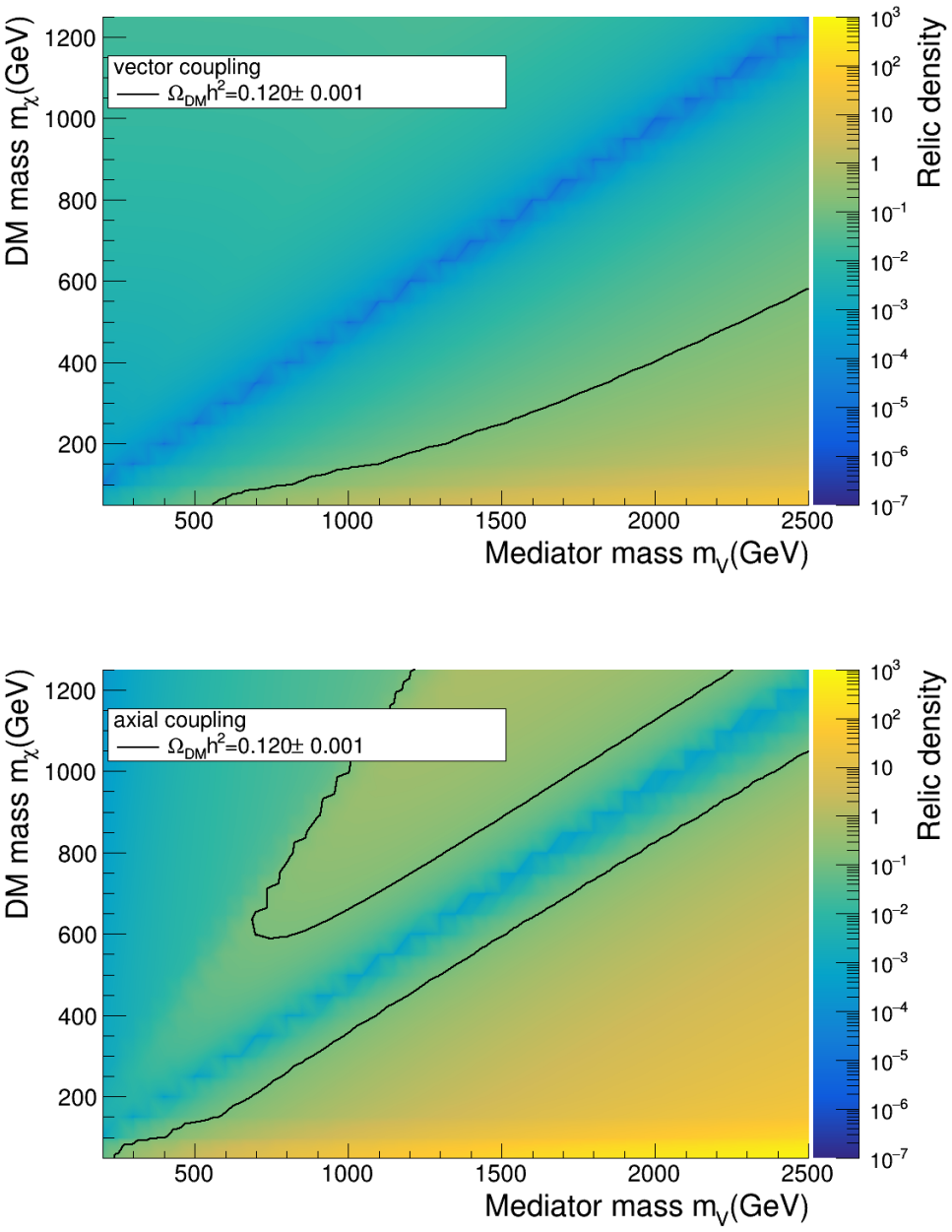

Figure 5.10: DM relic density for the pure vectorial mono-top model as a function of the mediator and DM candidate mass m_V and m_χ, respectively. The upper plot corresponds to the pure vectorial mono-top model, whereas the lower plot corresponds to a pure axial-vector coupling scenario. The measured value of the relic density is indicated by a black line [30].

by

$$\Gamma_u = \frac{m_\mathrm{V}}{4\pi} g_\mathrm{q}^2 \left(1 - \frac{m_\mathrm{t}^2}{m_\mathrm{V}^2}\right)\left(1 - \frac{m_\mathrm{t}^2}{2m_\mathrm{V}^2} - \frac{m_\mathrm{t}^4}{2m_\mathrm{V}^4}\right), \tag{5.15}$$

where m_t denotes the mass of the top quark. Again, the coupling strength g_q is either $g_\mathrm{V,q}$ or $g_\mathrm{A,q}$.

The partial width of the vector mediator V into a pair of DM candidates χ is given by

$$\Gamma_\chi = \frac{m_\mathrm{V}}{12\pi} g_\mathrm{V,\chi}^2 \sqrt{1 - \frac{4m_\chi^2}{m_\mathrm{V}^2}} \left(1 + 2\frac{m_\chi^2}{m_\mathrm{V}^2}\right) \tag{5.16}$$

for a pure vectorial coupling scenario. In the case of an axial-vector coupling, the partial width is given by

$$\Gamma_\chi = \frac{m_\mathrm{V}}{12\pi} g_\mathrm{A,\chi}^2 \left(1 - \frac{4m_\chi^2}{m_\mathrm{V}^2}\right)^{3/2}. \tag{5.17}$$

By considering the aforementioned partial widths, the BR of the vector mediator into a pair of DM particles is defined as follows:

$$\mathrm{BR}\left(\mathrm{V} \to \chi\chi\right) = \frac{\Gamma_\chi}{\Gamma_d + \Gamma_u + \Gamma_\chi}. \tag{5.18}$$

This relation has the interesting property that the BR is only dependent on the masses of the hypothetical particles of the mono-top model if the coupling strengths are taken as constant.

5.4 Simulation samples

An important ingredient of analyses in high-energy physics is the simulation of the relevant background processes. The simulation of these relevant background processes, as well as the signal samples, is described in the following. All simulation samples use Pythia 8.2 [50–52] for the simulation of the PS (fragmentation) as well as the hadronization. The PS is simulated using the `CP5` tune [134]. The hadronization utilizes the phenomenological Lund string model [48, 49]. The interaction of the particles with the CMS detector is simulated with Geant4 [135–137]. The samples considered in this thesis are summarized in tables 5.1 and 5.2, in which the used cross section, as well as the number of events per data-taking period, are given. The cross sections are taken directly from the generator if no reference is given. Otherwise, higher-order theory calculations are referenced and considered.

5.4.1 Electroweak production of a single vector boson in association with jets

Electroweak production of a single vector boson (W,Z,γ) in association with jets (V + jets) represents one of the most important background process in this analysis. The hard interaction of these processes is generated at NLO QCD accuracy using MadGraph5_aMC@NLO [43, 44]. Up to two additional hard jets arising from the matrix element (ME) are considered in the case of W + jets and Z + jets production. For γ + jets one additional jet at ME level is considered. In order to ensure a sufficient number of events in the whole phase space, the samples are split according to the number of additional jets produced at ME level as well as the transverse momentum of the vector boson.

For W + jets production, only leptonic decays of the W boson are considered. Hadronic decay modes will not contribute to the analysis since neither a lepton nor a significant amount of MET is present in the final state. The samples split according to the transverse momentum of the W boson do not populate the entire phase space. Therefore, samples split according to the number of additional jets are considered for W boson transverse momenta below 400 GeV. Using both samples has the advantage of maximizing the available event count in the full range of W boson transverse momenta.

In the case of the Z + jets production, decays of the Z boson into charged leptons and neutrinos are considered. Hadronic decay modes of the Z boson are not considered since no significant amount of MET is expected. For these samples, the Drell-Yan (DY) process is simulated. In order to enrich in events originating from Z boson rather than virtual photon decays, a minimum threshold of 50 GeV is applied to the transverse momentum of the Z boson.

The γ + jets sample considers events in which a prompt final-state photon is produced in association with at least one jet.

5.4.2 Top quark-antiquark pair ($t\bar{t}$) and single top quark production

Top quark-antiquark pair production, as well as single top quark in the t- and tW-channel, are simulated at NLO QCD accuracy with up to two additional jets in the final state using Powheg [45–47] as ME generator. The three different decay modes of the $t\bar{t}$ system are simulated separately [146, 147], whereas all top quark decays are allowed inclusively for the single top quark samples. The single top quark s-channel sample is simulated with the MadGraph5_aMC@NLO event generator.

Table 5.1: Samples for the production of an EWK boson in association with jets split according to the underlying process. The first column lists the phase space and the second column the cross section σ predicted by the generator at NLO QCD accuracy. The last three columns show the number of events produced for the different data-taking eras.

Phase space	σ (pb)	2016preVFP	2016postVFP	2017	2018
		W($\ell\nu$) + jets			
0 additional jet	53 300	152.37 M	158.35 M	169.42 M	171.90 M
1 additional jet	8947	173.25 M	158.05 M	180.02 M	183.89 M
2 additional jets	3335	87.75 M	84.90 M	96.03 M	94.83 M
$100 \leq p_{\mathrm{T}}^{\mathrm{W}}$ (GeV) ≤ 250	757.7	144.49 M	224.99 M	459.19 M	481.16 M
$250 \leq p_{\mathrm{T}}^{\mathrm{W}}$ (GeV) ≤ 400	27.53	54.87 M	43.43 M	102.60 M	104.85 M
$400 \leq p_{\mathrm{T}}^{\mathrm{W}}$ (GeV) ≤ 600	3.51	5.80 M	5.64 M	11.67 M	12.40 M
$600 \leq p_{\mathrm{T}}^{\mathrm{W}}$ (GeV)	0.54	2.10 M	1.79 M	3.68 M	3.74 M
		Z($\ell\ell$) + jets			
$0 \leq p_{\mathrm{T}}^{\mathrm{Z}}$ (GeV) ≤ 50	1490	100.84 M	97.20 M	198.36 M	198.26 M
$50 \leq p_{\mathrm{T}}^{\mathrm{Z}}$ (GeV) ≤ 100	399	60.12 M	59.79 M	123.05 M	123.10 M
$100 \leq p_{\mathrm{T}}^{\mathrm{Z}}$ (GeV) ≤ 250	96.22	39.58 M	38.41 M	80.73 M	79.62 M
$250 \leq p_{\mathrm{T}}^{\mathrm{Z}}$ (GeV) ≤ 400	3.73	12.08 M	12.20 M	24.28 M	24.20 M
$400 \leq p_{\mathrm{T}}^{\mathrm{Z}}$ (GeV) ≤ 650	0.50	1.75 M	1.92 M	4.04 M	3.95 M
$650 \leq p_{\mathrm{T}}^{\mathrm{Z}}$ (GeV)	0.05	2.00 M	2.02 M	4.03 M	3.99 M
		Z($\nu\nu$) + 1 jet			
$50 \leq p_{\mathrm{T}}^{\mathrm{Z}}$ (GeV) ≤ 150	580.7	6.57 M	6.68 M	12.01 M	12.19 M
$150 \leq p_{\mathrm{T}}^{\mathrm{Z}}$ (GeV) ≤ 250	17.36	19.19 M	19.30 M	37.93 M	37.41 M
$250 \leq p_{\mathrm{T}}^{\mathrm{Z}}$ (GeV) ≤ 400	1.98	9.62 M	9.18 M	18.75 M	18.37 M
$400 \leq p_{\mathrm{T}}^{\mathrm{Z}}$ (GeV)	0.22	0.79 M	0.81 M	1.68 M	1.62 M
		Z($\nu\nu$) + 2 jets			
$50 \leq p_{\mathrm{T}}^{\mathrm{Z}}$ (GeV) ≤ 150	314.5	9.78 M	10.42 M	19.24 M	18.29 M
$150 \leq p_{\mathrm{T}}^{\mathrm{Z}}$ (GeV) ≤ 250	28.8	43.39 M	42.18 M	84.05 M	83.26 M
$250 \leq p_{\mathrm{T}}^{\mathrm{Z}}$ (GeV) ≤ 400	4.99	37.38 M	39.90 M	72.97 M	77.43 M
$400 \leq p_{\mathrm{T}}^{\mathrm{Z}}$ (GeV)	0.82	5.71 M	5.86 M	11.78 M	11.32 M
		γ + jets			
$150 \leq p_{\mathrm{T}}^{\gamma}$ (GeV) ≤ 250	225.9	5.86 M	5.60 M	11.58 M	11.13 M
$250 \leq p_{\mathrm{T}}^{\gamma}$ (GeV) ≤ 400	26.98	1.96 M	2.82 M	5.99 M	6.00 M
$400 \leq p_{\mathrm{T}}^{\gamma}$ (GeV) ≤ 675	3.40	1.00 M	1.00 M	2.00 M	2.00 M
$675 \leq p_{\mathrm{T}}^{\gamma}$ (GeV)	0.25	0.29 M	0.25 M	0.50 M	0.50 M

Table 5.2: Background samples considered in this thesis split according to the corresponding physics process. Given are the number of events generated for each data-taking era and the cross section σ.

Phase space	σ (pb)	2016preVFP	2016postVFP	2017	2018
		$t\bar{t}$ (NNLO QCD) [138, 139]			
dileptonic	88.34	37.51 M	43.63 M	101.71 M	145.99 M
hadronic	377.96	97.60 M	109.74 M	235.72 M	342.43 M
semiLeptonic	365.46	130.22 M	144.95 M	355.67 M	478.29 M
		single top quark (NLO QCD) [140–142]			
s-channel leptonic	3.30	5.52 M	5.33 M	13.88 M	19.37 M
t-channel (anti-top)	80.95	31.00 M	30.61 M	69.92 M	95.70 M
t-channel (top)	136.02	55.96 M	59.92 M	129.69 M	179.46 M
tW-channel (anti-top)	35.85	2.30 M	2.55 M	5.67 M	7.75 M
tW-channel (top)	35.85	2.30 M	2.49 M	5.65 M	7.96 M
		diboson [143–145]			
WW	119 (NNLO QCD)	14.18 M	15.82 M	15.63 M	15.68 M
WZ	46.7 (NLO QCD)	7.93 M	7.58 M	7.89 M	7.94 M
ZZ	16.9 (NNLO QCD)	1.28 M	1.15 M	2.71 M	3.53 M
		QCD (LO)			
$30 \leq p_{\mathrm{T}}\,(\mathrm{GeV}) \leq 50$	1.07×10^{8}	18.94 M	19.57 M	19.83 M	19.99 M
$50 \leq p_{\mathrm{T}}\,(\mathrm{GeV}) \leq 80$	1.57×10^{7}	19.93 M	19.78 M	20.00 M	19.49 M
$80 \leq p_{\mathrm{T}}\,(\mathrm{GeV}) \leq 120$	2.34×10^{6}	29.74 M	30.13 M	29.40 M	29.69 M
$120 \leq p_{\mathrm{T}}\,(\mathrm{GeV}) \leq 170$	4.08×10^{5}	28.65 M	27.31 M	28.90 M	29.95 M
$170 \leq p_{\mathrm{T}}\,(\mathrm{GeV}) \leq 300$	1.04×10^{5}	27.95 M	29.93 M	29.81 M	29.68 M
$300 \leq p_{\mathrm{T}}\,(\mathrm{GeV}) \leq 470$	6.83×10^{3}	53.35 M	55.29 M	55.69 M	57.91 M
$470 \leq p_{\mathrm{T}}\,(\mathrm{GeV}) \leq 600$	5.51×10^{2}	49.82 M	51.77 M	50.89 M	52.41 M
$600 \leq p_{\mathrm{T}}\,(\mathrm{GeV}) \leq 800$	1.57×10^{2}	49.51 M	59.72 M	67.38 M	67.51 M
$800 \leq p_{\mathrm{T}}\,(\mathrm{GeV}) \leq 1000$	2.63×10^{1}	33.80 M	37.07 M	36.89 M	37.16 M
$1000 \leq p_{\mathrm{T}}\,(\mathrm{GeV}) \leq 1400$	7.48	19.08 M	16.24 M	19.78 M	19.67 M
$1400 \leq p_{\mathrm{T}}\,(\mathrm{GeV}) \leq 1800$	1.259×10^{-1}	11.00 M	9.18 M	10.99 M	10.98 M
$1800 \leq p_{\mathrm{T}}\,(\mathrm{GeV}) \leq 2400$	8.748×10^{-2}	5.26 M	4.31 M	5.49 M	5.49 M
$2400 \leq p_{\mathrm{T}}\,(\mathrm{GeV}) \leq 3200$	5.236×10^{-3}	3.00 M	2.85 M	3.00 M	3.00 M
$3200 \leq p_{\mathrm{T}}\,(\mathrm{GeV})$	1.35×10^{-4}	1.00 M	1.00 M	1.00 M	1.00 M

5.4.3 QCD multijet production

The production of QCD multijet events is simulated with the MadGraph5 [43, 44] event generator at leading order (LO). Since the subsequent PS can generate prompt photons, double counting can occur due to possible overlaps with the $\gamma + \text{jets}$ sample described earlier. Therefore, events with one or more prompt photons are removed from the QCD sample in the hadronic analysis, where the $\gamma + \text{jets}$ sample is considered.

5.4.4 Diboson production

Events, in which two electroweak bosons $\text{WW}, \text{WZ}, \text{ZZ}$ are produced, are simulated with the Pythia 8.2 [50–52] event generator at LO accuracy. The weak bosons are allowed to decay hadronically as well as leptonically.

5.4.5 Non-resonant vector mono-top production

The mono-top signal samples are generated using MadGraph5_aMC@NLO at NLO QCD accuracy, where no additional jets are considered besides one hard QCD radiation. The authors of the model directly provide a file which can be interfaced to the generator. Specifically, the `DMsimp_s_spin1` (v. 2.1) model [148] is used in this analysis. For the signal generation, different masses for both the mediator V as well as the DM candidate χ are considered in separate samples. The mass hypotheses considered and the cross section predicted by the generator are given in table 5.3. Generally, the mass hypotheses were chosen such that both one off-shell and two on-shell decays of each mediator mass m_{V} is available. A pure vectorial coupling is assumed during the event generation, where the coupling of the mediator to the DM candidates and the SM particles are chosen to be $g_{\text{V},q} = 0.25$ and $g_{\text{V},\chi} = 1$, respectively. However, during the generation weights are calculated, allowing for reweighting of the signal samples to alternative coupling scenarios. Furthermore, all couplings involving flavor-diagonal interactions and second-generation quarks are omitted. The choice of couplings follows the recommendations of the LHC DM Working Group [37].

5.5 Corrections for simulations

In order to obtain the best description of the data from the simulation, several corrections are applied. Corrections are either theory-based, such as a reweighting to a higher order in perturbation theory, or driven by known discrepancies between the measured data and the simulation, which are corrected by applying scale factors (SFs).

5.5.1 Reweighting to higher order in perturbation theory for single vector boson production

One of the most important backgrounds in MET+X searches is the production of a single electroweak boson in association with additional jets ($\text{V} + \text{jets}$). Due to possible invisible decays of the vector boson, such processes mimic the signature of a MET+X signal. Therefore, it is essential to have a good description of the SM $\text{V} + \text{jets}$ background in the simulation to not falsely claim a BSM discovery. The transverse momentum of the vector boson renders a crucial kinematic property in MET+X searches since it dictates the MET and consequently the hadronic recoil in an event.

As described earlier, the $\text{V} + \text{jets}$ samples are generated at NLO QCD accuracy using MadGraph5_aMC@NLO [43, 44]. The events are subsequently interfaced with Pythia 8.2 [50–52] to simulate the fragmentation and hadronization. The importance

Table 5.3: Signal mass hypotheses and production cross sections σ.

m_V in GeV	m_χ in GeV	cross section σ in pb
150	150	1.88×10^{-1}
200	50	5.76×10^{1}
200	150	2.53×10^{-1}
195	100	4.93×10^{0}
295	150	2.37×10^{0}
300	100	1.90×10^{1}
300	300	1.89×10^{-2}
500	150	4.32×10^{0}
495	250	7.04×10^{-1}
500	500	2.26×10^{-3}
750	150	1.12×10^{0}
745	325	8.97×10^{-1}
1000	150	3.73×10^{-1}
995	500	7.10×10^{-2}
1000	1000	5.34×10^{-5}
1245	625	2.81×10^{-2}
1250	150	1.44×10^{-1}
1500	150	6.21×10^{-2}
1495	750	1.21×10^{-2}
1500	1000	1.07×10^{-4}
1750	150	2.88×10^{-2}
1750	700	2.26×10^{-2}
1700	800	1.89×10^{-2}
2000	150	1.41×10^{-2}
2000	500	1.30×10^{-2}
1995	1000	2.66×10^{-3}
2000	1500	4.32×10^{-6}
2245	1125	1.32×10^{-3}
2250	150	7.30×10^{-3}
2500	750	3.24×10^{-3}
2495	1250	6.79×10^{-4}
2500	2000	2.68×10^{-7}
3000	1000	8.94×10^{-4}
2995	1500	1.90×10^{-4}
3000	2000	4.32×10^{-7}

of the accuracy of the NLO QCD has been studied in an earlier iteration of the hadronic mono-top analysis [126], in which samples with LO QCD accuracy were considered.

However, MadGraph5_aMC@NLO is only able to provide LO accuracy for EWK corrections. Figure 5.11 shows the NLO EWK corrections for different V + jets processes as a function of the transverse momentum of the vector boson. It can be observed that the NLO EWK corrections are especially important in regimes with high transverse momenta, which is also the region where most of the mono-top signal is expected.

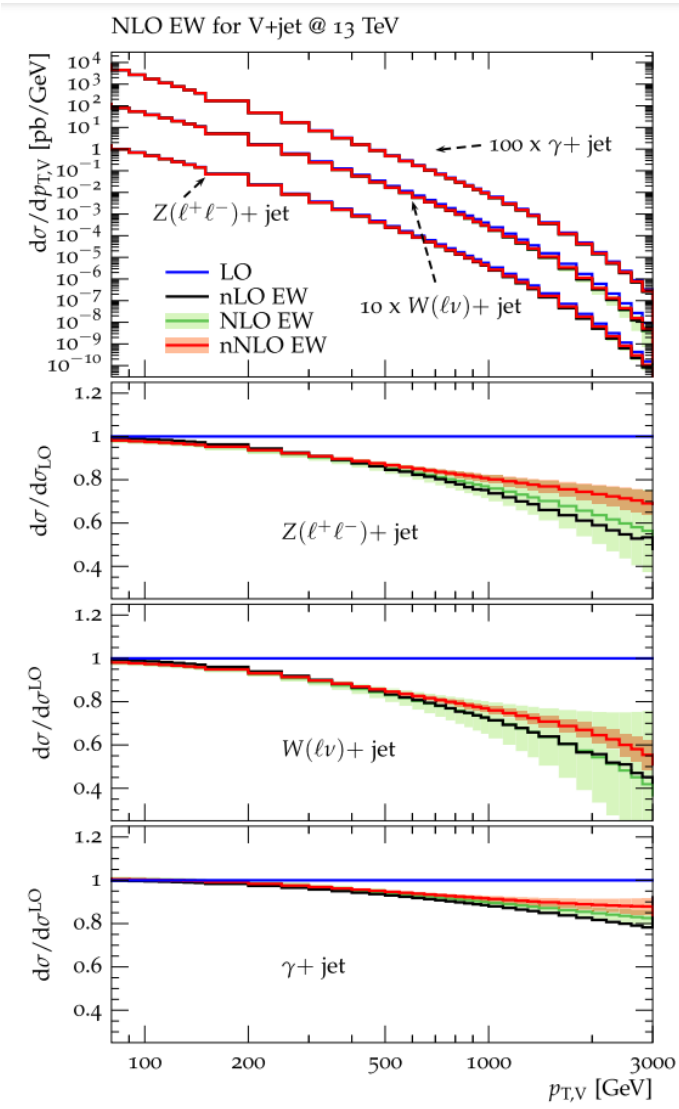

Figure 5.11: Fixed-order differential cross section for different orders of EWK corrections as a function of vector boson transverse momentum p_T for different V + jets processes. Taken from [149].

In order to obtain NLO precision also for the EWK corrections, a reweighting procedure is applied following [149]. For this reweighting the differential cross section as a function of the transverse momentum of the vector boson is used. The transverse momentum of the vector boson is considered since it dictates the hadronic recoil and consequently, the full event topology of an event. A k-factor k is calculated such that the differential cross

sections of the samples match the higher order differential cross section:

$$k\left(p_{\mathrm{T}}(\mathrm{V}), \epsilon_{\mathrm{TH}}, \epsilon_{\mathrm{MC}}\right) = \frac{\sigma_{\mathrm{TH}}\left(p_{\mathrm{T}}(\mathrm{V}), \epsilon_{\mathrm{TH}}\right)}{\sigma_{\mathrm{MC}}\left(p_{\mathrm{T}}(\mathrm{V}), \epsilon_{\mathrm{MC}}\right)}. \tag{5.19}$$

In this equation, σ_{TH} and σ_{MC} denote the differential cross sections of the higher order theory prediction and the MC generated sample, respectively. For the transverse momentum of the vector boson V, a particle-level-based definition is deployed. Particle-level refers to the state of the simulation after the PS and hadronization. Thus, the vector boson is reconstructed from the final state particles as opposed to using the vector boson directly from the MC truth. This approach offers the advantage of having more direct correspondence between $p_{\mathrm{T}}(\mathrm{V})$ and the hadronic recoil in an event. Furthermore, the cross sections depend on uncertainties parametrized via two parameters ϵ_{TH} and ϵ_{MC} for the theory and the MC sample, respectively. These uncertainties are taken into account in the statistical model.

5.5.2 Reweighting to higher order in perturbation theory for top quark-antiquark pair production

Sizable differences are observed when comparing the differential spectrum of the transverse momentum of the top quark or antiquark in $\mathrm{t\bar{t}}$ simulations and higher-order theory calculations. A comparison of theory calculations at next-to-next-to-leading order (NNLO) QCD and NNLO QCD +NLO EWK with various MC generators and PS tunes are shown on the upper plot of figure 5.12. The MC generators generally predict a softer top quark p_{T} spectrum than the theoretical calculations. This effect is especially pronounced in the high-p_{T} regime. The lower plot of figure 5.12 shows the ratio of the NNLO QCD +NLO EWK theory calculation to the NLO QCD Powheg sample considered in this thesis.

In order to account for these differences, a reweighting procedure is applied to the $\mathrm{t\bar{t}}$ samples. The CMS TOP Physics Analysis Group (PAG) provides the SF as a function of the top quark p_{T} which is derived by fitting a function to the ratio of the NNLO QCD +NLO EWK theory calculation to the NLO QCD Powheg sample [150, 151]:

$$\mathrm{SF}\left(p_{\mathrm{T}}\right) = 0.103 \cdot \exp\left(-0.0118 \cdot p_{\mathrm{T}}\right) - 0.000134 \cdot p_{\mathrm{T}} + 0.973. \tag{5.20}$$

Since both a top quark as well as top antiquark are generated, the final SF is the geometric mean of the two SFs for the top quark and top antiquark:

$$\mathrm{SF} = \sqrt{\mathrm{SF}\left(p_{\mathrm{T}}\left(\mathrm{t}\right)\right) \cdot \mathrm{SF}\left(p_{\mathrm{T}}\left(\bar{\mathrm{t}}\right)\right)}. \tag{5.21}$$

A conservative uncertainty on this reweighting is estimated by varying the SF such that the down-variation is equal to the nominal Powheg NLO QCD prediction and the absolute difference of the SF to the nominal prediction is doubled for the down-variation. This uncertainty is taken into account in the statistical model deployed in this analysis.

5.5.3 Pileup reweighting

The average number of proton-proton interactions in each bunch crossing in data is unknown during the simulation samples' generation. Therefore, a reweighting procedure is applied, correcting the distribution of average numbers of interactions in the simulation. The distribution in data is obtained by considering the luminosity profile and the total inelastic proton-proton cross section of 69.20 mb provided by the CMS luminosity Physics Object Group (POG). A systematic uncertainty on this reweighting procedure is considered by varying the total inelastic proton-proton cross section by $\pm 4.6\,\%$. This variation results in alternative weights, which can be used to construct alternative templates parameterizing the PU uncertainty. A corresponding nuisance parameter is introduced in the statistical model to account for this uncertainty.

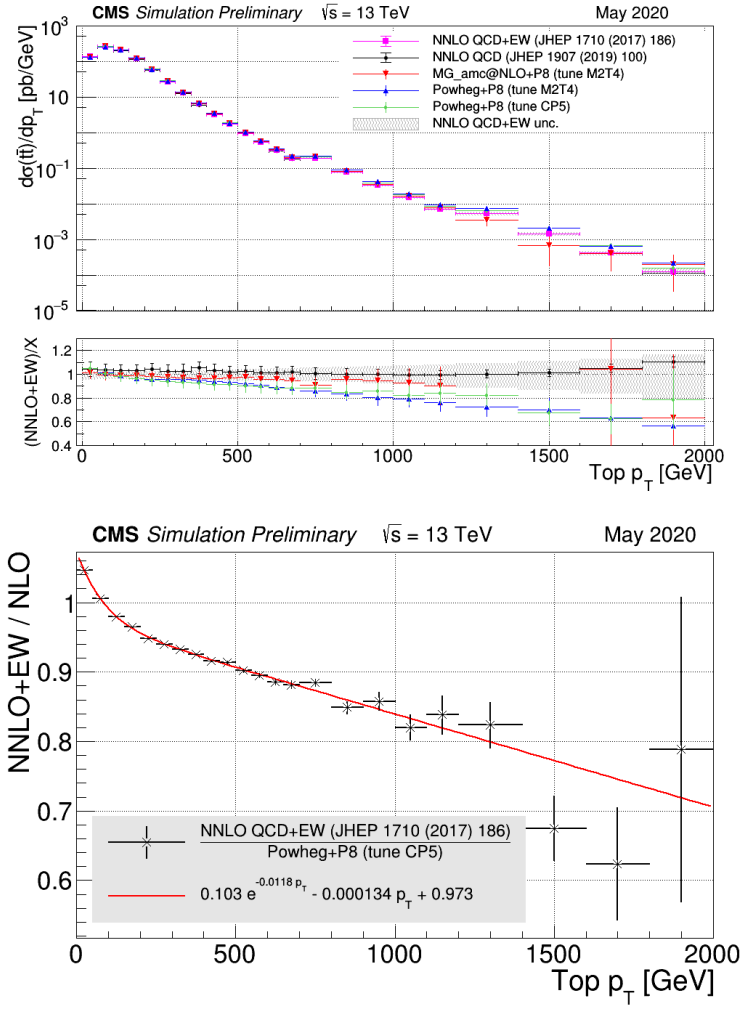

Figure 5.12: The differential cross section as a function of the transverse momentum of the generator level is shown for different MC generators and PS tunes and theory predictions at NNLO QCD as well as NNLO QCD +NLO EWK in perturbation theory on top. The lower pad shows the ratio to the NNLO QCD +NLO EWK of the top quark. The lower figure shows the ratio of the POWHEG sample to the NNLO QCD +NLO EWK calculation. Taken from [150].

5.5.4 Prefire reweighting

During data taking, an issue arose concerning the CMS trigger system. Some L1 trigger primitives were assigned to the wrong bunch crossing due to a timing shift of the ECAL. This issue is known as L1 prefiring issue [152] and can lead to a misassignment of the trigger decision. The issue is present in all data-taking periods but is most severe in 2016 and 2017. The prefiring effect led to the circumstance that the trigger primitives were not found in the correct bunch crossing. Additionally, due to the rule that an L1 trigger is not allowed to fire on two consecutive bunch crossings, an event could be discarded although it would have been selected by the L1 primitive. Since this issue is not modeled in the simulation, a correction is applied via event weights.

The event weight is constructed by assigning a weight to each object that can cause the L1 prefiring issue (jets and photons), characterizing the probability of causing the issue. The final event weight is the product of all non-prefiring probabilities and is provided centrally by the CMS luminosity POG [152].

Additionally, a systematic uncertainty is considered by varying the separate prefiring probabilities within their uncertainties. Again, a corresponding nuisance parameter is introduced in the statistical model to account for this uncertainty.

5.5.5 Angular MET correction

Due to the nature of the underlying physics of proton-proton collisions, no preferred emission direction of the decay products in the transverse plane is expected. Consequently, the azimuthal angle distribution of the MET is expected to be flat. However, due to minor asymmetries in the detector geometry and the fact that the interaction point is not perfectly centered inside the CMS experiment, an angular dependency is observed. This effect is known and corrected for in data and simulation, where different detector conditions during operation are taken into account. These corrections are derived by L. Thomas, a member of the CMS collaboration.

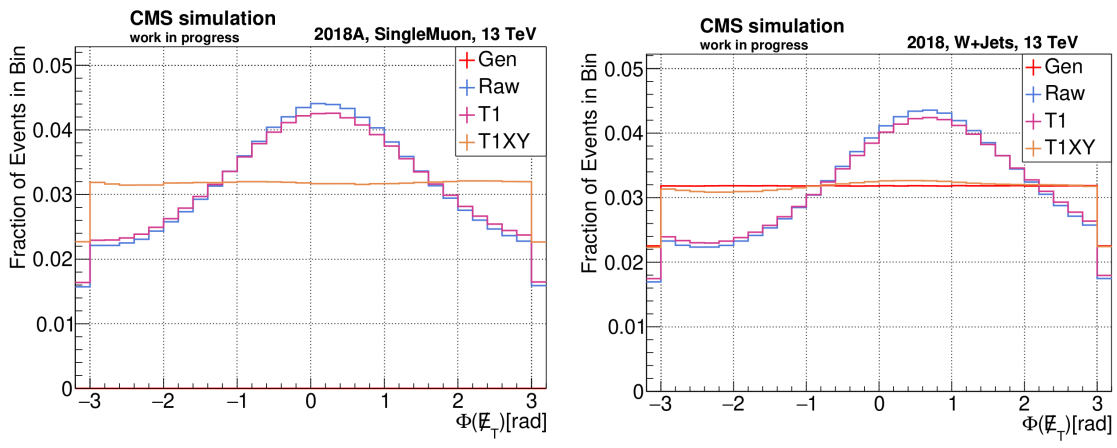

Figure 5.13: Exemplary distributions of the azimuthal angle of different types of MET for data (left-hand side) and simulation (right-hand side). The uncorrected MET is denoted as T1, whereas T1XY denotes the case in which the correction is applied. The correction is derived by L. Thomas and illustrated by M. Waßmer, both members of the CMS collaboration.

Figure 5.13 shows a comparison of the uncorrected MET (labeled as T1) and the case in which the correction is applied (labeled as T1XY). Only exemplary distributions are shown for the year 2018 for data and simulation to illustrate the effect. The clearly visible asymmetry in the uncorrected MET is corrected by the angular MET correction.

5.6 Recorded data

This thesis considers data taken with the CMS detector in the years 2016, 2017 and 2018, collectively referred to as full Run 2. The data is recorded at a center-of-mass energy of 13 TeV. Due to different detector conditions during data taking, the datasets are split according to the year of data taking. During data taking in 2016, the feedback preamplifier bias voltage of the silicon strip detector was changed. This was because a low signal-to-noise ratio was observed during high PU conditions, which turned out to be due to saturation effects in the readout chip [153]. Therefore, the 2016 data-taking era is split into two periods, referred to as pre- and postVFP, respectively.

The datasets per era are further split according to the logical OR of several HLT paths. In order to construct several signal-depleted control regions (CRs) and signal-enriched signal regions (SRs), different HLT paths and, therefore, datasets are required. Single electron/muon datasets contribute to the leptonic CRs of the hadronic mono-top analysis as well as the CRs and SRs of the leptonic mono-top analysis. The single photon dataset is used to construct a $\gamma + \text{jets}$ CR for the hadronic mono-top analysis. For the 2018 data-taking era, the single photon and single electron datasets are merged. The MET dataset is used to construct the SR of the hadronic mono-top analysis since a significant amount of MET is required. Since muons are not considered for the calculation of MET at HLT level, this dataset can also be used to construct single and double muon CRs for the hadronic mono-top analysis. More details on the analysis strategy and the various CRs and SRs are given in section 6.1 and section 7.1 for the hadronic and leptonic analyses, respectively. A dataset based on the scalar sum of transverse momenta of jets (H_T) is used to derive top-tagging efficiencies as will be described in section 5.7.5.3. A summary of which datasets are used for which regions is given in table 5.4. Table 5.5 shows the number of events in each dataset.

Table 5.4: Recorded datasets considered in this thesis. Given are the HLT paths and how the sample is used in this thesis.

HLT path	Application	
	leptonic mono-top	hadronic mono-top
Single Electron	CRs and SRs	single and double electron CRs
Single Muon	CRs and SRs	
Single Photon	-	single photon CR
Missing transverse momentum	-	single/double muon CR and SR
Jet H_T	-	top-tagging calibration

Table 5.5: Number of events in the recorded datasets considered in this thesis. Given are the HLT paths and the number of events per era.

HLT path	Number of events			
	2016preVFP	2016postVFP	2017	2018
Single Muon	459.9 M	327.1 M	739.1 M	946.9 M
Single Electron	654.4 M	288.0 M	460.1 M	-
Single Photon	138.4 M	67.4 M	108.2 M	-
Single Electron or Photon	-	-	-	1329.2 M
Missing transverse momentum	102.9 M	64.3 M	411.7 M	254.8 M
Jet H_T	-	-	-	643.7 M

5.7 Object definitions

The PF algorithm (see section 3.3.1) is used to reconstruct objects in the CMS detector. Thus, PF reconstructed photons, charged leptons, and charged and neutral hadrons are considered in this analysis. These PF candidates are subsequently used to reconstruct MET (see section 3.3.6). The charged and neutral hadrons are used to cluster jets (see section 3.3.5). Subsequently, additional requirements are imposed to these objects in order to define the final physic objects used for the offline analysis. These additional requirements mainly concern the reconstruction or identification quality of the objects. Additionally, the decisions of all HLT paths considered are evaluated.

The following describes the selection criteria of all objects considered, in which possible corrections and corresponding uncertainties are also introduced.

5.7.1 Trigger decisions

The information of all HLT paths is stored in the CMS event data format for a given event. Based on this list, an event is selected if a specific trigger or a specific trigger combination decides to keep the event. This trigger selection can then be used to define either signal-depleted CRs or signal-enriched SRs. The exact trigger selection is described in section 7.2 and section 6.2.2 for the hadronic and leptonic analyses, respectively.

A critical aspect of a trigger is its efficiency. The efficiency of a trigger describes how many events are selected by the trigger in question for a given offline selection compared to the total number of events fulfilling that offline selection. Therefore, trigger efficiency is a measure of how many events are expected in data. However, the trigger efficiency is found to differ when comparing data to simulation. By measuring the efficiency of a trigger in an independent data sample and simulation, SFs can be derived accounting for these differences. Often, these efficiencies are derived as a function of a specific kinematic variable, such as the transverse momentum of the relevant physics object.

The SFs for isolated muon triggers deployed in the leptonic mono-top analysis are provided centrally by the corresponding CMS muon POG [154–156]. In principle, the procedure for deriving these SFs (tag and probe (TnP) method) is very similar to the isolated electron trigger SFs described in the following. However, the SFs for the electron, photon and hadronic recoil triggers are not provided centrally. Therefore, the SFs are measured in the scope of this thesis. The derivation of these SFs is briefly described in the following.

5.7.1.1 Isolated electron trigger scale factors

The triggers considered in this analysis to select events with prompt electrons are listed in table 5.6 for all four data-taking eras. For low-p_{T} electrons, the HLT selects events in which an isolated electron is reconstructed with a minimum p_{T} threshold as given in the name of the HLT path. For high-p_{T} electrons, the performance of the track reconstruction is reduced, thus decreasing the HLT efficiency. For this reason, photon triggers are deployed for this kinematic regime, recovering this efficiency loss. Consequently, the logical OR of the electron and photon triggers are used to select events with prompt electrons.

A TnP method provided by the corresponding CMS POG is used to measure the SFs for the isolated electron trigger combination [157]. The TnP method is based on the following principle: The method considers a clean, well-established decay of a narrow resonance into two charged leptons, such as a Z boson decay. Then, strict reconstruction requirements are imposed to one of the leptons, ensuring that this so-called *tag* lepton is a prompt well-reconstructed lepton. Due to the constraint of the narrow resonance, the

Table 5.6: Electron HLT paths for all data-taking eras.

object	HLT path
2018	
electron (low p_T)	`HLT_Ele32_WPTight_Gsf`
electron/photon (high p_T)	`HLT_Photon200`
2017	
electron (low p_T)	`HLT_Ele35_WPTight_Gsf`
electron/photon (high p_T)	`HLT_Photon200`
2016[pre/post]VFP	
electron (low p_T)	`HLT_Ele27_WPTight_Gsf`
electron/photon (high p_T)	`HLT_Photon175`

other lepton, the *probe* lepton, is also expected to be prompt. Consequently, by deploying the HLT requirement, the efficiency can be measured by counting how many times the HLT requirement is fulfilled for the probe lepton. In order to capture kinematic effects, the efficiencies are measured as a function of the transverse momentum and pseudorapidity of the lepton. As it will be described in section 5.7.2, both a *loose* and a *tight* electron collection are used in this thesis. Therefore, the SFs are measured for both collections independently.

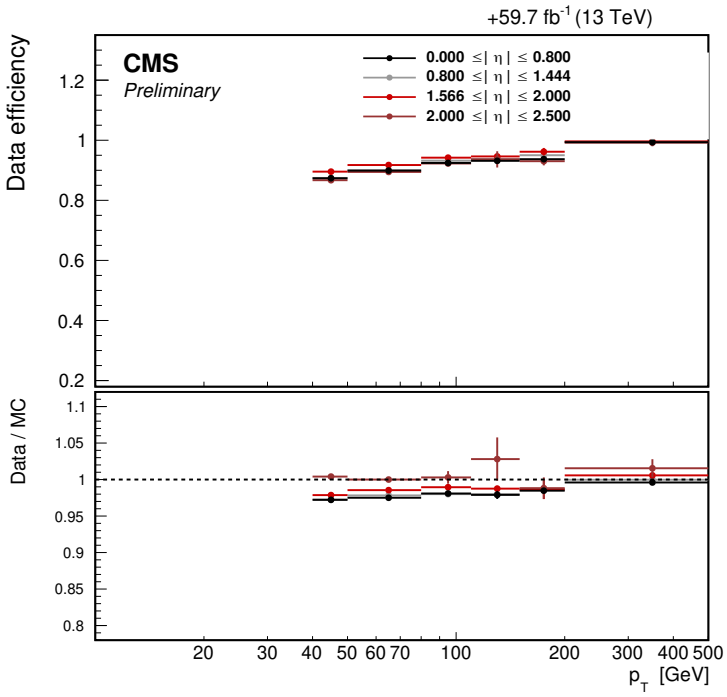

Figure 5.14: Trigger efficiency of the electron triggers in data for the 2018 data-taking era as a function of the transverse momentum for the tight electron collection. Different ranges in pseudorapidity are shown in different colors. The bottom panel shows the ratio of the efficiency in data to the efficiency in simulation and corresponds to the SF.

Figure 5.14 shows the electron trigger efficiency in data for the 2018 data-taking era as a function of the transverse momentum for different pseudorapidity ranges. The data to MC SF is shown in the bottom panel. It can be observed that the trigger combination is highly efficient, with an efficiency of more than 95 % in data. Furthermore, the SF is stable over the whole transverse momentum range. The efficiencies in data and the SFs for all data-taking eras and electron collections are shown in appendix A.

5.7.1.2 Isolated photon trigger scale factors

The single photon triggers listed in table 5.6 are used in the hadronic analysis to construct a CR enriched in $\gamma +$ jets events, see section 7.2.6. The photon HLT SFs are derived by using the jet H_T datasets as listed in table 5.5. Events are selected if a tight photon as defined later in section 5.7.4 is reconstructed. Furthermore, the scalar sum of the transverse momenta of all AK4 jets (H_T) is required to be above 1500 GeV. The trigger efficiency is derived by considering a reference trigger as listed in table 5.7.

Table 5.7: Reference HLT paths for the photon trigger SF derivation for all data-taking eras.

data-taking era	reference HLT path
2018	`HLT_PFHT1050`
2017	`HLT_PFHT1050`
2016[pre/post]VFP	`HLT_PFHT900`

The aforementioned requirement on H_T ensures that these reference triggers are fully efficient. The efficiency for a given photon trigger is then given by the ratio of events passing the photon trigger as well as reference H_T trigger to the number of events passing the reference trigger:

$$\epsilon_{\text{photon-trigger}} = \frac{N_{\text{reference \&\& photon}}}{N_{\text{reference}}} \tag{5.22}$$

In order to capture kinematic effects, the efficiencies are derived as a function of the transverse momentum of the photon. Figure 5.15 shows the photon trigger efficiency in data and simulation for the 2018 data-taking era as a function of the transverse momentum of the photon. It can be observed that the efficiency reaches its plateau at roughly 250 GeV. Furthermore, the SF shown in the bottom panel is compatible with unity in the plateau. Possible deviations from unity are considered via a flat 5 % uncertainty on the SF. The SFs for all data-taking eras are shown in appendix B.

5.7.1.3 Missing transverse momentum trigger scale factors

As it will be described later when discussing the analysis strategy targeting the hadronic mono-top signal (section 7.2.1), specialized triggers are deployed requiring a large amount of MET. In this reconstruction of MET at HLT level, muons are not considered. The exact trigger paths are listed in table 5.8. The logical OR is applied to select events if multiple trigger paths are given.

The procedure to derive corresponding SFs as a function of the hadronic recoil follows the same principle as for the photon trigger. The SFs were derived in the scope of a bachelor thesis [158]. In this derivation, both a single muon as well as a dimuon phase space region was considered. The studies showed that only minor differences exist between the two phase space regions. A single isolated muon trigger was deployed as reference trigger.

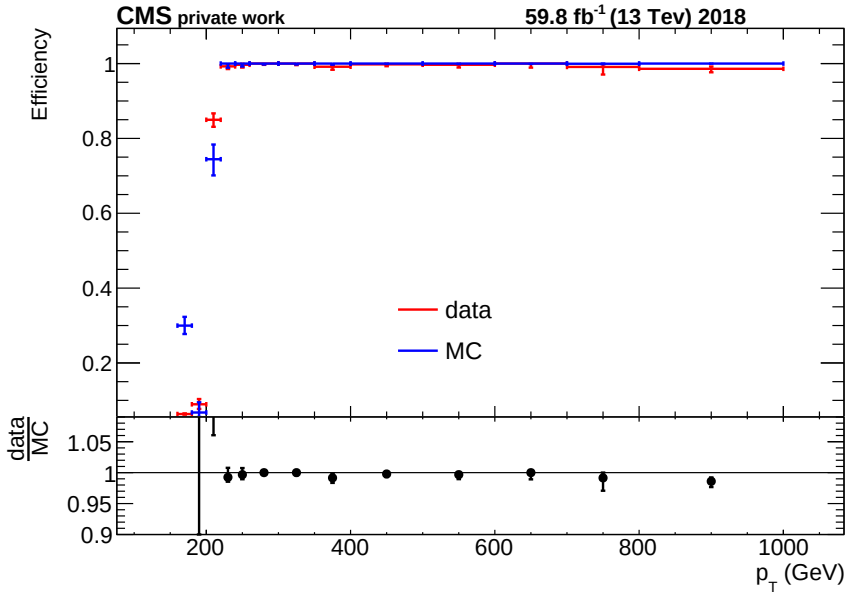

Figure 5.15: Trigger efficiency of the photon trigger in data and simulation for the 2018 data-taking era as a function of the transverse momentum. The bottom panel shows the ratio of the efficiency in data to the efficiency in simulation and corresponds to the SF.

Table 5.8: Hadronic recoil HLT paths considered in the hadronic analysis split across the data-taking eras.

signature	HLT path
	2018
$\not{E}_T/\not{U}_T$	`HLT_PFMETNoMu120_PFMHTNoMu120_IDTight` `HLT_PFMETNoMu120_PFMHTNoMu120_IDTight_PFHT60`
	2017
$\not{E}_T/\not{U}_T$	`HLT_PFMETNoMu120_PFMHTNoMu120_IDTight` `HLT_PFMETNoMu120_PFMHTNoMu120_IDTight_PFHT60`
	2016[pre/post]VFP

$\not{E}_T/\not{U}_T$	`HLT_PFMETNoMu90_PFMHTNoMu90_IDTight`
	`HLT_PFMETNoMu100_PFMHTNoMu100_IDTight`
	`HLT_PFMETNoMu110_PFMHTNoMu110_IDTight`
	`HLT_PFMETNoMu120_PFMHTNoMu120_IDTight`

Figure 5.16 shows the trigger efficiency in data and simulation for the 2018 data-taking era as a function of the hadronic recoil. The efficiencies reach their plateau at roughly 300 GeV. The SF shown in the bottom panel is compatible with unity in the plateau. However, below the plateau, significant differences from unity are observed. More details and an in-depth discussion, as well as the SFs for all data-taking eras, can be found in [158].

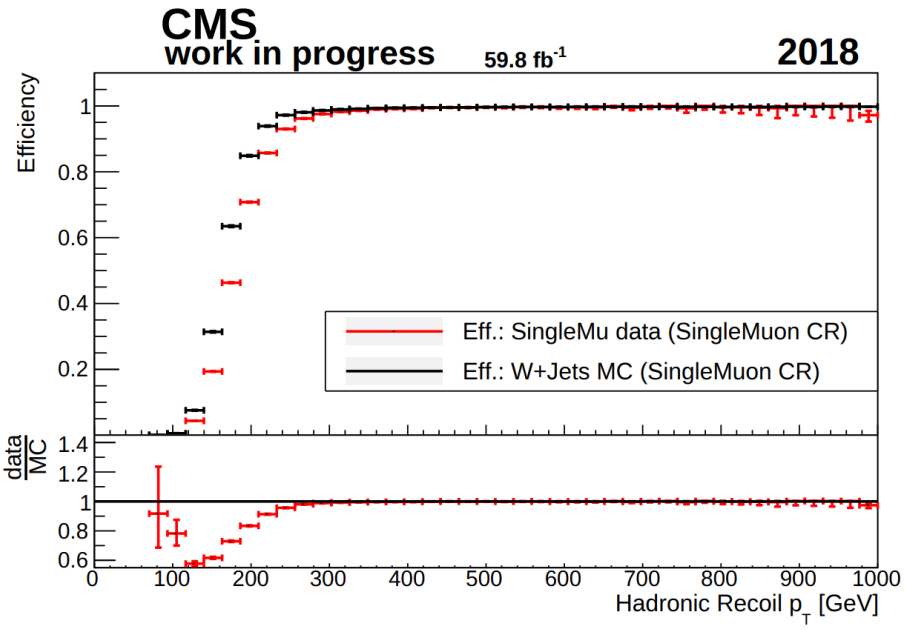

Figure 5.16: Trigger efficiency of the recoil trigger combination in data and simulation for the 2018 data-taking era as a function of the hadronic recoil. The bottom panel shows the ratio of the efficiency in data to the efficiency in simulation and corresponds to the SF. Taken from [158].

5.7.2 Electrons

Two kinds of electron collections are used in this thesis, referred to as *loose* and *tight* electrons. Less strict quality criteria are applied to the *loose* electrons to increase selection efficiency. However, the increased selection efficiency comes at the cost of an increased electron misidentification rate. This statement holds vice versa for the *tight* electrons. For both collections, PF reconstructed electrons are used. The quality criteria aim at selecting high-purity prompt electrons originating from weak vector boson decays. The selection criteria are summarized in table 5.9.

Table 5.9: Selection criteria for the *loose* and *tight* electron collections used in this thesis. Different requirements are made on the impact parameters (IP), depending on whether the electron is reconstructed in the barrel (B) or the endcap (EC) region.

collection	p_{T} [GeV]	$\lvert\eta\rvert$	ID	IP_{xy}[cm]	IP_z[cm]
loose	> 10	< 2.5	loose	< 0.05 (B), < 0.1 (EC)	< 0.1 (B), < 0.2 (EC)
tight	> 40	< 2.4	tight	< 0.05 (B), < 0.1 (EC)	< 0.1 (B), < 0.2 (EC)

The electron ID is a cut-based discriminant centrally provided by the CMS collaboration. It is based on several kinematic variables associated to the track and ECAL cluster matched to the electron. Several WPs are defined. The loose(tight) WP correspond to a efficiency of approximately 90(70) % [159]. More information on electron reconstruction and

identification can be found in [160]. The lower p_{T} threshold of 40 GeV is chosen to ensure that the single electron triggers (see section 5.7.1.1) are highly efficient. The selection requirement on the absolute value of the pseudorapidity is motivated by the geometric coverage of the CMS tracker. In addition, quality criteria are applied to the impact parameters both in transverse (IP_{xy}) and longitudinal (IP_z) direction with respect to the primary vertex. Different impact parameter cuts are applied depending on whether the electron is reconstructed in the barrel (B) or endcap (EC) region. Additionally, electrons are not considered if they are reconstructed in the transition region (crack) between the barrel and the endcap of the CMS ECAL ($1.4442 < |\eta| < 1.5660$). The loose electron collection will mainly be used to veto events containing prompt electrons in regions in which no electron is expected to be present, such as muon or photon CRs. The tight electron collection is used in analysis regions in which prompt electrons are expected.

Differences in the electron reconstruction and identification efficiency between data and simulation are taken into account by applying POG-provided SFs [161] based on a TnP method. These SFs depend on the transverse momentum and the supercluster η of the ECAL of the reconstructed electron. Uncertainties on these SFs are propagated to the final observables and considered in the statistical model via nuisance parameters.

5.7.3 Muons

Analogous to electrons, *loose* and *tight* collections are also defined for reconstructed muons. The selection criteria are summarized in table 5.10.

Table 5.10: Selection criteria for the *loose* and *tight* muon collections used in this thesis. If multiple numbers are given, the values correspond to different eras of data taking (2016/2017/2018).

collection	p_{T} [GeV]	$\lvert\eta\rvert$	ID	ISO ID
loose	$> 15/20/20$	< 2.4	loose	loose
tight	> 30	< 2.4	tight	tight

Again, a loose or tight WP of the identification (ID) discriminant is defined. This identification discriminant incorporates information from the silicon tracker and the muon system aiming at parameterizing the identification efficiency. The loose WP has an efficiency of approximately 99 % of selecting real muons, whereas the efficiency for the tight WP is approximately 96%. The misidentification rates are less than 0.5 % and 0.3 % for the tight and loose WP, respectively [162]. In addition to the ID discriminant, another quantity referred to as isolation (ISO) ID is used. The isolation is a measure of how much hadronic activity is present around the muon. Therefore, it is suited to discriminate between muons originating from the hard proton-proton interaction and muons stemming from hadron decays which may occur inside jets [162]. The offline cut on the absolute value of the pseudorapidity is motivated by the geometric coverage of the CMS tracker. In contrast, the lower thresholds on the transverse momentum are motivated by the range, where POG-provided SFs are available [154–156]. These SFs aim to correct the efficiencies for both the identification and isolation discriminant in simulation to match the efficiencies observed in data. They are provided as a function of the transverse momentum and pseudorapidity of the muon. The uncertainties on these SFs are propagated to the final observables and considered in the statistical model via nuisance parameters.

5.7.4 Photons

A *loose* and *tight* collection is also defined for photons. The selection criteria are summarized in table 5.11.

Table 5.11: Selection criteria for the *loose* and *tight* photon collections used in this thesis. If multiple numbers are given, the values correspond to different eras of data taking (2016/2017/2018).

collection	p_{T} [GeV]	$\lvert\eta\rvert$	ID
loose	> 20	< 2.5	loose
tight	$> 200/230/230$	< 1.479	medium

The different lower thresholds of the transverse momentum of the tight photons are motivated by the different trigger thresholds of the single photon triggers used in the different eras. Since it is vital not to misidentify an electron as a photon, the tight photon collection is only considered if it is reconstructed in the barrel region of the CMS ECAL ($|\eta| < 1.479$). For photons, the loose and medium WPs of the cut-based identification discriminant (ID) are used. This identification discriminant is based on kinematic information of the photon candidate based on information from the ECAL and the silicon tracker. The loose WP has an identification efficiency of approximately 90 %, whereas the medium WP still yields approximately 80 % efficiency [163]. If a loose electron or muon is found within a spatial distance of $\Delta R < 0.4$ of the photon, the photon is discarded. Similar to electrons and muons, tight photons are considered to construct regions enriched in prompt photons. In contrast, loose photons are used to veto events containing prompt photons in regions in which no photon is expected to be present, such as muon or electron CRs.

Again, discrepancies between the efficiencies for the identification discriminant in simulation and data are taken into account by applying POG-provided SFs [161]. Corresponding uncertainties are propagated to the final observables and considered in the statistical model via nuisance parameters.

5.7.5 Jets

As already mentioned in section 3.3.5, two kinds of jets, AK4 and AK15 jets, are considered in this thesis. Jets are required to fulfill several quality criteria to ensure they are well reconstructed and to reduce contamination from PU. The most important selections criteria are summarized in table 5.12.

Table 5.12: Selection criteria for the AK4 and AK15 jet collections used in this thesis.

collection	p_{T} [GeV]	$\lvert\eta\rvert$	ID	PU ID
AK4	> 30	< 2.4	tight lepton veto	loose for $p_{\mathrm{T}} < 50\,\mathrm{GeV}$
AK15	> 160	< 2.4	tight lepton veto	-

The AK4 (AK15) jets are required to have a transverse momentum of at least 30 (160) GeV and to be reconstructed in the region $|\eta| < 2.4$. Like leptons and photons, an identification (ID) WP is defined The jets are required to pass a so-called *tight lepton veto* WP. This WP has an efficiency of more than 98 % [164]. This ID incorporates different requirements on various energy fractions in the jet. For example, the energy fraction of a reconstructed muon with respect to the reconstructed jet should be less than 80 %, effectively vetoing muons that are misidentified as jets. The exact requirements are described in [164]. Since additional PU collisions might also result in reconstructed jets, a dedicated multivariate PU ID is provided by the CMS collaboration [165]. The loose PU ID is applied to jets with a transverse momentum below 50 GeV since jets originating from PU collisions are expected to be relatively soft. The loose PU ID WP corresponds to an efficiency of 99 % [165]. As

described in section 3.3.5, the CHS [80] algorithm is used for AK4 jets to mitigate energy deposits originating from PU interactions. For AK15 jets, the PUPPI [81] algorithm is deployed. In addition, jets are not considered in this analysis if a loose muon, electron or photon is reconstructed within a spatial distance of $\Delta R < 0.4$ or $\Delta R < 1.5$ of the AK4 or AK15 jet, respectively. Previous studies found that the description of AK15 jets can be improved by deploying additional criteria on the charged and neutral hadron fraction. The charged hadron fraction is required to be larger than 10 %, and the neutral hadron fraction must be smaller than 80 %, removing events with anomalously high MET [126].

5.7.5.1 Jet energy corrections

Jets and especially their energy needs to be calibrated. In general, these corrections are referred to as jet energy corrections (JECs). The following brief introduction is based on [166, 167]. More information on the derivation, as well as performance numbers, can be found in [168–170] It should be noted that no dedicated JECs are provided for AK15 jets. Therefore, centrally provided JECs derived for AK8 jets are applied to AK15 jets. Although this shortcoming, no sincere mismodeling of the jet transverse momentum is observed as shown in appendix K. Furthermore, the uncertainties on the JECs are estimated conservatively, accounting for potential mismodeling of the fatjets.

Jet energy scale corrections

In order to minimize the difference between the measured jet kinematics and the parton kinematics, jet energy scale (JES) are deployed. Different factorized corrections are centrally available [171]. The total uncertainty of the JES correction is propagated to the final observables and considered in the statistical model via a nuisance parameter. Each of these corrections is applied to the jet four-momentum in a separate step correcting for a specific effect. These corrections are dependent on jet properties such as the transverse momentum or the pseudorapidity.

The first effect to correct for arises due to additional energy deposits from PU collisions. By considering a QCD dijet sample simulated with and without PU interactions, the additional energy contributions from PU collisions can be estimated. Residual differences between data and MC are then corrected. Subsequently, the jet response is estimated by comparing the measured jet energy to the parton energy in a QCD dijet sample. Finally, the residual differences of the jet response between data and MC are corrected. These residual corrections are derived using a $\mathrm{Z} \to ee(\mu\mu)$ and $\gamma +$ jets sample as a function of the pseudorapidity of the jet.

Jet energy resolution corrections

The second kind of correction aims at correcting the jet energy resolution (JER) in MC to match the resolution in data. The correction is applied differently, depending on whether a particle-level jet is matched to the reconstructed jet. The criterion to consider a particle-level jet as matched to a reconstructed jet is based on the spatial distance between the two objects. The jet is considered matched if the distance is smaller than half of the jet cone radius. In the case of a matched jet, the jet four-momentum of the reconstructed jet is scaled with

$$c_{\mathrm{JER}} = 1 + (s_{\mathrm{JER}} - 1)\frac{p_{\mathrm{T}} - p_{\mathrm{T}}^{\mathrm{particle}}}{p_{\mathrm{T}}}, \tag{5.23}$$

where p_{T} denotes the transverse momentum of the reconstructed and $p_{\mathrm{T}}^{\mathrm{particle}}$ of the particle-level jet. The correction factor c_{JER} is truncated to zero. The data to simulation resolution SF is denoted by s_{JER}.

If no particle-level jet is matched to the reconstructed jet, the correction factor is determined via

$$c_{\mathrm{JER}} = 1 + \mathcal{N}\left(0, \sigma_{\mathrm{JER}}\right) \sqrt{\max\left(s_{\mathrm{JER}}^2 - 1, 0\right)}. \tag{5.24}$$

In this equation, $\mathcal{N}\left(0, \sigma_{\mathrm{JER}}\right)$ is a random number drawn from a normal distribution with zero mean and a standard deviation of σ_{JER}, the relative p_{T} resolution in simulation.

5.7.5.2 B-tagging corrections

As described in section 5.2.1, the `DeepJet` algorithm is deployed to identify jets originating from bottom quarks. It was observed that the b-tagging efficiencies are different in data with respect to MC simulation. In order to predict the correct event yields when applying b-tagging, a correction is applied to the MC simulation to mitigate this effect. These corrections depend both on the b-tagging efficiency in simulation and SFs provided by the b Tag & Vertexing (BTV) POG [172–175].

The efficiencies should be derived for the collection of jets used for b-tagging. Therefore, all aforementioned quality criteria are applied to the jets before the b-tagging efficiencies are determined. Furthermore, due to the event topology and analysis strategy in the hadronic mono-top analysis, AK4 jets are only considered for b-tagging if they do not overlap with an AK15 jet, i.e., if $\Delta R(\mathrm{AK4,AK15}) > 1.5$, see section 7.1. In order to get a good estimate of the b-tagging efficiency, the phase space in which the efficiencies are determined should be close to the analysis region. Therefore, the common preselections for both the hadronic and leptonic mono-top analysis, as described in sections 6.2 and 7.2, are applied. The efficiency ϵ is defined as the ratio of b-tagged jets, i.e., passing a given WP, and all jets:

$$\epsilon = \frac{\text{number of b-tagged jets}}{\text{number of all jets}} \tag{5.25}$$

In order to capture kinematic dependencies, the efficiencies are determined in bins of the transverse momentum of the jet and its pseudorapidity. Figures 5.17 and 5.18 show the efficiencies derived for the leptonic and hadronic mono-top analysis, respectively. They are shown for jets originating from a bottom quark. The efficiencies for LF quark (u, d, s) and a charm quark are shown in appendix C. Jets arising from b and c quarks are commonly referred to as HF jets. It can be observed that the efficiencies behave similarly across all data-taking eras. However, lower efficiencies are observed for the 2016 eras with respect to the 2017 and 2018 data-taking eras. A possible reason for this could be the pixel detector upgrade installed before data taking in 2017. The upgrade improved the tracking performance, directly impacting the b-tagging performance.

By using the efficiencies, the probability P of a given configuration can be defined both in data and in simulation. The efficiency in simulation is corrected by consider POG-provided SFs [176]:

$$P(\mathrm{MC}) = \prod_{i=\text{tagged}} \epsilon_i \prod_{j=\text{not tagged}} (1 - \epsilon_j) \tag{5.26}$$

$$P(\mathrm{DATA}) = \prod_{i=\text{tagged}} \mathrm{SF}_i \epsilon_i \prod_{j=\text{not tagged}} (1 - \mathrm{SF}_i \epsilon_j) \tag{5.27}$$

In these equations, both the efficiencies ϵ as well as the SF are functions of transverse momentum p_{T}, pseudorapidity η and jet flavor. The final event weight applied to the simulation is then the ratio of the two probabilities:

$$\mathrm{weight}_{\text{b-tagging}} = \frac{P(\mathrm{DATA})}{P(\mathrm{MC})}. \tag{5.28}$$

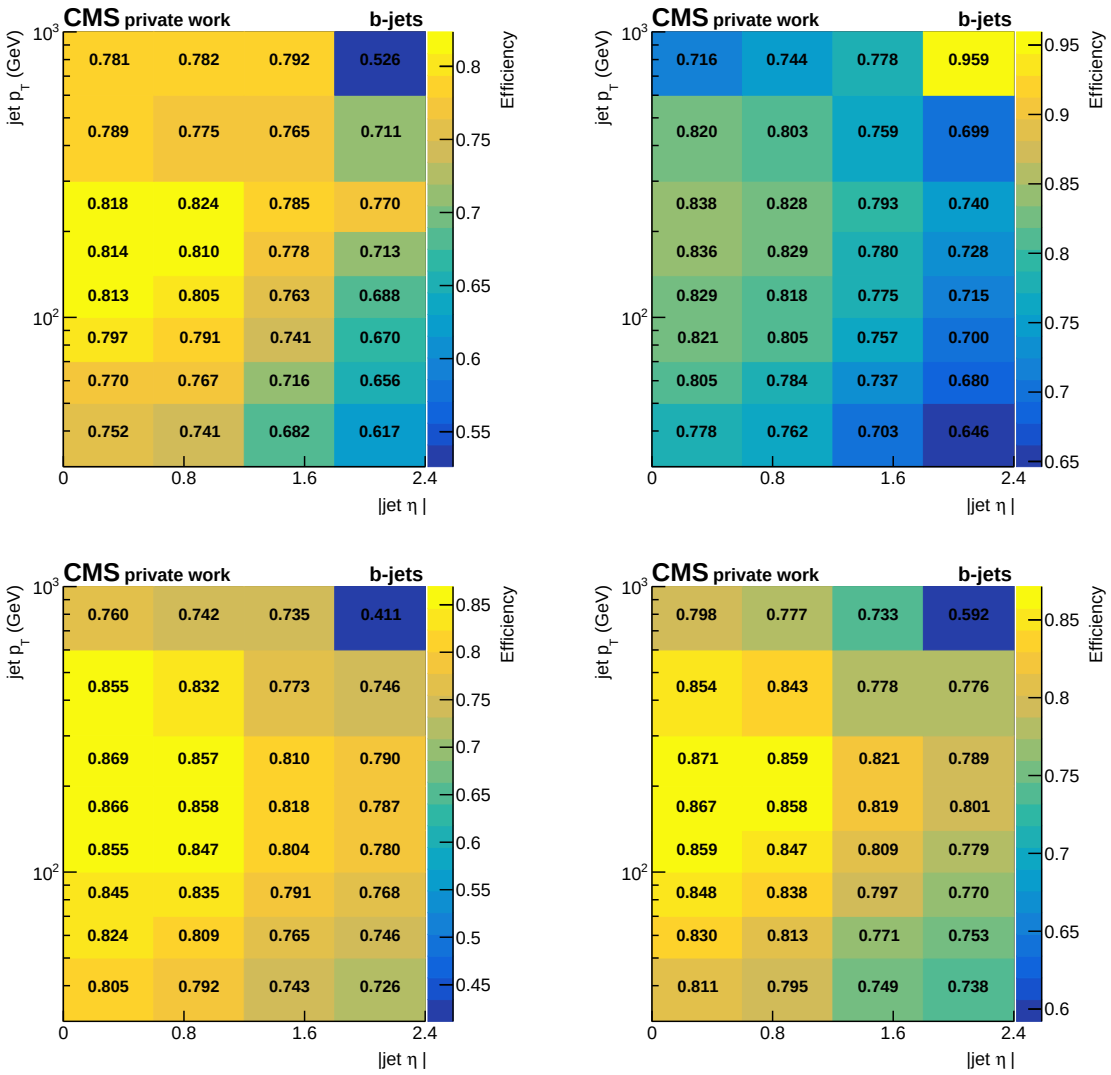

Figure 5.17: Shown are the b-tagging efficiencies for b-jets of the `DeepJet` algorithm for AK4 jets considered for b-tagging in the leptonic mono-top analysis in bins of transverse momentum p_{T} and the absolute value of pseudorapidity η. The top row corresponds to the 2016preVFP (left) and 2016postVFP (right) data-taking eras, whereas the 2017 (left) and 2018 (right) data-taking eras are shown in the bottom row.

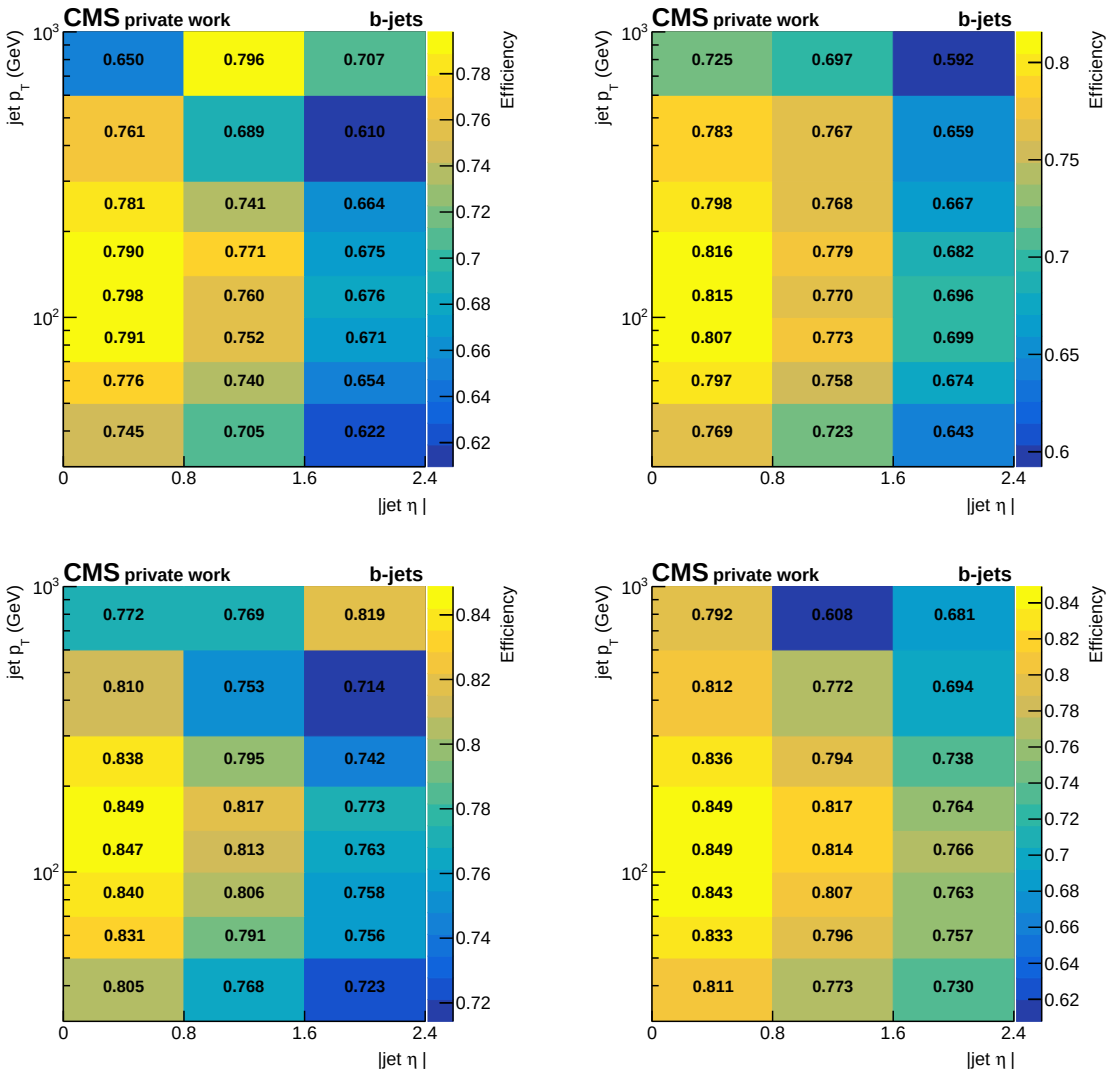

Figure 5.18: Shown are the b-tagging efficiencies for b-jets of the `DeepJet` algorithm for AK4 jets considered for b-tagging in the hadronic mono-top analysis in bins of transverse momentum p_{T} and the absolute value of pseudorapidity η. The top row corresponds to the 2016preVFP (left) and 2016postVFP (right) data-taking eras, whereas the 2017 (left) and 2018 (right) data-taking eras are shown in the bottom row.

The BTV POG also provides uncertainties on the SFs, which are propagated to final observables and considered in the statistical model via nuisance parameters. The SFs are derived based on a TnP method in phase space regions, enriched in $t\bar{t}$ decays.

5.7.5.3 Top-tagging corrections

In order to identify fatjets originating from top quark decays, the `ParticleNet` algorithm is deployed on AK15 jets (see also section 5.2.2). It should be noted that no dedicated `ParticleNet` algorithm for AK15 jets is available. Therefore, the `ParticleNet` algorithm for AK8 jets is deployed in this thesis. Although the algorithm is not optimized for AK15 jets, the performance is still satisfactory. Figure 5.19 shows the efficiency of correctly identifying AK15 jets originating from hadronic top quark decays versus the rejection rate of jets originating from QCD processes. Such distributions are referred to as receiver operating characteristic (ROC) curves. The area under such a curve is a measure of how well the classifier is able to separate the signal from the background. A receiver operating characteristic area under curve (ROCAUC) of 1.0 would indicate a perfect classifier, whereas a ROCAUC of 0.5 corresponds to a classifier that performs no better than random guessing. The ROCAUC for the `ParticleNet` for AK15 jets algorithm is 0.953, indicating a remarkable signal to background separation. In order to evaluate the performance of the top-tagging algorithm in this analysis, the base selections for the hadronic mono-top analysis, as described in section 7.2.1, are applied.

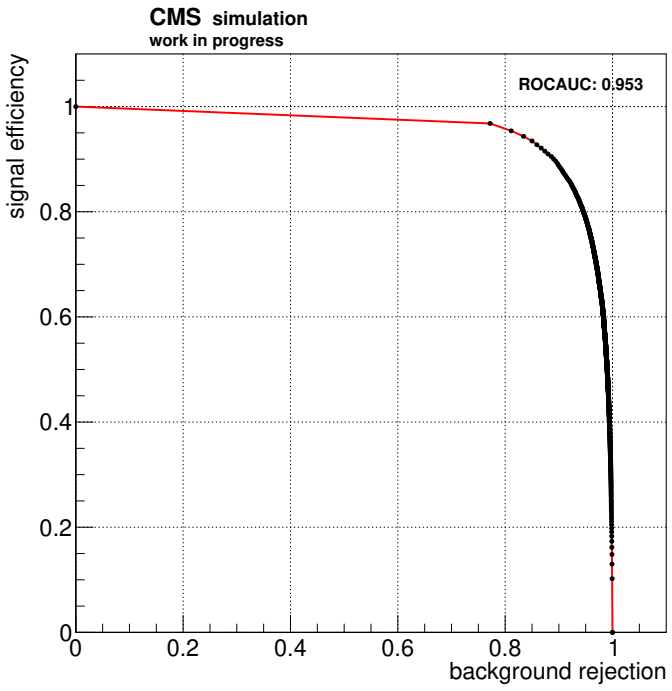

Figure 5.19: Signal efficiency versus background rejection of the `ParticleNet` algorithm for AK15 jets.

The WP of the `ParticleNet` tagger is chosen to be 0.26, corresponding to an efficiency of 2.5 % for misidentifying jets originating from QCD processes as top quark decays. The efficiency of correctly tagging a jet arising from top quarks at this WP is 66.5 %.

Although the application of such top-tagging techniques is very powerful, a crucial aspect is to model not just the top-tagging efficiency but also the top-tagging mistag rate correctly in simulation. Consequently, the efficiencies in simulation need to be corrected to match

those observed in the data. Ideally, the efficiencies should be measured separately for each data-taking era to account for effects due to changes in the detector conditions during data-taking. In principle, the efficiencies should be derived for each data-taking era separately in order to capture the effects on the efficiencies due to the different detector conditions. However, due to time constraints, the efficiencies are measured only for the 2018 data-taking era in the scope of this thesis and the corresponding uncertainties are estimated conservatively. Furthermore, they are considered decorrelated between the different data-taking eras in the statistical model. The decorrelation scheme in conjunction with the conservative uncertainties offers the advantage to constrain the top-tagging efficiencies in-situ during the maximum likelihood estimation separately for each data-taking era.

Derivation of the top-tagging efficiencies

The decay products of a hadronically decaying top quark are expected to be clustered into the fatjet if the transverse momentum of the top quark is large enough. However, not all decay products may be clustered into a single fatjet. This effect increases/decreases with decreasing/increasing top quark transverse momentum. In addition, fatjets can also occur by pure QCD processes without any heavy resonance involved. The jets are categorized into three classes according to which extent a hadronically decaying top quark is merged into the single jet:

- `top`: All three top quark decay products are within a spatial distance of $\Delta R \leq 1.5$ from the jet axis.
- `unmerged top`: Not all top quark decay products are within a spatial distance of $\Delta R \leq 1.5$ from the jet axis.
- `QCD`: The jet does not originate from a hadronically decaying top quark.

Since the top-tagging algorithm behaves differently depending on the type of jet, efficiencies are estimated for each of the three classes separately. The dependency on the transverse momentum of the fatjet is considered by measuring the efficiencies in bins of the transverse momentum of the jet. A possible dependency on pseudo-rapidity is neglected in the scope of this thesis, but might be a subject to study in the future.

For the estimation of these efficiencies in data, events with exactly two AK15 jets are considered, where a lower threshold of 250 GeV is applied on the transverse momentum of both jets. Due to the conservation of momentum, the two jets are expected to be recoiling against each other. Therefore, the opening angle in the transverse plane between the two jets is required to be larger than 2.5 rad. Events with $\not{E}_{\mathrm{T}}$ larger than 50 GeV are rejected as well. Events containing loose electrons, muons or photons are discarded. Additionally, events are selected by a `HLT_PFHT430` HLT, which estimates the scalar sum of the transverse momenta of all PF candidates in the event and is required to be larger than 430 GeV. This phase space region was chosen to construct a phase space region orthogonal to the regions considered in the actual mono-top analysis. Due to these event selection criteria, the two selected jets are expected to have a similar transverse momentum. Therefore, events are only considered if both jets are within the same or neighboring p_{T} bin. In total, five bins are considered:

1. $250\,\mathrm{GeV} \leq p_{\mathrm{T}} < 300\,\mathrm{GeV}$
2. $300\,\mathrm{GeV} \leq p_{\mathrm{T}} < 350\,\mathrm{GeV}$
3. $350\,\mathrm{GeV} \leq p_{\mathrm{T}} < 400\,\mathrm{GeV}$
4. $400\,\mathrm{GeV} \leq p_{\mathrm{T}} < 500\,\mathrm{GeV}$

5. $500\,\mathrm{GeV} \leq p_\mathrm{T}$

Based on this p_T binning, a categorization is defined based on the bin indices i_1, i_2. A further sub-categorization is deployed by considering the jet classes k_1, k_2 with $k_{1/2} \in$ {top,unmerged top,QCD}.

The two main backgrounds for this selection are $\mathrm{t\bar{t}}$ and QCD, where in the case of $\mathrm{t\bar{t}}$ production, both top quarks decay hadronically. Depending on whether a jet is top-tagged or not, four different categories can be defined:

- (tag, tag): Both jets are top-tagged, labeled as `2T`.
- (tag, no tag)/(no tag, tag): Only one of the jets is top-tagged, labeled as `1T`.
- (no tag, no tag): Neither of the two jets is top-tagged, labeled as `0T`.

The $\mathrm{t\bar{t}}$ contribution is expected to be enhanced if top-tags are required. However, since the cross section for QCD production exceeds the cross section for $\mathrm{t\bar{t}}$ production by several orders of magnitude, the QCD process remains dominant in all categories. In order to reduce the QCD contribution as much as possible, only the `2T` and `1T` categories, in addition to the total event count in each i_1, i_2 category, are considered further. The observed total event count $N^\mathrm{obs}_{\mathrm{total},i_1,i_2}$ is assumed to follow a Poisson distribution around the total expected value, which is given by the sum of all contributing processes $N^\mathrm{exp}_{\mathrm{total},i_1,i_2} = \sum_X N_{X,i_1,i_2}$ with $X = \{\mathrm{t\bar{t}}, \mathrm{QCD}\}$:

$$\mathcal{P}_{\mathrm{Poisson},i_1,i_2} = \mathrm{Pois}(N^\mathrm{obs}_{\mathrm{total},i_1,i_2} | N^\mathrm{exp}_{\mathrm{total},i_1,i_2})\,. \tag{5.29}$$

The number of events in each category follows a multinomial distribution, which can be approximated by a multivariate Gaussian (MVG) distribution for large enough samples [177, 178]. The probability density function of the MVG distribution is given by

$$\mathcal{P}_{\mathrm{MVG},i_1,i_2} = \frac{1}{\sqrt{(2\pi)^3 \det \boldsymbol{\Sigma}_{i_1,i_2}}} \exp\left(-\frac{1}{2}\left(\mathbf{x}_{i_1,i_2} - \boldsymbol{\mu}_{i_1,i_2}\right)^T \boldsymbol{\Sigma}^{-1}_{i_1,i_2}\left(\mathbf{x}_{i_1,i_2} - \boldsymbol{\mu}_{i_1,i_2}\right)\right)\,. \tag{5.30}$$

In this equation, the vector $\mathbf{x}_{i_1,i_2}$ contains the number of observed events in each subcategory, represented by the superscript $\alpha \in \{\mathtt{2T}, \mathtt{1T}\}$, as its elements:

$$(\mathbf{x}_{i_1,i_2})^\alpha = N^\alpha_{i_1,i_2}. \tag{5.31}$$

The corresponding expectation is denoted with the vector

$$\begin{aligned}(\boldsymbol{\mu}_{i_1,i_2})^\alpha &= \mu^\alpha_{i_1,i_2} && (5.32)\\ &= \sum_X \mu^\alpha_{X,i_1,i_2} && (5.33)\\ &= \sum_{X,k_1,k_2} \mu^\alpha_{X,i_1,i_2,k_1,k_2}\,. && (5.34)\end{aligned}$$

Here, $X = \{\mathrm{t\bar{t}}, \mathrm{QCD}\}$ represents the contributing processes. The expectation values are given by the product of the total number of expected events of process X and the probability P for a event to enter a region α

$$\mu^\alpha_{X,i_1,i_2,k_1,k_2} = N_{X,i_1,i_2} \cdot P(\alpha | i_1, i_2, k_1, k_2)\,.$$

Finally, the probabilities can be parametrized via the efficiencies:

$$\begin{aligned}P(\text{tag, tag}|i_1, i_2, k_1, k_2) &= \epsilon_{i_1,k_1} \cdot \epsilon_{i_2,k_2}\\ P(\text{tag, no tag or no tag, tag}|i_1, i_2, k_1, k_2) &= \epsilon_{i_1,k_1} \cdot (1 - \epsilon_{i_2,k_2}) + \epsilon_{i_2,k_2} \cdot (1 - \epsilon_{i_1,k_1})\,.\end{aligned}$$

Here, $\epsilon_{i,k}$ denotes the efficiency for tagging a jet of class k with a p_{T} in the transverse momentum bin i.

The covariance matrix elements, represented by the superscripts $\alpha_1, \alpha_2 \in \{\mathtt{2T}, \mathtt{1T}\}$ are given by

$$(\mathbf{\Sigma}_{i_1,i_2})^{\alpha_1,\alpha_2} = \sum_{X,k_1,k_2} (\mathbf{\Sigma}^{\alpha_1,\alpha_2}_{X,i_1,i_2,k_1,k_2}) \tag{5.35}$$

$$= \sum_{X,k_1,k_2} N_{X,i_1,i_2} \cdot P(\alpha_1|i_1,i_2,k_1,k_2) \cdot (1 - P(\alpha_2|i_1,i_2,k_1,k_2)) \text{ with } \alpha_1 = \alpha_2 \tag{5.36}$$

$$(\mathbf{\Sigma}_{i_1,i_2})^{\alpha_1,\alpha_2} = \sum_{X,k_1,k_2} (\mathbf{\Sigma}^{\alpha_1,\alpha_2}_{X,i_1,i_2,k_1,k_2}) \tag{5.37}$$

$$= \sum_{X,k_1,k_2} -N_{X,i_1,i_2} \cdot P(\alpha_1|i_1,i_2,k_1,k_2) \cdot P(\alpha_2|i_1,i_2,k_1,k_2) \text{ with } \alpha_1 \neq \alpha_2\,. \tag{5.38}$$

The probabilities in these covariance matrix elements can again be expressed in terms of efficiencies as was done above.

Ultimately, the efficiencies are estimated via a maximum likelihood fit to data. The likelihood function is given by

$$\mathcal{L} = L_{\mathrm{Poisson}} \times L_{\mathrm{MVG}} \times L_{\mathrm{constraints}}. \tag{5.39}$$

The additional term $L_{\mathrm{constraints}}$ is introduced to incorporate some prior knowledge into the maximum likelihood estimation:

Since the QCD process is inherently hard to predict in simulation, the overall rate of this process in each category, i.e., N_{QCD,i_1,i_2} is a-priori set to the total number of observed events $N^{\mathrm{obs}}_{\mathrm{total},i_1,i_2}$ and then taken as a free parameter in the fit. This is justified due to the fact mentioned above, that the QCD multijet production exceeds all remaining backgrounds by several orders of magnitude.

In addition, prior knowledge on the efficiencies is obtained by considering a simple counting estimation based on the MC simulation. An efficiency for class X can be assessed by considering the event count entering the (tag, tag) category for class X $N^{\mathrm{X}}_{\mathrm{tag,tag}}$ and dividing it by the total event count for class X $N^{\mathrm{X}}_{\mathrm{total}}$. Since two tagged jets are entering the (tag, tag) category, a quadratic dependence on the efficiency is realized. Consequently, the a-priori estimation of the efficiency for class X is given by

$$\epsilon_{\mathrm{X}} = \sqrt{\frac{N^{\mathrm{X}}_{\mathrm{tag,tag}}}{N^{\mathrm{X}}_{\mathrm{total}}}}. \tag{5.40}$$

This prior knowledge is incorporated into the statistical model via a Gaussian constraint with a width of 30 %. Thus a conservative estimation of the efficiencies is obtained. Figure 5.20 shows a comparison between the observed event counts in the 2T and 1T categories and the a-posteriori prediction by the statistical model for the bins of the transverse momentum of the two AK15 jets considered. The prediction is in good agreement with the observed data. Thus, the statistical model deployed is able to describe the measured data.

The maximum likelihood estimators of the efficiencies are shown in figure 5.21. Several observations can be made. First, the efficiencies for the top and unmerged top classes are different, motivating a dedicated treatment of cases in which the top quark is not

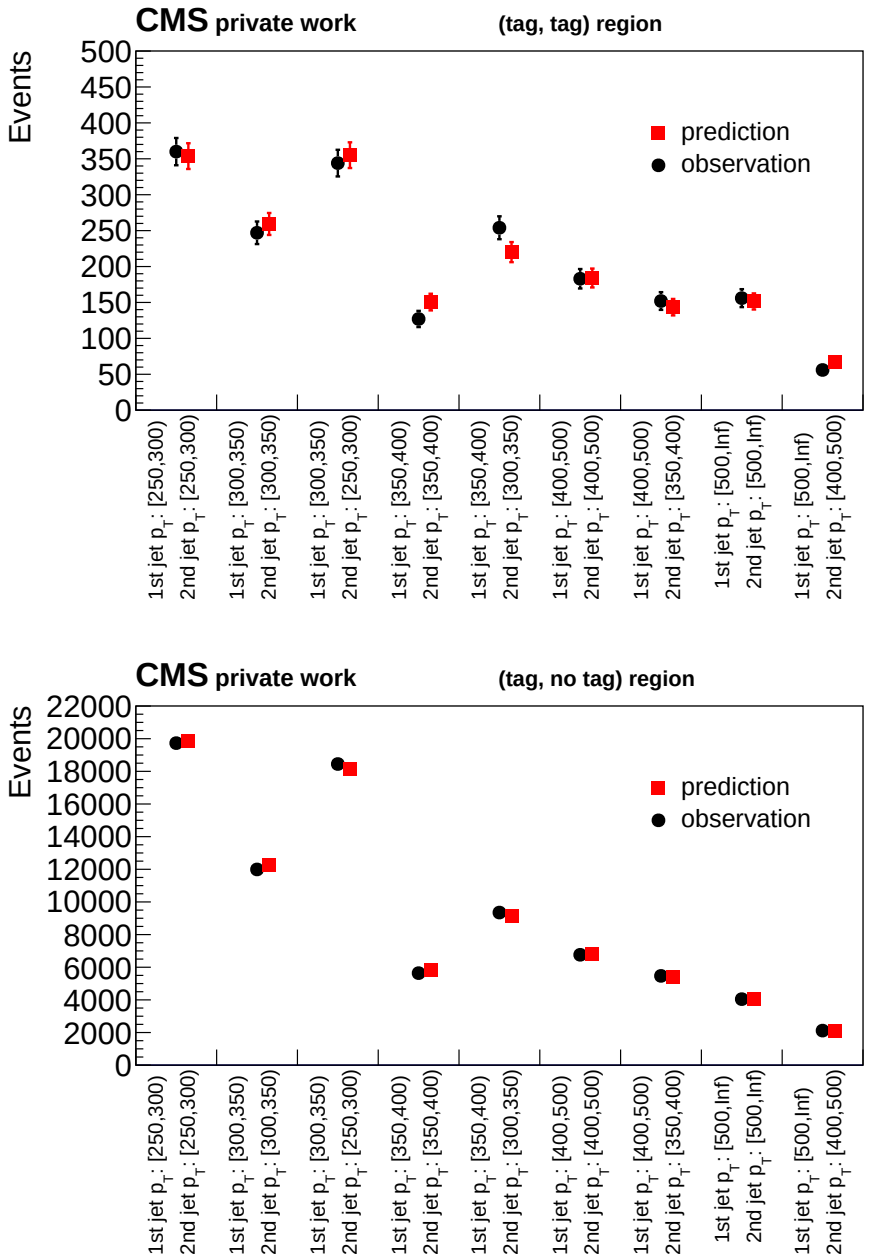

Figure 5.20: Comparison between the observed data (black) in the (tag, tag) and (tag, no tag) categories and the prediction (red) by the statistical model in bins of the transverse momentum of the two jets. Here, (tag, no tag) refers to `1T`.

fully merged into the single fatjet. Second, the efficiencies for the top class are well in agreement with the value of 66.5 % corresponding to the definition of the WP. In principle, the QCD efficiency is also in good agreement with the WP definition of 2.5 %. However, a sizable dependency on the transverse momentum of the AK15 jet is observed, which is not captured by the WP definition. Third, the uncertainties on the MLEs of the QCD efficiency are significantly smaller in comparison to the uncertainties on the MLEs of the top and unmerged top efficiencies. This can be explained by the fact that the QCD process has a major impact due to its large cross section. Even in the `1T` category, the QCD process is still dominant, enabling the maximum likelihood estimation to constrain the QCD efficiency well using the observed data.

Efficiency reweighting

The MC simulation is reweighted such that the efficiencies match the ones obtained in data. Contrary to the application for b-tagging, the simulation is not corrected via a scale factor but rather via a direct reweighting approach. Consequently, no direct cut on the top-tagging score is applied for the MC simulation, which offers the advantage of increasing the available simulation event counts. The efficiency in data, when the AK15 jet is top-tagged, is matched by applying a weight of $w_{\text{tag}} = \epsilon$, where ϵ corresponds to the previously obtained efficiency, which depends on the type of jet (top, unmerged top or QCD) as well as the transverse momentum of the fatjet. Accordingly, if the fatjet is not top-tagged in data, a weight of $w_{\text{not tagged}} = 1 - \epsilon$ is applied. This methodology also accounts naturally for the migration of events between analysis regions, where a jet is top-tagged and regions where the jet fails the WP if the efficiencies are changed within their uncertainties.

5.7.6 Missing transverse momentum

As already described in section 3.3.6 the MET is calculated by considering all PF candidates via

$$\vec{\not{E}}_{\text{T}} = - \sum_{i=\text{reconstructed particles}} \vec{p_{\text{T,i}}}. \tag{5.41}$$

In order to propagate the JECs described in section 5.7.5.1 to the MET, all PF candidates that are clustered into a jet are replaced by the corresponding jet in the calculation, where the JECs are applied. Consequently, the corresponding JES uncertainties are also propagated to the MET and considered in the statistical model via nuisance parameters. All PF candidates not clustered into a jet are considered for an additional uncertainty referred to as unclustered energy uncertainty. For estimating this uncertainty, the kinematics of all unclustered PF candidates are varied within their energy resolution, propagating the effect to the MET. More information on the reconstruction of MET and performance numbers are available in [179, 180].

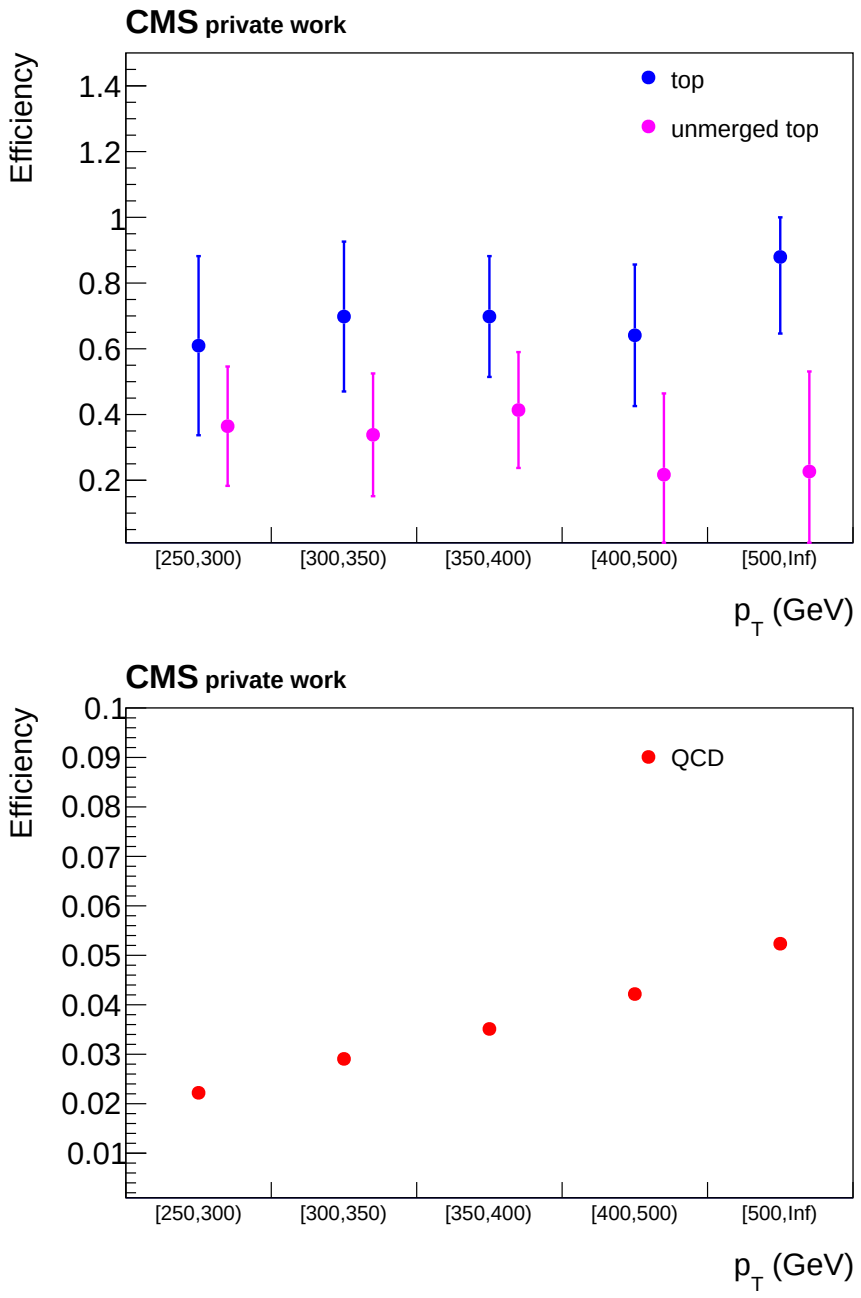

Figure 5.21: Measured efficiencies in data for the `ParticleNet` algorithm based on the dataset in bins of the transverse momentum of the AK15 jet. The upper figure shows the efficiency for the top and unmerged top classes, whereas the lower figure depicts the efficiency for the QCD class.

5.8 Systematic uncertainties

As already hinted throughout the previous sections, the analysis is subject to various systematic uncertainties. These uncertainties are incorporated into the statistical model as nuisance parameters. Depending on the source of the uncertainty, only the overall yield (rate uncertainty) or also the shape of a given distribution can be affected (shape uncertainty). An overview of all systematic uncertainties considered is shown in table 5.13. More details are provided in the following. In general, uncertainties related to detector effects are taken as uncorrelated across the four data-taking eras, whereas theory-motivated uncertainties are correlated across the eras. The naming of the nuisance parameters is supposed to be self-explanatory. The exact naming is given in appendix D

Renormalization and factorization scales: The effect due to missing higher orders in perturbation theory on observables is often estimated by varying the renormalization and factorization scales. The scales are varied independently by a factor of 0.5 or 2 corresponding to $\pm 1\sigma$ Gaussian variations modeled via nuisance parameters. The scale variation uncertainty is treated as uncorrelated among the $\mathrm{t\bar{t}}$, single top quark, $\mathrm{W}+$jets, $\mathrm{Z}+$jets, $\gamma+$jets and signal processes. However, a correlation across the four data-taking eras is deployed since it models a theory uncertainty.

Parton distribution functions During the central production of simulation samples by the CMS collaboration, NNPDF3.1 [41] was used as the nominal PDF set. This PDF set considers QCD calculations at NNLO in QCD perturbation theory providing 100 variations. These variations are used to construct an envelope around the nominal PDF estimating a 68 % confidence interval. The difference of the nominal value to this envelope is used as an uncertainty and incorporated into the statistical model via nuisance parameters. The uncertainty is considered correlated across the four data-taking eras.

Parton shower scales (ISR/FSR): In order to evaluate the impact of the choice of the strong coupling constant α_s in the PS simulation, the scale in the shower simulation is varied by a factor of 0.5 and 2 via weights obtained directly from the generator information. This is done independently for the ISR and FSR showers. Since the same PS algorithm (Pythia 8.2) is used for all main processes, the ISR and FSR uncertainties are treated as correlated among the $\mathrm{t\bar{t}}$, single top quark, $\mathrm{W}+$jets, $\mathrm{Z}+$jets, $\gamma+$jets and signal processes as well as across all data-taking eras.

Top quark p_T reweighting As described in section 5.5.2 the $\mathrm{t\bar{t}}$ sample is reweighted to match the transverse momentum distribution of the top quark in NNLO (QCD)-NLO (EWK) calculation [150, 151]. The uncertainties are constructed such that the down-variation corresponds to the initial unweighted $\mathrm{t\bar{t}}$ simulation. For the up-variation, the residual to the unweighted sample is enhanced by a factor of two. The uncertainty arising from this reweighting procedure is correlated across all four data-taking eras.

Inclusive cross section uncertainties: For the minor backgrounds (diboson, QCD), rate uncertainties on the cross sections are considered as shown in table 5.14. The uncertainty on the diboson normalization is estimated based on theory predictions [143–145]. In addition, a normalization/cross section uncertainty of 10 % is deployed for the $\gamma+$jets and QCD mulitjet production processes which are known to be difficult to model. This additional freedom is needed to account for normalization effects which are especially notable in the $\gamma+$jets control region (see section 7.2.6). The values are chosen rather conservatively in order to cover uncertainties due to variations of the μ_R and μ_F scales as well as variations of the underlying PDF set. The uncertainty is considered to be correlated across all years.

$\mathrm{V}+$jets EWK correction: As described in Chapter 5.5.1, the $\mathrm{V}+$jets samples are reweighted to NLO EWK following [149]. Theoretical uncertainties as a function of

Table 5.13: Systematic uncertainties considered in the analysis. The *Type* columns refer to whether the uncertainty is rate (R) or shape (S) changing. *Correlation* indicates whether the uncertainty is treated as correlated, partially correlated (as detailed below), or uncorrelated across the four data-taking eras.

Source	Type	Correlation	Remarks
μ_{R} scale	S	correlated	Renormalisation scale uncertainty of the ME generator, independent for $\mathrm{t\bar{t}}$, W + jets, Z + jets, γ + jets and signal
μ_{F} scale	S	correlated	Factorisation scale uncertainty of the ME ME generator, independent for $\mathrm{t\bar{t}}$, W + jets, Z + jets, γ + jets and signal
PDF	S	correlated	From NNPDF variations
PS scale initial-state radiation (ISR)	S	correlated	Initial state radiation uncertainty of the PS (Pythia 8.2)
PS scale final-state radiation (FSR)	S	correlated	Final state radiation uncertainty of the PS (Pythia 8.2)
Top quark p_{T} reweighting	S	correlated	Correction of $\mathrm{t\bar{t}}$ to NNLO (QCD)-NLO (EWK)
Incl. cross section uncertainties	R	correlated	inclusive cross section uncertainties for minor backgrounds (single top quark, diboson, QCD)
V + jets EWK correction (1)	S	correlated	Uncertainties related to higher order EWK reweighting
V + jets EWK correction (2)	S	correlated	Uncertainties related to higher order EWK reweighting, independent for W + jets, Z($\ell\ell$) + jets, Z($\nu\nu$) + jets and γ + jets
V + jets EWK correction (3)	S	correlated	Uncertainties related to higher order EWK reweighting, independent for W + jets, Z($\ell\ell$) + jets, Z($\nu\nu$) + jets and γ + jets
Integrated luminosity	R	partially	Signal and all (minor) backgrounds in the leptonic (hadronic) analysis channel
Electron identification/reconstruction	S	uncorrelated	Signal and all backgrounds
Muon identification/isolation	S	uncorrelated	Signal and all backgrounds
Photon identification	S	uncorrelated	Signal and all backgrounds
Trigger efficiency	S	uncorrelated	Signal and all backgrounds
L1 prefiring correction	S	uncorrelated	Signal and all backgrounds
Pileup	S	uncorrelated	Signal and all backgrounds
Jet energy scale	S	uncorrelated	Signal and all backgrounds
HEM15/16 (only for 2018)	S	uncorrelated	Signal and all backgrounds
Jet energy resolution	S	uncorrelated	Signal and all backgrounds
$\not{E}_{\mathrm{T}}$ unclustered energy	S	uncorrelated	Signal and all backgrounds
b tag (correlated)	S	correlated	Signal and all backgrounds
b mistag (correlated)	S	correlated	Signal and all backgrounds
b tag (uncorrelated)	S	uncorrelated	Signal and all backgrounds
b mistag (uncorrelated)	S	uncorrelated	Signal and all backgrounds
TopTag	S	uncorrelated	Signal and all backgrounds, decorrelated across five p_{T} bins (see section 5.7.5.3)
TopMisTag	S	uncorrelated	Signal and all backgrounds, decorrelated across five p_{T} bins (see section 5.7.5.3)
unmergedTopTag	S	uncorrelated	Signal and all backgrounds, decorrelated across five p_{T} bins (see section 5.7.5.3)
Size of the MC samples	S	uncorrelated	Statistical uncertainty of signal and background prediction due to limited sample size

Table 5.14: Cross section uncertainties for the minor background processes single top quark, diboson and QCD:

Process	Uncertainty in %
diboson	5
QCD	10
$\gamma + \text{jets}$	10

the transverse momentum of the vector boson are provided by the authors of the paper. Three uncertainties are related to the NLO EWK correction, which can vary the rate as well as the shape of the distributions. One is considered as correlated across all $\mathrm{V} + \text{jets}$ processes, whereas two uncertainties are considered as uncorrelated. Since these uncertainties are of a purely theoretical nature, they are assumed to be correlated across the years.

Luminosity: The uncertainty on the luminosity estimate [181–183] per year follows the recommendation of the corresponding PAG. The integrated luminosity determines the overall normalization of the MC prediction. Consequently, this uncertainty affects the rates of all processes in a correlated manner. However, as it will be described later on section 7.3 a modified statistical model is deployed in the hadronic analysis, in which the normalizations of the main backgrounds ($\mathrm{V} + \text{jets}$ and $\mathrm{t\bar{t}}$) are determined directly from the data. Consequently, the luminosity uncertainty is only considered for minor backgrounds in the hadronic analysis. Due to the method of how the integrated luminosity is measured, a partial correlation across the data-taking eras is recommended as shown in table 5.15.

Table 5.15: Luminosity uncertainty in percent per year. In the fits for the individual years, the luminosity uncertainty is implemented, as shown in the first row. For the combined fit corresponding to $137.5\,\mathrm{fb}^{-1}$ the uncertainties are partially correlated as recommended in [184].

Year	2016[pre/post]VFP in %	2017 in %	2018 in %
Uncorrelated 2016	1.0	—	—
Uncorrelated 2017	—	2.0	—
Uncorrelated 2018	—	—	1.5
Correlated 2016,2017,2018	0.6	0.9	2.0
Correlated 2017,2018	—	0.6	0.2

Electron identification/reconstruction: As described in section 5.7.2, quality criteria regarding the identification and reconstruction algorithm are applied to electrons considered in this analysis. Since differences in the efficiencies are observed between the simulation and recorded data, SFs are applied to the MC samples to account for this effect. These SFs are provided by the POG [161] in conjunction with corresponding uncertainties. The uncertainties are incorporated into the statistical model via nuisance parameters and are decorrelated between effects concerning isolation and reconstruction efficiencies. Since the reconstruction and isolation algorithms depend on the detector conditions, the uncertainties are uncorrelated across the data-taking eras.

Muon identification/isolation: Similar to electrons POG provided SFs [154–156] are applied to correct for differences in the efficiencies between simulation and recorded data for the muon identification and isolation algorithms, see section 5.7.3. Uncertainties on these

SFs are taken into account in the statistical model via nuisance parameters decorrelated between effects on the isolation and identification efficiency. Furthermore, the uncertainties are taken as uncorrelated across the data-taking eras due to possible dependencies on the detector conditions.

Photon identification: In order to account for differences in the identification efficiencies between simulation and recorded data, SFs are provided by the POG [161], see section 5.7.4, and corresponding uncertainties are considered in the statistical model via nuisance parameters decorrelated across the four data-taking eras.

Trigger efficiency: Different trigger efficiencies are observed between simulation and recorded data. More details on the exact HLT combinations used in the analysis are given in section 5.7.1. The impact on the final discriminants due to the trigger efficiency SFs is estimated by varying the scale factors within their uncertainties. Since the different trigger paths trigger on different objects, the uncertainties are considered to be uncorrelated. Furthermore, the uncertainties are taken as uncorrelated across the data-taking eras due to possible dependencies on the detector conditions.

L1 prefiring correction: As described in section 5.5.4, an L1 prefiring correction is applied to the MC samples. The correction is provided by the POG [152], and a corresponding uncertainty is considered in the statistical model via nuisance parameters. In order to estimate the effect conservatively, the uncertainty is taken as uncorrelated across the data-taking eras.

Pileup: In order to correct the PU distribution in the MC simulation, a reweighting according to the number of primary interactions is applied, see section 5.5.3. By varying the total inelastic proton-proton cross section by $\pm 4.6\%$, an uncertainty on the PU reweighting is estimated. The uncertainty is treated as fully correlated among all processes and years.

Jet energy corrections: As described in section 5.7.5.1, dedicated corrections are applied to the jet energy. Uncertainties on these calibrations are evaluated by shifting the jet energy scale applied to the reconstructed jets by one standard deviation up and down. Subsequently, the events are reanalyzed, including reapplying all jet-based selection criteria and recalculating all kinematic quantities. This process yields varied final discriminant distributions quantifying the impact of the JEC uncertainty which is considered in the statistical model via three nuisance parameters parameterizing effects due to the JES, JER and unclustered energy. Since this calibration is dependent on the actual detector conditions, the uncertainty is fully decorrelated across the data-taking eras.

HEM15/16: During data taking in 2018, false fire alarms lead to power interruptions. Following these interruptions, two sectors of the HCAL in the negative-z endcaps, referred to as HEM15/16 were unable to be operated any longer. Effectively, this issue led to a loss of HCAL information in a 40 degree section in azimuthal angle ($-3.0 < \eta < 1.3$ and $-1.57 < \phi < -0.87$). Since this effect is not modeled in the MC simulations, events are rejected if a jet is reconstructed in this detector region throughout the whole analysis. Although this event veto can substantially mitigate the effect, residual effects remain. In order to account for this, a dedicated uncertainty source is provided by the corresponding POG [171]. This uncertainty source is considered in the statistical model via a nuisance parameter.

Jet energy resolution: The uncertainty related to the correction of JER, see section 5.7.5.1 is evaluated by increasing/decreasing the difference between reconstructed and particle level jet energy. The events are then reanalyzed, including reapplying the jet-based selection and recalculating all kinematic quantities. This source of uncertainty is considered as a shape uncertainty in the final fit, which is fully decorrelated across the data-taking eras.

$\not{E}_T$ unclustered energy: The effect of unclustered energy, see section 5.7.6 is propagated to the MET by varying each particle type by its own resolution. The events are then reanalyzed, including reapplying the selections based on MET and recalculating all kinematic quantities. This source is considered as a shape uncertainty in the final fit, which is fully decorrelated across the years.

b tag scale factors: As described in section 5.7.5.2, the b-tagging efficiencies vary between simulation and recorded data. Uncertainties related to the correction of this effect are provided by the BTV POG [172–175]. These uncertainties affect both the b-tagging efficiency as well as the mistag rate. Furthermore, the uncertainties are split into two components. One component is uncorrelated between the different data-taking eras due to the dependence on the detector conditions of the underlying uncertainty source. In contrast, the other component is taken as uncorrelated across the years. Consequently, a total of ten uncertainties enter the fit:

- mistag, tag: correlated across all eras (2 nuisances)
- mistag, tag: decorrelated for each era (8 nuisances)

Top tagging As described in section 5.7.5.3, the efficiencies of the `ParticleNet` tagger in data are derived via events containing exactly two AK15 jets. The efficiencies are derived for jets that contain either all three top quark decay products `(TopTag)` or fewer `(unmergedTopTag)`. The efficiency to misidentify a jet not originating from a top quark is referred to as `TopMisTag`. Sizable dependencies as a function of the AK15 jet transverse momentum are observed. Therefore, the uncertainties on these efficiencies are taken as uncorrelated depending on the jet transverse momentum. Furthermore, due to the dependence on the detector conditions, the uncertainties are considered to be decorrelated across the data-taking eras.

Size of the MC samples: The limited size of the background and signal MC samples results in statistical fluctuations of the nominal prediction. This is taken into account via the Barlow-Beeston-lite method [185]. For histogram bins with more than ten effective entries, a single Gaussian-constrained nuisance parameter is introduced in each bin that is able to scale the total yield in this bin. A Poisson p.d.f. is used for bins with fewer entries for each process, respectively. It should be noted here that signal events are not considered when determining if a Gaussian or Poisson constraint is used.

6 Leptonic mono-top analysis

The analysis targeting the leptonic decay channel of the mono-top signal is described in this chapter. After motivating the analysis strategy, the event selections are laid out in detail. After validating the background modeling and the statistical model, the analysis results are presented and discussed.

6.1 Analysis strategy

The leptonic mono-top analysis targets the leptonic decay channel of the top quark. As described in section 5.1 an (anti-)neutrino, a charged lepton as well a b-jet are emitted in leptonic top quark decays, where the b-jet can be identified via b-tagging, see section 5.2.1. The decay products of the top quark provide distinct signatures measurable in the detector to construct an analysis region enriched in the mono-top signal. The (anti-)neutrino provides a source of MET in addition to the invisible decay of the DM candidates. However, since the top quark is expected to be recoiling against the dark mediator, the neutrino is expected to be emitted in the opposite direction of the DM candidate lowering the total amount of MET. Although this mono-top signature is quite distinct, two main SM processes also contribute as dominant backgrounds.

The SM $\mathrm{W}+\mathrm{jets}$ process, where the W boson decays leptonically, provides the signature of a lepton and MET. If an additional jet is produced in a given event, the event may be selected for the SR in case the jet is b-tagged. Since the production of additional b-jets is unlikely, the more pronounced effect is that the jet is mistagged as a b-jet. Given the medium working point of the tagger, this is expected to happen only for approximately 1% of the LF jets. Nonetheless, due to the high cross section of the $\mathrm{W}+\mathrm{jets}$ process, a sizable background contribution is expected.

The second important background is the SM production of top quark-antiquark pairs. Due to the decays of the top quarks, b-jets are present, likely fulfilling the b-tagging requirement. Moreover, leptonic decays of a top quark provide the presence of a lepton and MET. As the cross section of this process is large in comparison to the mono-top signal, this process is expected to be the dominant background in the analysis.

In order to constrain those backgrounds, two additional analysis regions are constructed based on the number of b-tags, enriched in $\mathrm{W}+\mathrm{jets}$ and $\mathrm{t\bar{t}}$ events, respectively. The exact event selections will be described in the following section section 6.2.

A well motivated discriminant variable, which is sensitive to the mono-top signal, is the transverse mass m_{T} defined as

$$m_{\mathrm{T}} = \sqrt{2 p_{\mathrm{T},\ell} \not{E}_{\mathrm{T}} \left(1 - \cos \Delta\phi \left(\ell, \not{E}_{\mathrm{T}}\right)\right)}. \tag{6.1}$$

The transverse mass is able to constrain the mass of a particle decaying into two decay products, where one of them is invisible (see also the *Kinematics* review in [4]). Consequently, the transverse mass spectrum peaks at roughly the W boson mass for the leptonic W + jets background and falls sharply afterward as shown in figure 6.1. The sharp decline beyond the W boson mass is based on the fact that only off-shell W bosons contribute in this regime which strongly suppresses the cross section. On reconstruction level, this sharp decline is smeared out due to the limited resolution of the CMS detector.

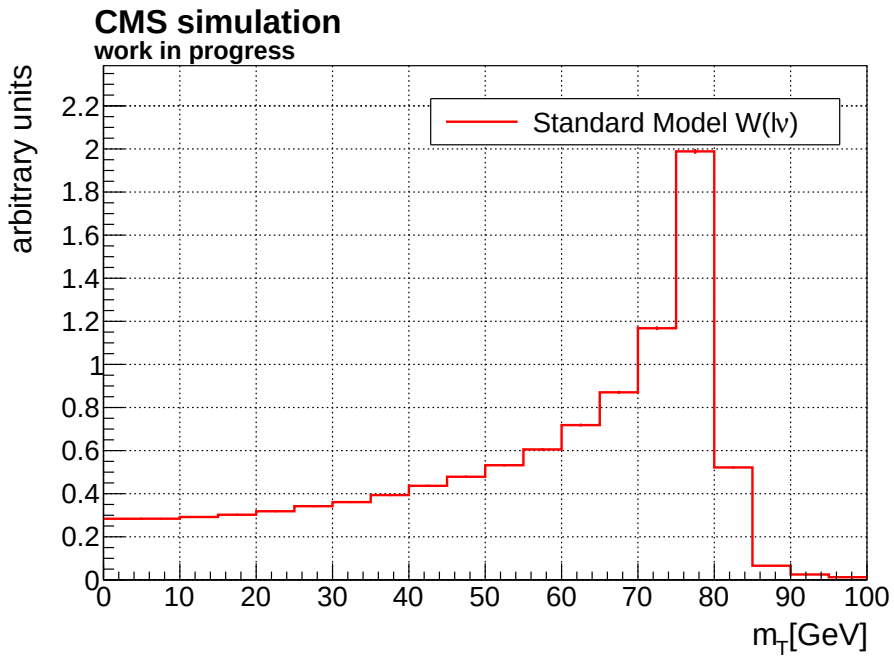

Figure 6.1: Distribution of the transverse mass of the W + jets background at generator level. Taken from [126].

For the mono-top signal both the (anti-)neutrino from the top quark decay as well as the invisible decay of the DM candidates contribute to the MET. Therefore, the spectrum of the transverse mass reaches significantly beyond the mass of the W boson as shown in figure 6.2.

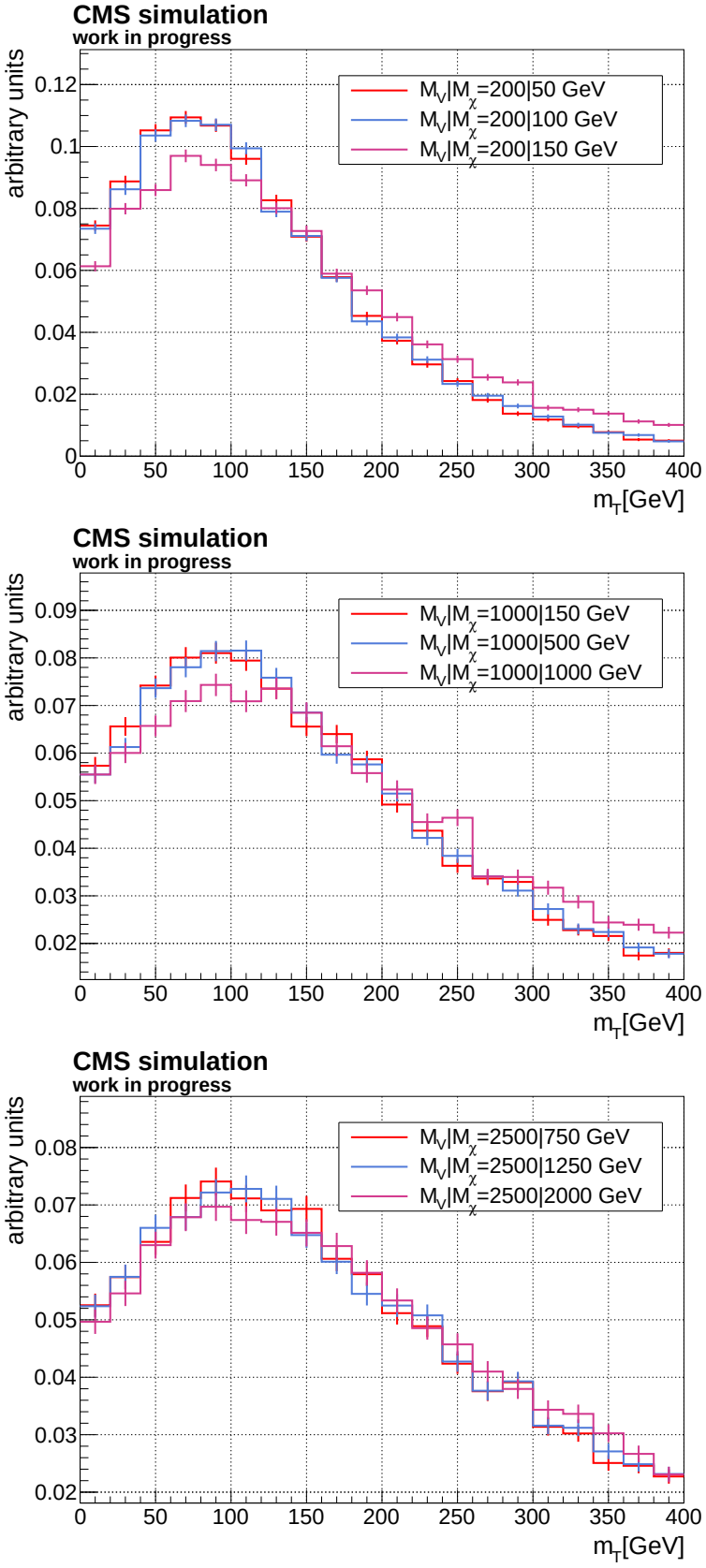

Figure 6.2: Distributions of the transverse mass for the mono-top signal for different mediator V and DM candidate (χ) masses, M_V and M_χ. All distributions are normalized to a yield of one. Taken from [126]

6.2 Event Selection

As described earlier, dedicated requirements are applied to select phase regions either enhanced in leptonically decaying mono-top events or the main background processes. The details of the event selection for the leptonic mono-top analysis are described in the following.

6.2.1 General selections

At leading order, the expected signature of the mono-top signal, where the top quark decays leptonically, consists of a single isolated lepton, a significant amount of MET, and a jet originating from a bottom quark. The general event selection applied to all analysis regions follows this signature. First, events are selected if exactly one tight electron (muon) and no other loose muon (electron) is present in the event. The MET is required to be larger than 100 GeV, accounting for both the DM candidate as well as the neutrino originating from the leptonic top quark decay. The mediator V is expected to be rather heavy. Therefore, the top quark recoils against the mediator. Consequently, the transverse momentum of the top quark decay products is enhanced. Thus, a minimum transverse momentum of 70 GeV is required for the leading jet in the event. Additionally, the opening angle in the transverse plane between the MET and the leading jet is required to be larger than 2 rad in order to also spatially reflect the recoiling of the two particles.

As motivated in section 6.1, the transverse mass m_{T} is a powerful variable to distinguish between the mono-top signal and SM background processes. Since the signal reaches transverse mass values significantly above the W boson mass of approximately 80 GeV, m_{T} is required to be larger than 150 GeV enhancing, the ratio of signal to background.

6.2.2 Analysis region definitions

Top quarks decay almost exclusively into a W boson and a bottom quark, see section 5.1. Therefore, b-tagging provides a powerful tool to enhance a phase space region with processes that involve top quarks. For the leptonic mono-top analysis, a jet is considered b-tagged according to the medium WP of the `DeepJet` algorithm. Consequently, a signal enriched region (SR) is constructed by requiring exactly one b-tag in the event since only a single top quark is expected. The process of top quark-antiquark pair production enters the SR mostly due to the limited b-tagging efficiency. Although the efficiency is in the order of 80% for the medium WP (see figure 5.17), the high $\mathrm{t\bar{t}}$ cross section leads to a significant contribution of the $\mathrm{t\bar{t}}$ process in the SR. In order to control this major background process, a dedicated CR is defined by requiring at least two b-tagged jets in the event, referred to as $\mathrm{t\bar{t}}$-CR.

The second main background process in the SR is the production of a W boson in association with additional jets. This background is able to enter the SR due to the mistag rate of approximately 1% for the medium WP (see figure 5.17). Although this mistagging rate is rather low, the large W boson cross section leads to a significant contribution of the W + jets process in the SR. Again, a dedicated CR is defined by vetoing events that contain any number of b-tags. This CR is referred to as W-CR in the following.

Additionally, all regions are further split according to the flavor of the charged lepton into electron and muon channels. This separation offers the advantage of disentangling the effects of the lepton reconstruction and identification, which might be different for electrons and muons. Consequently, different trigger selection requirements are applied for the two channels. The exact trigger paths are given in table 6.1. In general, the trigger paths require the presence of an isolated muon or electron with a transverse momentum above

a certain threshold at HLT level. The thresholds are given by the number in the HLT path name as shown in table 6.1. For the 2016 data-taking era, an additional trigger path exists for isolated muons based on tracker muons. In order to enhance selection efficiency, the logical OR of both HLT paths is considered. Furthermore, trigger paths targeting high-p_{T} photons are also considered in the electron channels since these trigger paths are also sensitive to the presence of high-p_{T} electrons due to their signature in the ECAL being similar to photons.

Table 6.1: HLT paths considered in the leptonic analysis split across the data-taking eras.

lepton flavor	HLT path
	2018
muon	`HLT_IsoMu24`
electron (low p_{T})	`HLT_Ele32_WPTight_Gsf`
electron (high p_{T})	`HLT_Photon200`
	2017
muon	`HLT_IsoMu27`
electron (low p_{T})	`HLT_Ele35_WPTight_Gsf`
electron (high p_{T})	`HLT_Photon200`
	2016[pre/post]VFP
muon	`HLT_IsoMu24,HLT_IsoTkMu24`
electron (low p_{T})	`HLT_Ele27_WPTight_Gsf`
electron (high p_{T})	`HLT_Photon175`

Figure 6.3 shows the transverse mass distribution of the SRs and CRs for the 2018 data-taking era. The distributions in all data-taking eras are shown in appendix E. Overall a good description of the data by the MC simulation within the uncertainties is observed in all analysis regions. When looking at the SRs, the aforementioned effect of having significant contributions of the $\mathrm{t\bar{t}}$ and $\mathrm{W}+\mathrm{jets}$ processes as dominant SM backgrounds is confirmed. Moreover, the mono-top signal reaches significantly higher values of m_{T} than the SM processes. Consequently, the feature shown on generator-level is also established on reconstruction level. Furthermore, a sizable enhancement of the $\mathrm{t\bar{t}}$ process in the $\mathrm{t\bar{t}}$-CRs is visible. The same holds for the $\mathrm{W}+\mathrm{jets}$ process in the W-CRs.

Various kinematic distributions are shown in appendix E, indicating good agreement between data and simulation.

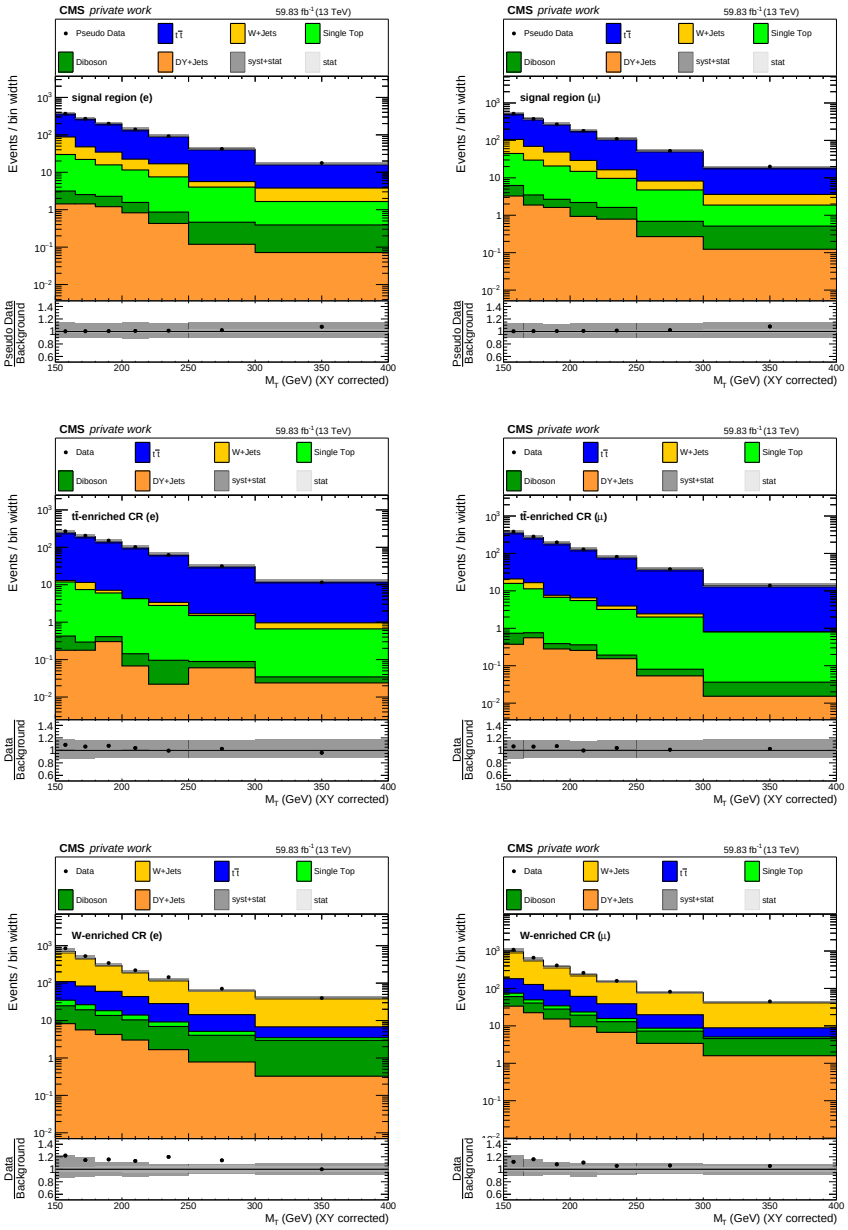

Figure 6.3: Transverse mass distribution with all selections of the leptonic mono-top analysis applied for the 2018 data-taking era. Shown are the signal regions as well as the $t\bar{t}$ and $W+$jets enriched control regions from top to bottom. The electron channels are shown on the left-hand side, whereas the muonic regions are depicted on the right-hand side. The measured data in black points are compared to the background prediction from the simulation as colored stacked histograms for different processes. In the case of the SRs a signal-plus-background pseudo dataset is deployed. The lower pad in each plot shows the ratio of data to the total background prediction. The dark grey shaded area illustrates the one standard deviation uncertainty band by adding all shape-affecting uncertainties in quadrature. The light grey shaded area corresponds to the uncertainty due to the limited statistical precision of the MC-simulation samples. For the signal regions, an exemplary signal prediction with a mediator mass of 1000 GeV and DM candidate mass of 150 GeV scaled to the total sum of expected backgrounds is overlaid in cyan.

6.3 Validation of the statistical model

Before performing the maximum likelihood fit to actual data, the statistical model is validated. After checking the behavior using toy data, the description of the data using the background-only model predictions is validated in the analysis CRs. For all statistical analysis procedures, the CMS `combine` tool [186] is deployed.

6.3.1 Maximum likelihood fit to Asimov datasets

Before considering the measured data, the statistical model is validated by only considering toy datasets. This is done to make sure that the model is self-consistent and to verify that the statistical model yields the expected results.

One particularly interesting toy dataset is called Asimov dataset [101]. The Asimov dataset is precisely equal to the model expectation by fixing all nuisance parameters to their central values. Consequently, no sampling from the underlying p.d.f. is performed. The choice of this toy dataset has several consequences. First, suppose the statistical model works as expected. In that case, the MLEs of all parameters, including the parameter of interest, in the model should not change when performing a fit on the Asimov dataset since the data is already described perfectly. Thus the likelihood function is already at its maximum. Secondly, the expected sensitivity of the analysis can be assessed by inspecting the estimated uncertainty on the signal strength modifier. For the tests performed in this work, the Asimov dataset is generated based on the signal-plus-background prediction, where a benchmark mono-top signal with a mediator mass of 1 TeV and a DM candidate mass of 150 GeV is chosen.

Figure 6.4 illustrates the pulls, see equation (4.4) of the MLEs for the nuisance parameters when performing a fit using the signal-plus-background Asimov dataset. As expected, no pulls are observed when performing a signal-plus-background fit.

Some uncertainties on the nuisance parameter are smaller than one after performing the fit, which can happen if the system is sensitive to such a systematic uncertainty. Consequently, information can be extracted when performing the fit and thus constraining the nuisance parameter to an uncertainty value smaller than its initial one. Most constrained nuisance parameters are related to the JECs. Since the event selection is based on the presence of a jet, the sensitivity of the analysis to the JECs is plausible. The uncertainty parameterizing effects due to FSR is also constrained. This can be explained by the fact that additional jets can be produced by FSR and thus directly impact the event selection. Furthermore, theory uncertainties of the $\mathrm{t\bar{t}}$ and $\mathrm{W}+\mathrm{jets}$ processes, such as variations of the μ_{R} scale are constrained. Since these processes are the most dominant processes in this analysis, the sensitivity of the analysis to these uncertainties is also expected.

The picture concerning the constraints on the MLEs remains the same when performing a background-only fit. However, now the model is not able to describe the data perfectly, and thus the MLEs of the nuisance parameters are pulled in order to account for these differences. However, only small pulls are necessary to describe the data, indicating that only small adjustments are necessary to describe the toy dataset.

6.3.2 Validation of unblinded control regions

After the statistical model was validated without considering actual recorded data in the previous section the model is further validated without considering the SRs. This approach allows scrutinizing the statistical model without any bias due to potential signal contributions.

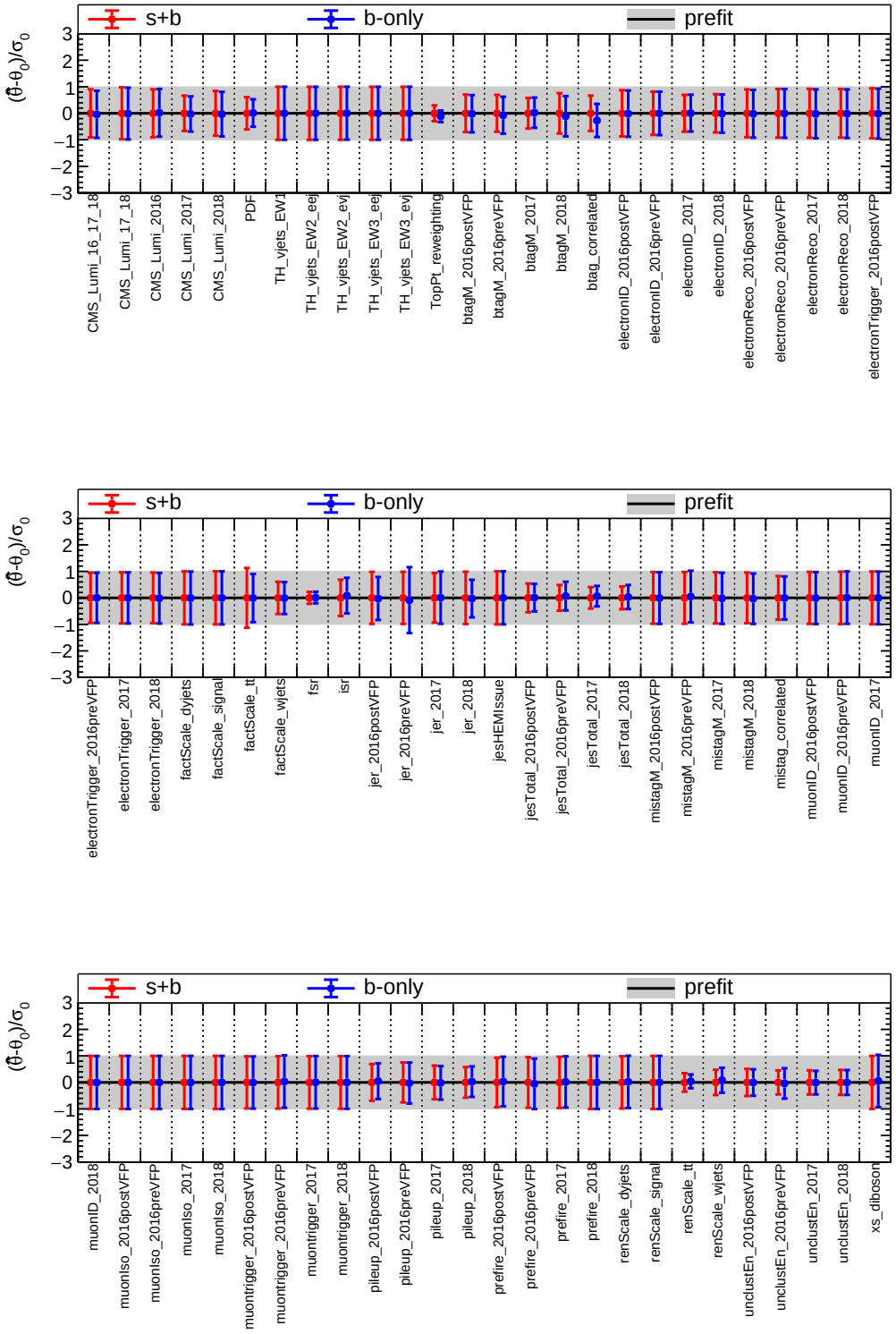

Figure 6.4: Pulls of the nuisance parameters after performing the background-only and signal-plus-background fit in all analysis regions combined across all data-taking eras for a signal-plus-background Asimov toy dataset.

First, the values of all nuisance parameters after performing the maximum likelihood fit are investigated. Due to the absence of any signal contributions, only the background-only fit is performed. Figure 6.5 shows the pulls of the nuisance parameters for the combination of all four data-taking eras. Two aspects are of interest here. First, no nuisance parameter is pulled more than one standard deviation with respect to their initial value. This indicates that the initial description of data is already satisfactory, and only minor adjustments are needed during the maximum likelihood fit to further improve the agreement with the observed data. Secondly, some nuisance parameters are constrained to a uncertainty smaller than their initial one. The affected parameters are related to the JECs, the FSR and the $t\bar{t}$ and $W + \text{jets}$ theory uncertainties, yielding a similar picture as when considering the Asimov dataset in the previous section. Therefore, the statistical model behaves as expected. The pulls for the background-only fit of the CRs when considering each era separately are shown in appendix F.

In order to quantify the compatibility of the background-only model with the data further, saturated-model GoF tests, see section 4.6, are performed. Table 6.2 shows the obtained p-values. All p-values are well above the commonly considered threshold of 5 %, indicating that the model can describe the observed data in the CRs.

Table 6.2: P-values obtained in goodness-of-fit tests using a saturated model in the CRs for the four data-taking eras separately as well as for the full Run 2 combination.

era	p-value
2016preVFP	0.33
2016postVFP	0.99
2017	0.38
2018	0.73
full Run 2	0.72

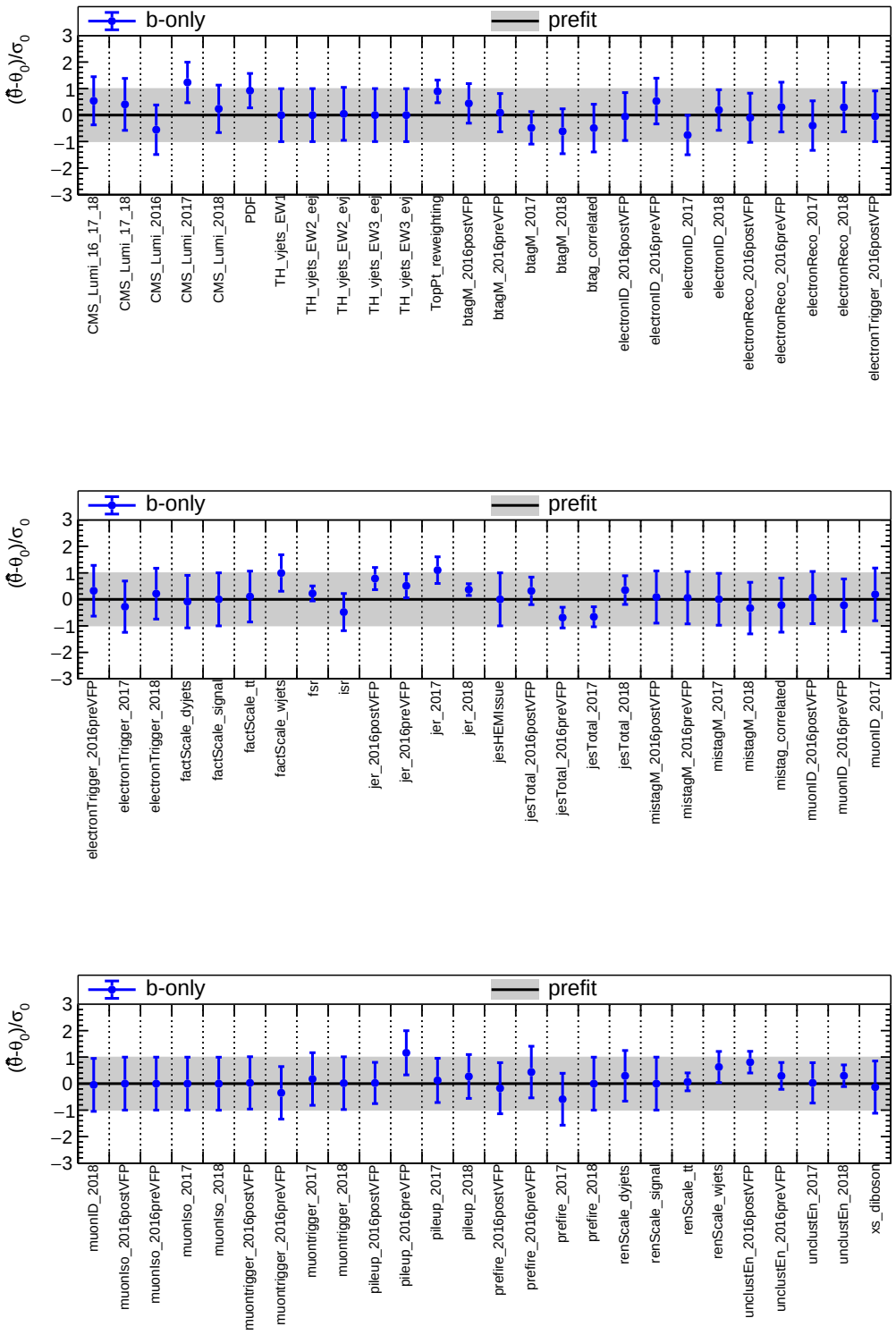

Figure 6.5: Pulls of the nuisance parameters after performing the background-only fit in all CRs combined across all data-taking eras.

6.3.3 Validation in all unblinded analysis regions combined

After validating that the statistical model is able to describe the data in the CRs, the SRs are also included to verify the modeling. For this test, the signal-plus-background fit is performed considering all systematic uncertainties, as described in section 5.8. For the unblinded tests and results in this thesis only a partial dataset of the full Run 2 corresponding to data taken in the year 2016 is considered. Figure 6.6 shows the a-posteriori values and uncertainties of the nuisance parameters for both the background-only as well as signal-plus-background fit. Again, a benchmark signal hypothesis with a mediator mass of 1 TeV and a DM candidate mass of 150 GeV is deployed. When comparing the pulls and constraints to the case in which the SRs were not included (figure 6.5), the picture is very similar. Only a few parameters are pulled more than one standard deviation, and some parameters are getting constrained to a smaller uncertainty than their initial one. The most notable difference is the more pronounced pull of the b-tagging related nuisances. The SRs are affected by the b-tagging uncertainties due to being defined by the presence of exactly one b-tag. Consequently, possible differences in the modeling in the SRs can be mitigated by adjusting the a-posteriori value of the related nuisance parameters. In general, all pulls and constraints look reasonable. Another finding is that the pulls of the signal-plus-background and background-only fit are very similar, indicating that possible signal contributions are either small or neglectable. A quantifying assessment of how much signal is observed in data will be discussed in section 6.5.1, where the observed significances are scrutinized. The pulls and constraints when considering the two 2016 data-taking erass separately are shown in appendix G.

In order to quantify that the statistical model is able to describe the data saturated GoF, tests are performed. The results are shown in table 6.3 for the two 2016 data-taking eras separately as well as for the combination of the latter. All p-values are above the 5 % threshold, indicating that the statistical model can describe the data well.

Table 6.3: P-values obtained in goodness-of-fit tests using a saturated model in all analysis regions for the two 2016 data-taking eras separately as well as for the 2016 combination.

era	p-value
2016preVFP	0.30
2016postVFP	0.99
2016	0.74

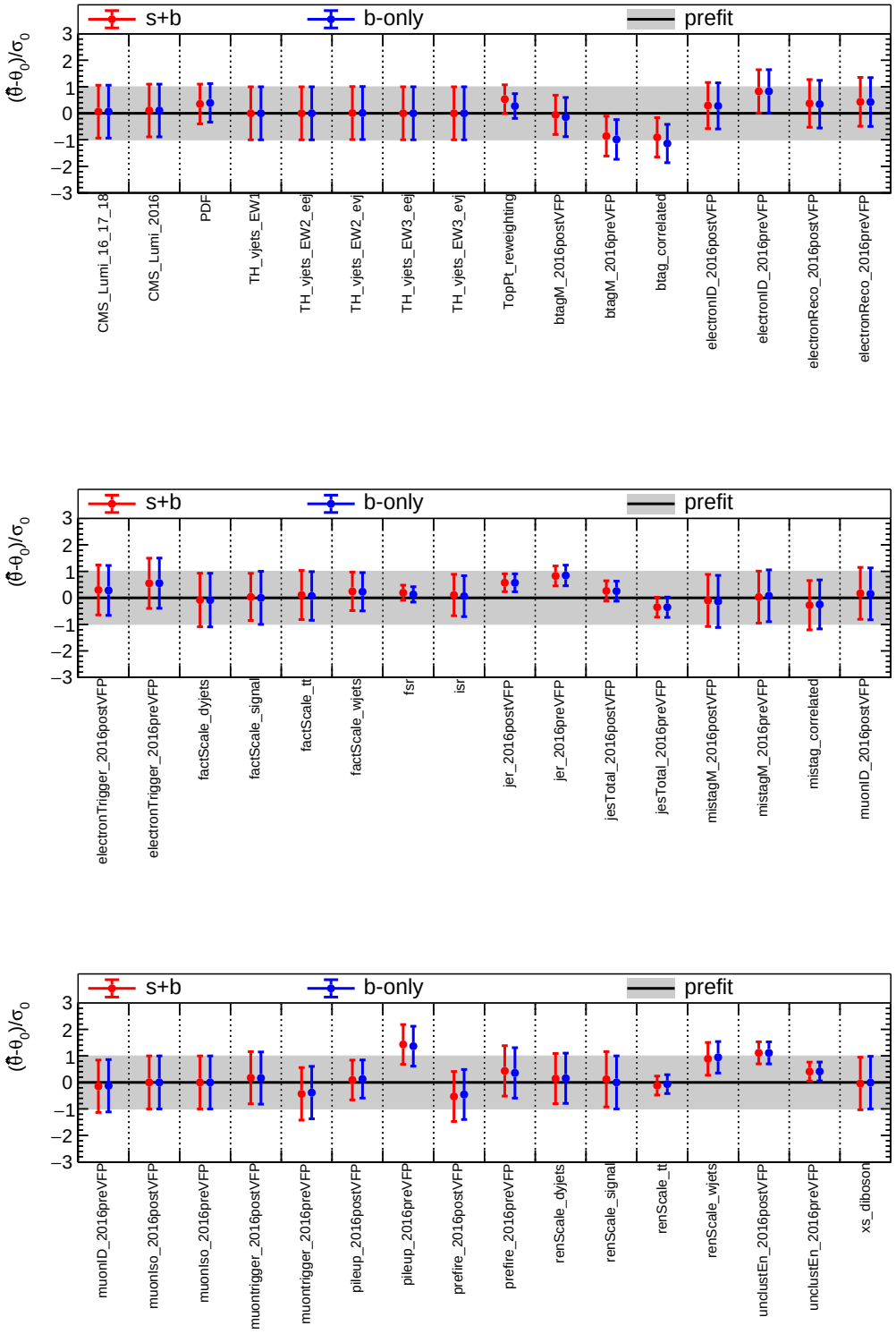

Figure 6.6: Pulls of the nuisance parameters after performing a background-only and signal-plus-background fit for the leptonic mono-top analysis in blue and red, respectively. The combination of both 2016 data-taking eras is considered.

6.4 Expected results

After validating the statistical model exclusively on toy data for one specific mono-top hypothesis, see section 6.3.1, the statistical model is evaluated on the full available range of mediator and DM candidate masses.

6.4.1 Expected significances

Expected significances provide a way of quantifying the expected sensitivity of the analysis to a specific mono-top hypothesis. As described in section 4.4, the likelihood ratio for a vanishing signal strength

$$\tilde{q}_0 = -2 \ln \left(\frac{\mathcal{L}\left(0, \hat{\boldsymbol{\theta}}_\mu\right)}{\mathcal{L}\left(\hat{\mu}, \hat{\boldsymbol{\theta}}_\mu\right)} \right), \tag{6.2}$$

is considered as test statistic. Considering Wilk's theorem, a p-value and consequently a Gaussian significance is obtained. In the case of an expected significance, an a-posteriori signal-plus-background Asimov toy is deployed as a pseudo dataset. A-posteriori refers to the values of all MLEs after performing a signal-plus-background fit to the observed data. Therefore, the expected significance indicates how well a signal can be detected, assuming the data behaves like the signal-plus-background model. Figure 6.7 shows the expected significances for all mono-top mass hypotheses considered in units of Gaussian standard deviations for a combination of all four data-taking eras. Especially for low mediator and DM candidate masses, the expected significances are often above the $5\,\sigma$ threshold. This can be explained by the relatively large cross sections expected from these low mass hypotheses in the order of 0.1 pb to 10 pb if the DM candidate is produced on-shell. Thus, if such a mono-top signal with relatively low masses is realized in nature, this analysis is expected to claim an observation. With increasing masses, the expected significances decrease since the cross sections decrease as well, and possible minor deviations originating from the signal contribution are more compatible with a background fluctuation.

6.4.2 Expected exclusion limits

Suppose no mono-top signal is present in the data. In that case, parts of the mono-top parameter space can be excluded by calculating upper exclusion limits on the signal strength modifier $\mu = \sigma_{\text{obs}}/\sigma_{\text{theory}}$, where σ_{obs} is the observed signal cross section and σ_{theory} denotes the theoretical prediction. Consequently, if the upper exclusion limit is below one, the allowed signal cross section is lower than the theoretical prediction and can be excluded. In this analysis, the upper exclusion limits are calculated at a confidence level of 95 % using the asymptotic approach with the CL_s construction, see section 4.4. In this thesis a-posteriori expected limits are deployed, meaning that the Asimov toy dataset is constructed with the values of all MLEs after performing a fit to the observed data.

Due to the computational effort of generating MC datasets for various mono-top mass hypotheses, only a relatively sparse grid in the plane of mediator and DM candidate masses is generated, see section 5.4.5. However, a physically motivated interpolation of the limit between the available mass points is performed to set a continuous exclusion region in the parameter space mentioned above. As described in section 5.3.2.5, the BRs of the mediator into DM candidates only depend on the mass of the dark particles involved. Consequently, the exclusion limit for a given pair of masses can be used to assess the exclusion limit for a mass point with the same mediator mass but different DM candidate mass m'_χ, by multiplying with BR/BR'. However, this approximation is only valid if the kinematic distributions are comparable between different mass hypotheses. As shown in figure 6.2,

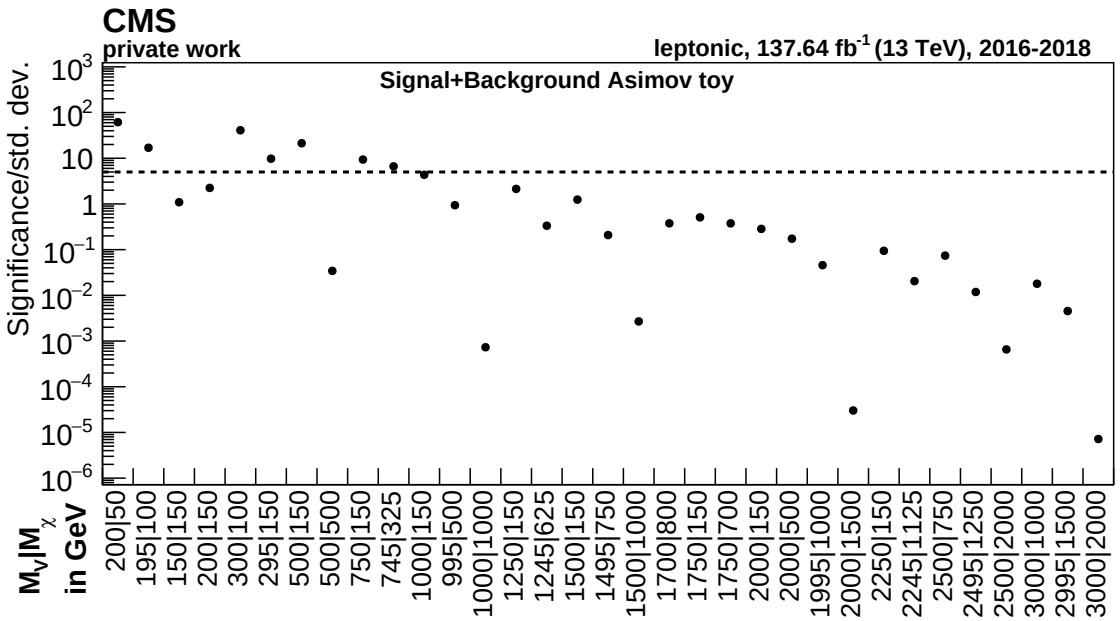

Figure 6.7: Expected significances for all mono-top mass hypotheses considered in units of Gaussian standard deviations in the combination of all four data-taking eras. The mass of the mediator is denoted by M_V and the mass of the DM candidate by M_χ. The 5σ discovery threshold is indicated by a dashed line.

this criterion is fulfilled. This extrapolation is only used for mass hypotheses for which the decay into DM candidates is kinematically allowed (on-shell).

The expected exclusion limits are shown in figure 6.8 for the combination of all four data-taking eras as a function of the mediator and DM candidate masses. The upper plot corresponds to a pure vector coupling scenario, whereas the lower figure shows the exclusion limits for a pure axial-vector coupling scenario. The area enclosed by the solid black line is parameter space expected to be excluded for the given mono-top model. Mediator masses of up to approximately 1.3 TeV can be excluded for DM candidate masses of up to approximately 600 GeV. Due to the relatively large cross sections of the low mass hypotheses, this parameter space is expected to be excluded with high confidence. The opposite is the case for the high-mass regime, where the signal cross sections are relatively small and thus directly impact the sensitivity of the analysis. Additionally, no parameter space is expected to be excluded where the decay of the mediator into the two DM candidates is kinematically forbidden (off-shell). This is because the cross-section is strongly suppressed, and the signal contribution is not large enough to be detected.

For mediator masses below 300 GeV an interesting feature is visible. The analysis is sensitive enough to start probing heavily suppressed off-shell parameter spaces such that the expected upper limits on μ are close to one, leading to a spiky exclusion contour in this mass regime.

The expected exclusion limits when considering each data-taking era separately are shown in appendix I, where a similar behavior as for the combination of the full Run 2 data is observed. However, the smaller phase spaces are expected to be excluded when only considering single eras due to the lower amount of data limiting the sensitivity of the analysis.

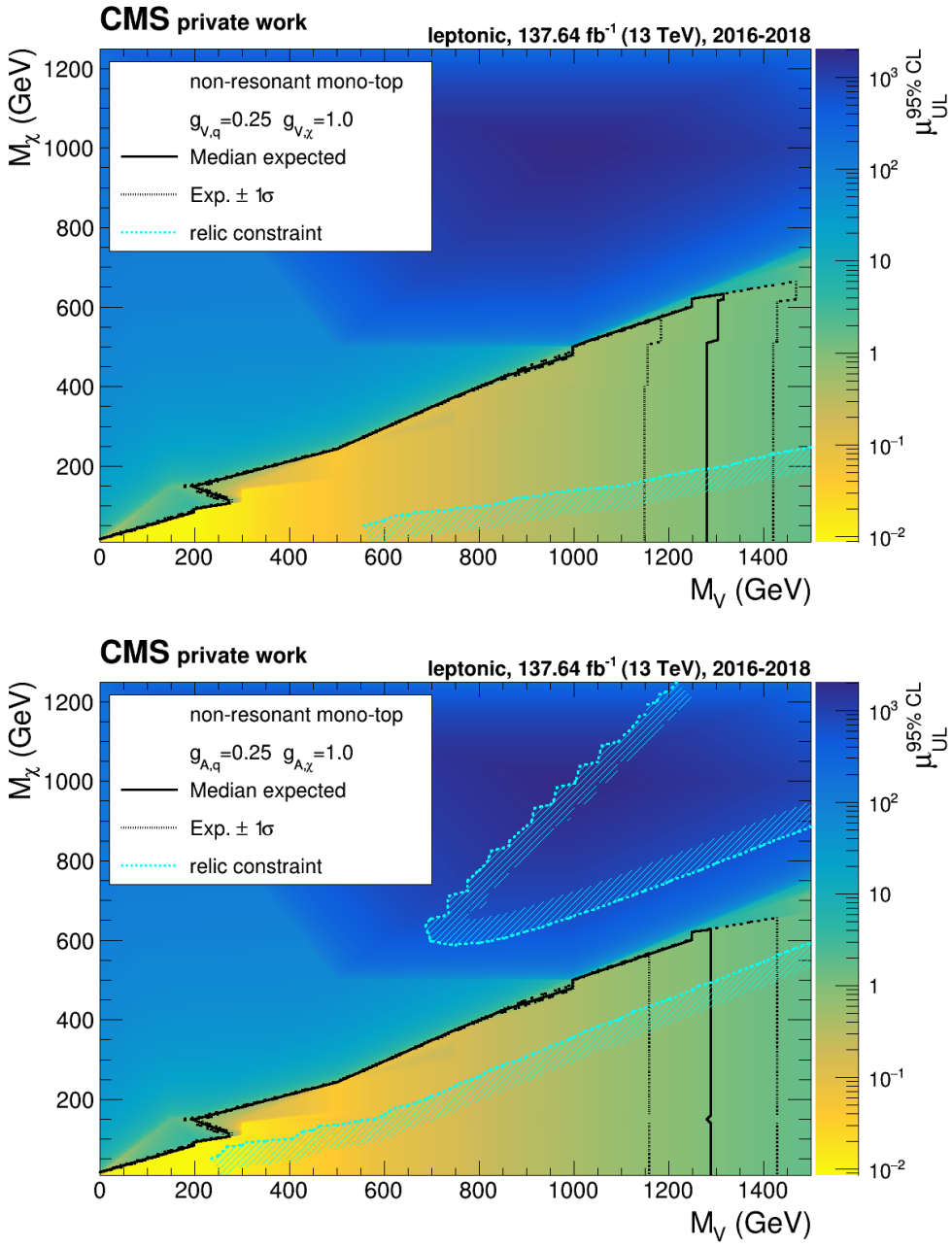

Figure 6.8: Expected upper limits on the signal strength modifier μ at a confidence level of 95 % for the vector mono-top model in the combination of all four data-taking eras in the plane of mediator and DM candidate masses M_V and M_χ. The solid black line indicates the contour for which the median, upper exclusion limit is equal to unity. The 68 % confidence interval on this contour is shown as a dashed black line. The area enclosed by the solid black line is parameter space expected to be excluded for the given mono-top model. The cyan, dashed exclusion line indicates a constraint on allowed masses in order to explain the measured DM relic density by the Planck Collaboration [30]. The upper exclusion plot corresponds to a pure vector coupling scenario, whereas the lower figure shows the exclusion limits for a pure axial-vector coupling scenario.

6.5 Observed results

After the statistical model was validated and the expected results were studied, the unblinded results of the leptonic mono-top analysis are presented in this section. In the scope of this thesis only a partial dataset corresponding to data taken in 2016 is considered.

6.5.1 Observed significances

Analogously to the calculation of expected significances in section 6.4.1, observed significances are calculated with respect to the background-only hypothesis for the leptonic mono-top analysis by considering the actual recorded data. The observed significances are shown in figure 6.9 for all mass hypotheses considered in the 2016 combination as dots. In addition, the expected significances are shown as open circles. It can be observed that, especially for high mediator masses, the observed significances are higher than the expected ones. This finding indicates a slight over fluctuation of the data. However, all observed significances are below one Gaussian standard deviation, indicating that no significant deviation from the background-only hypothesis is observed. Consequently, no discovery or evidence is claimed for any of the mass hypotheses considered.

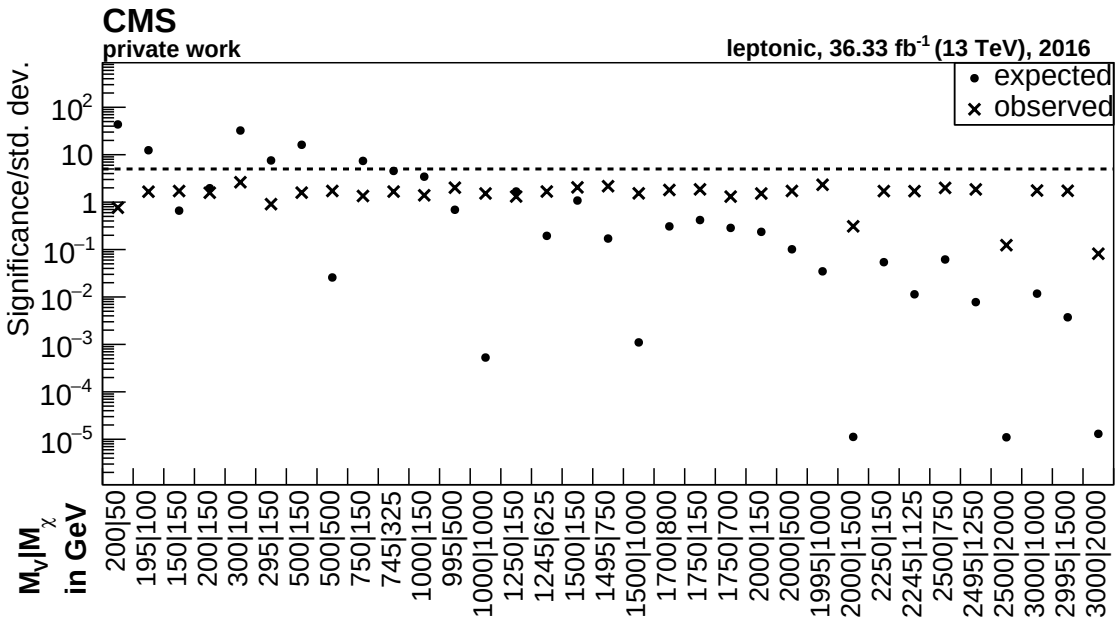

Figure 6.9: Significances for all considered mono-top mass hypothesis in units of Gaussian standard deviations in the combination of the two 2016 data-taking eras for the leptonic analysis. The expected significances shown as dots are compared to the observed significances shown as crosses. The mass of the mediator is denoted by M_V and the mass of the DM candidate by M_χ. A dashed line indicates the $5\,\sigma$ discovery threshold.

6.5.2 A-posteriori distributions

Since no significant deviations from the background-only hypothesis are observed, the background-only statistical model is deployed to describe the measured data. By checking the a-posteriori agreement between the data and the simulation, further validation of the statistical model is performed. The a-posteriori distributions for the 2016preVFP data-taking era are shown in figure 6.10, where a background-only maximum likelihood fit of the 2016 dataset is considered. Very good agreement between the data and the

simulation is observed, confirming that the statistical model is able to describe the data well. However, it should be noted that a minor data over fluctuation is observed in the last bin of the SR in the electron channel. This over fluctuation is possibly the reason for the slightly higher observed significances in figure 6.9. The distributions for all data-taking eras are shown in appendix H.

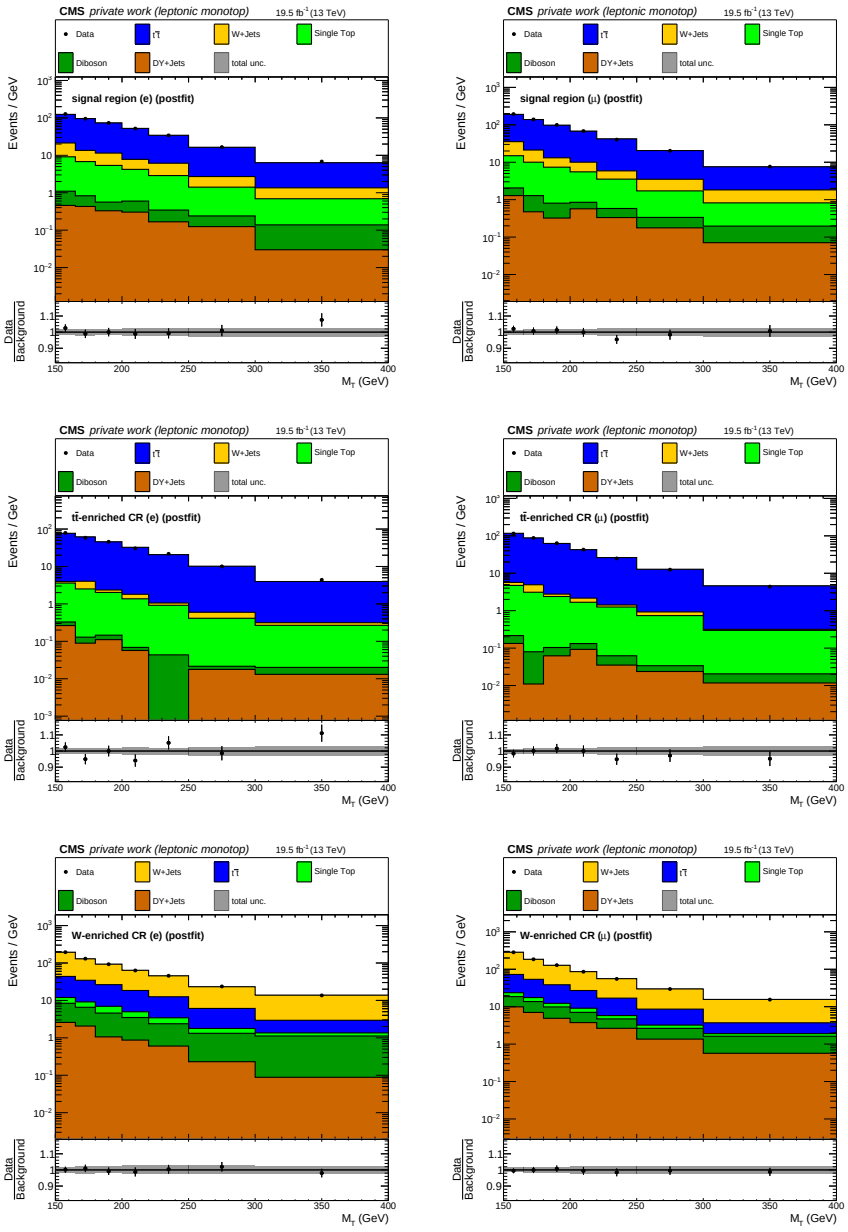

Figure 6.10: Transverse mass distributions in the leptonic mono-top analysis for the 2016pre-VFP data-taking era after performing a background-only fit to the 2016 data. Shown are the signal regions as well as the $t\bar{t}$ and $W + jets$ enriched control regions from top to bottom. The electron channels are shown on the left-hand side, whereas the muonic regions are depicted on the right-hand side. The measured data in black points are compared to the background prediction from the simulation as colored stacked histograms for different processes. The lower pad in each plot shows the ratio of data to the total background prediction. The grey shaded area illustrates the one standard deviation uncertainty band.

6.5.3 Observed exclusion limits

As shown in the previous section, no significant deviations from the background-only hypothesis are observed in the leptonic mono-top analysis. Therefore, the goal is to restrict the allowed parameter space in the plane of mediator and DM candidate masses M_V and M_χ. Figure 6.11 shows the expected exclusion limits for the leptonic mono-top analysis in the combination of the two 2016 data-taking eras, where the observed upper limit is equal to unity, is indicated by a red line. Consequently, the enclosed parameter space is excluded for the leptonic mono-top model. For low mediator masses, the observed exclusion contour follows the expected one closely. Only for mediator masses above 1 TeV the observed exclusion contour is shifted to lower DM candidate masses, which is due to the slight over fluctuation of the data. The lower observed exclusion limits are compatible with the previous finding in section 6.5.1 that, especially for high mediator masses the observed significances are higher than the expected ones. When considering the 68 % confidence interval on the expected exclusion contour, an approximately $1\,\sigma$ upward fluctuation of the data is observed. Ultimately, mediator masses of up to approximately 1 TeV are excluded for DM candidate masses of up to approximately 500 GeV at a confidence level of 95 %.

The exclusion limits, when considering both 2016 data-taking eras separately, are shown in appendix J.

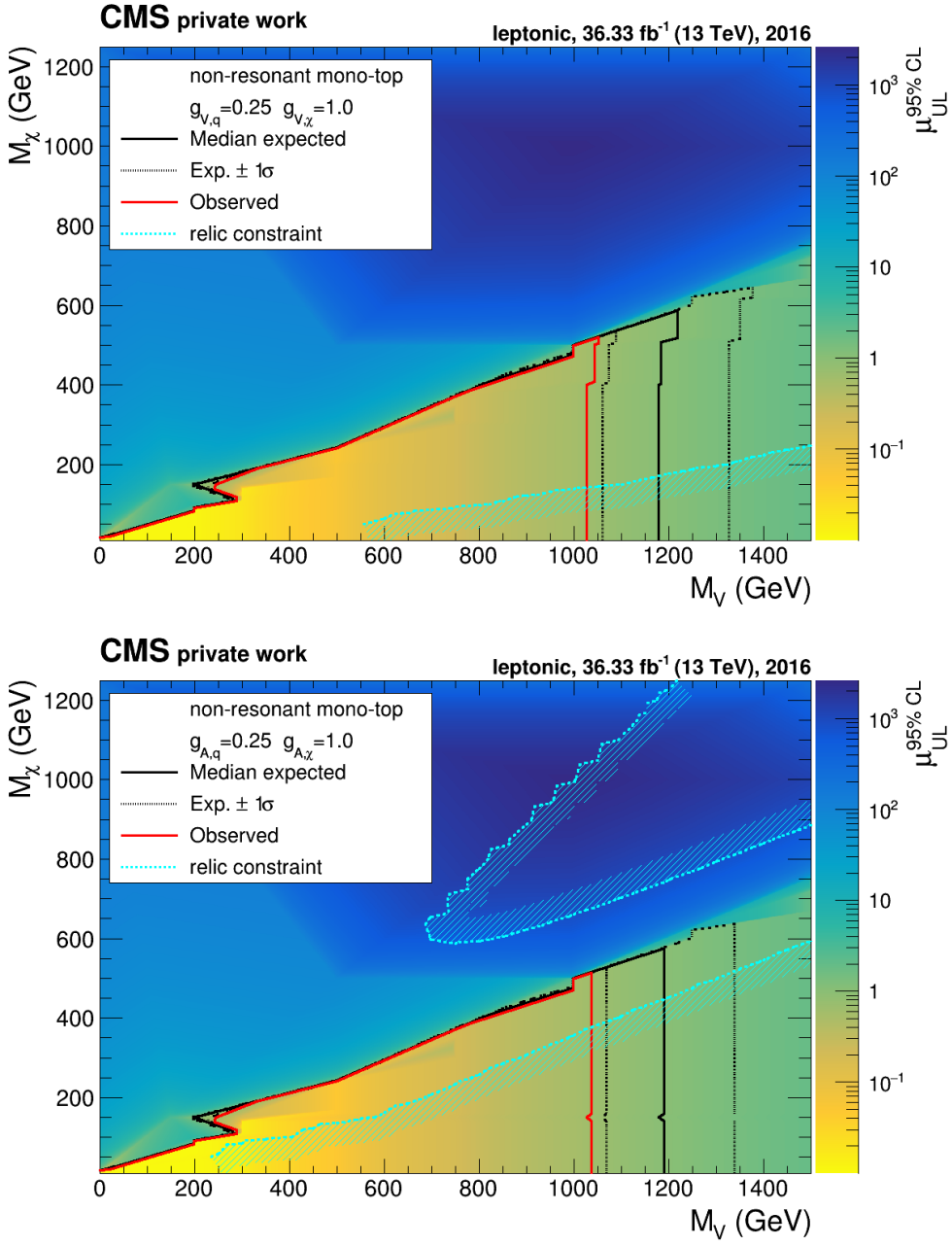

Figure 6.11: Upper limits on the signal strength modifier μ at a confidence level of 95 % for the vector mono-top model in the combination of the two 2016 data-taking eras in the plane of mediator and DM candidate masses M_V and M_χ. The solid black line indicates the contour, where the median, upper exclusion limit is equal to unity. The 68 % confidence interval on this contour is shown as a dashed black line. The area enclosed by the solid black line is parameter space expected to be excluded for the given mono-top model. The red line indicates the contour for which the observed upper limit is equal to unity, excluding the enclosed parameter space. The cyan, dashed exclusion line indicates a constraint on allowed masses in order to explain the measured DM relic density by the Planck Collaboration [30]. The upper exclusion plot corresponds to a pure vector coupling scenario, whereas the lower figure shows the exclusion limits for a pure axial-vector coupling scenario.

7 Hadronic mono-top analysis

The hadronic mono-top analysis targets the hadronic decay of the top quark. The general analysis strategy is motivated in the following. Afterward, the detailed selection criteria to enrich the mono-top signal in the SR as well as for the various CRs considered in this analysis are presented. Finally, the expected and observed results are presented after discussing the statistical model of the hadronic mono-top analysis. In general, the analysis strategy follows a previous iteration [126], where additional improvements are deployed in this thesis to further improve the sensitivity of the analysis. The main improvements are expected due to the usage of a more advanced top-tagging algorithm.

7.1 Analysis strategy

The analysis strategy targeting the hadronic mono-top signal is motivated in the following. The targeted final state of the signal consists of a large amount of MET due to the DM candidates escaping the detector in conjunction with hadronic jets originating from the top quark decay. Since the hypothetical new mediator recoils against the top quark, a significant Lorentz boost of the top quark is expected due to momentum conservation. Therefore, the decay products of the top quark are getting collimated, and large radius fatjets are expected to be formed, allowing for the deployment of powerful state-of-the-art algorithms to tag top quarks decaying hadronically as described in section 5.2.2. In this thesis, the `ParticleNet` algorithm is deployed on AK15 jets. To summarize, the event signature of the hadronic mono-top signal consists of a large amount of MET and a high-p_{T} fatjet in the opposite direction. Nonetheless, several SM processes can also create a similar experimental signature, which will be briefly described in the following.

The main background consists of the production of a Z boson with additional jets (Z + jets), where the Z boson decays into a pair of neutrinos (Z($\nu\nu$) + jets) providing a source of MET. An exemplary leading-order Feynman diagram is shown on the left-hand side of figure 7.1. Since the Z boson recoils against the quark, a large-momentum AK15 jet can be formed. Although the process gets kinematically suppressed with increasing p_{T} of the Z boson, the process is still relevant for the analysis due to the large cross section in comparison to the signal process, see tables 5.1 and 5.3. Moreover, this background is irreducible without the deployment of top-tagging techniques, and no dedicated CRs in data can be constructed to control this background. Therefore, special care must be taken to estimate this background, accomplished by a modified statistical model with respect to the statistical model deployed

in the leptonic analysis channel aiming to estimate this background contribution directly from data. More details on this will be given in section 7.3.

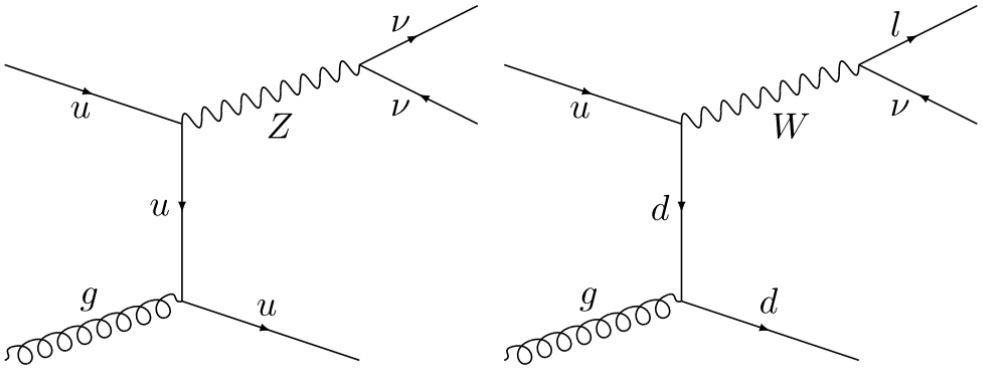

Figure 7.1: Exemplary leading-order Feynman diagrams for the production of electroweak bosons with an additional jet. The left-hand side shows the production of a Z boson decaying into a pair of neutrinos. On the right-hand side, the production of a W boson decaying into a charged lepton and a neutrino is depicted. Taken from [126]

The second important background is given by the production of a W boson with additional jets (W + jets), where the W boson decays into a charged lepton and a neutrino W($\ell\nu$) + jets. In the case for electrons and muons, this background mimics the signal signature if the lepton is not detected due to limited reconstruction efficiencies or detector acceptance effects. Since τ leptons are heavy enough to decay hadronically, the signature can become more similar to the signal. Again, although these effects are small, the large cross section in the order of several thousand pb of the W + jets production yields a significant background contribution (see tables 5.1 and 5.3). An exemplary leading order Feynman diagram is shown on the right-hand side of figure 7.1.

The third major background is given by top quark-antiquark pair ($t\bar{t}$) production. The effect of a large production cross section of approximately 832 pb [138, 139] is enhanced when deploying top-tagging techniques since backgrounds not containing top quarks are significantly reduced. The main $t\bar{t}$ background contribution arises from semileptonic decays of the top quark-antiquark pair system, where the hadronically decaying top quark results in a high-p_T fatjet and the charged lepton of the leptonically decaying top quark is not detected similarly as for the W + jets background. Fully hadronic $t\bar{t}$ decays do not result in a large amount of MET and are therefore heavily suppressed. Similarly, dileptonic $t\bar{t}$ decays are subdominant due to the low probability that none of the two charged leptons are reconstructed.

In summary, several SM backgrounds provide a similar experimental signature as the hadronic mono-top signal. Therefore, special care has to be taken to suppress those backgrounds as much as possible. As mentioned earlier, one powerful way to reduce backgrounds not containing top quarks is the deployment of top-tagging techniques. However, top-tagging is not able to suppress the $t\bar{t}$ background but rather increases its contribution. Additionally, the V + jets backgrounds are still present due to their large cross sections. Consequently, the main challenge of the hadronic mono-top analysis is to predict and understand the mentioned backgrounds as well as possible. For this, dedicated modifications are deployed to the statistical model, as deployed in the leptonic analysis channel, utilizing dedicated CRs enhanced in the main backgrounds. The detailed event selection criteria

to construct the signal and background CRs are described in section 7.2. The statistical model will be described in section 7.3.

The variable employed in the hadronic analysis to extract the signal is the hadronic recoil. It is defined as the vectorial sum of the MET and the transverse momentum of all prompt reconstructed electrons, muons, and photons

$$\vec{\not{U}}_{\mathrm{T}} = \vec{\not{E}}_{\mathrm{T}} + \sum_{i=\mathrm{e},\mu,\gamma} \vec{p}_{\mathrm{T},i}. \tag{7.1}$$

The magnitude of $\vec{\not{U}}_{\mathrm{T}}$ is denoted as $\not{U}_{\mathrm{T}}$. If no prompt electrons, muons, or photons are reconstructed, $\vec{\not{U}}_{\mathrm{T}}$ is equal to $\vec{\not{E}}_{\mathrm{T}}$, which will be the case for the SR. For $\mathrm{Z}(\nu\nu)$ + jets, one of the most important backgrounds in the SR, the hadronic recoil is a proxy for the transverse momentum of the Z boson. As mentioned above, no dedicated CRs are available to control the $\mathrm{Z}+$jets background, where the Z boson decays into a pair of neutrinos. Information on this process can be extracted by considering the hadronic recoil of Z boson decays into a pair of electrons or muons. Due to the distinct signature of such dileptonic events, in which the invariant mass of the two charged leptons can be exploited, a very pure CR can be constructed. Similarly, the hadronic recoil can be utilized to extract information on the $\mathrm{W}+$jets background, where the W boson decays into a charged lepton and a neutrino. Again, the hadronic recoil is a proxy for the transverse momentum of the W boson. In addition, the production of a photon in association with jets is also suitable to gain insight on the $\mathrm{Z}(\nu\nu)$ + jets background in the SR. In general, the hadronic recoil offers the advantage of gaining information on the $\mathrm{V}+$jets processes in CRs and connecting it to the $\mathrm{Z}(\nu\nu)$ + jets and $\mathrm{W}(\ell\nu)$ + jets background in the SR. This connection is established via transfer factors (TFs) incorporated directly in a flexible statistical model, as it will be described in section 7.3. This statistical model aims to estimate the yield of the main background processes in the SR directly from data.

7.2 Event selection

As motivated before, a crucial ingredient to the analysis is a precise estimation of contributions arising from SM background processes. For this background estimation, several CRs are constructed in addition to the SR. In the following, detailed event selections are provided targeting the desired phase space regions.

7.2.1 General selection

The advantage of using the hadronic recoil is that it provides a comparable quantity regardless of the presence of prompt leptons or photons. Consequently, a general event selection is applied to all events, regardless of the CR or SR, in order to keep the targeted phase space regions as similar as possible. The general event selection is motivated by the expected signature of the mono-top signal, where the top quark decays hadronically.

Since the hypothetical mediator is expected to be heavy, a significant amount of MET or hadronic recoil, respectively, is expected. For selecting high-p_{T} hadronic recoil events, specialized HLT paths are employed as listed in table 7.1. If multiple HLT paths are given for the same signature, the logical OR of the paths is employed in order to maximize the selection efficiency. The given hadronic recoil triggers are considering a MET definition, in which muons are neglected in the MET reconstruction at HLT level, offering the advantage to also select events containing prompt muons.

Table 7.1: HLT paths considered in the hadronic analysis, targeting different final signatures split across the data-taking eras.

signature	HLT path
	2018
$\not{E}_{\mathrm{T}}/\not{U}_{\mathrm{T}}$	`HLT_PFMETNoMu120_PFMHTNoMu120_IDTight`
	`HLT_PFMETNoMu120_PFMHTNoMu120_IDTight_PFHT60`
electron (low p_{T})	`HLT_Ele32_WPTight_Gsf`
electron/photon (high p_{T})	`HLT_Photon200`
	2017
$\not{E}_{\mathrm{T}}/\not{U}_{\mathrm{T}}$	`HLT_PFMETNoMu120_PFMHTNoMu120_IDTight`
	`HLT_PFMETNoMu120_PFMHTNoMu120_IDTight_PFHT60`
electron (low p_{T})	`HLT_Ele35_WPTight_Gsf`
electron/photon (high p_{T})	`HLT_Photon200`
	2016[pre/post]VFP
$\not{E}_{\mathrm{T}}/\not{U}_{\mathrm{T}}$	`HLT_PFMETNoMu90_PFMHTNoMu90_IDTight`
	`HLT_PFMETNoMu100_PFMHTNoMu100_IDTight`
	`HLT_PFMETNoMu110_PFMHTNoMu110_IDTight`
	`HLT_PFMETNoMu110_PFMHTNoMu120_IDTight`
electron (low p_{T})	`HLT_Ele27_WPTight_Gsf`
electron/photon (high p_{T})	`HLT_Photon175`

A lower threshold of 350 GeV is applied to the magnitude of the hadronic recoil. This threshold is chosen such that the corresponding hadronic recoil triggers are fully efficient, as shown in figure 5.16. The analysis strategy is based on the fact that the hadronic decay products of the top quark are clustered into a single AK15 jet. Therefore, at least one AK15 jet with a minimum transverse momentum of 250 GeV is required.

Since the top quark is expected to be recoiling against the hypothetical mediator, the opening angle in the transverse plane between the leading AK15 jet and the hadronic recoil is required to be greater than 1.5 rad. In order to suppress backgrounds arising from QCD multijet production as well as events in which the MET is mismeasured, the opening angle of the hadronic recoil and all AK4 jets is required to be greater than 0.5 rad. The latter requirement is motivated by the fact that the MET should not point in the direction of jets. This effect is known to be poorly modeled in simulation, motivating the rejection of such events.

As described earlier, powerful top-tagging techniques are utilized in this analysis to gain sensitivity to the mono-top signal. The requirement on the top-tagging discriminant will be introduced later in section 7.2.7. Not deploying the top-tagging requirement in the general event selection yields the advantage of validating the modeling in the analysis regions without a dependency on potential mismodellings of the top-tagging efficiency in simulation.

As a general remark, all leptonic CRs, as defined in more detail in the following, are split according to the flavor of the charged lepton. Similarly to the region definitions in the leptonic analysis, see section 6.2, only electrons and muons are considered. This separation has the advantage of disentangling efficiency effects specific to the lepton flavor.

7.2.2 Signal region

The above general selection criteria almost correspond to the phase space targeted for the hadronic mono-top signal. Only a few additional selection criteria are applied, as described in the following. Events are discarded if none of the $\not{E}_{\mathrm{T}}$ HLT paths as listed in table 7.1 selected the event. Since no leptons are expected in the final state, events are vetoed if any loose muon or electron is present. Considering that all decay products of the hadronically decaying top quark are expected to be clustered inside the leading AK15 jet, no b-jets are expected outside this fatjet. Consequently, events are vetoed if any b-tagged AK4 jet is found outside the leading AK15 jet based on the loose WP of the `DeepJet` tagger. As described in section 5.8, an issue occurred during the 2018 data-taking era (HEM15/16). Although events are vetoed if a jet is reconstructed in the affected detector region, residual effects are still present, as shown by the CMS mono-jet analysis [187]. In order to account for this issue, events are rejected if the MET is smaller than 470 GeV and the azimuthal angle of the MET is in the range $-1.62 \leq \Phi \leq -0.62$. Figure 7.2 shows the distribution of the transverse momentum of the hadronic recoil and the leading AK15 jet data-taking era as an example. The distributions for all data-taking eras are shown in appendix K. As already laid out before, the main backgrounds in the SR are the production of a Z boson decaying into a pair of neutrinos in association with jets. The subdominant background is $\mathrm{W}(\ell\nu)$ + jets production followed by the production of a top quark-antiquark pair. However, the $\mathrm{t\bar{t}}$ background will significantly increase when deploying top-tagging techniques, as shown in section 7.2.7. Furthermore, the overlaid signal indicates that the mono-top signal tends towards higher hadronic recoil values than the SM backgrounds, rendering the hadronic recoil a powerful search variable. Additional kinematic distributions are shown for all eras in appendix K, where a similarly good agreement between data and simulation is observed.

7.2.3 Z boson control regions

The Z boson CRs aim at a phase space enhanced in dileptonic Z boson decays, where only decays into electrons or muons are targeted. Consequently, the primary selection requirement is given by the presence of either two electrons or muons. Due to the low

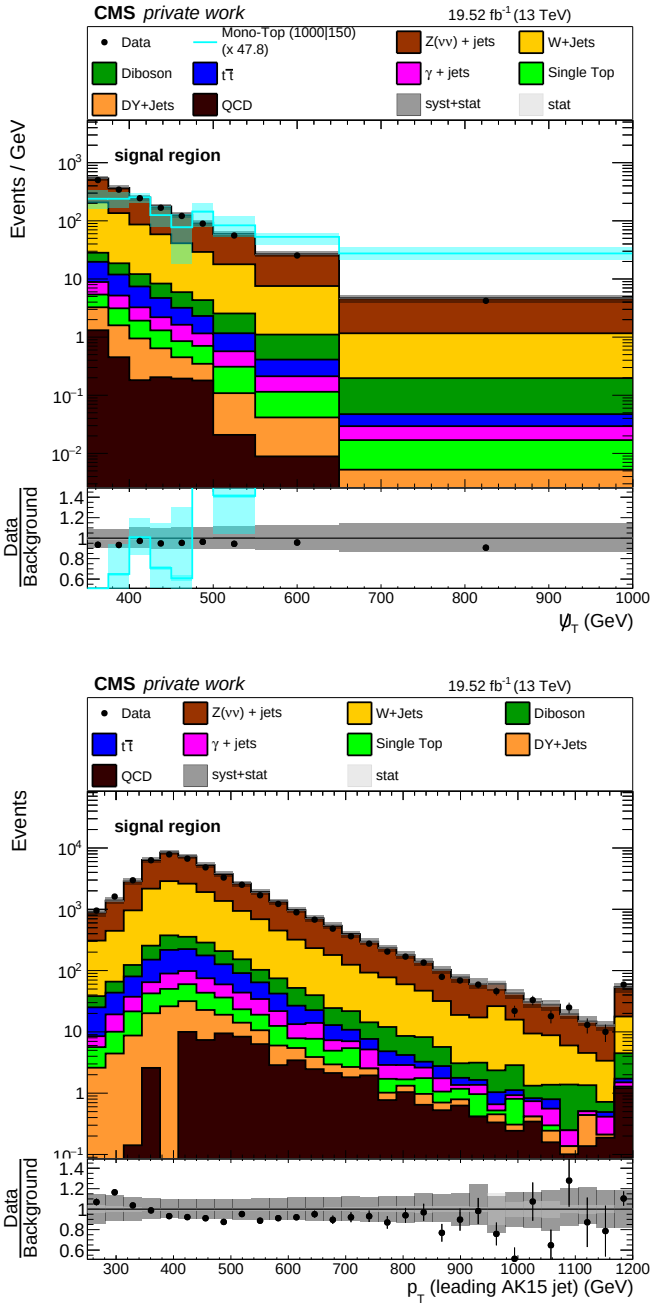

Figure 7.2: Distributions of the hadronic recoil p_{T} (top) as well as the transverse momentum of the leading AK15 jet (bottom) in the hadronic SR with no top-tagging requirement applied for the 2016preVFP data-taking era. The observed data is shown as black points. The lower pad in each plot shows the ratio of data to the total background prediction. The dark grey shaded area illustrates the one standard deviation uncertainty band by adding all shape-affecting uncertainties in quadrature. The light grey shaded area corresponds to the uncertainty due to the limited statistical precision of the MC-simulated samples. An exemplary signal prediction with a mediator mass of 1000 GeV and DM candidate mass of 150 GeV scaled to the total sum of expected backgrounds is overlaid in cyan on the left-hand side.

branching fraction of Z bosons decaying into a pair of charged leptons and the desired high-p_{T} phase space, the number of selected events is significantly reduced compared to the other CRs. This effect is enhanced further when deploying top-tagging techniques. Therefore, two loose instead of tight electrons or muons are considered for the Z boson CRs, increasing the selection efficiency. Due to the nature of reconstructing electrons, the gain in selection efficiency of non-prompt electrons is more pronounced than for muons. Since this effect decreases with increasing transverse momentum of the electron, a lower threshold of 40 GeV is applied for the leading electron. Events are discarded if a loose photon is reconstructed. Events are selected if one of the hadronic recoil HLT paths is fired for the muon channel, whereas a single electron trigger is used for the electron channel, as given in table 7.1. Since the two leptons arise from the decay of a Z boson, the invariant mass of the lepton pair is expected to be close to the mass of the Z boson of approximately 91.2 GeV. Accordingly, events are rejected if the invariant mass of the two leptons is smaller than 60 GeV or larger than 120 GeV. No MET is expected in dileptonic $\mathrm{Z}(\ell\ell)$ + jets events, motivating an upper threshold of $\not{E}_{\mathrm{T}} < 120$ GeV. Figure 7.3 shows the distribution of the hadronic recoil and the invariant mass of the lepton pair as well as the transverse momentum of the leading AK15 for the 2016preVFP data-taking era as an example. Good modeling of the measured data is observed within the uncertainties. Furthermore, an excellent enrichment of the $\mathrm{Z}(\ell\ell)$ + jets background is visible. Additional kinematic distributions are shown for all eras in appendix K, where a similarly good agreement between data and simulation is observed.

7.2.4 W boson control regions

The W boson CR targets a phase space enriched in leptonic W boson decays. Again, only decays into electrons or muons are focused, motivating the selection of events by either the hadronic recoil or isolated electron HLTs as listed in table 7.1. Being a single lepton CR, exactly one tight electron or muon is required. Events are vetoed if any additional loose lepton of the other flavor or a loose photon is reconstructed. Semileptonic $\mathrm{t\bar{t}}$ events are suppressed by requiring that no AK4 outside the leading AK15 jet is b-tagged based on the loose WP of the `DeepJet` tagger. Since the leptonic mono-top analysis also considers a W boson CR, events are required to have a transverse mass of less than 150 GeV. This requirement ensures that the analysis regions of the hadronic and leptonic mono-top analyses are mutually exclusive. The distributions of the transverse momentum of the hadronic recoil and the leading AK15 jet are shown in figure 7.4 for the 2016preVFP data-taking era as an example. A very good description of the data by the simulation considering the systematic uncertainties is observed. As expected, the main background in this region is given by $\mathrm{W}(\ell\nu)$ + jets production. The subdominant background is $\mathrm{t\bar{t}}$ production, which is expected to be enhanced when employing top-tagging techniques. Additional kinematic distributions are shown in appendix K for all data-taking eras, where a similarly good description of the measured data is observed.

7.2.5 Top Quark-Antiquark Pair control regions

An important background in the SR as well as the W boson CRs is the production of top quark-antiquark pairs. Therefore, dedicated CRs are constructed, targeting semileptonic $\mathrm{t\bar{t}}$ events. As in the W boson CRs, events are selected if either exactly one tight electron or muon is reconstructed while vetoing events containing a loose lepton of the other flavor or a loose photon. Analogously, events are selected if either one of the hadronic recoil or isolated electron HLT is fired as listed in table 7.1. As for the SR, the decay products of the hadronically decaying top quark are expected to be clustered in the leading AK15 jet. Consequently, the b-jet originating from the leptonically decaying top quark is expected to

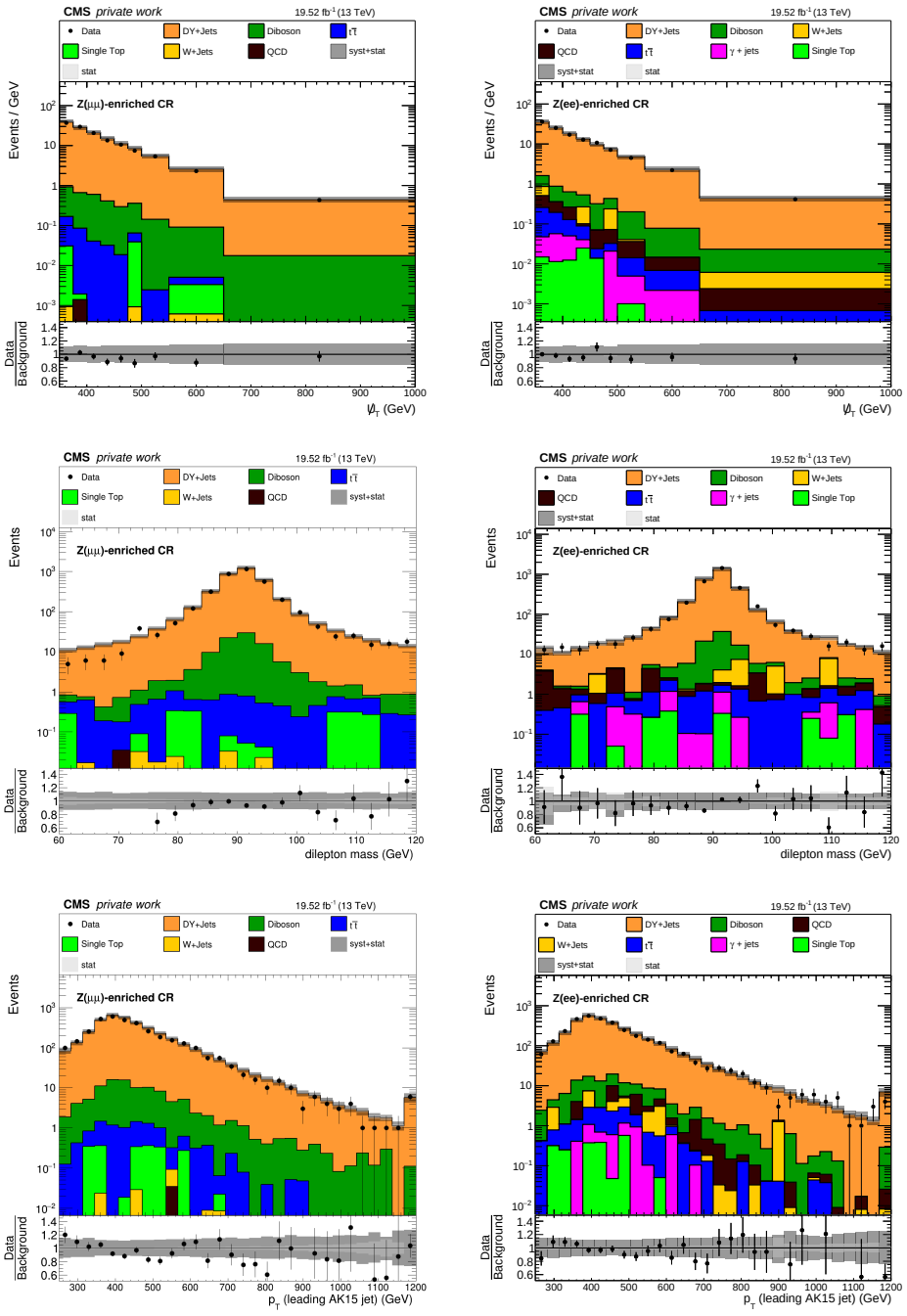

Figure 7.3: Distributions of the hadronic recoil p_{T}, the mass of the dilepton system and as well as the transverse momentum of the leading AK15 jet in the Z boson CRs with no top-tagging requirement applied for the 2016preVFP data-taking era. The muonic CR is shown on the left-hand side, whereas the electronic CR is shown on the right-hand side. The black data points correspond to the measured data, whereas the stacked histograms correspond to the background prediction from simulation for different processes. The lower pad in each plot shows the ratio of data to the total background prediction. The dark grey shaded area illustrates the one standard deviation uncertainty band by adding all shape-affecting uncertainties in quadrature. The light grey shaded area corresponds to the uncertainty due to the limited statistical precision of the MC-simulated samples.

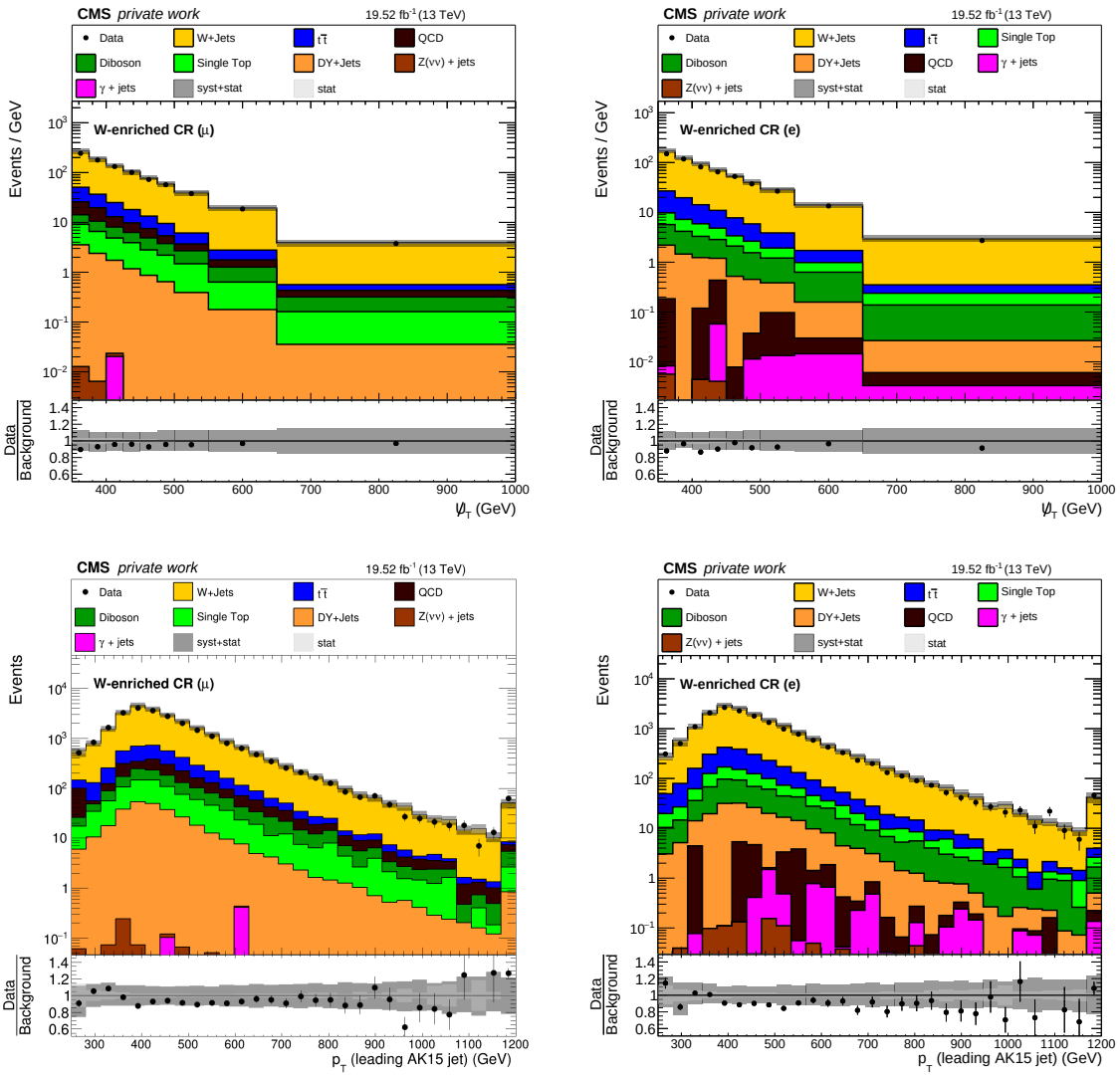

Figure 7.4: Distributions of the transverse momentum of the hadronic recoil and the leading AK15 jet in the W boson CRs with no top-tagging requirement applied for the 2016preVFP data-taking era. The muonic CR is shown on the left-hand side, whereas the electronic CR is shown on the right-hand side. The black data points correspond to the measured data, whereas the stacked histograms correspond to the background prediction from simulation for different processes. The lower pad in each plot shows the ratio of data to the total background prediction. The dark grey shaded area illustrates the one standard deviation uncertainty band by adding all shape-affecting uncertainties in quadrature. The light grey shaded area corresponds to the uncertainty due to the limited statistical precision of the MC-simulated samples.

be reconstructed as a AK4 jet outside the leading AK15 jet. This event signature motivates a selection on the existence of a b-tagged AK4 jet outside the leading AK15 jet based on the loose WP of the `DeepJet` tagger. As for the W boson CRs, the leptonic mono-top analysis also deploys a $t\bar{t}$ CR. Again, the regions of the two analyses are made mutually exclusive by requiring that the transverse mass is greater than 150 GeV. Figure 7.5 shows the distributions of the transverse momentum of the hadronic recoil and the leading AK15 jet for the 2016preVFP data-taking era. Again, good modeling of the measured data by the simulation is observed. The main process is given by $t\bar{t}$ production. However, a sizable contribution of $W(\ell\nu)$ + jets events still enters the $t\bar{t}$ CR, which could be reduced by applying a tighter b-tagging requirement. Although this would enhance the purity of the CR, it would also reduce the overall yield and statistical precision due to the lower efficiency of a tighter WP. Furthermore, the $t\bar{t}$ yield will be enhanced significantly when deploying top-tagging techniques. Appendix K shows additional kinematic distributions for all data-taking eras, where a similarly good description of the measured data is observed.

7.2.6 Photon control region

Considering the hadronic recoil, the production of a photon in association with jets (γ + jets) can also be used to gain information on the $Z(\nu\nu)$ + jets process in the SR. Therefore, a dedicated γ + jets CR is constructed by requiring that the event contains at least one tight photon while vetoing events with additional loose electrons or muons. Following this event signature, a high-p_T photon trigger is employed as listed in table 7.1. Similarly to the W boson CRs, no b-jets are expected. Therefore no b-tagged AK4 jets outside the leading AK15 jet are required, based on the loose WP of the `DeepJet` tagger. Due to the nature of having a single photon in the final state, QCD multijet production yields a comparable signature if a quark or gluon radiates a photon. In order to avoid double-counting, events are vetoed in the simulated QCD samples if an isolated photon is present on generator level. Figure 7.6 shows the distributions of the transverse momentum of the hadronic recoil and the leading AK15 jet for the 2016preVFP data-taking era. First, a good enrichment in the γ + jets process is observed, where the subdominant process is given by QCD multijet production. The simulation describes the shapes of the distributions in data well. However, a normalization difference of about 15 to 20 % is observed. Since the γ + jets is known to be difficult to predict in such extreme high-p_T phase space regions, a possible explanation for this offset could be the limited accuracy of the MadGraph5_aMC@NLO simulation. Similar issues with the γ + jets CR were also observed in a previous iteration of this analysis [126]. Additional kinematic variables are shown in appendix K for all data-taking eras, where a similar normalization issue is realized. In order to give the statistical model enough freedom to capture this mismodeling a conservative normalization uncertainty of 10 % is applied to the γ + jets process. During the maximum likelihood fit, this uncertainty allows determining the normalization of the γ + jets process in-situ.

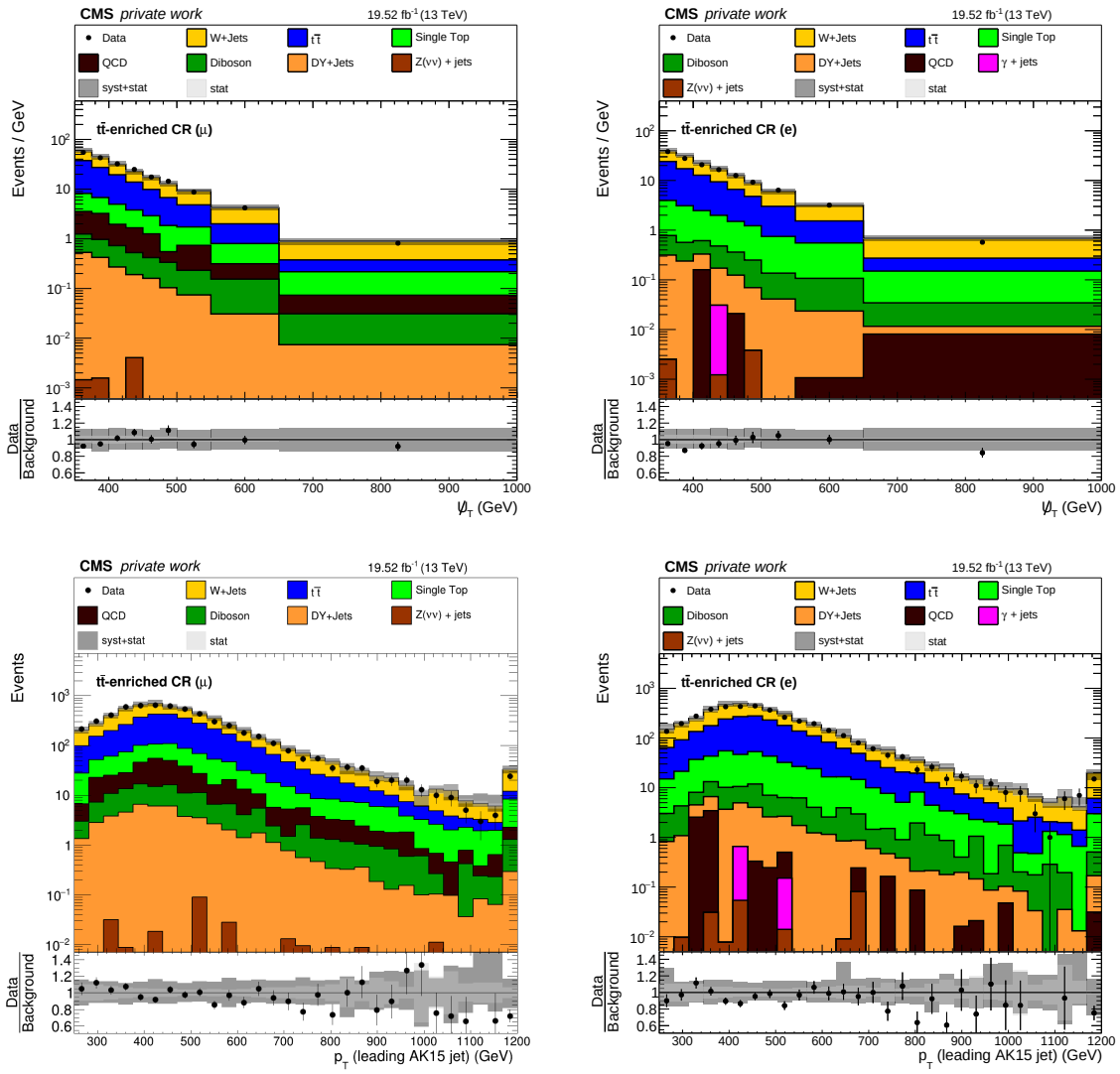

Figure 7.5: Distributions of the transverse momentum of the hadronic recoil and the leading AK15 jet in the $t\bar{t}$ CRs with no top-tagging requirement applied for the 2016preVFP data-taking era. The muonic CR is shown on the left-hand side, whereas the electronic CR is shown on the right-hand side. The black data points correspond to the measured data, whereas the stacked histograms correspond to the background prediction from simulation for different processes. The lower pad in each plot shows the ratio of data to the total background prediction. The dark grey shaded area illustrates the one standard deviation uncertainty band by adding all shape-affecting uncertainties in quadrature. The light grey shaded area corresponds to the uncertainty due to the limited statistical precision of the MC-simulated samples.

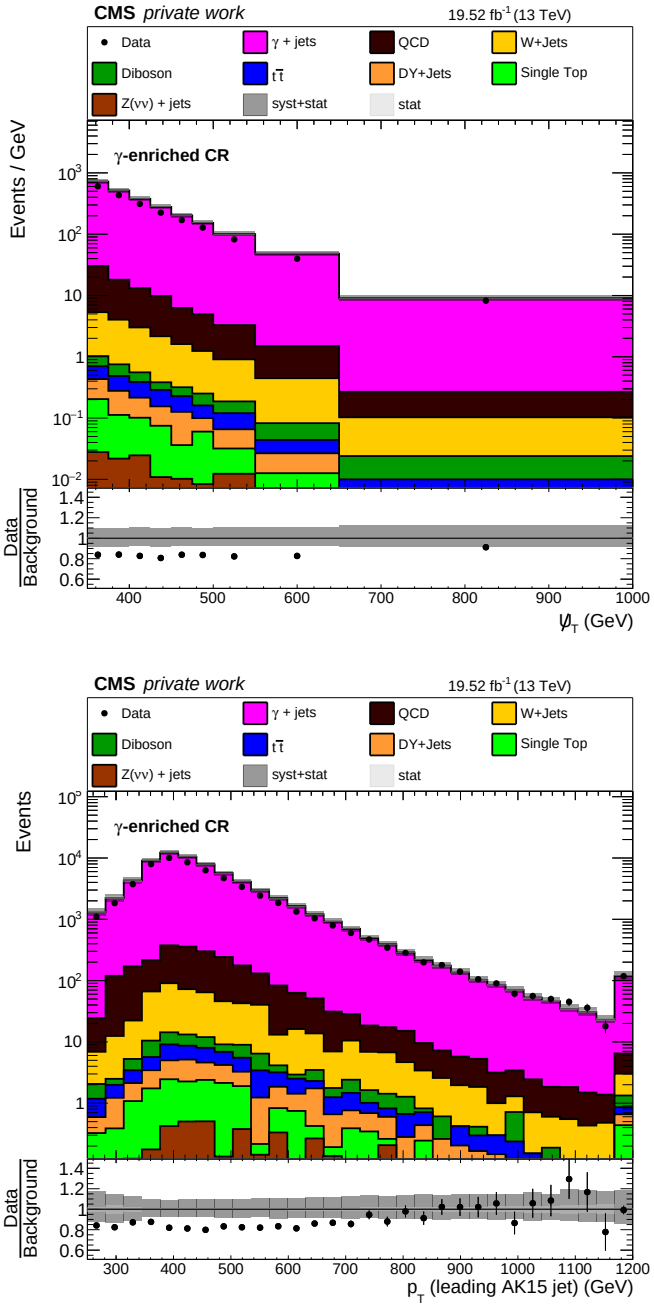

Figure 7.6: Distributions of the transverse momentum of the hadronic recoil (top) and the leading AK15 jet (bottom) in the photon CR with no top-tagging requirement applied for the 2016preVFP data-taking era. The black data points correspond to the measured data, whereas the stacked histograms correspond to the background prediction from simulation for different processes. The lower pad in each plot shows the ratio of data to the total background prediction. The dark grey shaded area illustrates the one standard deviation uncertainty band by adding all shape-affecting uncertainties in quadrature. The light grey shaded area corresponds to the uncertainty due to the limited statistical precision of the MC-simulated samples.

7.2.7 Top-tagging selection

Following the general analysis strategy, the decay products of the hadronically decaying top quark are expected to be reconstructed as a single AK15 jet. As described in section 5.2.2, state-of-the-art top-tagging algorithms offer the advantage of identifying such jets with high efficiency. The WP considered in this thesis corresponds to a probability of misidentifying a fatjets not originating from a top quark of 2.5 %, see section 5.7.5.3. The application of this top-tagging requirement yields two consequences. First, the signal contribution is enhanced significantly due to the high efficiency of the top-tagging algorithm for selecting AK15 jets originating from a top quark of 66.5 %. Second, background contributions arising from non top quark related processes, such as the main $Z(\nu\nu)$ + jets background, are reduced significantly at the cost of enhancing the $t\bar{t}$ background process. However, the events in which the leading AK15 jet is not tagged provide a phase space enriched in V + jets processes, which can be used to constrain these backgrounds further. Following this reasoning, all previously defined CRs and the SR are further split according to whether the leading AK15 jet is top-tagged (pass region) or not (fail region). The SR split into the pass and fail region is shown in figure 7.7 for the 2016preVFP data-taking era. Especially for low hadronic recoil transverse momenta, the relative $t\bar{t}$ background contamination is significantly enhanced in the pass region, whereas the V + jets background is reduced. In contrast, the $t\bar{t}$ background is subdominant in the fail region. Furthermore, the signal-to-background ratio is enhanced by a factor of approximately 22 in the pass region with respect to the case in which no top-tagging is employed, illustrating the power of the top-tagging requirement. Consequently, large signal fractions are expected in the pass region, depending on the cross section of the signal mass hypothesis under scrutiny. In order to avoid potential instabilities during the maximum likelihood fit, the signal cross section is scaled to 1 fb in the maximum likelihood fit. This approach is valid since the parameter of interest (μ) is the signal strength, defined as the ratio of the observed and theoretically expected cross sections. Therefore, the actual observed cross section value can be inferred by rescaling μ.

The transverse momentum of the hadronic recoil in the pass region is shown for the photon and single-lepton CRs in figure 7.8. Figure 7.9 shows the same distributions for the Z + jets CR for the 2016preVFP data-taking era. It can be observed that the main process in the single-lepton regions is now given by $t\bar{t}$ production. Since the photon and Z boson CRs show a non-significant $t\bar{t}$ contamination in the first place, $t\bar{t}$ remains a subdominant process. In general, good modeling of the data is observed in all analysis regions. However, there are some discrepancies between the data and the MC prediction in the Z + jets and photon CRs. Especially, the photon CR shows a normalization discrepancy between data and MC prediction. Moreover, a general slight overprediction of the data is observed in the pass regions. Consequently, a flexible statistical model that is able to precisely predict both the shape and normalization of the V + jets and $t\bar{t}$ background processes considering all analysis regions simultaneously is required. The statistical model deployed in the hadronic mono-top analysis is described in the following section 7.3.

The distributions, including also the fail regions, for all data-taking eras are shown in appendix L, where no significant mismodeling is observed.

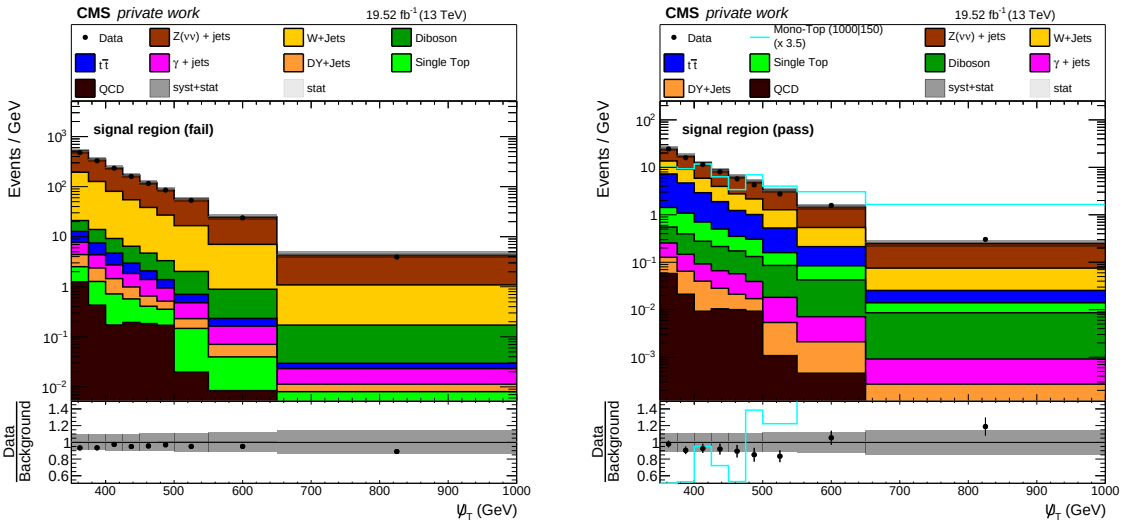

Figure 7.7: Distributions of the hadronic recoil p_{T} after applying the top-tagging requirement in the SR. The pass region is shown on the left-hand side, whereas the right-hand side corresponds to the fail region. The black data points correspond to a signal-plus-background pseudo dataset, whereas the stacked histograms correspond to the background prediction from simulation for different processes. The lower pad in each plot shows the ratio of data to the total background prediction. The dark grey shaded area illustrates the one standard deviation uncertainty band by adding all shape-affecting uncertainties in quadrature. The light grey shaded area corresponds to the uncertainty due to the limited statistical precision of the MC-simulated samples. An exemplary signal prediction with a mediator mass of 1000 GeV and DM candidate mass of 150 GeV scaled to the total sum of expected backgrounds is overlaid in cyan.

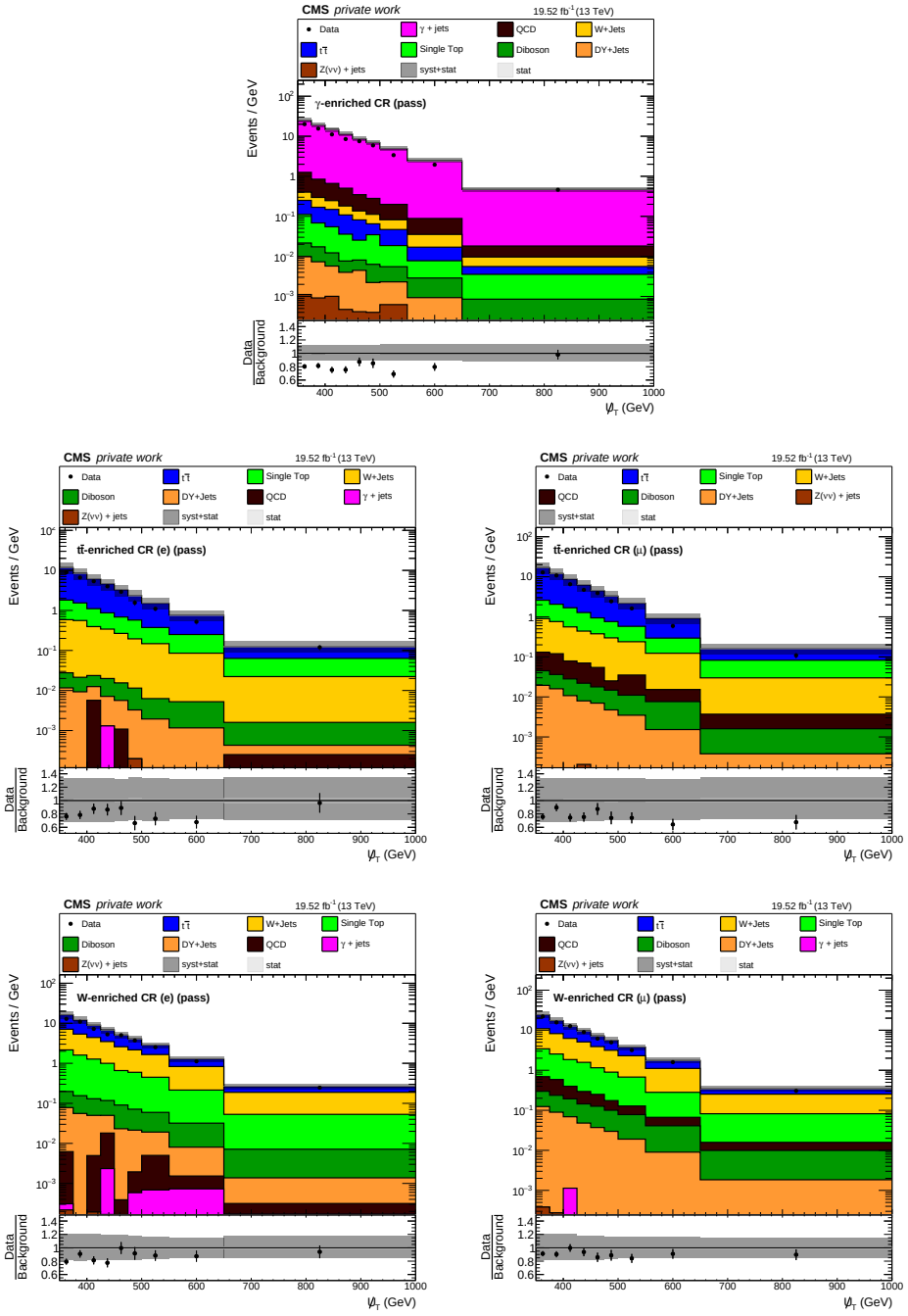

Figure 7.8: Distributions of the hadronic recoil p_{T} for the photon, W boson and $\mathrm{t\bar{t}}$ CRs where the leading AK15 is top-tagged for the 2018 data-taking era. The black data points correspond to the measured data, whereas the stacked histograms correspond to the background prediction from simulation for different processes. The lower pad in each plot shows the ratio of data to the total background prediction. The dark grey shaded area illustrates the one standard deviation uncertainty band by adding all shape-affecting uncertainties in quadrature. The light grey shaded area corresponds to the uncertainty due to the limited statistical precision of the MC-simulated samples.

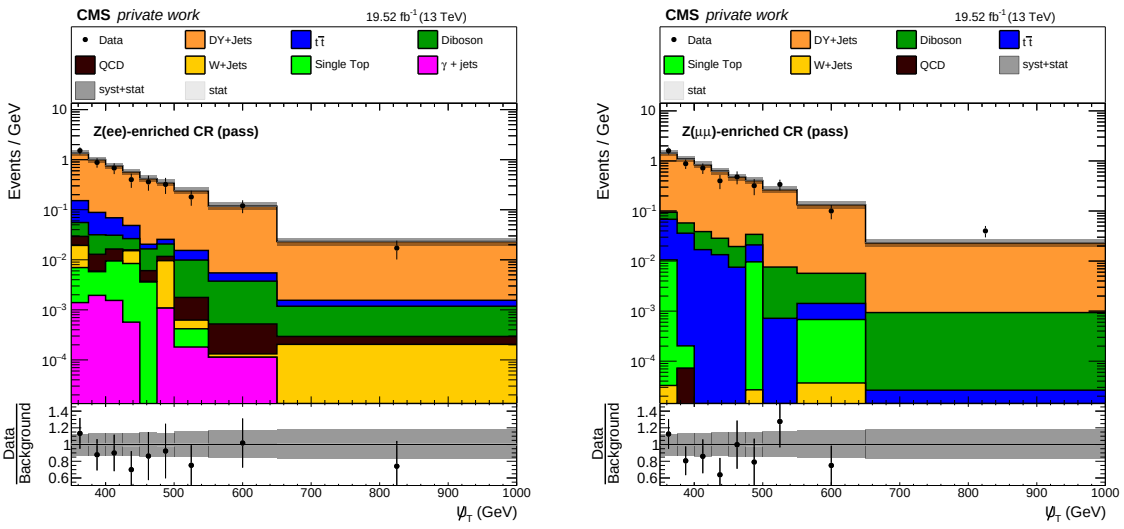

Figure 7.9: Distributions of the hadronic recoil p_{T} for the Z boson CRs where the leading AK15 is top-tagged for the 2018 data-taking era. The black data points correspond to a signal-plus-background pseudo dataset, whereas the stacked histograms correspond to the background prediction from simulation for different processes. The lower pad in each plot shows the ratio of data to the total background prediction. The dark grey shaded area illustrates the one standard deviation uncertainty band by adding all shape-affecting uncertainties in quadrature. The light grey shaded area corresponds to the uncertainty due to the limited statistical precision of the MC-simulated samples.

7.3 Statistical model

As laid out before, a crucial aspect of the hadronic mono-top analysis is the precise estimation of the background processes. In particular, estimating the non-reducible $\mathrm{Z}(\nu\nu)$ + jets process is challenging since it provides the same experimental signature as the mono-top signal. Additionally, after applying top-tagging techniques, the production of top quark-antiquark pairs also yields a significant background contribution. Therefore, modifications are made to the statistical model introduced in chapter 4. The hadronic recoil as a variable sensitive to the mono-top signal allows for a connection between the CRs and the SR. This connection is established via TFs, which are defined as the ratio of predictions of process A in analysis region X ($n^A_{i,X}$) with process B in analysis region Y ($n^B_{i,Y}$)

$$\mathrm{TF}^{A/B}_{i,X/Y} = \frac{n^A_{i,X}}{n^B_{i,Y}}, \tag{7.2}$$

where the subscript i denotes the bin number assuming the identical binning in both regions. By using this definition, the prediction of a given process A in region X can be expressed as

$$n^A_{i,X} = \mathrm{TF}^{A/B}_{i,\mathrm{X/Y}} \cdot n^B_{i,Y}. \tag{7.3}$$

It should be noted that the TFs are subject to systematic uncertainties, modeled via nuisance parameters θ, since the predictions themselves are affected by them. The construction of such TFs comes with important consequences: First, only ratios of predictions are taken directly from the simulation. Systematic effects similarly modifying processes A and B cancel out in the ratio and thus decrease the overall systematic uncertainty. The overall normalization of the $\mathrm{t\bar{t}}$ and V + jets processes is determined by data directly. The second main consequence is that no assumption is made on the shape of the hadronic recoil distribution in the SR. The reason for this is that the prediction in each bin regarding the $\mathrm{t\bar{t}}$ and $\mathrm{Z}(\nu\nu)$ + jets process ($n_{i,\mathrm{Z}(\nu\nu)}$) and $\mathrm{t\bar{t}}$ ($n_{i,\mathrm{t\bar{t}}}$) is left freely floating in the fit separately.

The following relations are considered in the statistical model, where the predictions of the $\mathrm{Z}(\nu\nu)$ + jets ($n_{i,\mathrm{Z}(\nu\nu)}$) and $\mathrm{t\bar{t}}$ ($n_{i,\mathrm{t\bar{t}}}$) background processes are left freely-floating in the fit and are therefore estimated from data directly:

- $n^{\mathrm{W}(\ell\nu)}_{i,SR} = \mathrm{TF}^{\mathrm{W}(\ell\nu)/\mathrm{Z}(\nu\nu)}_{i,\mathrm{SR/SR}} \cdot n^{\mathrm{Z}(\nu\nu)}_{i,SR}$
- $n^{\mathrm{Z}(\ell\ell)}_{i,CR(Z)} = \mathrm{TF}^{\mathrm{Z}(\ell\ell)/\mathrm{Z}(\nu\nu)}_{i,\mathrm{CR(Z)/SR}} \cdot n^{\mathrm{Z}(\nu\nu)}_{i,SR}$
- $n^{\mathrm{W}(\ell\nu)}_{i,CR(W)} = \mathrm{TF}^{\mathrm{W}(\ell\nu)/\mathrm{Z}(\nu\nu)}_{i,\mathrm{CR(W)/SR}} \cdot n^{\mathrm{Z}(\nu\nu)}_{i,SR}$
- $n^{\gamma}_{i,CR(\gamma)} = \mathrm{TF}^{\gamma/\mathrm{Z}(\nu\nu)}_{i,\mathrm{CR}(\gamma)/\mathrm{SR}} \cdot n^{\mathrm{Z}(\nu\nu)}_{i,SR}$
- $n^{\mathrm{t\bar{t}}}_{i,CR(\mathrm{t\bar{t}})} = \mathrm{TF}^{\mathrm{t\bar{t}}/\mathrm{t\bar{t}}}_{i,\mathrm{CR}(\mathrm{t\bar{t}})/\mathrm{SR}} \cdot n^{\mathrm{t\bar{t}}}_{i,SR}$
- $n^{\mathrm{t\bar{t}}}_{i,CR(W)} = \mathrm{TF}^{\mathrm{t\bar{t}}/\mathrm{t\bar{t}}}_{i,\mathrm{CR(W)/SR}} \cdot n^{\mathrm{t\bar{t}}}_{i,SR}$

These connections are illustrated in figure 7.10.

As described in section 7.2, all leptonic CRs are split according to the flavor of the lepton. Consequently, separate TFs are defined for each lepton flavor channel. Furthermore, all analysis regions are split according to whether the leading AK15 jet is top-tagged, see section 7.2.7. In order to conservatively account for effects that might be different between

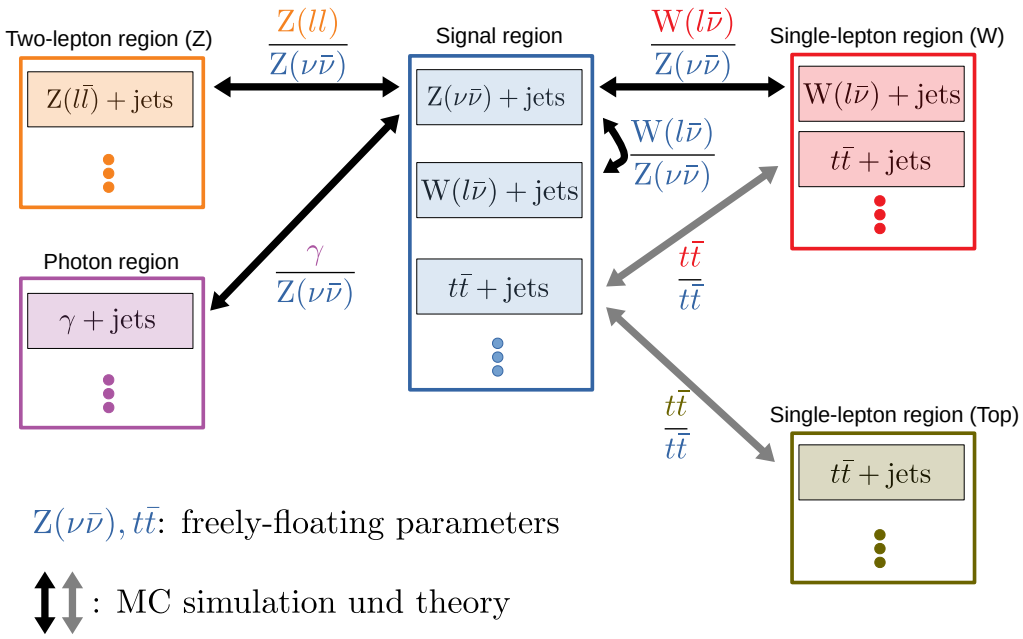

Figure 7.10: Schematic of the statistical model deployed in the hadronic mono-top analysis. Adapted from [126].

the pass and the fail region, the predictions on the $Z(\nu\nu)$ + jets and $t\bar{t}$ background are left floating independently between the pass and fail regions.

A consequence of this model is that contributions of all V + jets processes are varied in a coherent way during the maximum-likelihood estimation. In order to describe the observed data well, comparable prediction regarding their shape and normalization of the processes and, therefore, the TFs, across the analysis regions is required. Residual differences between the TFs are accounted for by varying nuisance parameters parameterizing the systematic uncertainties. Figure 7.11 shows the TFs for the pass and fail regions. First, a similar behavior is observed shape-wise when comparing the TFs for channels with different lepton flavors. The same is true when comparing TFs between the W boson and Z boson CRs. The normalization of the TFs differs when comparing cases that connect the $t\bar{t}$ and W boson CRs with the SR. This difference is expected since a low $W(\ell\nu)$ + jets background is expected in the $t\bar{t}$ CR, for instance. Additionally, the TFs connecting the Z boson CR with the SR are flat within their uncertainties as a function of the hadronic recoil p_T. Since the only difference is the decay mode of the Z boson, no shape differences are expected between the two processes. Furthermore, the actual value of the TFs in the range of 0.1 to 0.2 matches the ratio of branching fractions of the Z boson decaying into either a pair of leptons (BR $\approx$ 3.4 %) or a pair of neutrinos (BR $\approx$ 20 %). The TFs involving the $t\bar{t}$ background show a similar behavior across all analysis regions, indicating a similar shape of the $t\bar{t}$ background in all regions.

The TFs for all data-taking eras are shown in appendix M.

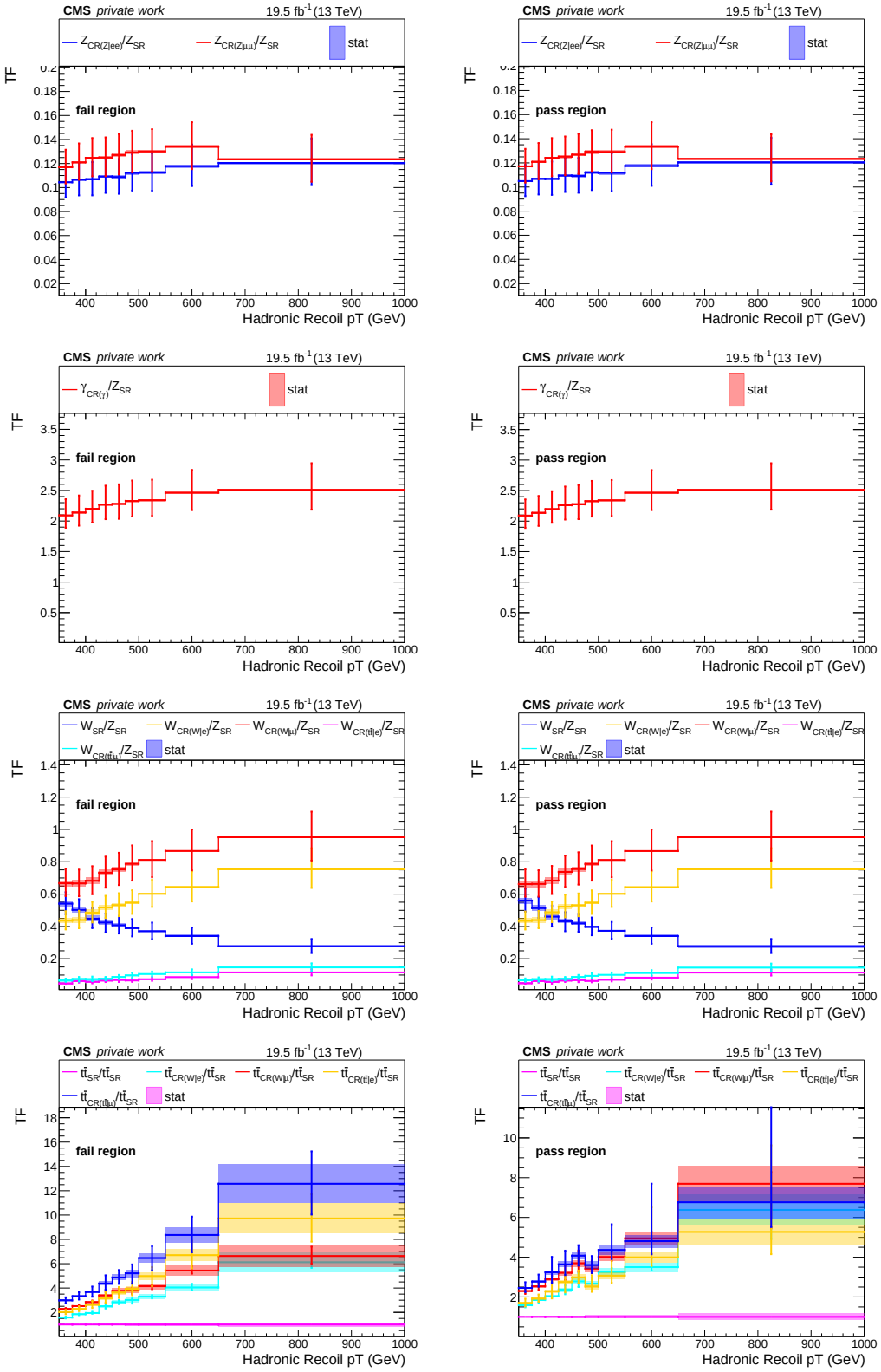

Figure 7.11: Transferfactors in the fail (left-hand side) and pass (right-hand side) regions of the 2016preVFP data-taking era as a function of the hadronic recoil p_{T}. The error bars represent the total uncertainty, whereas the shaded area corresponds to the uncertainty due to the limited statistical precision of the MC-simulated samples.

7.4 Validation of the statistical model

Analogously to the leptonic mono-top analysis, the statistical model of the hadronic mono-top analysis is validated in this section. For this validation, expected and observed constraints and pulls are inspected in addition to conducting saturated-model GoF tests. Again, the CMS `combine` tool [186] is employed for all statistical procedures and tests.

7.4.1 Expected constraints and pulls

The expected constraints and pulls in the hadronic mono-top analysis are assessed by considering Asimov datasets. Figure 7.12 shows the pulls and constraints on all nuisance parameters in the hadronic mono-top analysis for background-only and signal-plus-background fits on a signal-plus-background Asimov dataset in blue and red, respectively. Shown is the fit across all four data-taking eras. As expected, no pulls are observed when applying the signal-plus-background statistical model since all signal contributions are absorbed into the signal strength parameter. Correspondingly, nuisance parameters are pulled when deploying the background-only fit model, which is expected since the signal strength is fixed to zero. In general, several nuisance parameters are constrained, indicating that the statistical model is able to extract information on the corresponding systematic uncertainties. Consequently, the a-posteriori values of these nuisance parameters are reduced with respect to the a-priori ones. The systematic experimental uncertainties for which this effect is most prominent are related to the JECs, which is expected since the most important signature in the targeted final state consists of a AK15 jet as well as MET. Both of these final state objects are subject to JECs, motivating the sensitivity to those. Moreover, the a-priori uncertainty on the JEC source is estimated rather conservatively. Furthermore, uncertainties related to photons, such as the trigger SF and cross section uncertainty, are constrained. These uncertainties only affect the normalization of the $\gamma + \text{jets}$ background. Using the very pure photon-enriched CR, the normalization of the $\gamma + \text{jets}$ background can be determined to a high degree of precision and thus constrains the corresponding systematic uncertainties. Regarding theoretical modeling uncertainties, constraints are observed concerning the $\text{V} + \text{jets}$ processes, such as the variation of the factorization scale. Since the construction of dedicated CRs enriches the event selection in the various $\text{V} + \text{jets}$ processes, a potential sensitivity to such uncertainties is expected. When inspecting the maximum-likelihood fit result for the signal-plus-background model, several nuisance parameter pulls are observed. Some pulls are expected since the signal-plus-background model is not able to describe the Asimov dataset perfectly. The rather large pulls on the diboson and QCD cross section uncertainties can be explained by the fact that these processes also enter the SR. Since these processes are not determined by the TF model, they might be used by the fit to account for the signal contribution in the signal-plus-background Asimov dataset. Although this effect is not desired, no issue is observed, when using actual recorded data, as it will be shown later on. Consequently, the pulls and constraints look reasonable when deploying a signal-plus-background Asimov dataset.

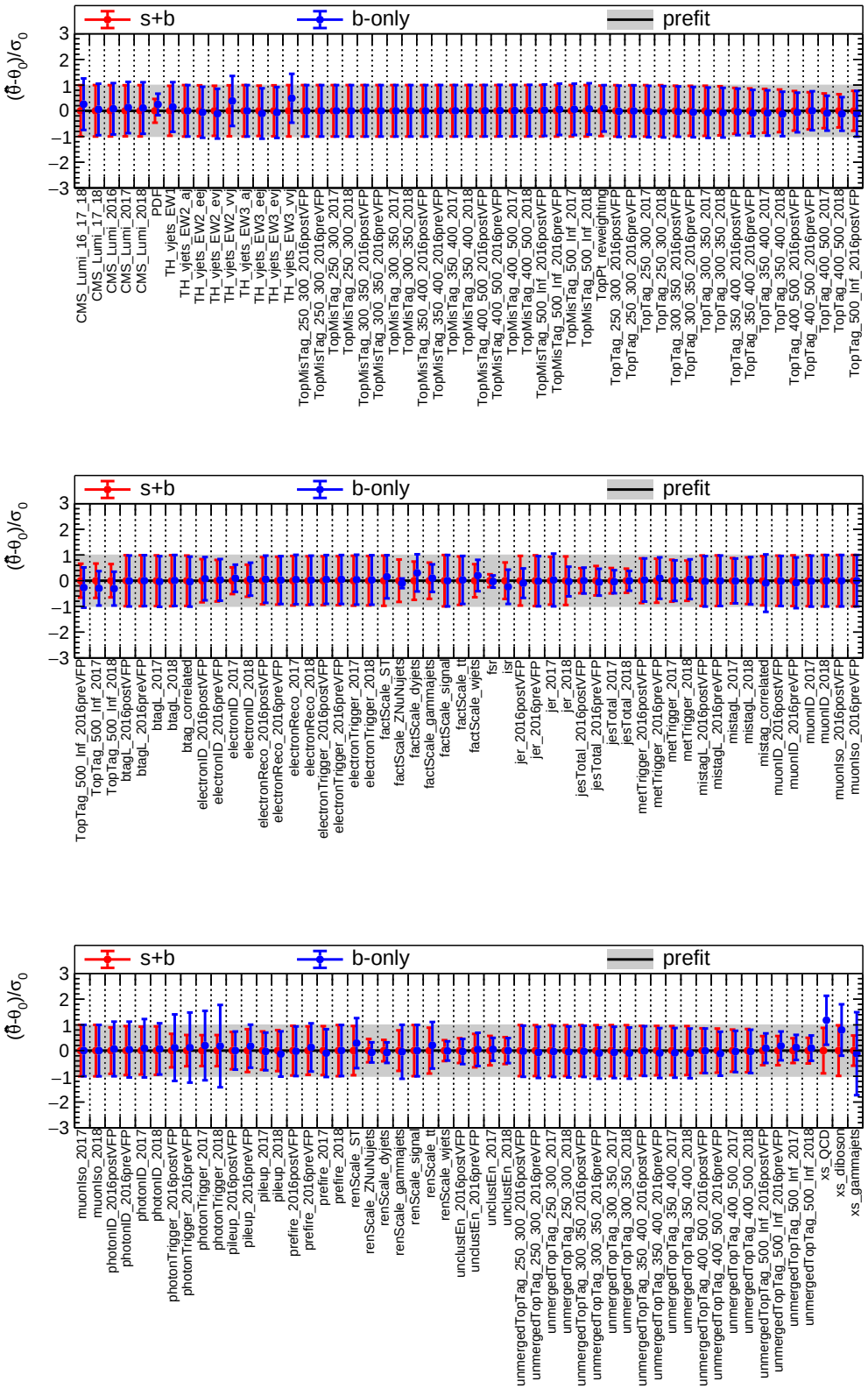

Figure 7.12: Pulls and constraints on nuisance parameters in the hadronic mono-top analysis for background-only and signal-plus-background Asimov datasets in blue and red, respectively, for the combination of all four data-taking eras.

7.4.2 Observed constraints and pulls

After validating that the statistical model works as expected based on Asimov datasets, the behavior of the statistical model is assessed on real measured data. In order to avoid a possible bias towards a potential signal contribution, a test in which only the CRs are considered is performed. Since the statistical TF model is built as described in section 7.3, the contributions of the $\mathrm{V}+\mathrm{jets}$ and $\mathrm{t\bar{t}}$ processes depend on the SR. Consequently, the SR is technically included in the fit. However, contributions from the SR are masked, which means any influence on the likelihood function is neglected. Moreover, since all bins with a potential signal contribution are masked, only the background-only model is evaluated. The pulls and constraints for this statistical test are shown in figure 7.13. A similar behavior regarding the constraints is observed as for the Asimov datasets. The nuisance parameters are now pulled away from their initial value in order to account for differences between the prediction and the observed data. However, the magnitude of most of the pulls is below one standard deviation, indicating that no significant adjustment to the a-priori modeling is required. Only a few nuisance parameters show sizable pulls, such as top-tagging related uncertainties. Since the definition of the pass and fail analysis regions directly depends on the top-tagging efficiency, these uncertainties can control the relative background predictions between the pass and fail regions. Consequently, pulls are observed to mitigate differences between the prediction and the observed data.

After inspecting the pulls and constraints for the background-only fit in the CRs, the SRs are included. In the scope of this thesis, only data taken in the year 2016 is considered for the derivation of the unblinded results. Figure 7.14 shows all nuisance pulls and constraints after performing the signal-plus-background and background-only fit on the observed data for all analysis regions considering the two 2016 data-taking eras combined. Two observations can be made. First, the pulls for the signal-plus-background do not vary significantly compared to the background-only fit. This similarity already indicates that no significant signal contribution is present in the data, as it will be confirmed by the observed significances discussed in section 7.6.1. Second, similar pulls are generally observed compared to figure 7.13, where the SRs are masked. This similarity indicates that the statistical model is able to describe the backgrounds in a similar way as when excluding the SRs emphasizing the importance of the CRs. No significant pulls or constraints are observed indicating, that the statistical model is also for a partial dataset able to describe the observed data in a similar way as for the full Run 2 dataset where the SRs were not considered.

7.4.3 Goodness-of-fit tests

After inspecting the nuisance parameter pulls, a more quantifying assessment is made to validate that the statistical model is able to describe the data. For this purpose, saturated-model GoF tests are performed as described in section 4.6. The first test aims to validate the modeling in the CRs. Again, since the statistical model relies on all analysis regions due to the TFs, the SR is technically included in the fit but masked in order not to influence the likelihood function. The p-values for the GoF tests are shown in table 7.2 for each data-taking era separately as well as for the combination of all four eras. In general, all the p-values are above the 5 % threshold commonly used to indicate good modeling of the data in the CRs.

Table 7.3 shows the p-values when including the SRs for the two 2016 data-taking eras consiered as well as for the combination of both. The p-values are lower than for the GoF tests where the SRs are masked, indicating minor modeling issues in the SRs. However, the p-values are still well above the 5 % threshold, indicating that the statistical model is able to describe the data.

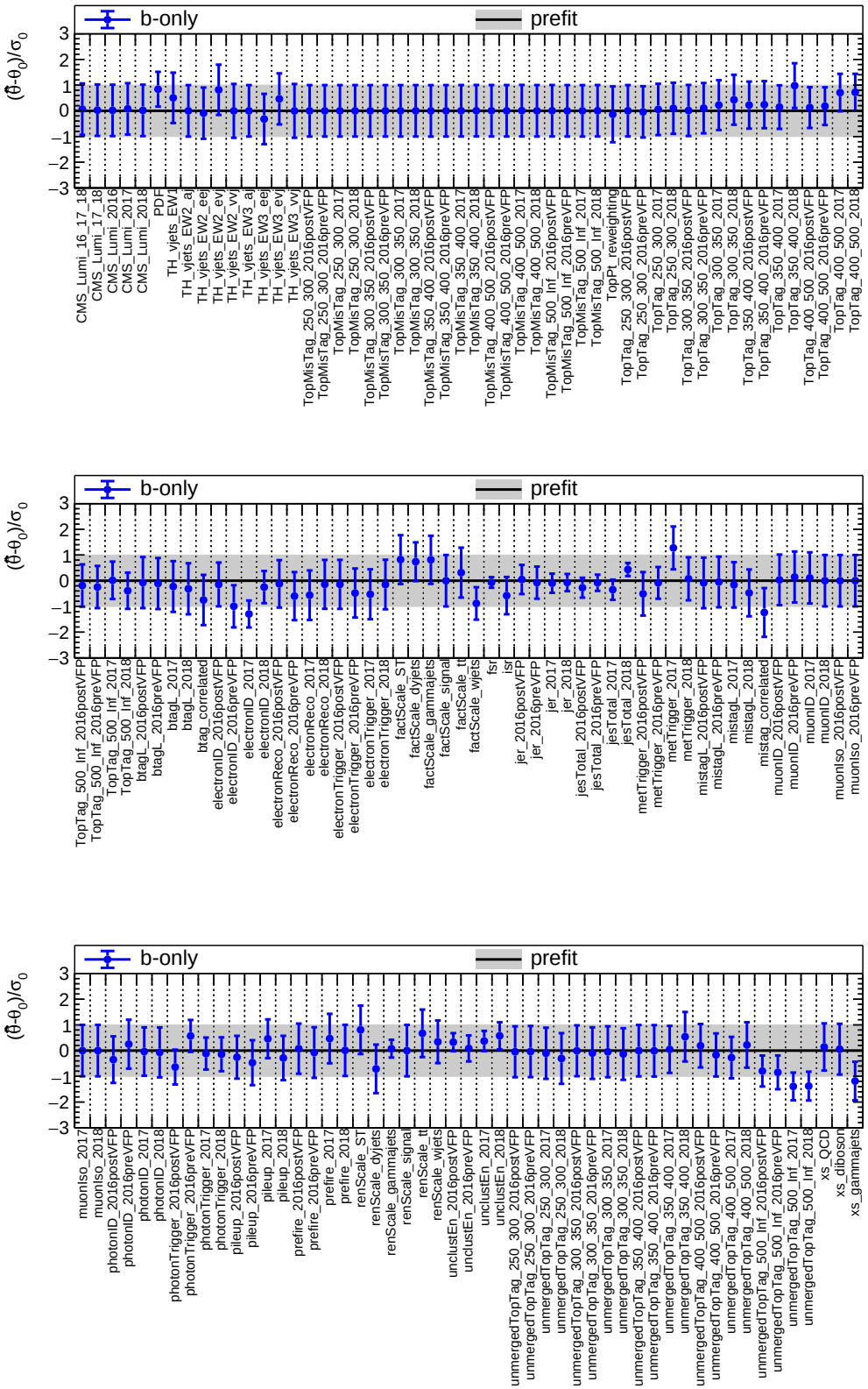

Figure 7.13: Pulls and constrains on nuisance parameters in the hadronic mono-top analysis for the background-only fit, where the SRs are masked for the combination across all four data-taking eras.

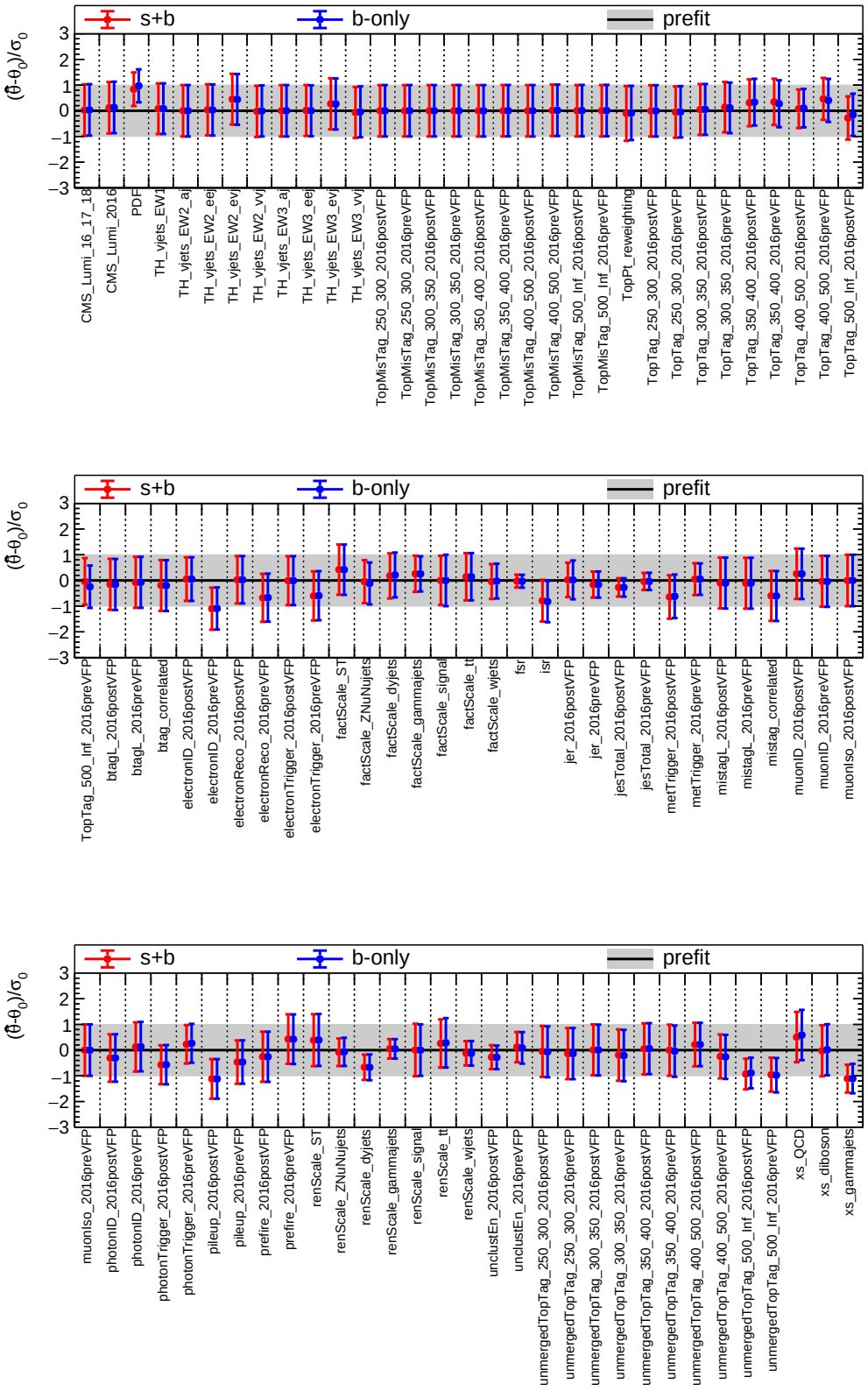

Figure 7.14: Unblinded pulls and constraints on nuisance parameters in the hadronic mono-top analysis for the signal-plus-background and background-only fit red and blue, respectively, for the combination of the two 2016 data-taking eras.

Table 7.2: P-values obtained in goodness-of-fit tests using a saturated model in the hadronic mono-top analysis for the background-only fit, without considering the SRs.

era	p-value
2016preVFP	0.70
2016postVFP	0.48
2017	0.40
2018	0.34
full Run 2	0.39

Table 7.3: P-values obtained in goodness-of-fit tests using a saturated model in the hadronic mono-top analysis including the SRs.

era	p-value
2016preVFP	0.41
2016postVFP	0.55
2016	0.13

7.5 Expected results

As for the leptonic mono-top analysis, the expected results of the hadronic mono-top analysis are presented before discussing the actual observations. Only a single mono-top mass hypothesis was considered for the statistical model validation discussed previously. The full range of available mono-top mass hypotheses is considered in the following. After discussing the expected significances, the expected exclusion limits are presented.

7.5.1 Expected significances

The statistical procedure to determine the expected significances is identical to the one used for the leptonic mono-top analysis as described in section 6.4.1. A likelihood ratio combined with Wilk's theorem is employed to extract a Gaussian significance. The expected significances are calculated using an a-posteriori signal-plus-background Asimov dataset and are shown in figure 7.15.

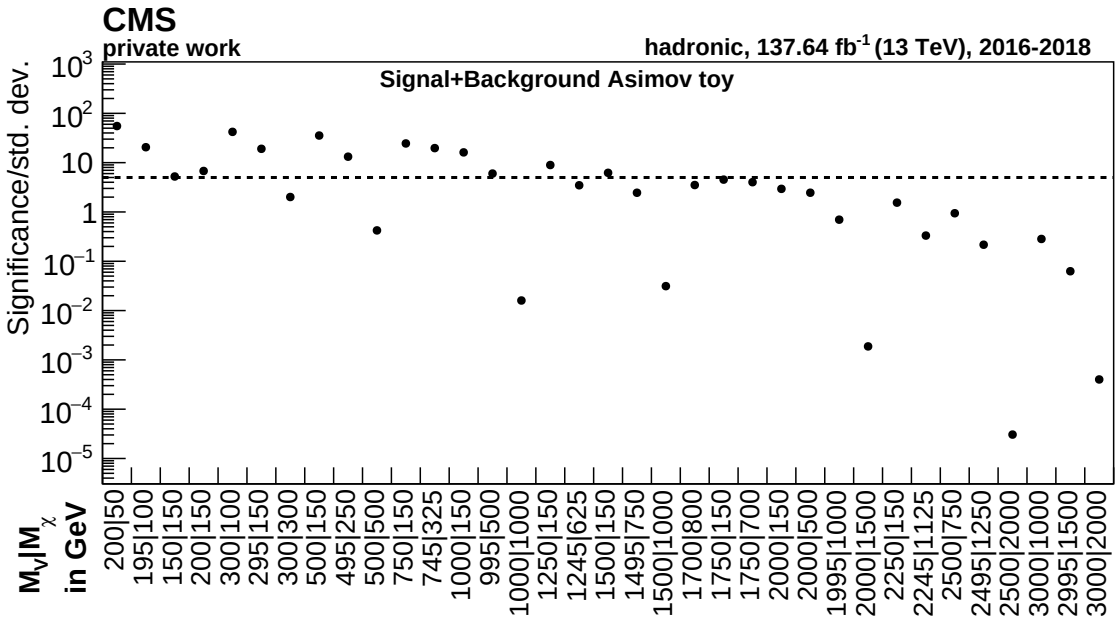

Figure 7.15: Expected significances for all mono-top mass hypotheses considered in units of Gaussian standard deviations in the combination of all four data-taking eras. The mass of the mediator is denoted by M_V and the mass of the DM candidate by M_χ. The $5\,\sigma$ discovery threshold is indicated by a dashed line.

Similarly to the leptonic mono-top analysis, the expected significances are above the $5\,\sigma$ discovery threshold for signal hypothesis involving low masses. Due to the relatively high cross sections of these signal hypotheses, a significant signal contribution is expected in the SR. The cross section is heavily suppressed if an off-shell decay of the hypothetical mediator into the two DM candidates is involved. Consequently, the expected significances are lower in these cases. Another important observation is that the expected significances decrease with increasing mediator mass. Since the cross section decreases with increasing mediator mass, the expected signal contributions also decrease.

7.5.2 Expected exclusion limits

If no signal is observed, parts of the mono-top parameter phase can be excluded. In this thesis, the targeted parameter space is given by the mediator and DM candidate masses M_V and M_χ, respectively. In order to assess the sensitivity reach of the analysis based on the

full Run 2 dataset, expected exclusion limits are calculated. Analogously to the leptonic mono-top analysis (see section 6.4.2), a-posteriori upper limits at a 95 % CL on the signal strength modifier μ are derived. Figure 7.16 shows the expected exclusion limits for the hadronic mono-top analysis in the combination of all four data-taking eras. The upper exclusion plot corresponds to a pure vector coupling scenario, whereas the lower figure shows the exclusion limits for a pure axial-vector coupling scenario.

Mediator masses of up to approximately 2.1 TeV are expected to be excluded for DM candidate masses of up to 900 GeV. Furthermore, the $\pm 1\,\sigma$ expected exclusion contours indicate that especially the lower mass regime is expected to be excluded with high confidence. A possible reason for this is again the relatively high cross sections of the signal hypotheses in this regime, resulting in significant signal contributions. No parameter space is expected to be excluded where the hypothetical mediator has an off-shell decay into the two DM candidates due to a strong suppression of the cross section.

Compared to the sensitivity of the leptonic analysis (figure 6.8) a significantly larger parameter space of the mono-top model is expected to be excluded. This increase in sensitivity can be attributed to the branching ratio of top quarks into hadrons being larger by a factor of approximately three, compared to the branching ratio of top quarks into leptons when only considering electrons and muons. Consequently, the expected signal yields are larger. Furthermore, the deployment of top-tagging techniques in conjunction with the advanced TF-based statistical model offers superior discrimination of the mono-top signal against the SM backgrounds.

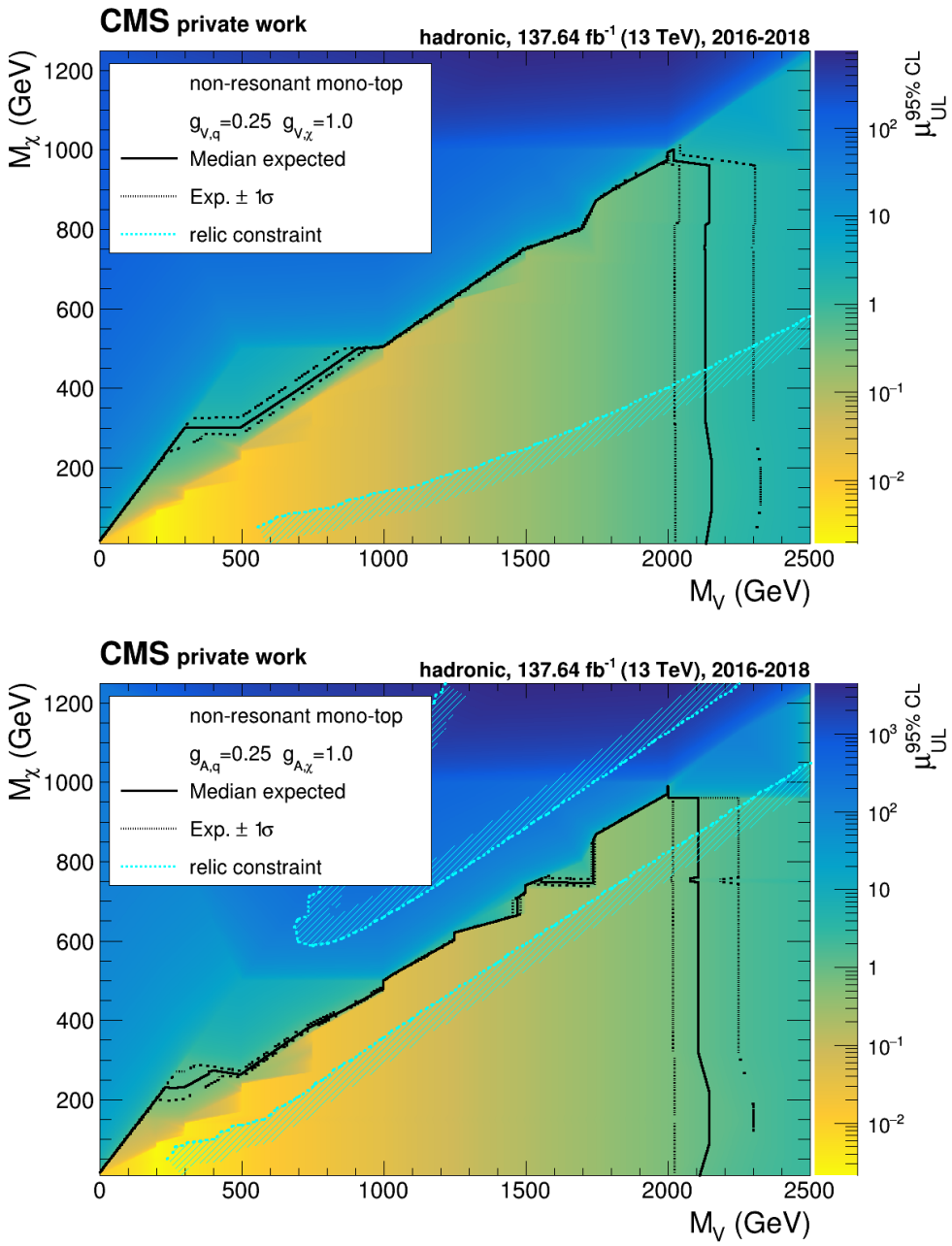

Figure 7.16: Expected upper limits on the signal strength modifier μ at a confidence level of 95 % for the vector mono-top model in the combination of all four data-taking eras in the plane of mediator and DM candidate masses M_V and M_χ, respectively. The solid black line indicates the contour, where the median, upper exclusion limit is equal to unity. The 68 % confidence interval on this contour is shown as a dashed black line. The area enclosed by the solid black line is parameter space expected to be excluded for the given mono-top model. The cyan, dashed exclusion line indicates a constraint on allowed masses in order to explain the measured DM relic density by the Planck Collaboration [30]. The upper exclusion plot corresponds to a pure vector coupling scenario, whereas the lower figure shows the exclusion limits for a pure axial-vector coupling scenario.

7.6 Observed results

After validating the statistical model and discussing the expected results of this analysis in the previous sections, the observed results are presented in this section. The observed results are presented in terms of the observed significances and the observed exclusion limits. As already mentioned, only a partial dataset corresponding to data taken in 2016 is considered in this thesis for the derivation of the observed results.

7.6.1 Observed significances

The observed significances are derived with respect to the background-only hypothesis for all available mass hypotheses. Figure 7.17 shows both the expected and observed significances in the combination of the two 2016 data-taking eras. It can be observed, that generally, all observed significances are sizable lower than the expected ones. Furthermore, all observed significances are way below the $5\,\sigma$ discovery threshold. Thus, no discovery or evidence is claimed, and parts of the mono-top parameter space are excluded in the following.

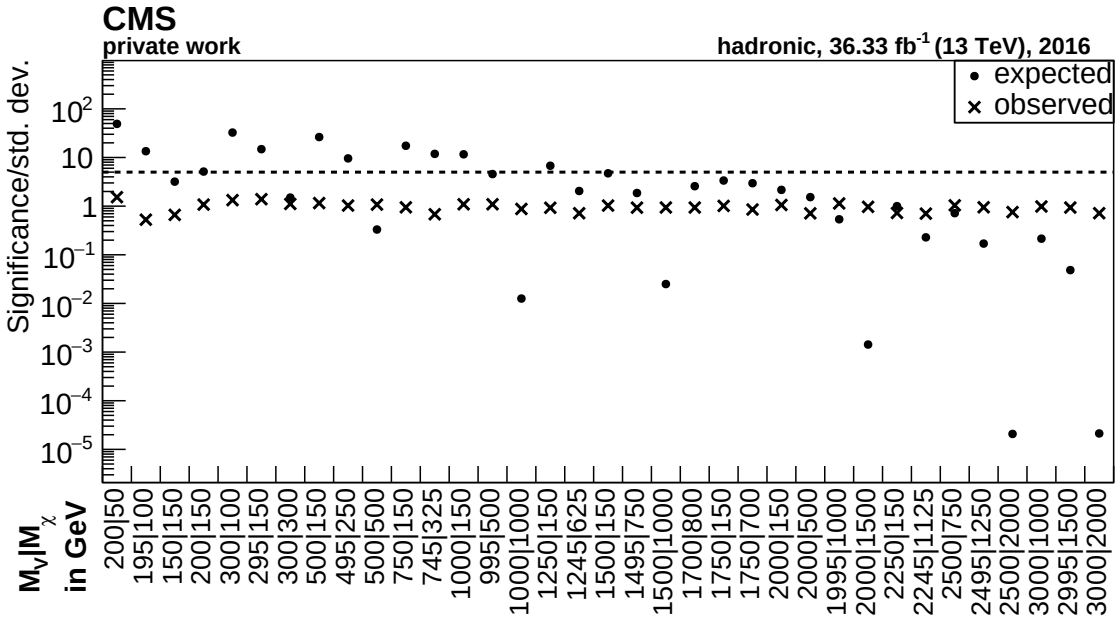

Figure 7.17: Observed significances for all considered mono-top mass hypothesis in units of gaussian standard deviations in the combination of the 2016 data-taking eras for the hadronic analysis. The expected significances shown as dots are compared to the observed significances shown as crosses. The mass of the mediator is denoted by M_V and the mass of the DM candidate by M_χ. A dashed line indicates the $5\,\sigma$ discovery threshold.

7.6.2 A-posteriori distributions

As seen in the previous section, no deviations from the background-only hypothesis are observed. Consequently, the measured data can be described by the statistical background-only model. The corresponding a-posteriori distributions for the 2016preVFP data-taking era are shown in figure 7.18 for the SR. In general, a good agreement is observed. When comparing the a-posterior magnitude of the systematic uncertainty with the a-priori one as in figure 7.7, for example, a sizable reduction of the systematic uncertainty is observed. As described earlier, systematic effects that are similar between the analysis regions are

canceling due to the construction of the TFs. Furthermore, the constraints on the nuisance parameter further reduce the magnitude of the systematic uncertainty. All analysis regions of all data-taking eras are shown in appendix N.

In summary, the data is described well by the statistical background-only model.

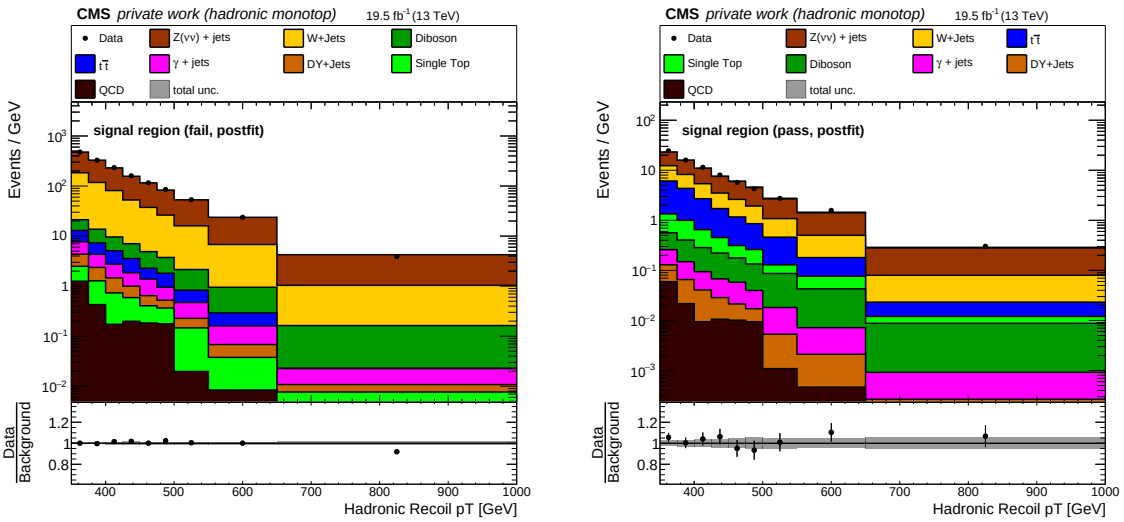

Figure 7.18: Distributions of the hadronic recoil p_{T} for all four data-taking eras after performing the maximum likelihood fit to the combined 2016 dataset. Shown are the fail (pass) SRs on the left (right)-hand side. The black points correspond to data, whereas the stacked histograms correspond to the background prediction from simulation for different processes. The lower pad in each plot shows the ratio of data to the total background prediction. The grey-shaded area corresponds to all considered uncertainties.

7.6.3 Observed exclusion limits

Due to the low observed significances, no discovery or evidence is claimed, as shown in the previous section. Consequently, this analysis is able to restrict the allowed parameter space of the mono-top model in the plane of the mediator and DM candidate masses m_{V} and m_{χ}, respectively. Figure 7.19 shows the expected exclusions, where the observed exclusion contour is overlaid in red. Thus, the enclosed parameter space is excluded at a confidence level of 95 %. The observed exclusion contour is almost compatible with the expected one within one gaussian standard deviation validating that the statistical model is able to describe the data. The observed exclusion contour is shifted towards lower m_{V} and m_{χ} values compared to the expected one due to a overfluctuation of the data which was also seen in the leptonic analysis (see figure 6.11). Mediator masses up to 2 TeV for DM candidate masses up to 1 TeV are excluded due to this analysis.

When considering each data-taking era separately, the exclusion limits are shown in appendix P with a similar behavior as the combination of both 2016 eras.

A previous iteration of this analysis, in which the full Run 2 data was analyzed, was able to exclude masses of the hypothetical mediator up to 2 TeV for DM candidate masses up to 500 GeV [126]. Consequently, approximately the same sensitivity is achieved in this analysis, although only approximately a quarter of the full Run 2 data was used. The main reason for this improvement is using a superior top-tagging algorithm in conjunction with considering the fail region in the statistical model. The enhanced efficiency of the `ParticleNet`

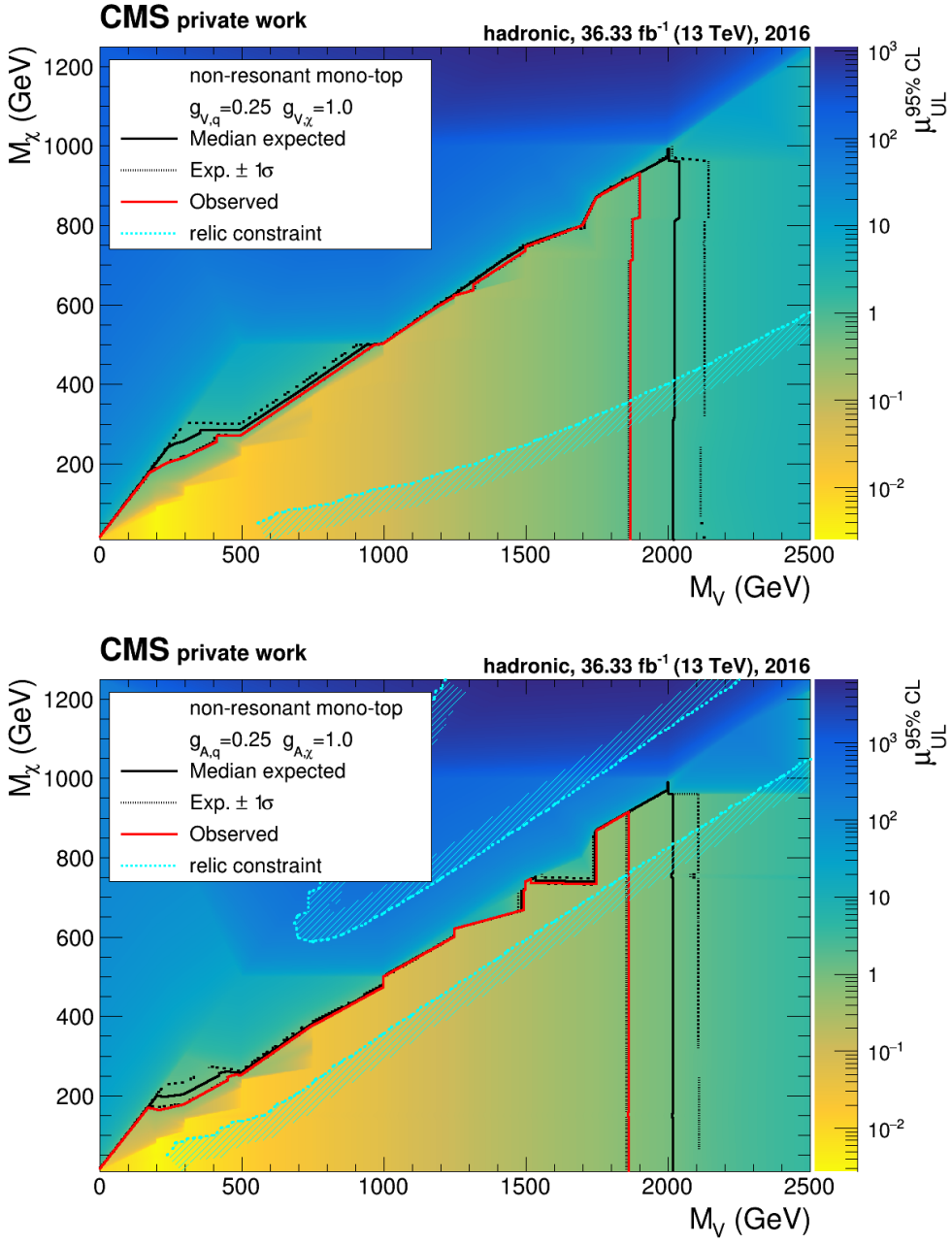

Figure 7.19: Upper limits on the signal strength modifier μ at a confidence level of 95 % for the vector mono-top model in the combination of all four data-taking eras in the plane of mediator and DM candidate masses M_V and M_χ, respectively. The solid black line indicates the contour, where the median, upper exclusion limit is equal to unity. The 68 % confidence interval on this contour is shown as a dashed black line. The area enclosed by the solid black line is parameter space expected to be excluded for the given mono-top model. The red line indicates the contour, where the observed upper limit is equal to unity, excluding the enclosed parameter space. The cyan, dashed exclusion line indicates a constraint on allowed masses in order to explain the measured DM relic density by the Planck Collaboration [30]. The upper exclusion plot corresponds to a pure vector coupling scenario, whereas the lower figure shows the exclusion limits for a pure axial-vector coupling scenario.

algorithm increases the signal-to-background ratio in the pass region. Furthermore, by adding the fail region, the statistical model is able to constrain the SM backgrounds to a greater extent due to the increased number of background events.

8 Combined Mono-top Analysis

In order to gain the most sensitivity, a combined analysis of the leptonic (chapter 6) and hadronic (chapter 7) channels is performed. The hadronic analysis channel excludes a phase space region of the mono-top model approximately 60 % larger than the leptonic analysis channel. Since the hadronic mono-top analysis deploys a more sophisticated statistical model, in which the normalizations, as well as the shapes of the main backgrounds, are estimated directly from data, a more precise estimation of the SM backgrounds is expected. Furthermore, the usage of state-of-the-art multivariate top-tagging techniques offers a more powerful enhancement of potential signal contributions. In addition, the BR of the top quark into a fully hadronic final state is approximately a factor three higher than the one into a final state containing an electron or muon, resulting in a higher signal efficiency. Therefore, a higher sensitivity is expected in the hadronic analysis, which is also reflected in the signal-to-background ratio being higher by approximately a factor 24 in the hadronic SRs. Nonetheless, a combination of both channels adds the value of effectively increasing the signal selection efficiency.

8.1 Statistical model

A potent property of using a maximum likelihood fit is that the statistical model can be easily extended to include additional channels. This feature enables the combination of the leptonic and hadronic analysis by multiplying the likelihood functions of both channels

$$\mathcal{L} = \mathcal{L}_{\text{lep}} \times \mathcal{L}_{\text{had}} \,. \tag{8.1}$$

Subsequently, all statistical methods are applied to the combined likelihood function. Since the nuisance parameters parameterize the same source of uncertainties in both analysis channels, they are fully correlated between the two likelihood functions. This correlation scheme implies that the effect of the corresponding uncertainties on the observed distributions is similar in both analysis channels. However, it should be noted, that the background estimation is different in both channels. The contributions of the main backgrounds ($\mathrm{t\bar{t}}$, $\mathrm{V} + \text{jets}$) are estimated directly from data in the hadronic analysis channel, whereas the background predictions are taken directly from MC simulations in the leptonic analysis channel. This difference might introduce the need of a more sophisticated statistical model in the combination of both channels which is not in the scope of this thesis.

To validate the statistical model only the CRs are considered first before including the SRs. In both cases the pulls and constraints of the parameters are inspected in addition to performing GoF tests using the saturated model.

8.1.1 Validation of statistical model in control regions

As for the separate analysis channels, the SRs are masked in order to not introduce any bias towards a potential signal contribution. The pulls and constraints of the nuisance parameters are shown in figure 8.1 for the background-only model using the full Run 2 data. In general, the behavior of the pulls is similar to the separate analysis channels. However, nuisance parameters that enter both analysis channels are constrained to a higher degree than before. An example is the JER-related nuisance parameters. Since many categories containing jets enter the statistical model, an increased sensitivity to these uncertainties is observed. Theory uncertainties related to the renormalization and factorization scales of the main backgrounds are also constrained to a higher extent. Especially uncertainties related to the $t\bar{t}$ and $W + \text{jets}$ show this behavior. Since these processes are major backgrounds in both analysis channels, combining the channels increases the sensitivity to this uncertainties.

In order to validate the statistical model further, GoF tests are performed. The p-values of this GoF test are shown in table 8.1. All p-values are well above the commonly considered 5 % threshold, indicating that the statistical model is able to describe the observed data in the combination of the two analysis channels in the CRs.

Table 8.1: P-values obtained in goodness-of-fit tests using a saturated model in the CRs for the four data-taking eras separately as well as for the full Run 2 combination.

era	p-value
2016preVFP	0.30
2016postVFP	0.62
2017	0.24
2018	0.50
full Run 2	0.28

8.1.2 Validation of statistical model in all analysis regions

After validating the statistical model in the CRs, the SRs are included for both 2016 data-taking eras and the statistical model is validated further. The pulls and constraints of the nuisance parameters are shown in figure 8.2 for the background-only and signal-plus-background model using the combined 2016 data in red and blue, respectively. In general, the behavior of the nuisance parameters is similar to the case in which the SRs are excluded, indicating that the CRs are able to constrain the major backgrounds. However, when performing the saturated-model GoF tests a low p-value is observed in the combination of both 2016 data-taking eras. One possible reason for this behavior is that the naive combination of the likelihood functions of the hadronic and leptonic analysis channels is not sufficient, leading to a poor description of the data when including the SRs. A possible solution would be to study a more sophisticated combination of the two analysis channels regarding the correlation scheme of the nuisance parameters, which could lead to more freedom in the maximum likelihood fit. Due to this issue, when including the SRs in the combination of the leptonic and hadronic analysis channels, further scrutiny of the statistical model is required, which is beyond the scope of this thesis. Therefore, only expected results are discussed in the following.

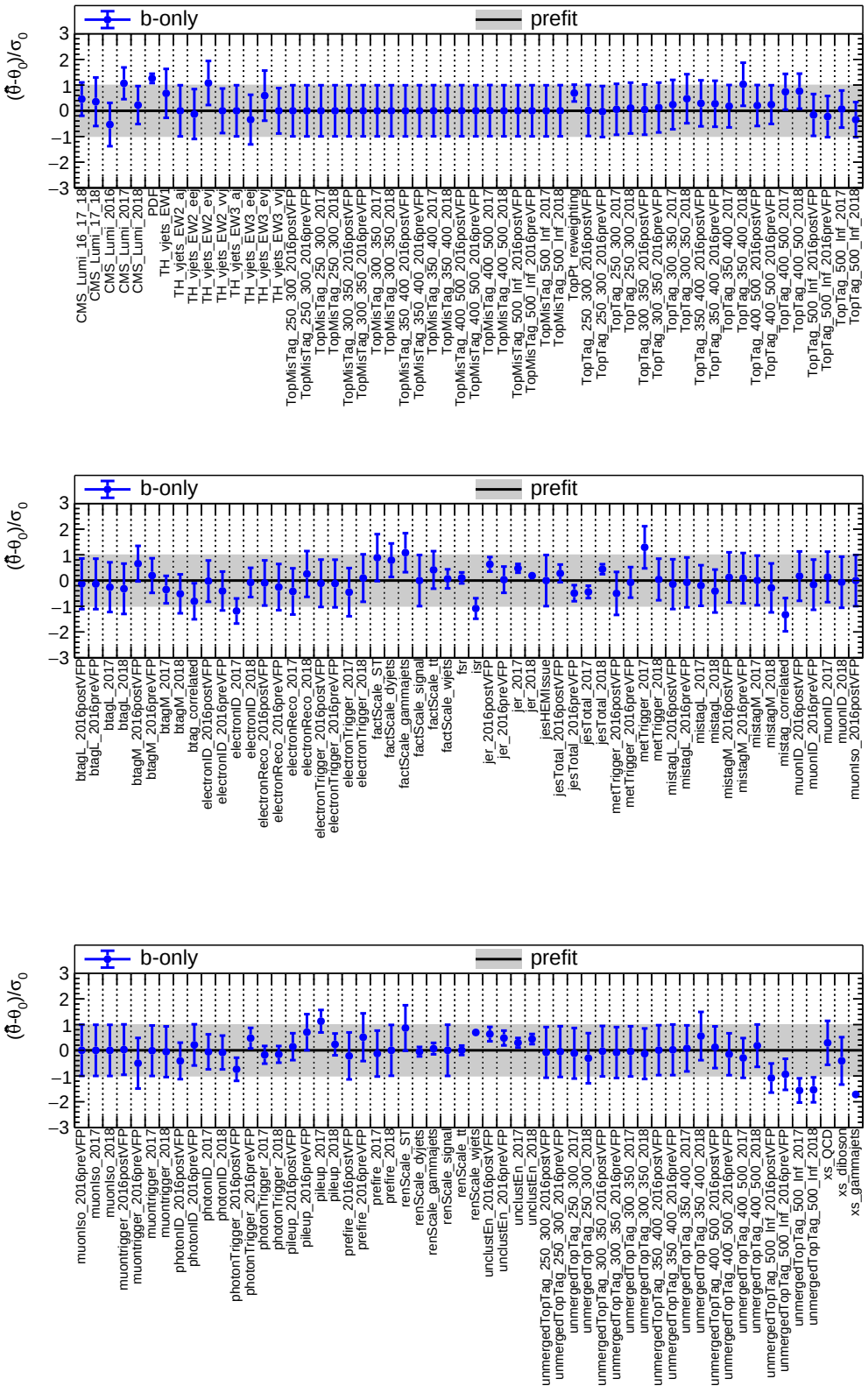

Figure 8.1: Unblinded pulls and constraints on nuisance parameters in the combined mono-top analysis for the background-only fit without considering the SRs, for the combination across all four data-taking eras.

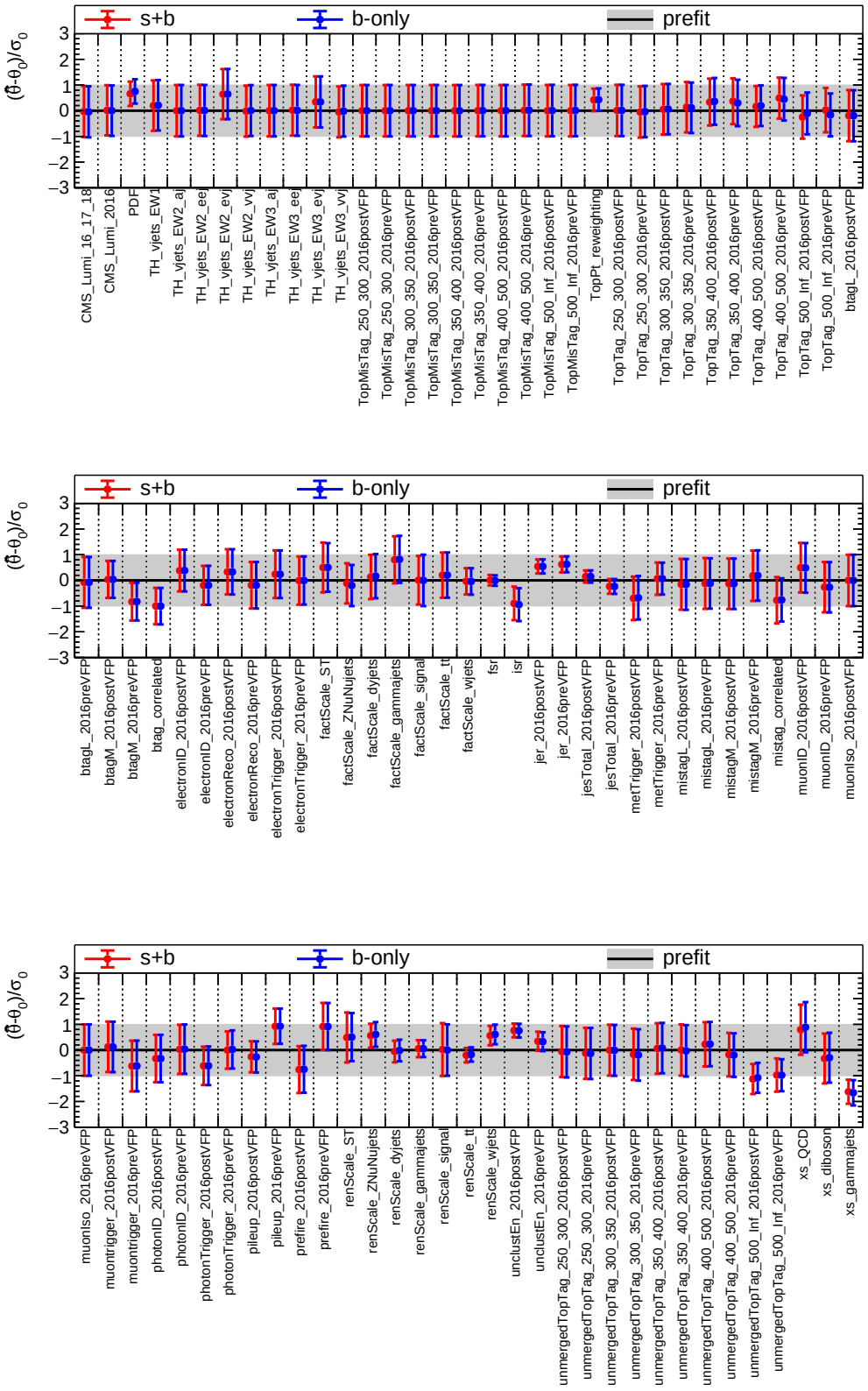

Figure 8.2: Unblinded pulls and constraints on nuisance parameters in the hadronic mono-top analysis for the signal-plus-background and background-only fit red and blue, respectively, for the combination of the two 2016 data-taking eras and both analysis channels.

Table 8.2: P-values obtained in goodness-of-fit tests using a saturated model in all analysis regions for the two 2016 data-taking eras separately as well as for the 2016 combination.

era	p-value
2016preVFP	0.15
2016postVFP	0.58
2016	0.04

8.2 Expected results

The combined analysis results are presented as exclusion limits at a 95 % confidence level in the plane of the mediator and DM candidate mass. The expected exclusion contours are shown in figure 8.3 for the combination of all four data-taking eras as well as the individual analysis channels. Interestingly, no additional phase space region is expected to be excluded when combining the two analysis channels. Only the uncertainty on the expected exclusion regions is reduced.

The general analysis sensitivity is limited by the sharp decline of the signal cross sections as a function of the mediator and DM candidate mass, as discussed in section 5.3.2.3. The collection of larger datasets at the LHC would potentially offer the possibility to extend the analysis sensitivity to higher mediator masses. In addition, the sensitivity of the leptonic analysis channels could be enhanced by employing a more sophisticated analysis method. For example, state-of-the-art multivariate techniques could be used to potentially outperform the current signal-to-background discrimination of the transverse mass.

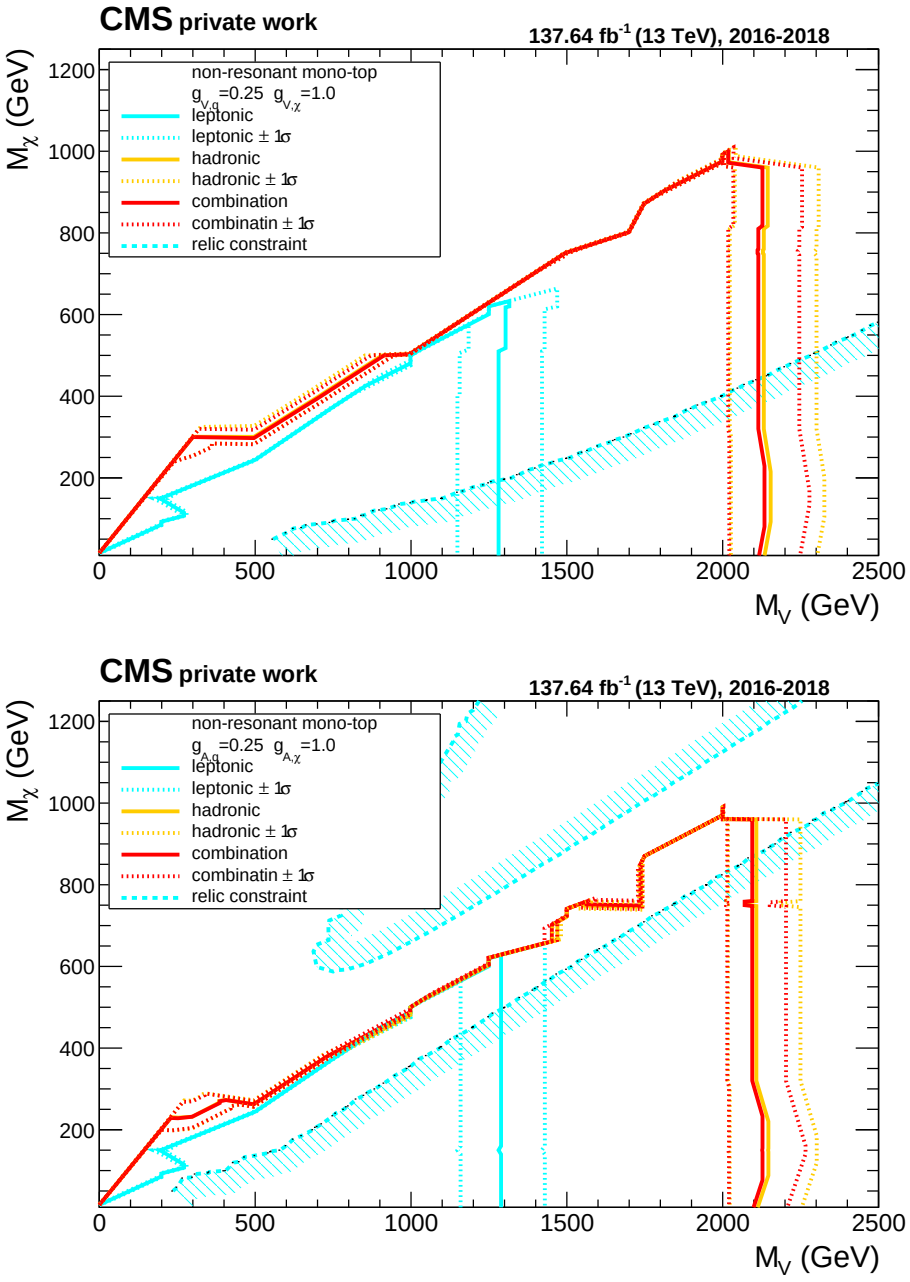

Figure 8.3: Expected exclusion contours at a confidence level of 95 % for the vector (top) and axial-vector (bottom) mono-top model in the combination of all four data-taking eras in the plane of mediator and DM candidate masses M_V and M_χ. The cyan (orange) lines depict the expected exclusion contours for the leptonic (hadronic) analysis channel, whereas the red line corresponds to the expected results for the full combination. The blue, dashed exclusion line indicates a constraint on allowed masses in order to explain the measured DM relic density by the Planck Collaboration [30].

9 Conclusion and outlook

One of the major unsolved puzzles of science is the nature of Dark Matter. In this thesis, a search for Dark Matter produced in association with a top quark was performed in hadronic and leptonic final states. The analysis is based on proton-proton collision data recorded by the CMS experiment at the Large Hadron Collider (LHC) at a center-of-mass energy of 13 TeV. Expected results are presented assuming the full Run 2 dataset, which corresponds to an integrated luminosity of 137 fb. In addition, observed results are obtained based on data collected in the year 2016, equivalent to an integrated luminosity of $36\,\mathrm{fb}^{-1}$.

A simplified model as an extension of the Standard Model of particle physics (SM) is considered, in which two new particles are introduced, a bosonic mediator and a fermionic Dark Matter candidate. The final state of the signal model is characterized by the presence of a top quark and Dark Matter candidate particles. This signature is established via a flavor-changing neutral current interaction by the new mediator at leading order. Since the Dark Matter particles are not expected to interact with the detector, they lead to a momentum imbalance in the event called missing transverse energy. There is no leading order SM process that leads to an event signature consisting of a top quark and missing transverse energy.

Top quarks can decay either fully hadronically or leptonically. In order to capture the full signal potential, both decay modes are considered in two separate analysis channels.

In the leptonic analysis channel, a kinematic variable, the transverse mass, is used to discriminate between signal and background events. In order to constrain the main backgrounds ($\mathrm{t\bar{t}}$ and $\mathrm{W}+$jets production), dedicated control regions are defined using b-jet identification techniques. For the 2016 dataset, no significant excess of events with respect to the SM expectation is observed and exclusion limits are set to restrict the allowed parameter space of the mono-top model. Dark Matter candidate masses up to 500 GeV are excluded for mediator masses up to approximately 1 TeV at a 95 % confidence level. When assuming the full Run 2 dataset, mediator masses up to 1.3 TeV are expected to be excluded.

For the hadronic analysis channel, the transverse momentum of the hadronic recoil is used to extract potential signal contributions. The hadronically decaying top quark is expected to recoil against the new mediator and therefore experience a large Lorentz boost leading to a collimation of its decay products. Consequently, large-radius anti-k_T jets with a radius parameter of 1.5 are used to reconstruct the decay products in a single object which is used

as a proxy for the top quark. A significant gain in sensitivity is achieved by identifying large-radius jets as coming from a top quark decay via state-of-the-art multivariate top-tagging techniques. Due to the limited efficiency of the top-tagging algorithm, the production of a Z boson decaying into a pair of neutrinos in association with jets remains as an irreducible background. Similarly, due to the limited selection efficiency of leptons, semi-leptonic $t\bar{t}$ production also contributes to the background. Therefore, the precise determination of these SM backgrounds is essential. For this purpose, a sophisticated statistical model is considered, which utilizes several CRs defined via the presence of photons, charged leptons and b-tags. By establishing a relation between the hadronic recoil in the signal and control regions via transfer factors, the shape and normalization of the main SM backgrounds are determined in situ. As for the leptonic analysis channel, no significant deviations from the SM expectation are observed using the 2016 dataset and the allowed parameter space of the mono-top model is restricted. Dark Matter candidate masses up to 900 GeV are excluded for mediator masses up to approximately 1.8 TeV at a 95 % confidence level. Mediator masses up to 2 TeV are expected to be excluded based on the full Run 2 dataset. The hadronic analysis using the 2016 dataset presented in this thesis already exceeds the sensitivity achieved in a previous iteration of this analysis, in which the full Run 2 dataset was used [126]. The reasons for this improvement are manifold, such as an improved top-tagging algorithm with a dedicated calibration procedure, the inclusion of events in which the large-radius jet is not top-tagged and the usage of simulation samples at NLO perturbative order in QCD.

When comparing the expected sensitivities of the two analysis channels, the hadronic channel is significantly more sensitive. This is because the hadronic branching ratio of the top quark decay is larger than the leptonic one, leading to a higher signal efficiency in the first place. Also, the usage of powerful top-tagging techniques increases the signal selection purity significantly. In addition, the more sophisticated statistical model used in the hadronic analysis allows for a more precise determination of the SM backgrounds. The sensitivity of the leptonic analysis channel could potentially be improved by using multivariate techniques to better discriminate the mono-top signal from the SM backgrounds as currently done with the transverse mass. Moreover, the normalization of the main backgrounds could also be determined directly from data instead from simulation as done presently.

In order to potentially gain the most sensitivity, a straightforward combination of the two analysis channels was studied in this thesis based on the full Run 2 expectation. However, the excluded parameter space of the mono-top model is not increased in the combination but is entirely covered by the hadronic analysis channel. Since the expected signal cross sections are falling very sharply with increasing mediator mass, the number of expected signal events limits the analysis sensitivity. Consequently, further improvements in the analysis techniques or even larger datasets are required in the future to further constrain the parameter space of the mono-top model. In addition, a higher center-of-mass energy at the LHC is expected to be available in Run 3 of the LHC and potential future colliders, which offers the opportunity to probe even higher mass regimes.

To summarize, the search for Dark Matter produced in association with a top quark presented in this thesis provides a powerful way to probe physics beyond the Standard Model at the LHC and leads to strong constraints on the allowed parameter space of the mono-top model already with a partial dataset. The full Run 2 dataset is expected to be analyzed in the near future, increasing the expected sensitivity even further. In addition, the potential improvements in the leptonic analysis channel, such as an in situ determination of the SM background normalizations, offer a perspective to narrow down the allowed parameter space of the non-resonant mono-top model.

In a broader sense, generic MET+X searches at the LHC are approaching a sensitivity limit underpinned by the fact that even an analysis targeting a more generic jet+$\not{E}_{\mathrm{T}}$ final state is also only able to exclude a similar mediator mass range in the order of 2 TeV [188] as the mono-top analysis presented in this thesis. In addition, direct detection experiments are reaching higher and higher sensitivities as well. Ultimately, the allowed parameter space of generic WIMP Dark Matter models is already and will be even more in the future restricted. Consequently, if Dark Matter is indeed a WIMP, the upcoming years of data-taking will be crucial to detect WIMP Dark Matter.

Acronyms

AK Anti-k_{T}. 23, 24, 43

ALP axion-like particle. 12, 13

BR branching ratio. 45, 47, 49, 51, 97, 122, 137

BSM Beyond the Standard Model. 1, 2, 5, 13, 19, 55

BTV b Tag & Vertexing. 70, 73, 84

CERN European Organization for Nuclear Research. 1, 17

CHS charged hadron subtraction. 24, 69

CKM Cabibbo-Kobayashi-Maskawa. 8, 37

CL confidence level. 32, 33, 131

CMB cosmic microwave background. 1, 10–12

CMS Compact Muon Solenoid. 1, 2, 17, 19–22, 39, 40, 52, 58, 60–62, 66–68, 80, 86, 91, 109, 124, 143

CR control region. 61, 62, 64, 67, 68, 88, 89, 91, 93–95, 105–109, 111–117, 119–122, 124, 126, 138, 144, 173, 174, 177, 178, 181–186, 197–216, 219–225, 232–238

DGLAP Dokshitzer-Gribov-Lipatov-Altarelli-Parisi. 14

DM Dark Matter. 1, 2, 5, 9–14, 17, 24, 25, 27, 44–51, 55, 85–88, 90, 91, 95, 97–100, 102, 103, 105, 110, 118, 130–135, 141, 142, 171, 172, 175, 176, 179, 180, 191–198, 202, 203, 207, 208, 239–242

DY Drell-Yan. 52

ECAL electromagnetic calorimeter. 21, 23, 60, 66–68, 89

EFT effective field theory. 13, 14

EWK electroweak. 7–9, 53, 57–59, 80–82, 170

FCNC flavor-changing neutral current. 2, 44–46

FSR final-state radiation. 80, 81, 91, 93, 170

GIM Glashow–Iliopoulos–Maiani. 44

GoF goodness-of-fit. 29, 31, 33, 93, 95, 124, 126, 138

HCAL hadron calorimeter. 21, 23, 83

HF heavy-flavor. 7, 70, 169

HLT high-level trigger. 22, 61–65, 74, 83, 89, 108, 109, 111

IP impact parameter. 39

ISR initial-state radiation. 80, 81, 170

JEC jet energy correction. 69, 78, 83, 91, 93, 124

JER jet energy resolution. 69, 83, 138, 169, 170

JES jet energy scale. 69, 78, 83, 169, 170

L1 level 1. 22, 60, 169

LF light-flavor. 7, 40, 42, 70, 85, 167–169

LHC Large Hadron Collider. 1, 2, 17, 19–21, 44–46, 55, 141, 143–145

LINAC Linear Accelarator. 17

LO leading order. 55, 57

LSTM long short-term memory. 40

MC Monte Carlo. 15, 58, 59, 64, 69, 70, 76, 78, 82–84, 89, 90, 97, 110, 112, 113, 115–120, 123, 137, 227–230

ME matrix element. 52, 81

MET missing transverse energy. 2, 24, 27, 37, 44, 52, 55, 60–62, 64, 69, 78, 84–86, 88, 105–109, 111, 124

MLE maximum likelihood estimator. 30, 78, 91, 97

MLP multilayer perceptron. 41

MPI multiple parton-parton interactions. 15

MVG multivariate Gaussian. 75

NLO next-to-leading order. 15, 47, 49, 52, 53, 55, 57–59, 80, 81, 144

NNLO next-to-next-to-leading order. 58, 59, 80, 81

p.d.f. probability density function. 29, 30, 32–34, 84, 91

PAG Physics Analysis Group. 58, 82

PBS Proton Synchrotron Booster. 17

PDF parton distribution function. 14, 15, 45, 80, 81, 170

PF particle-flow. 22, 23, 39, 41, 62, 66, 74, 78

POG Physics Object Group. 58, 60, 62, 67, 68, 70, 73, 82–84

PS parton shower. 15, 52, 55, 58, 59, 80, 81, 170

PU pileup. 20, 24, 58, 61, 68, 69, 83, 169

PUPPI pileup per particle identification. 24, 69

QCD quantum chromodynamics. 7, 12, 14, 15, 23, 37, 41–43, 47, 49, 52, 53, 55, 57–59, 69, 73–76, 78–81, 109, 114, 124, 144, 169, 170

QFT quantum field theory. 5

ReLU rectified linear unit. 41

ROC receiver operating characteristic. 73

ROCAUC receiver operating characteristic area under curve. 73

SD SoftDrop. 43

SF scale factor. 55, 58, 62–70, 73, 82, 83, 124, 163–166

SM Standard Model of particle physics. 1, 2, 5, 7–9, 11, 13, 14, 19, 24, 25, 27, 44, 45, 47, 49, 55, 85, 88, 89, 105, 106, 108, 109, 131, 136, 137, 143, 144

SPS Super Proton Synchrotron. 17

SR signal region. 61, 62, 85, 88–91, 95, 101, 105, 107–111, 114, 117, 118, 121, 122, 124, 126, 127, 129, 130, 133, 134, 137–139, 171, 172, 175, 176, 179, 180, 197, 198, 202, 203, 207, 208, 217, 218, 231

SV secondary vertex. 39, 41

TF transfer factor. 107, 121, 122, 124, 126, 131, 134

TnP tag and probe. 62, 67, 73

VEV vacuum expectation value. 8, 9

WIMP weakly interacting massive particle. 11–13, 24–26, 145

WP working point. 40, 66–68, 70, 73, 78, 88, 109, 111, 114, 117, 169

Bibliography

[1] M. D. Schwartz. *Quantum Field Theory and the Standard Model*. Cambridge University Press, Dec. 2013. DOI: 10.1017/9781139540940.

[2] M. E. Peskin. *An Introduction To Quantum Field Theory*. CRC Press, May 2018. DOI: 10.1201/9780429503559.

[3] D. Griffiths. *Introduction to elementary particles*. Weinheim: Wiley-VCH, 2004. ISBN: 978-3-527-61847-7.

[4] R. L. Workman et al. "Review of Particle Physics". In: *PTEP* 2022 (2022), p. 083C01. DOI: 10.1093/ptep/ptac097.

[5] E. Fermi. "Zur Quantelung des idealen einatomigen Gases". In: *Zeitschrift für Physik* 36.11 (Nov. 1926), pp. 902–912. ISSN: 0044-3328. DOI: 10.1007/BF01400221.

[6] F. Englert and R. Brout. "Broken Symmetry and the Mass of Gauge Vector Mesons". In: *Physical Review Letters* 13 (9 Aug. 31, 1964), pp. 321–323. DOI: 10.1103/PhysRevLett.13.321.

[7] P. W. Higgs. "Broken Symmetries and the Masses of Gauge Bosons". In: *Physical Review Letters* 13 (16 Oct. 19, 1964), pp. 508–509. DOI: 10.1103/PhysRevLett.13.508.

[8] Wikimedia Commons. *Standard Model of Elementary Particles*. URL: https://upload.wikimedia.org/wikipedia/commons/thumb/0/00/Standard_Model_of_Elementary_Particles.svg/2140px-Standard_Model_of_Elementary_Particles.svg.png (visited on 03/10/2023).

[9] D. J. Gross and F. Wilczek. "Ultraviolet Behavior of Non-Abelian Gauge Theories". In: *Physical Review Letters* 30.26 (June 25, 1973), pp. 1343–1346. DOI: 10.1103/physrevlett.30.1343.

[10] H. D. Politzer. "Reliable Perturbative Results for Strong Interactions?" In: *Physical Review Letters* 30.26 (June 25, 1973), pp. 1346–1349. DOI: 10.1103/physrevlett.30.1346.

[11] D. J. Gross and F. Wilczek. "Asymptotically Free Gauge Theories. I". In: *Physical Review D* 8 (10 Nov. 15, 1973), pp. 3633–3652. DOI: 10.1103/PhysRevD.8.3633. URL: https://link.aps.org/doi/10.1103/PhysRevD.8.3633.

[12] D. J. Gross and F. Wilczek. "Asymptotically free gauge theories. II". In: *Physical Review D* 9 (4 Feb. 15, 1974), pp. 980–993. DOI: 10.1103/PhysRevD.9.980. URL: https://link.aps.org/doi/10.1103/PhysRevD.9.980.

[13] A. Salam and J. C. Ward. "Electromagnetic and Weak Interactions". In: *Selected Papers of Abdus Salam*. WORLD SCIENTIFIC, May 1994, pp. 210–213. DOI: 10.1142/9789812795915_0029.

[14] S. Weinberg. "A Model of Leptons". In: *Physical Review Letters* 19.21 (Nov. 20, 1967), pp. 1264–1266. DOI: 10.1103/physrevlett.19.1264.

[15] S. L. Glashow. "Partial-symmetries of weak interactions". In: *Nuclear Physics* 22.4 (Sept. 9, 1969), pp. 579–588. DOI: 10.1016/0029-5582(61)90469-2.

[16] N. Cabibbo. "Unitary Symmetry and Leptonic Decays". In: *Physical Review Letters* 10.12 (June 15, 1963), pp. 531–533. DOI: 10.1103/physrevlett.10.531.

[17] M. Kobayashi and T. Maskawa. "CP-Violation in the Renormalizable Theory of Weak Interaction". In: *Progress of Theoretical Physics* 49.2 (Feb. 1, 1973), pp. 652–657. DOI: 10.1143/ptp.49.652.

[18] P. Higgs. "Broken symmetries, massless particles and gauge fields". In: *Physics Letters* 12.2 (Sept. 1964), pp. 132–133. DOI: 10.1016/0031-9163(64)91136-9.

[19] G. Bertone and D. Hooper. "History of dark matter". In: *Reviews of Modern Physics* 90.4 (Oct. 2018). DOI: 10.1103/revmodphys.90.045002.

[20] G. Bertone, D. Hooper, and J. Silk. "Particle dark matter: evidence, candidates and constraints". In: *Physics Reports* 405.5-6 (Jan. 2005), pp. 279–390. DOI: 10.1016/j.physrep.2004.08.031.

[21] F. Zwicky. "Die Rotverschiebung von extragalaktischen Nebeln". In: *Helvetica Physica Acta* 6 (Jan. 1933), pp. 110–127.

[22] F. Zwicky. "On the Masses of Nebulae and of Clusters of Nebulae". In: *The Astrophysical Journal* 86 (Oct. 1937), p. 217. DOI: 10.1086/143864.

[23] V. C. Rubin and J. F. W. Kent. "Rotation of the Andromeda Nebula from a Spectroscopic Survey of Emission Regions". In: *The Astrophysical Journal* 159 (Feb. 1970), p. 379. DOI: 10.1086/150317.

[24] D. H. Rogstad and G. S. Shostak. "Gross Properties of Five Scd Galaxies as Determined from 21-CENTIMETER Observations". In: *The Astrophysical Journal* 176 (Sept. 1972), p. 315. DOI: 10.1086/151636.

[25] E. Corbelli and P. Salucci. "The extended rotation curve and the dark matter halo of M33". In: *Monthly Notices of the Royal Astronomical Society* 311.2 (Jan. 2000), pp. 441–447. DOI: 10.1046/j.1365-8711.2000.03075.x.

[26] M. Kamionkowski. *Possible Relics from New Physics in the Early Universe: Inflation, the Cosmic Microwave Background, and Particle Dark Matter*. 1998. DOI: 10.48550/ARXIV.ASTRO-PH/9809214.

[27] R. Massey, T. Kitching, and J. Richard. "The dark matter of gravitational lensing". In: *Reports on Progress in Physics* 73.8 (July 2010), p. 086901. DOI: 10.1088/0034-4885/73/8/086901.

[28] D. Clowe et al. "A Direct Empirical Proof of the Existence of Dark Matter". In: *The Astrophysical Journal* 648.2 (Aug. 2006), pp. L109–L113. DOI: 10.1086/508162.

[29] D. Samtleben, S. Staggs, and B. Winstein. "The Cosmic Microwave Background for Pedestrians: A Review for Particle and Nuclear Physicists". In: *Annual Review of Nuclear and Particle Science* 57.1 (Nov. 2007), pp. 245–283. DOI: 10.1146/annurev.nucl.54.070103.181232.

[30] N. Aghanim et al. "Planck 2018 results. VI. Cosmological parameters". In: *Astron. Astrophys.* 641 (2020). [Erratum: Astron.Astrophys. 652, C4 (2021)], A6. DOI: 10.1051/0004-6361/201833910. arXiv: 1807.06209 [astro-ph.CO].

[31] V. Springel et al. "Simulations of the formation, evolution and clustering of galaxies and quasars". In: *Nature* 435.7042 (June 2005), pp. 629–636. DOI: 10.1038/nature03597.

[32] B. Dev and S. Qutub. "Constraining Non-thermal and Thermal properties of Dark Matter". In: *Frontiers in Physics* 2 (Nov. 2013). DOI: 10.3389/fphy.2014.00026.

[33] H. Baer et al. "Dark matter production in the early Universe: Beyond the thermal WIMP paradigm". In: *Physics Reports* 555 (Feb. 2015), pp. 1–60. DOI: 10.1016/j.physrep.2014.10.002.

[34] R. D. Peccei. "The Strong CP Problem and Axions". In: *Lecture Notes in Physics*. Springer Berlin Heidelberg, 2008, pp. 3–17. DOI: 10.1007/978-3-540-73518-2_1.

[35] C. Abel et al. "Measurement of the Permanent Electric Dipole Moment of the Neutron". In: *Physical Review Letters* 124.8 (Feb. 2020). DOI: 10.1103/physrevlett.124.081803.

[36] Y. K. Semertzidis and S. Youn. "Axion dark matter: How to see it?" In: *Science Advances* 8.8 (Feb. 2022). DOI: 10.1126/sciadv.abm9928.

[37] A. Boveia et al. "Recommendations on presenting LHC searches for missing transverse energy signals using simplified s-channel models of dark matter". In: *Physics of the Dark Universe* 27 (2020), p. 100365. ISSN: 2212-6864. DOI: https://doi.org/10.1016/j.dark.2019.100365. URL: https://www.sciencedirect.com/science/article/pii/S2212686419301633.

[38] G. Altarelli and G. Parisi. "Asymptotic freedom in parton language". In: *Nuclear Physics B* 126.2 (Aug. 1977), pp. 298–318. DOI: 10.1016/0550-3213(77)90384-4.

[39] Y. L. Dokshitzer. "Calculation of the Structure Functions for Deep Inelastic Scattering and e+ e- Annihilation by Perturbation Theory in Quantum Chromodynamics." In: *Sov. Phys. JETP* 46 (1977), pp. 641–653.

[40] V. N. Gribov and L. N. Lipatov. "Deep inelastic e p scattering in perturbation theory". In: *Sov. J. Nucl. Phys.* 15 (1972), pp. 438–450.

[41] R. D. Ball et al. "Parton distributions from high-precision collider data". In: *The European Physical Journal C* 77.10 (Oct. 2017). DOI: 10.1140/epjc/s10052-017-5199-5.

[42] A. Buckley et al. "General-purpose event generators for LHC physics". In: *Physics Reports* 504.5 (July 2011), pp. 145–233. ISSN: 0370-1573. DOI: 10.1016/j.physrep.2011.03.005. URL: https://www.sciencedirect.com/science/article/pii/S0370157311000846.

[43] J. Alwall et al. "The automated computation of tree-level and next-to-leading order differential cross sections, and their matching to parton shower simulations". In: *Journal of High Energy Physics* 07.79 (July 17, 2014). DOI: 10.1007/JHEP07(2014)079. arXiv: 1405.0301v2 [hep-ph].

[44] J. Alwall et al. "MadGraph 5: going beyond". In: *Journal of High Energy Physics* 2011.6 (June 2011). DOI: 10.1007/jhep06(2011)128.

[45] P. Nason. "A New Method for Combining NLO QCD with Shower Monte Carlo Algorithms". In: *Journal of High Energy Physics* 2004.40 (Dec. 10, 2004). DOI: 10.1088/1126-6708/2004/11/040. arXiv: hep-ph/0409146 [hep-ph].

[46] S. Frixione, P. Nason, and C. Oleari. "Matching NLO QCD computations with Parton Shower simulations: the POWHEG method". In: *Journal of High Energy Physics* 11 (Sept. 13, 2007). DOI: 10.1088/1126-6708/2007/11/070. arXiv: 0709.2092v1 [hep-ph].

[47] S. Alioli et al. "A general framework for implementing NLO calculations in shower Monte Carlo programs: the POWHEG BOX". In: *Journal of High Energy Physics* 2010.6 (June 2010). DOI: 10.1007/jhep06(2010)043. URL: https://doi.org/10.1007/jhep06(2010)043.

[48] T. Sjöstrand. "Jet fragmentation of multiparton configurations in a string framework". In: *Nuclear Physics B* 248.2 (Dec. 24, 1984), pp. 469–502. DOI: 10.1016/0550-3213(84)90607-2.

[49] B. Andersson et al. "Parton fragmentation and string dynamics". In: *Physics Reports* 97.2-3 (July 1983), pp. 31–145. DOI: 10.1016/0370-1573(83)90080-7.

[50] T. Sjöstrand, S. Mrenna, and P. Skands. "A brief introduction to PYTHIA 8.1". In: *Computer Physics Communications* 178.11 (June 2008), pp. 852–867. DOI: 10.1016/j.cpc.2008.01.036.

[51] T. Sjöstrand et al. "An Introduction to PYTHIA 8.2". In: *Computer Physics Communications* 191 (June 2015), pp. 159–177. DOI: 10.1016/j.cpc.2015.01.024. arXiv: 1410.3012v1 [hep-ph].

[52] T. Sjöstrand. "The Lund Monte Carlo for jet fragmentation". In: *Computer Physics Communications* 27.3 (Sept. 1982), pp. 243–284. DOI: 10.1016/0010-4655(82)90175-8.

[53] L. Evans and P. Bryant. "LHC Machine". In: *Journal of Instrumentation* 3.08 (Aug. 14, 2008). DOI: 10.1088/1748-0221/3/08/s08001. URL: https://doi.org/10.1088/1748-0221/3/08/s08001.

[54] O. S. Brüning et al. *LHC Design Report*. CERN Yellow Reports: Monographs. Geneva: CERN, 2004. DOI: 10.5170/CERN-2004-003-V-1. URL: https://cds.cern.ch/record/782076.

[55] O. S. Brüning et al. *LHC Design Report*. CERN Yellow Reports: Monographs. Geneva: CERN, 2004. DOI: 10.5170/CERN-2004-003-V-2. URL: http://cds.cern.ch/record/815187.

[56] M. Benedikt et al. *LHC Design Report*. CERN Yellow Reports: Monographs. Geneva: CERN, 2004. DOI: 10.5170/CERN-2004-003-V-3. URL: http://cds.cern.ch/record/823808.

[57] E. Mobs. *The CERN accelerator complex - 2019. Complexe des accélérateurs du CERN - 2019*. Tech. rep. General Photo. July 29, 2019. URL: https://cds.cern.ch/record/2684277.

[58] T. Sakuma and T. McCauley. "Detector and Event Visualization with SketchUp at the CMS Experiment". In: *Journal of Physics: Conference Series* 513.022032 (2 2014). Ed. by D. L. Groep and D. Bonacorsi. DOI: 10.1088/1742-6596/513/2/022032. arXiv: 1311.4942 [physics.ins-det].

[59] CMS Collaboration. "The CMS experiment at the CERN LHC". In: *Journal of Instrumentation* 3.S08004 (Aug. 2008). URL: http://stacks.iop.org/1748-0221/3/i=08/a=S08004.

[60] F. Hartmann. *Evolution of Silicon Sensor Technology in Particle Physics*. Springer International Publishing, 2017. DOI: 10.1007/978-3-319-64436-3.

[61] The Tracker Group of the CMS Collaboration. "The CMS Phase-1 Pixel Detector Upgrade". In: *Journal of Instrumentation* 16.P02027 (Feb. 22, 2021). DOI: 10.1088/1748-0221/16/02/P02027. arXiv: 2012.14304 [physics.ins-det].

[62] V. Karimäki et al. *The CMS tracker system project: Technical Design Report*. Technical Design Report CMS. Geneva: CERN, 1997. URL: https://cds.cern.ch/record/368412.

[63] CMS Collaboration. *The CMS tracker: addendum to the Technical Design Report*. Technical Design Report CMS. Geneva: CERN, 2000. URL: http://cdsweb.cern.ch/record/490194.

[64] CMS Collaboration. *The CMS electromagnetic calorimeter project: Technical Design Report*. Technical Design Report CMS. Geneva: CERN, 1997. URL: https://cds.cern.ch/record/349375.

[65] P. Bloch et al. *Changes to CMS ECAL electronics: addendum to the Technical Design Report*. Technical design report. CMS. Geneva: CERN, 2002. URL: http://cds.cern.ch/record/581342.

[66] A. Benaglia. "The CMS ECAL performance with examples". In: *Journal of Instrumentation* 9.C02008 (Feb. 11, 2014). URL: http://stacks.iop.org/1748-0221/9/i=02/a=C02008.

[67] CMS Collaboration. *ECAL 2016 refined calibration and Run2 summary plots*. Tech. rep. Apr. 20, 2020. URL: https://cds.cern.ch/record/2717925.

[68] CMS Collaboration. *The CMS hadron calorimeter project: Technical Design Report*. Technical Design Report CMS. Geneva: CERN, 1997. URL: https://cds.cern.ch/record/357153/?ln=de.

[69] C. Collaboration. "Performance of the CMS hadron calorimeter with cosmic ray muons and LHC beam data". In: *Journal of Instrumentation* 5.T03012 (Mar. 19, 2010). URL: http://stacks.iop.org/1748-0221/5/i=03/a=T03012.

[70] CMS Collaboration. *HCAL Energy Reconstruction Performance*. Tech. rep. Nov. 25, 2016. URL: http://cds.cern.ch/record/2235509.

[71] CMS Collaboration. *HCAL Calibration Status in Summer 2017*. Tech. rep. Aug. 17, 2017. URL: http://cds.cern.ch/record/2281146.

[72] CMS Collaboration. *Results related to the Phase1 HE upgrade*. Tech. rep. May 29, 2018. URL: https://cds.cern.ch/record/2320857.

[73] CMS Collaboration. *The CMS muon project: Technical Design Report*. Technical Design Report CMS. Geneva: CERN, 1997. URL: https://cds.cern.ch/record/343814.

[74] C. collaboration. "Performance of the CMS muon detector and muon reconstruction with proton-proton collisions at $\sqrt{s} = 13$ TeV". In: *JINST* 13 (2018), P06015. DOI: 10.1088/1748-0221/13/06/P06015. arXiv: 1804.04528 [physics.ins-det].

[75] CMS Collaboration. "The CMS trigger system". In: *Journal of Instrumentation* 12.01 (Jan. 2017), P01020–P01020. DOI: 10.1088/1748-0221/12/01/p01020. URL: https://doi.org/10.1088/1748-0221/12/01/p01020.

[76] CMS Collaborations. *CMS TriDAS project: Technical Design Report, Volume 1: The Trigger Systems*. Technical design report. CMS. URL: https://cds.cern.ch/record/706847.

[77] CMS Collaboration. *CMS The TriDAS Project: Technical Design Report, Volume 2: Data Acquisition and High-Level Trigger. CMS trigger and data-acquisition project*. Technical Design Report CMS. Geneva: CERN, 2002. URL: http://cds.cern.ch/record/578006.

[78] CMS Collaboration. "Particle-flow reconstruction and global event description with the CMS detector". In: *Journal of Instrumentation* 12.P10003 (June 15, 2017). DOI: 10.1088/1748-0221/12/10/P10003. arXiv: 1706.04965v2 [physics.ins-det].

[79] M. Cacciari, G. P. Salam, and G. Soyez. "The anti-k_t jet clustering algorithm". In: *Journal of High Energy Physics* 2008.63 (4 Apr. 16, 2008). DOI: 10.1088/1126-6708/2008/04/063. arXiv: 0802.1189v2 [hep-ph].

[80] *Pileup Removal Algorithms*. Tech. rep. Geneva: CERN, 2014. URL: https://cds.cern.ch/record/1751454.

[81] D. Bertolini et al. "Pileup per particle identification". In: *Journal of High Energy Physics* 2014.10 (Oct. 2014). DOI: 10.1007/jhep10(2014)059.

[82] B. Penning. "The pursuit of dark matter at colliders—an overview". In: *Journal of Physics G: Nuclear and Particle Physics* 45.6 (May 2018), p. 063001. DOI: 10.1088/1361-6471/aabea7.

[83] J. Jochum et al. "The CRESST dark matter search". In: *Prog. Part. Nucl. Phys.* 66 (2011). Ed. by A. Faessler and V. Rodin, pp. 202–207. DOI: 10.1016/j.ppnp.2011.01.007.

[84] H. Lattaud. "Sub-GeV Dark Matter Searches with EDELWEISS: New results and prospects". In: *14th International Workshop on the Identification of Dark Matter 2022*. Nov. 2022. arXiv: 2211.04176 [astro-ph.GA].

[85] D. S. Akerib et al. "The Large Underground Xenon (LUX) Experiment". In: *Nucl. Instrum. Meth. A* 704 (2013), pp. 111–126. DOI: 10.1016/j.nima.2012.11.135. arXiv: 1211.3788 [physics.ins-det].

[86] D. Akerib et al. "The LUX-ZEPLIN (LZ) experiment". In: *Nuclear Instruments and Methods in Physics Research Section A: Accelerators, Spectrometers, Detectors and Associated Equipment* 953 (Feb. 2020), p. 163047. DOI: 10.1016/j.nima.2019.163047. URL: https://doi.org/10.1016%2Fj.nima.2019.163047.

[87] A. Molinario. "The XENON project for dark matter direct detection at LNGS". In: *EPJ Web Conf.* 164 (2017). Ed. by L. Bravina, Y. Foka, and S. Kabana, p. 07049. DOI: 10.1051/epjconf/201716407049.

[88] E. Aprile et al. "Search for New Physics in Electronic Recoil Data from XENONnT". In: *Physical Review Letters* 129.16 (Apr. 12, 2023). DOI: 10.1103/physrevlett.129.161805. URL: https://doi.org/10.1103%2Fphysrevlett.129.161805.

[89] M. Schumann. "Direct detection of WIMP dark matter: concepts and status". In: *Journal of Physics G: Nuclear and Particle Physics* 46.10 (Aug. 2019), p. 103003. DOI: 10.1088/1361-6471/ab2ea5. URL: https://doi.org/10.1088/1361-6471/ab2ea5.

[90] J. Aalbers et al. *First Dark Matter Search Results from the LUX-ZEPLIN (LZ) Experiment*. 2022. DOI: 10.48550/ARXIV.2207.03764.

[91] XENON Collaboration et al. *First Dark Matter Search with Nuclear Recoils from the XENONnT Experiment*. 2023. DOI: 10.48550/ARXIV.2303.14729.

[92] J. Billard et al. "Direct detection of dark matter - APPEC committee report". In: *Reports on Progress in Physics* 85.5 (Apr. 2022), p. 056201. DOI: 10.1088/1361-6633/ac5754.

[93] W. B. Atwood et al. "The Large Area Telescope on the Fermi Gamma-ray Space Telescope Mission". In: *Astrophys. J.* 697 (2009), pp. 1071–1102. DOI: 10.1088/0004-637X/697/2/1071. arXiv: 0902.1089 [astro-ph.IM].

[94] G. Vasileiadis. "The HESS experimental project". In: *Nucl. Instrum. Meth. A* 553 (2005). Ed. by J. Engelfried and G. Paic, pp. 268–273. DOI: 10.1016/j.nima.2005.08.056.

[95] D. Ferenc. "The MAGIC gamma-ray observatory". In: *Nucl. Instrum. Meth. A* 553 (2005). Ed. by J. Engelfried and G. Paic, pp. 274–281. DOI: 10.1016/j.nima.2005.08.085.

[96] E. Resconi. "Status and prospects of the IceCube neutrino telescope". In: *Nucl. Instrum. Meth. A* 602 (2009). Ed. by G. Hallewell et al., pp. 7–13. DOI: 10.1016/j.nima.2008.12.013. arXiv: 0807.3891 [astro-ph].

[97] M. Ageron et al. "ANTARES: the first undersea neutrino telescope". In: *Nucl. Instrum. Meth. A* 656 (2011), pp. 11–38. DOI: 10.1016/j.nima.2011.06.103. arXiv: 1104.1607 [astro-ph.IM].

[98] A. Margiotta. "The KM3NeT deep-sea neutrino telescope". In: *Nucl. Instrum. Meth. A* 766 (2014). Ed. by T. Sumiyoshi et al., pp. 83–87. DOI: 10.1016/j.nima.2014.05.090. arXiv: 1408.1392 [astro-ph.IM].

[99] C. P. de los Heros. "Status, Challenges and Directions in Indirect Dark Matter Searches". In: *Symmetry* 12.10 (Oct. 2020), p. 1648. DOI: 10.3390/sym12101648.

[100] O. Buchmueller, C. Doglioni, and L.-T. Wang. "Search for dark matter at colliders". In: *Nature Physics* 13.3 (Mar. 2017), pp. 217–223. DOI: 10.1038/nphys4054.

[101] G. Cowan et al. "Asymptotic formulae for likelihood-based tests of new physics". In: *The European Physical Journal C* 71.1554 (Feb. 9, 2011). DOI: 10.1140/epjc/s10052-011-1554-0. arXiv: 1007.1727v3 [physics.data-an].

[102] LHC Higgs Combination Group. *Procedure for the LHC Higgs boson search combination in Summer 2011*. Tech. rep. CMS-NOTE-2011-005. ATL-PHYS-PUB-2011-11. Geneva: CERN, Aug. 2011. URL: https://cds.cern.ch/record/1379837.

[103] S. S. Wilks. "The Large-Sample Distribution of the Likelihood Ratio for Testing Composite Hypotheses". In: *The Annals of Mathematical Statistics* 9.1 (Mar. 1938), pp. 60–62. ISSN: 00034851. DOI: 10.1214/aoms/1177732360.

[104] J. Neyman and E. S. Pearson. "On the Problem of the Most Efficient Tests of Statistical Hypotheses". In: *Philosophical Transactions of the Royal Society A: Mathematical, Physical and Engineering Sciences* 231.694-706 (Feb. 16, 1933), pp. 289–337. DOI: 10.1098/rsta.1933.0009. URL: http://rsta.royalsocietypublishing.org/content/231/694-706/289.

[105] R. D. Cousins. *Generalization of Chisquare Goodness-of-Fit Test for Binned Data Using Saturated Models, with Application to Histograms*. Tech. rep. Mar. 3, 2013. URL: http://www.physics.ucla.edu/%5C~cousins/stats/cousins_saturated.pdf.

[106] I. Bigi et al. "Production and decay properties of ultra-heavy quarks". In: *Physics Letters B* 181.1-2 (Nov. 1986), pp. 157–163. DOI: 10.1016/0370-2693(86)91275-x.

[107] U. Husemann. "Top-quark physics: Status and prospects". In: *Progress in Particle and Nuclear Physics* 95 (July 2017), pp. 48–97. DOI: 10.1016/j.ppnp.2017.03.002.

[108] A. Quadt. "Top quark physics at hadron colliders". In: *The European Physical Journal C* 48.3 (Nov. 2006), pp. 835–1000. DOI: 10.1140/epjc/s2006-02631-6.

[109] CMS Collaboration. "Identification of heavy-flavour jets with the CMS detector in pp collisions at 13 TeV". In: *Journal of Instrumentation* 13.P05011 (May 8, 2018). DOI: 10.1088/1748-0221/13/05/P05011. arXiv: 1712.07158v1 [physics.ins-det].

[110] "Performance summary of AK4 jet b tagging with data from proton-proton collisions at 13 TeV with the CMS detector". In: (2023). URL: https://cds.cern.ch/record/2854609.

[111] E. Bols et al. "Jet flavour classification using DeepJet". In: *Journal of Instrumentation* 15.12 (Dec. 2020), P12012–P12012. DOI: 10.1088/1748-0221/15/12/p12012.

[112] CMS Collaboration. *Performance of the DeepJet b tagging algorithm using 41.9/fb of data from proton-proton collisions at 13TeV with Phase 1 CMS detector*. Tech. rep. CMS Collaboration, Apr. 9, 2019. URL: http://cds.cern.ch/record/2646773.

[113] K. O'Shea and R. Nash. *An Introduction to Convolutional Neural Networks*. 2015. DOI: 10.48550/ARXIV.1511.08458.

[114] S. Hochreiter and J. Schmidhuber. "Long short-term memory". In: *Neural computation* 9.8 (1997), pp. 1735–1780.

[115] CMS Collaboration. *Jet Flavour Identification*. CMS internal url: https://twiki.cern.ch/twiki/bin/view/CMSPublic/SWGuideBTagMCTools r41.

[116] J. S. Bridle. "Probabilistic Interpretation of Feedforward Classification Network Outputs, with Relationships to Statistical Pattern Recognition". In: *Neurocomputing* (1990). Ed. by F. F. Soulié and J. Hérault, pp. 227–236. DOI: 10.1007/978-3-642-76153-9_28.

[117] H. Qu and L. Gouskos. "Jet tagging via particle clouds". In: *Physical Review D* 101.5 (Mar. 2020). DOI: 10.1103/physrevd.101.056019.

[118] CMS Collaboration. "Identification of heavy, energetic, hadronically decaying particles using machine-learning techniques". In: *JINST* 15.06 (2020), P06005. DOI: 10.1088/1748-0221/15/06/P06005. arXiv: 2004.08262. URL: https://cds.cern.ch/record/2715432.

[119] Y. Wang et al. "Dynamic Graph CNN for Learning on Point Clouds". In: *ACM Transactions on Graphics* 38.5 (Nov. 2019), pp. 1–12. DOI: 10.1145/3326362.

[120] S. Ioffe and C. Szegedy. *Batch Normalization: Accelerating Deep Network Training by Reducing Internal Covariate Shift*. 2015. DOI: 10.48550/ARXIV.1502.03167.

[121] X. Glorot, A. Bordes, and Y. Bengio. "Deep Sparse Rectifier Neural Networks". In: vol. 15. Jan. 2010.

[122] H. Gholamalinezhad and H. Khosravi. *Pooling Methods in Deep Neural Networks, a Review*. 2020. DOI: 10.48550/ARXIV.2009.07485.

[123] A. J. Larkoski et al. "Soft Drop". In: (2014). DOI: 10.48550/ARXIV.1402.2657.

[124] "Identification of highly Lorentz-boosted heavy particles using graph neural networks and new mass decorrelation techniques". In: (2020). URL: https://cds.cern.ch/record/2707946.

[125] S. L. Glashow, J. Iliopoulos, and L. Maiani. "Weak Interactions with Lepton-Hadron Symmetry". In: *Physical Review D* 2.7 (Oct. 1970), pp. 1285–1292. DOI: 10.1103/physrevd.2.1285.

[126] M. Waßmer. "Search for the production of Dark Matter in hadronic mono-top signatures with the CMS experiment". PhD thesis. Karlsruher Institut für Technologie (KIT), 2021. 247 pp. DOI: 10.5445/IR/1000129768.

[127] J. Andrea, B. Fuks, and F. Maltoni. "Monotops at the LHC". In: *Physical Review D* 84.7 (Oct. 2011). DOI: 10.1103/physrevd.84.074025.

[128] J.-L. Agram et al. "Monotop phenomenology at the Large Hadron Collider". In: *Physical Review D* 89.1 (Jan. 2014). DOI: 10.1103/physrevd.89.014028.

[129] I. Boucheneb et al. "Revisiting monotop production at the LHC". In: *Journal of High Energy Physics* 2015.1 (Jan. 2015). DOI: 10.1007/jhep01(2015)017.

[130] M. Fath. *Generatorstudien für nicht-resonante Mono-Top-Produktion am LHC*. Bachelor's Thesis. 2022.

[131] E. W. Kolb and M. S. Turner. *The early universe*. Vol. 69. 1990.

[132] M. Backovic, K. Kong, and M. McCaskey. "MadDM v.1.0: Computation of Dark Matter Relic Abundance Using MadGraph5". In: *Physics of the Dark Universe* 5-6 (2014), pp. 18–28. DOI: 10.1016/j.dark.2014.04.001. arXiv: 1308.4955 [hep-ph].

[133] F. Ambrogi et al. "MadDM v.3.0: a Comprehensive Tool for Dark Matter Studies". In: *Phys. Dark Univ.* 24 (2019), p. 100249. DOI: 10.1016/j.dark.2018.11.009. arXiv: 1804.00044 [hep-ph].

[134] CMS collaboration. "Extraction and validation of a new set of CMS pythia8 tunes from underlying-event measurements". In: *The European Physical Journal C* 80.1 (Jan. 2020). DOI: 10.1140/epjc/s10052-019-7499-4.

[135] S. Agostinelli et al. "Geant4—a simulation toolkit". In: *Nuclear Instruments and Methods in Physics Research Section A: Accelerators, Spectrometers, Detectors and Associated Equipment* 506.3 (July 1, 2003), pp. 250–303. ISSN: 0168-9002. DOI: https://doi.org/10.1016/S0168-9002(03)01368-8. URL: http://www.sciencedirect.com/science/article/pii/S0168900203013688.

[136] J. Allison et al. "Geant4 developments and applications". In: *IEEE Transactions on Nuclear Science* 53.1 (Feb. 2006), pp. 270–278. DOI: 10.1109/tns.2006.869826.

[137] J. Allison et al. "Recent developments in Geant4". In: *Nuclear Instruments and Methods in Physics Research Section A: Accelerators, Spectrometers, Detectors and Associated Equipment* 835 (Nov. 2016), pp. 186–225. DOI: 10.1016/j.nima.2016.06.125.

[138] M. Czakon, P. Fiedler, and A. Mitov. "Total Top-Quark Pair-Production Cross Section at Hadron Colliders Through $\mathcal{O}(\alpha_S^4)$". In: *Phys. Rev. Lett.* 110 (25 June 2013), p. 252004. DOI: 10.1103/PhysRevLett.110.252004. URL: https://link.aps.org/doi/10.1103/PhysRevLett.110.252004.

[139] M. Czakon and A. Mitov. "Top++: a program for the calculation of the top-pair cross-section at hadron colliders". In: *Computer Physics Communications* 185.11 (Dec. 23, 2011), pp. 2930–2938. DOI: 10.1016/j.cpc.2014.06.021. arXiv: 1112.5675v4 [hep-ph].

[140] M. Aliev et al. "HATHOR – HAdronic Top and Heavy quarks crOss section calculatoR". In: *Computer Physics Communications* 182.4 (Apr. 2011), pp. 1034–1046. DOI: 10.1016/j.cpc.2010.12.040.

[141] P. Kant et al. "HatHor for single top-quark production: Updated predictions and uncertainty estimates for single top-quark production in hadronic collisions". In: *Computer Physics Communications* 191 (June 2015), pp. 74–89. DOI: 10.1016/j.cpc.2015.02.001.

[142] N. Kidonakis. "Two-loop soft anomalous dimensions for single top quark associated production with a W- or H-". In: *Physical Review D* 82.5 (May 24, 2010). DOI: 10.1103/PhysRevD.82.054018. arXiv: 1005.4451v1 [hep-ph].

[143] T. Gehrmann et al. "W^+W^- Production at Hadron Colliders in Next to Next to Leading Order QCD". In: *Phys. Rev. Lett.* 113 (21 Nov. 2014), p. 212001. DOI: 10.1103/PhysRevLett.113.212001. URL: https://link.aps.org/doi/10.1103/PhysRevLett.113.212001.

[144] J. M. Campbell, R. K. Ellis, and C. Williams. "Vector boson pair production at the LHC". In: *Journal of High Energy Physics* 2011.7 (Apr. 29, 2011). DOI: 10.1007/JHEP07(2011)018. arXiv: 1105.0020v1 [hep-ph].

[145] F. Cascioli et al. "ZZ production at hadron colliders in NNLO QCD". In: *Physics Letters B* 735 (July 2014), pp. 311–313. DOI: 10.1016/j.physletb.2014.06.056.

[146] J. M. Campbell et al. "Top-pair production and decay at NLO matched with parton showers". In: *Journal of High Energy Physics* 2015.4 (Apr. 2015). DOI: 10.1007/jhep04(2015)114.

[147] S. Alioli, S.-O. Moch, and P. Uwer. "Hadronic top-quark pair-production with one jet and parton showering". In: *Journal of High Energy Physics* 2012.1 (Jan. 2012). DOI: 10.1007/jhep01(2012)137.

[148] *DMsimp: Simplified dark matter models.* URL: https://feynrules.irmp.ucl.ac.be/wiki/DMsimp.

[149] J. M. Lindert et al. "Precise predictions for V + jets dark matter backgrounds". In: *The European Physical Journal C* 77.12 (Dec. 2017). DOI: 10.1140/epjc/s10052-017-5389-1.

[150] CMS Collaboration. *CMS Top PAG: Top pT reweighting.* CMS internal url: https://twiki.cern.ch/twiki/bin/view/CMS/BTagSFMethods r37. (Visited on 10/31/2022).

[151] M. Czakon et al. "Top-pair production at the LHC through NNLO QCD and NLO EW". In: *Journal of High Energy Physics* 2017.10 (Oct. 2017). DOI: 10.1007/jhep10(2017)186.

[152] CMS Collaboration. *Reweighting recipe to emulate Level 1 ECAL prefiring.* CMS internal url: https://twiki.cern.ch/twiki/bin/view/CMS/L1ECALPrefiringWeightRecipe r11.

[153] "Simulation of the Silicon Strip Tracker pre-amplifier in early 2016 data". In: (2020). URL: https://cds.cern.ch/record/2740688.

[154] CMS collaboration. *Muon scale factors for 2016.* URL: https://twiki.cern.ch/twiki/bin/view/CMS/MuonUL2016#Medium_pT_from_15_to_120_GeV (visited on 10/26/2022).

[155] CMS collaboration. *Muon scale factors for 2017.* URL: https://twiki.cern.ch/twiki/bin/view/CMS/MuonUL2017#Medium_pT_from_15_to_120_GeV (visited on 10/26/2022).

[156] CMS collaboration. *Muon scale factors for 2018.* URL: https://twiki.cern.ch/twiki/bin/view/CMS/MuonUL2018#Medium_pT_from_15_to_120_GeV (visited on 10/26/2022).

[157] CMS collaboration. *Tag and Probe Framework for derivation of electron trigger scale factors.* URL: https://twiki.cern.ch/twiki/bin/view/CMSPublic/ElectronTagAndProbe (visited on 02/01/2023).

[158] J. Janik. *Bestimmung von Trigger-Effizienzen und zugehörigen Daten-Simulation-Skalenfaktoren im Rahmen einer Monotop-Analyse am CMS-Experiment.* Bachelor's Thesis. 2022. URL: https://publish.etp.kit.edu/record/22131.

[159] CMS collaboration. *Electron Cut-based Identification Efficiencies.* URL: https://twiki.cern.ch/twiki/bin/view/CMS/CutBasedElectronIdentificationRun2#Electron_ID_Working_Points_WP_de (visited on 10/26/2022).

[160] CMS Collaboration. "Performance of electron reconstruction and selection with the CMS detector in proton-proton collisions at sqrt(s) = 8 TeV". In: *Journal of Instrumentation* 10.P06005 (June 10, 2015). DOI: 10.1088/1748-0221/10/06/P06005. arXiv: 1502.02701v2 [physics.ins-det].

[161] CMS collaboration. *Electron and photon scale factors.* URL: https://twiki.cern.ch/twiki/bin/view/CMS/EgammaUL2016To2018 (visited on 10/26/2022).

[162] CMS Collaboration. "Performance of the CMS muon detector and muon reconstruction with proton-proton collisions at $\sqrt{s} = 13$ TeV". In: *Journal of Instrumentation* 13.P06015 (Apr. 12, 2018). DOI: 10.1088/1748-0221/13/06/P06015. arXiv: 1804.04528 [physics.ins-det].

[163] CMS collaboration. *Photon Cut-based Identification Efficiencies.* URL: https://twiki.cern.ch/twiki/bin/view/CMS/CutBasedPhotonIdentificationRun2#Photon_ID_Working_Points_WP_defi (visited on 10/26/2022).

[164] CMS collaboration. *Jet Identification for the 13 TeV UL data.* URL: https://twiki.cern.ch/twiki/bin/view/CMS/JetID13TeVUL#Preliminary_Recommendations_for (visited on 10/27/2022).

[165] CMS collaboration. *Jet identification in high pile-up environment.* URL: https://twiki.cern.ch/twiki/bin/view/CMS/PileupJetIDUL (visited on 10/27/2022).

[166] CMS Collaboration. *Introduction to Jet Energy Corrections at CMS.* CMS internal url: https://twiki.cern.ch/twiki/bin/view/CMS/IntroToJEC r7. Oct. 27, 2022. (Visited on 10/04/2021).

[167] CMS Collaboration. *Jet Energy Resolution Correction.* CMS internal url: https://cms-jerc.web.cern.ch/JER/. (Visited on 10/31/2022).

[168] CMS Collaboration. "Determination of jet energy calibration and transverse momentum resolution in CMS". In: *Journal of Instrumentation* 6.11 (July 21, 2011). DOI: 10.1088/1748-0221/6/11/P11002. arXiv: 1107.4277v1 [physics.ins-det].

[169] CMS Collaboration. "Jet energy scale and resolution in the CMS experiment in pp collisions at 8 TeV". In: *Journal of Instrumentation* 12.P02014 (July 13, 2016). DOI: 10.1088/1748-0221/12/02/P02014. arXiv: 1607.03663v2 [hep-ex].

[170] CMS Collaboration. *Jet energy scale and resolution performance with 13 TeV data collected by CMS in 2016-2018.* Tech. rep. CMS Collaboration, Apr. 23, 2020. URL: http://cds.cern.ch/record/2715872.

[171] CMS collaboration. *Recommended JEC corrections.* URL: https://twiki.cern.ch/twiki/bin/view/CMS/JECDataMC (visited on 10/31/2022).

[172] CMS Collaboration. *Heavy flavour tagging for 13 TeV data in 2016preVFP Ultra-Legacy reprocessing and 10_6_X MC.* CMS internal url: https://twiki.cern.ch/twiki/bin/view/CMS/BtagRecommendation106XUL16preVFP r6. Oct. 31, 2022.

[173] CMS Collaboration. *Heavy flavour tagging for 13 TeV data in 2016postVFP Ultra-Legacy reprocessing and 10_6_X MC.* CMS internal url: https://twiki.cern.ch/twiki/bin/view/CMS/BtagRecommendation106XUL16postVFP r8. Oct. 31, 2022.

[174] CMS Collaboration. *Heavy flavour tagging for 13 TeV data in 2017 and 94X MC.* CMS internal url: https://twiki.cern.ch/twiki/bin/viewauth/CMS/BtagRecommendation94X r40. Feb. 16, 2021.

[175] CMS Collaboration. *Heavy flavour tagging for 13 TeV data in 2018 and 10_2_X MC*. CMS internal url: https://twiki.cern.ch/twiki/bin/viewauth/CMS/BtagRecommendation102X r22. Feb. 16, 2021.

[176] CMS Collaboration. *Methods to apply b-tagging efficiency scale factors*. CMS internal url: https://twiki.cern.ch/twiki/bin/view/CMS/BTagSFMethods r37. Oct. 31, 2022.

[177] T. Severini. *Elements of Distribution Theory*. Cambridge Series in Statistical and Probabilistic Mathematics. Cambridge University Press, 2005. ISBN: 9780521844727. URL: https://books.google.ca/books?id=QsVl8FDmld8C.

[178] *Stat 5101 Notes: Brand Name Distributions*. https://www.stat.umn.edu/geyer/5102/notes/brand.pdf.

[179] CMS collaboration. "Performance of missing transverse momentum reconstruction in proton-proton collisions at $\sqrt{s} = 13$ TeV using the CMS detector". In: *Journal of Instrumentation* 14.07 (July 2019), P07004–P07004. DOI: 10.1088/1748-0221/14/07/p07004.

[180] CMS collaboration. *Mitigation of anomalous missing transverse momentum measurements in data collected by CMS at sqrt(s) = 13 TeV during the LHC Run 2*. URL: https://cds.cern.ch/record/2714938?ln=deC (visited on 10/31/2022).

[181] CMS collaboration. "Precision luminosity measurement in proton-proton collisions at $\sqrt{s} = 13$ TeV in 2015 and 2016 at CMS". In: (2021). DOI: 10.48550/ARXIV.2104.01927.

[182] *CMS luminosity measurement for the 2017 data-taking period at $\sqrt{s} = 13$ TeV*. Tech. rep. Geneva: CERN, 2018. URL: https://cds.cern.ch/record/2621960.

[183] *CMS luminosity measurement for the 2018 data-taking period at $\sqrt{s} = 13$ TeV*. Tech. rep. Geneva: CERN, 2019. URL: https://cds.cern.ch/record/2676164.

[184] CMS Collaboration. *Lumi POG - Year-to-year combinations and correlations*. CMS internal url: https://twiki.cern.ch/twiki/bin/view/CMS/LumiRecommendationsRun2 r179. (Visited on 11/30/2022).

[185] R. Barlow and C. Beeston. "Fitting using finite Monte Carlo samples". In: *Computer Physics Communications* 77.2 (Mar. 27, 1993), pp. 219–228. DOI: 10.1016/0010-4655(93)90005-w.

[186] CMS Collaboration. *CMS Combine Tool*. Oct. 1, 2021. URL: https://cms-analysis.github.io/HiggsAnalysis-CombinedLimit/ (visited on 10/01/2021).

[187] CMS collaboration. *Run-II monojet/mono-V analysis*. Tech. rep. DOI: CMSAN-20-042.2020.

[188] CMS collaboration. "Search for new particles in events with energetic jets and large missing transverse momentum in proton-proton collisions at $\sqrt{s} = 13$ TeV". In: *Journal of High Energy Physics* 2021.11 (Nov. 2021). DOI: 10.1007/jhep11(2021)153.

Appendix

A Electron trigger scale factors

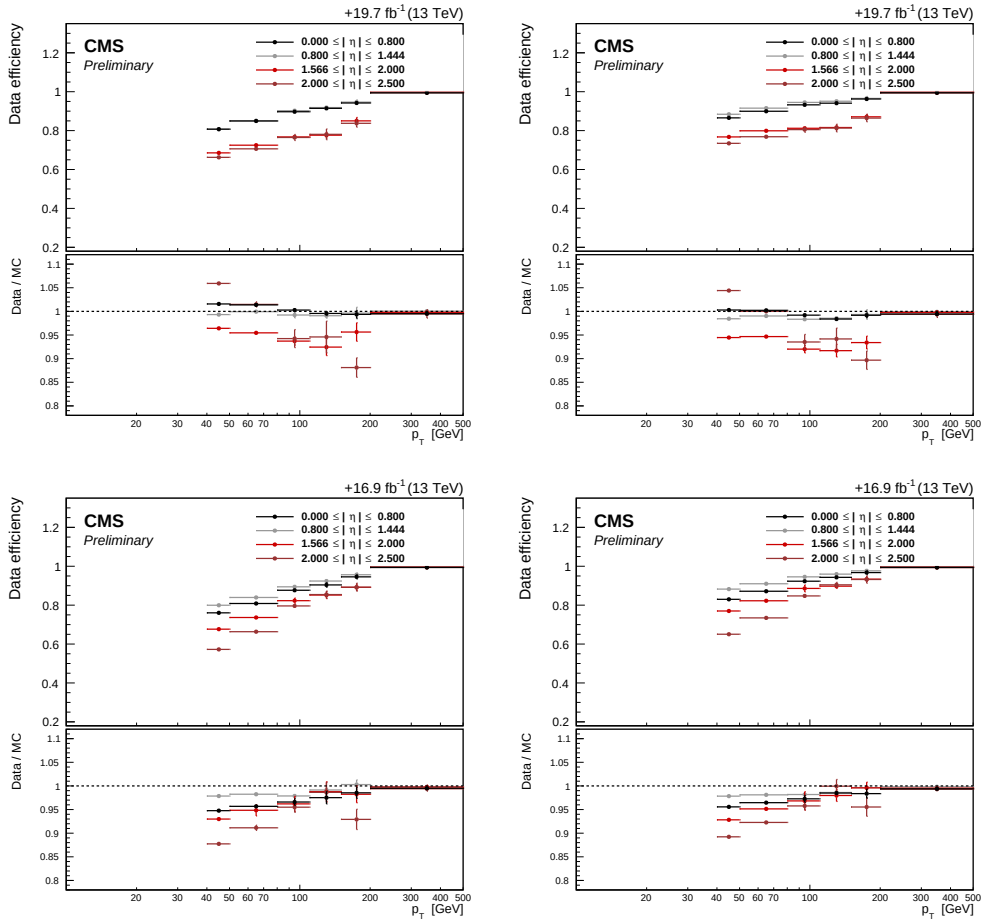

Figure A.1: Trigger efficiency of the electron triggers in data as a function of the transverse momentum of the electron for the 2016 data-taking eras. The rows correspond to the different data-taking eras 2016preVFP, 2016postVFP from top to bottom. The left-hand side shows the efficiency for the loose electron collection, whereas the right-hand side shows the efficiency for the tight electron collection. Different ranges in pseudorapidity are shown in different colors. The bottom panel shows the ratio of the efficiency in data to the efficiency in simulation corresponding to the SF.

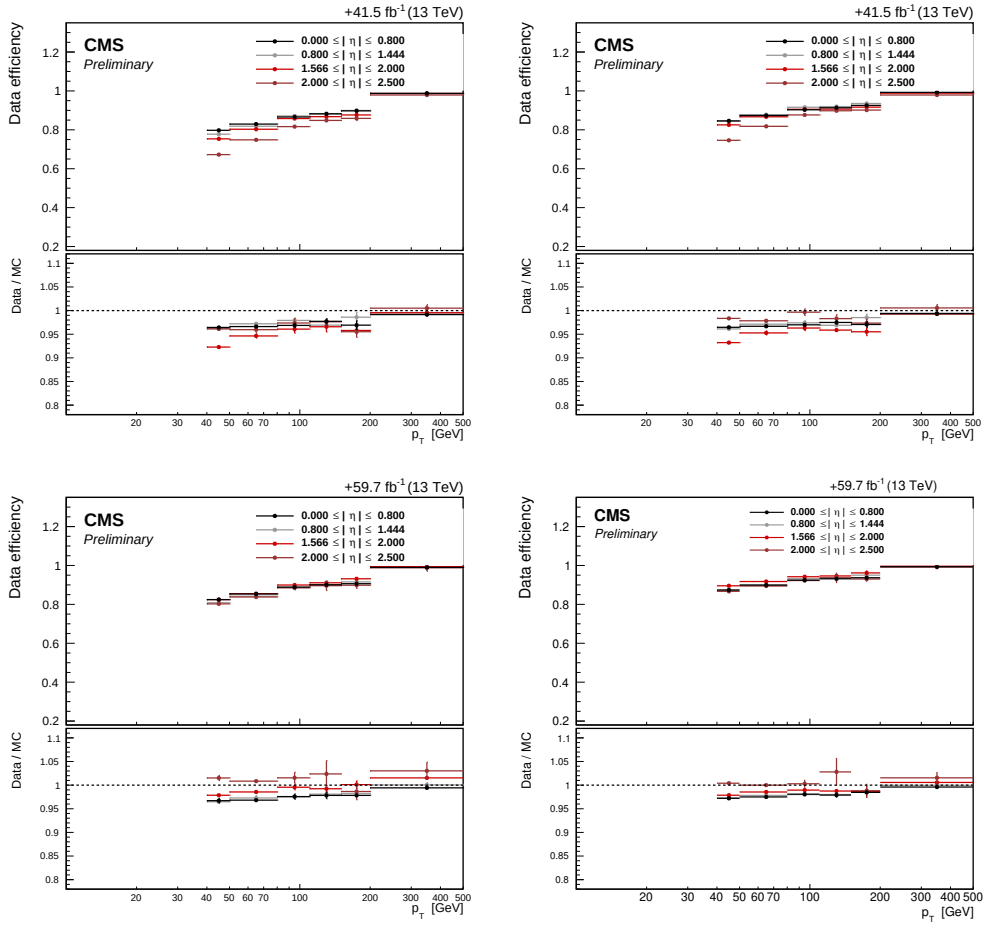

Figure A.2: Trigger efficiency of the electron triggers in data as a function of the transverse momentum of the electron for the 2017 (top) and 2018 (bottom) data-taking eras. The left-hand side shows the efficiency for the loose electron collection, whereas the right-hand side shows the efficiency for the tight electron collection. Different ranges in pseudorapidity are shown in different colors. The bottom panel shows the ratio of the efficiency in data to the efficiency in simulation corresponding to the SF.

B Photon trigger scale factors

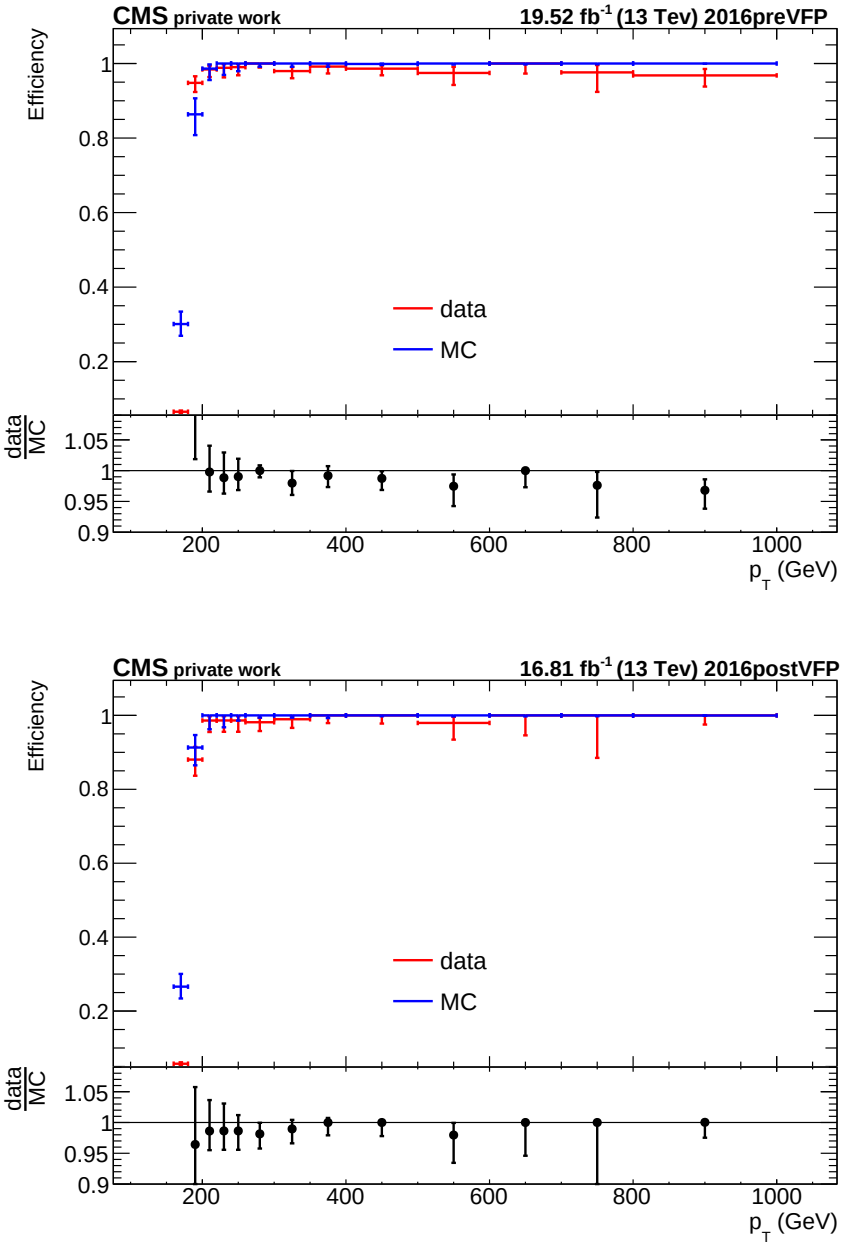

Figure B.1: Trigger efficiency of the photon triggers in data and simulation as a function of the transverse momentum of the photon for the 2016 data-taking eras. The rows correspond to the different data-taking eras 2016preVFP, 2016postVFP from top to bottom. The bottom panel shows the ratio of the efficiency in data to the efficiency in simulation corresponding to the SF.

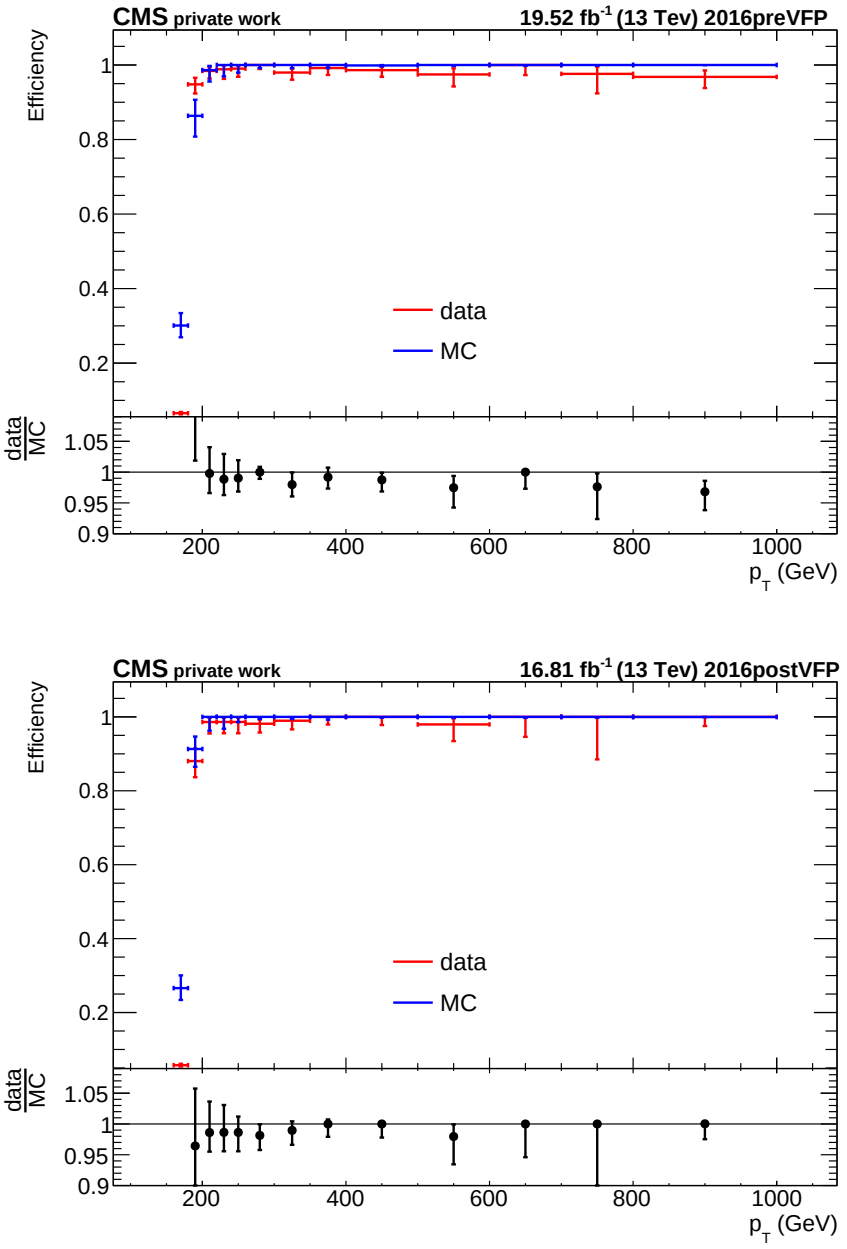

Figure B.2: Trigger efficiency of the photon triggers in data and simulation as a function of the transverse momentum of the photon for the 2017 (top) and 2018 (bottom) data-taking eras. The bottom panel shows the ratio of the efficiency in data to the efficiency in simulation corresponding to the SF.

C B-tagging efficiencies

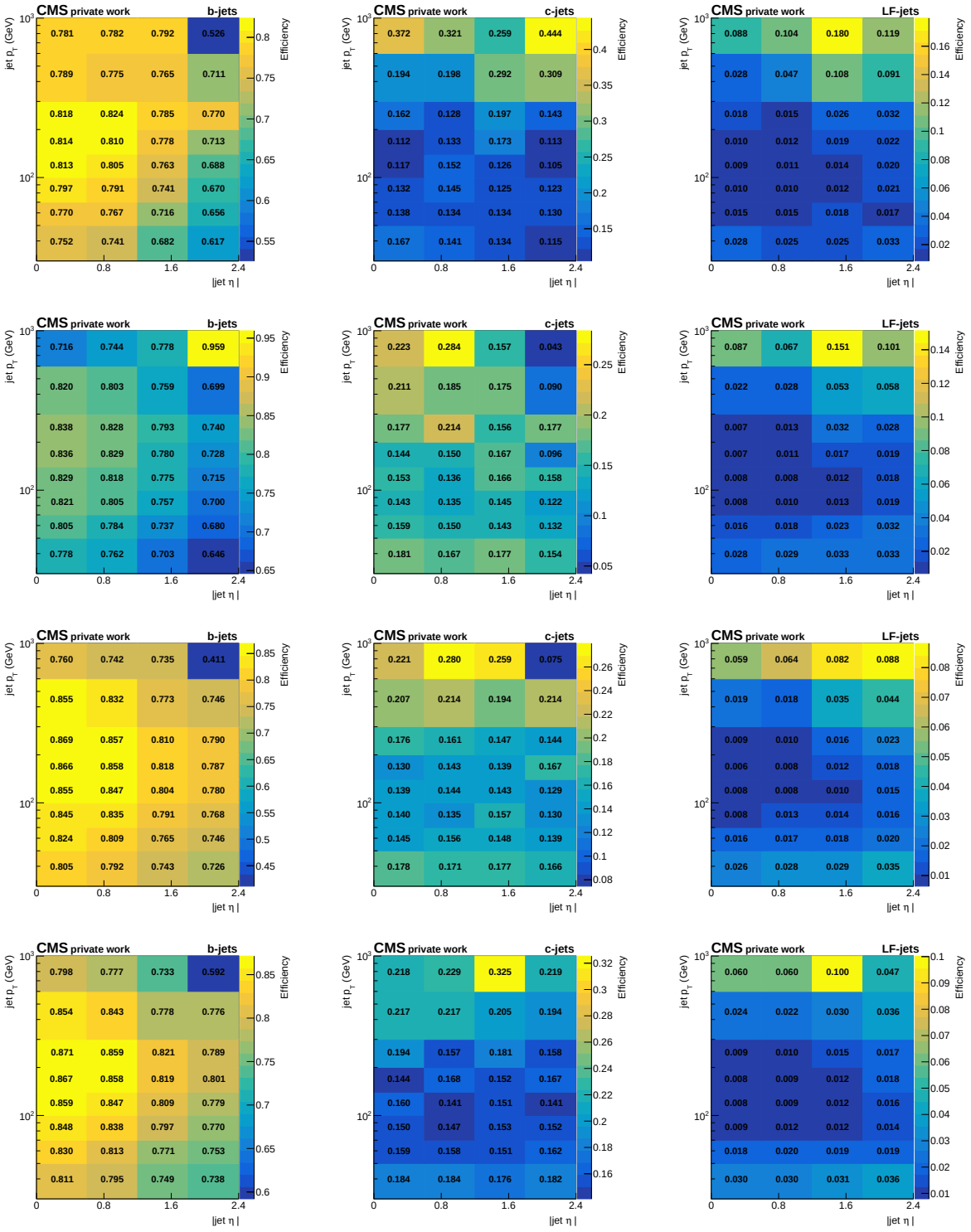

Figure C.1: Shown are the b-tagging efficiencies of the `DeepJet` algorithm for AK4 jets considered for b-tagging in the leptonic mono-top analysis in bins of transverse momentum p_T and the absolute value of pseudorapidity η. The efficiencies are shown separately for b,c and LF jets (from left to right). The rows correspond to the four data-taking eras 2016preVFP, 2016postVFP, 2017 and 2018 from top to bottom.

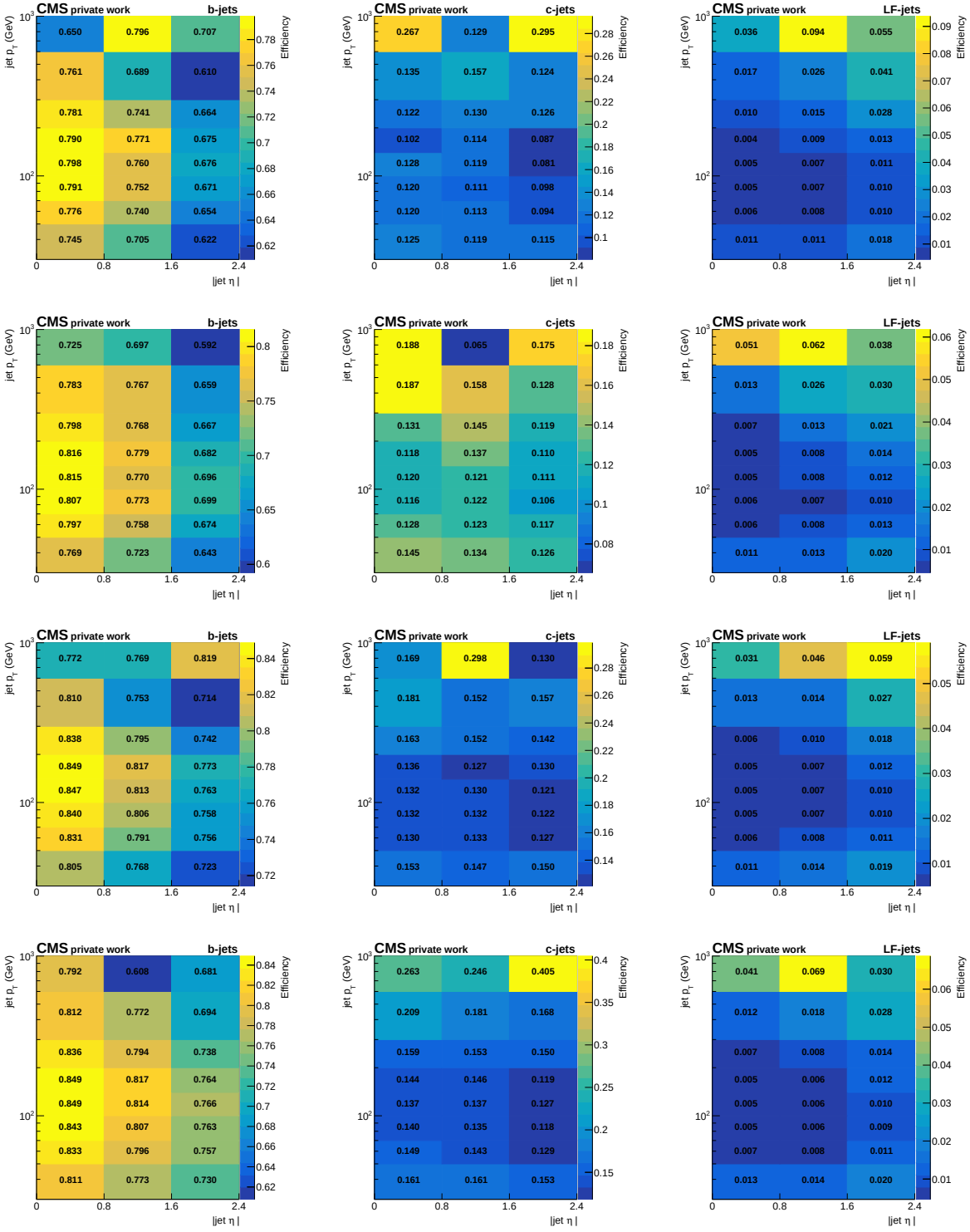

Figure C.2: Shown are the b-tagging efficiencies of the `DeepJet` algorithm for AK4 jets in considered for b-tagging in the hadronic mono-top analysis in bins of transverse momentum p_T and the absolute value of pseudorapidity η. The efficiencies are shown separately for b,c and LF jets (from left to right). The rows correspond to the four data-taking eras 2016preVFP, 2016postVFP, 2017 and 2018 from top to bottom.

D Naming of nuisance parameters

Table D.1: Labels of nuisance parameters parametrizing experimental uncertainties in the statistical model.

Source	Label
b-tagging (HF, loose WP, uncorrelated)	`btagL_YEAR`
b-tagging (HF, medium WP, uncorrelated)	`btagM_YEAR`
b-tagging (HF, correlated)	`btag_correlated`
b-tagging (LF, loose WP, uncorrelated)	`mistagL_YEAR`
b-tagging (LF, medium WP, uncorrelated)	`mistagM_YEAR`
b-tagging (HF, correlated)	`mistag_correlated`
Electron identification	`electronID_YEAR`
Electron reconstruction	`electronReco_YEAR`
Muon identification	`muonID_YEAR`
Muon isolation	`muonIso_YEAR`
Photon identification	`photonID_YEAR`
Electron trigger	`electronTrigger_YEAR`
Muon trigger	`muonTrigger_YEAR`
Photon trigger	`photonTrigger_YEAR`
$\not{E}_\mathrm{T}$/recoil trigger	`metTrigger_YEAR`
JER	`jer_YEAR`
JES	`jesTotal_YEAR`
$\not{E}_\mathrm{T}$ unclustered energy	`unclustEn_YEAR`
top efficiency unc. ($250\,\mathrm{GeV} \leq p_\mathrm{T}^{\mathrm{AK15\ jet}} < 300\,\mathrm{GeV}$)	`TopTag_250_300_YEAR`
top efficiency unc. ($300\,\mathrm{GeV} \leq p_\mathrm{T}^{\mathrm{AK15\ jet}} < 350\,\mathrm{GeV}$)	`TopTag_300_350_YEAR`
top efficiency unc. ($350\,\mathrm{GeV} \leq p_\mathrm{T}^{\mathrm{AK15\ jet}} < 400\,\mathrm{GeV}$)	`TopTag_350_400_YEAR`
top efficiency unc. ($400\,\mathrm{GeV} \leq p_\mathrm{T}^{\mathrm{AK15\ jet}} < 500\,\mathrm{GeV}$)	`TopTag_400_500_YEAR`
top efficiency unc. ($500\,\mathrm{GeV} \leq p_\mathrm{T}^{\mathrm{AK15\ jet}}$	`TopTag_500_inf_YEAR`
unmerged top efficiency unc. ($250\,\mathrm{GeV} \leq p_\mathrm{T}^{\mathrm{AK15\ jet}} < 300\,\mathrm{GeV}$)	`unmergedTopTag_250_300_YEAR`
unmerged top efficiency unc. ($300\,\mathrm{GeV} \leq p_\mathrm{T}^{\mathrm{AK15\ jet}} < 350\,\mathrm{GeV}$)	`unmergedTopTag_300_350_YEAR`
unmerged top efficiency unc. ($350\,\mathrm{GeV} \leq p_\mathrm{T}^{\mathrm{AK15\ jet}} < 400\,\mathrm{GeV}$)	`unmergedTopTag_350_400_YEAR`
unmerged top efficiency unc. ($400\,\mathrm{GeV} \leq p_\mathrm{T}^{\mathrm{AK15\ jet}} < 500\,\mathrm{GeV}$)	`unmergedTopTag_400_500_YEAR`
unmerged top efficiency unc. ($500\,\mathrm{GeV} \leq p_\mathrm{T}^{\mathrm{AK15\ jet}}$	`unmergedTopTag_500_inf_YEAR`
QCD efficiency unc. ($250\,\mathrm{GeV} \leq p_\mathrm{T}^{\mathrm{AK15\ jet}} < 300\,\mathrm{GeV}$)	`TopMisTag_250_300_YEAR`
QCD efficiency unc. ($300\,\mathrm{GeV} \leq p_\mathrm{T}^{\mathrm{AK15\ jet}} < 350\,\mathrm{GeV}$)	`TopMisTag_300_350_YEAR`
QCD efficiency unc. ($350\,\mathrm{GeV} \leq p_\mathrm{T}^{\mathrm{AK15\ jet}} < 400\,\mathrm{GeV}$)	`TopMisTag_350_400_YEAR`
QCD efficiency unc. ($400\,\mathrm{GeV} \leq p_\mathrm{T}^{\mathrm{AK15\ jet}} < 500\,\mathrm{GeV}$)	`TopMisTag_400_500_YEAR`
QCD efficiency unc. ($500\,\mathrm{GeV} \leq p_\mathrm{T}^{\mathrm{AK15\ jet}}$)	`TopMisTag_500_inf_YEAR`
PU	`pileup_YEAR`
L1 pre-firing issue uncertainty	`prefire_YEAR`
luminosity uncertainty, decorrelated across data-taking eras	`CMS_Lumi_YEAR`
luminosity uncertainty, correlated across data-taking eras	`CMS_Lumi_16_17_18`
luminosity uncertainty, correlated between 2017 and 2018	`CMS_Lumi_17_18`

Table D.2: Labels of nuisance parameters parametrizing theoretical modeling uncertainties in the statistical model.

Source	Label
PDF uncertainty	`PDF`
V + jets EWK correction (1)	`TH_vjets_EW1`
EWK correction (2)	`TH_vjets_EW2_aj`
V + jets EWK correction (2)	`TH_vjets_EW2_eej`
V + jets EWK correction (2)	`TH_vjets_EW2_evj`
V + jets EWK correction (2)	`TH_vjets_EW2_vvj`
V + jets EWK correction (3)	`TH_vjets_EW3_aj`
V + jets EWK correction (3)	`TH_vjets_EW3_eej`
V + jets EWK correction (3)	`TH_vjets_EW3_evj`
V + jets EWK correction (3)	`TH_vjets_EW3_vvj`
top quark p_{T} reweighting	`TopPt_reweighting`
μ_{F} variation for single top quark	`factScale_ST`
μ_{F} variation for $\mathrm{Z}(\nu\nu)$ + jets	`factScale_ZNuNujets`
μ_{F} variation for $\mathrm{Z}(\ell\ell)$ + jets	`factScale_dyjets`
μ_{F} variation for γ + jets	`factScale_gammajets`
μ_{F} variation for mono-top signal	`factScale_signal`
μ_{F} variation for $\mathrm{t\bar{t}}$	`factScale_tt`
μ_{F} variation for $\mathrm{W}(\ell\nu)$ + jets	`factScale_wjets`
μ_{R} variation for single top quark	`renScale_ST`
μ_{R} variation for $\mathrm{Z}(\nu\nu)$ + jets	`renScale_ZNuNujets`
μ_{R} variation for $\mathrm{Z}(\ell\ell)$ + jets	`renScale_dyjets`
μ_{R} variation for γ + jets	`renScale_gammajets`
μ_{R} variation for mono-top signal	`renScale_signal`
μ_{R} variation for $\mathrm{t\bar{t}}$	`renScale_tt`
μ_{R} variation for $\mathrm{W}(\ell\nu)$ + jets	`renScale_wjets`
PS ISR variation	`fsr`
PS FSR variation	`isr`
JER	`jer_YEAR`
JES	`jesTotal_YEAR`
$\not{E}_{\mathrm{T}}$ unclustered energy	`unclustEn_YEAR`
QCD cross section uncertainty	`xs_QCD`
diboson cross section uncertainty	`xs_diboson`
γ + jets cross section uncertainty	`xs_gammajets`

E Control distribution in the leptonic analysis channel

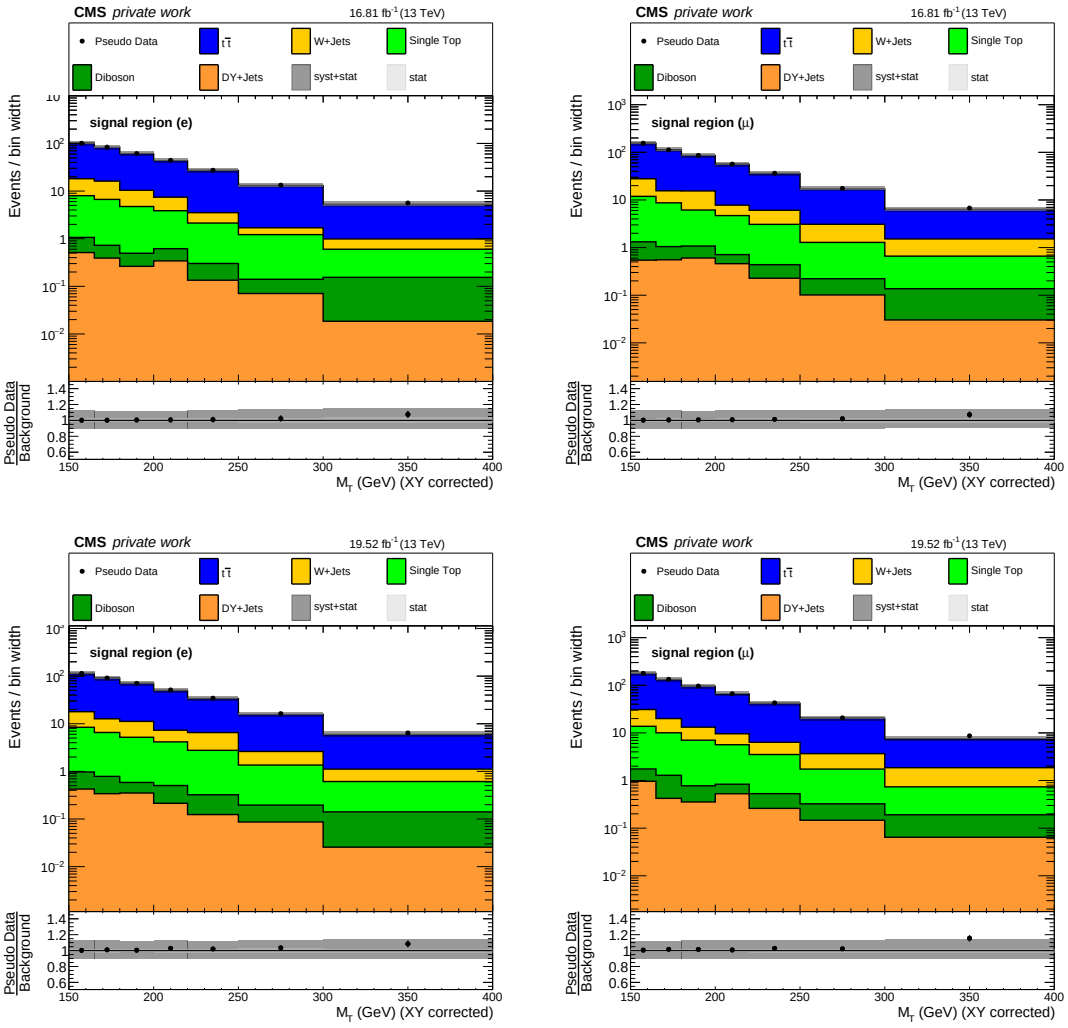

Figure E.1: Transverse mass distribution in the SRs of the leptonic mono-top analysis for the 2016 data-taking eras. The 2016postVFP and 2016preVFP data-taking eras are shown from top to bottom. The left-hand side shows the electron channel, whereas the right-hand side corresponds to the muon channel. A signal-plus-background pseudo dataset in black points is compared to the background prediction from simulation as colored stacked histograms for different processes. The lower pad in each plot shows the ratio of a signal-plus-background pseudo dataset to the total background prediction. An exemplary signal prediction with a mediator mass of 1000 GeV and DM candidate mass of 150 GeV scaled to the total sum of expected backgrounds is overlaid in cyan.

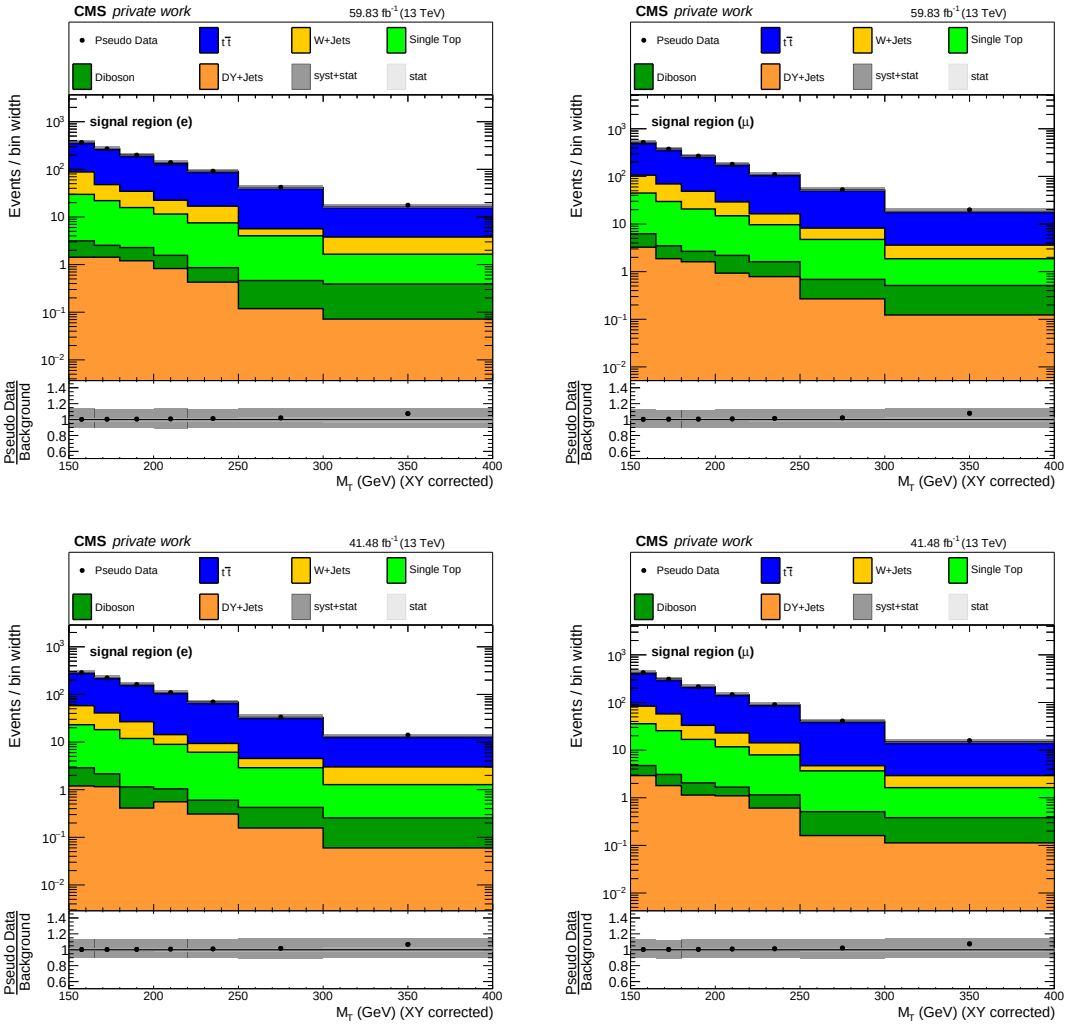

Figure E.2: Transverse mass distribution in the SRs of the leptonic mono-top analysis for the 2017 (top) and 2018 (bottom) data-taking eras. The left-hand side shows the electron channel, whereas the right-hand side corresponds to the muon channel. A signal-plus-background pseudo dataset in black points is compared to the background prediction from simulation as colored stacked histograms for different processes. The lower pad in each plot shows the ratio of a signal-plus-background pseudo dataset to the total background prediction. An exemplary signal prediction with a mediator mass of 1000 GeV and DM candidate mass of 150 GeV scaled to the total sum of expected backgrounds is overlaid in cyan.

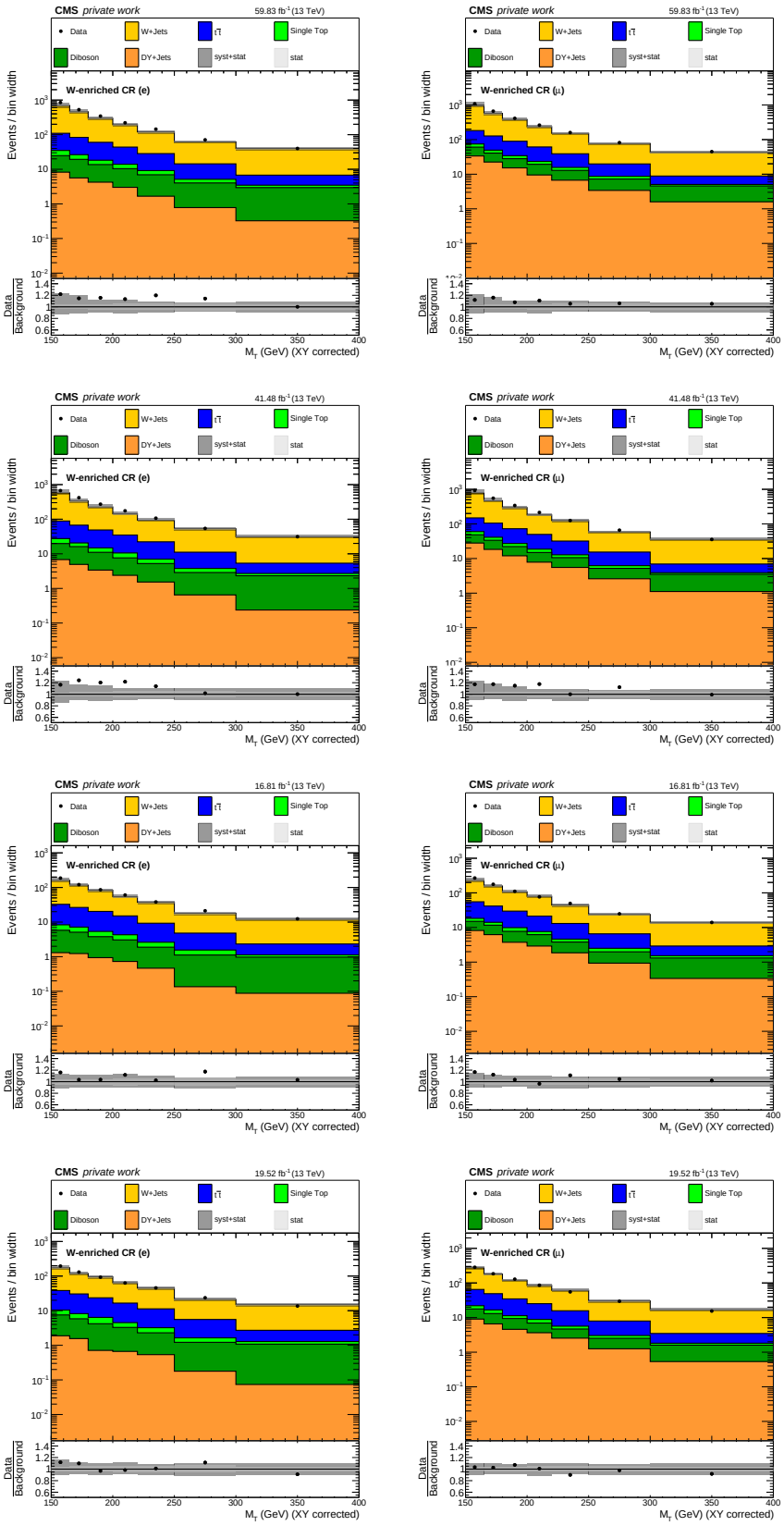

Figure E.3: Transverse mass distribution in the W boson CRs of the leptonic mono-top analysis for all four data-taking eras. The 2018, 2017, 2016postVFP, 2016pre-VFP data-taking eras are shown from top to bottom. The left-hand side shows the electron channel, whereas the right-hand side corresponds to the muon channel. The measured data in black points are compared to the background prediction from simulation as colored stacked histograms for different processes. The lower pad in each plot shows the ratio of data to the total background prediction.

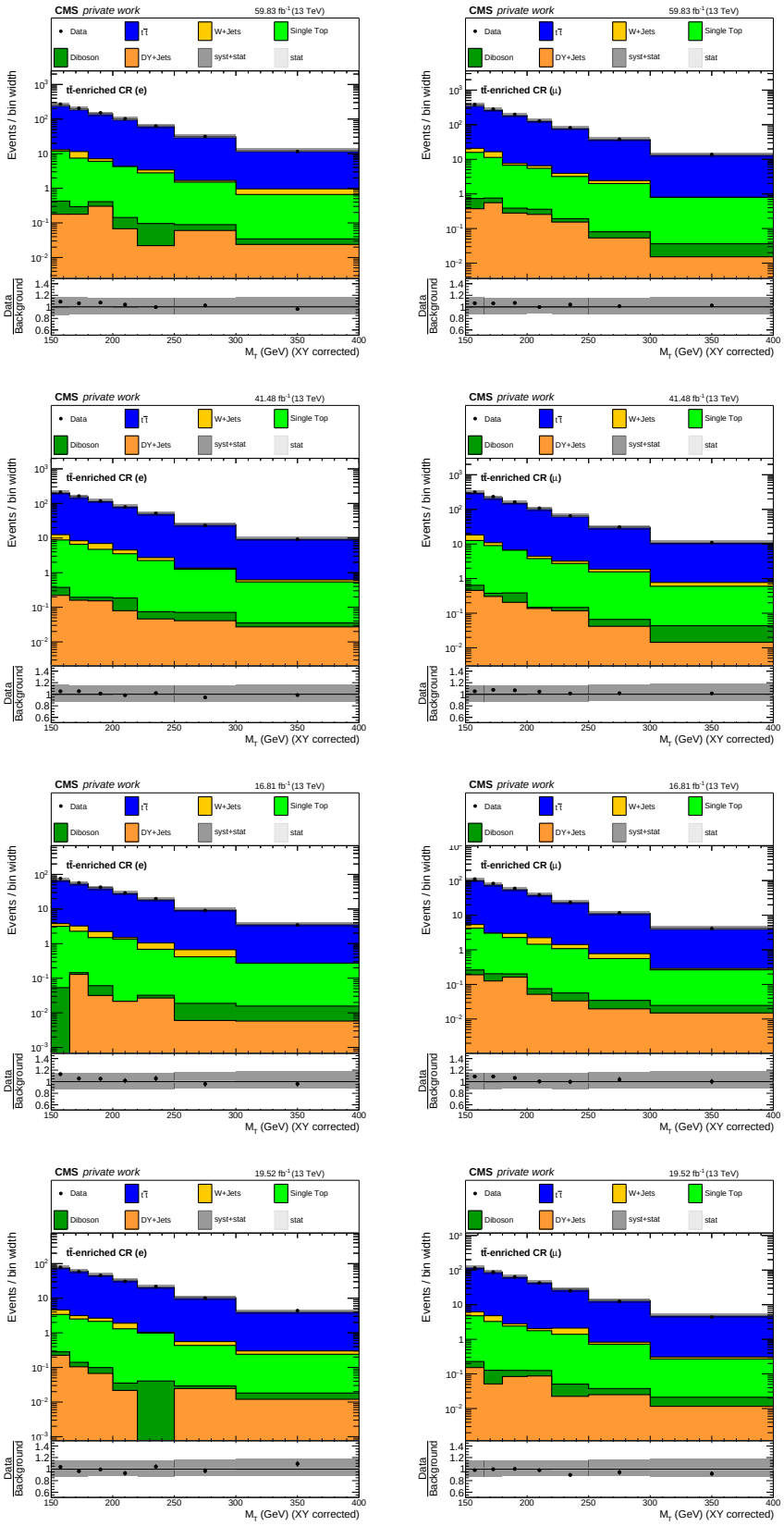

Figure E.4: Transverse mass distribution in the $t\bar{t}$ CRs of the leptonic mono-top analysis for all four data-taking eras. The 2018, 2017, 2016postVFP, 2016preVFP data-taking eras are shown from top to bottom. The left-hand side shows the electron channel, whereas the right-hand side corresponds to the muon channel. The measured data in black points are compared to the background prediction from simulation as colored stacked histograms for different processes. The lower pad in each plot shows the ratio of data to the total background prediction.

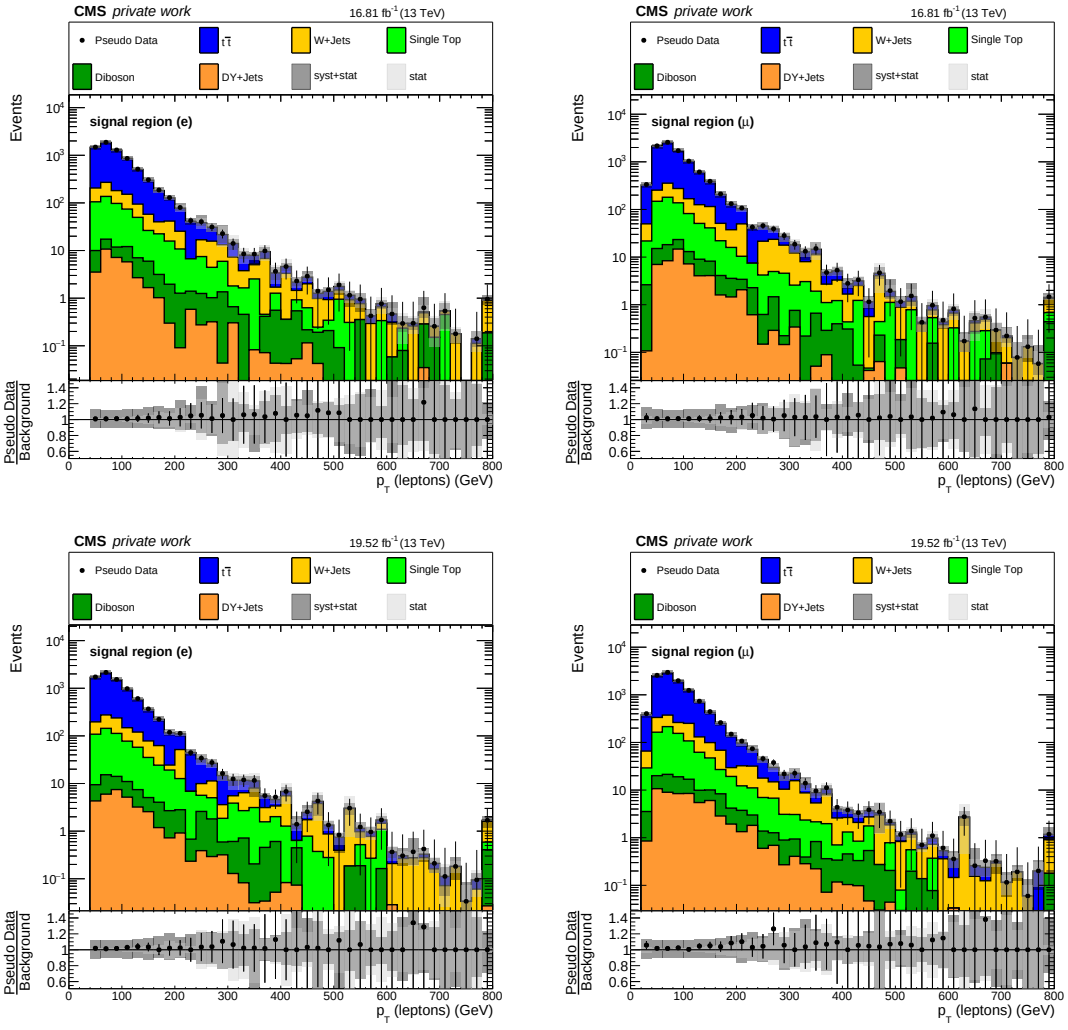

Figure E.5: Lepton p_{T} in the SRs of the leptonic mono-top analysis for the 2016 data-taking eras. The 2016postVFP and 2016preVFP data-taking eras are shown from top to bottom. The left-hand side shows the electron channel, whereas the right-hand side corresponds to the muon channel. A signal-plus-background pseudo dataset in black points is compared to the background prediction from simulation as colored stacked histograms for different processes. The lower pad in each plot shows the ratio of a signal-plus-background pseudo dataset to the total background prediction. An exemplary signal prediction with a mediator mass of 1000 GeV and DM candidate mass of 150 GeV scaled to the total sum of expected backgrounds is overlaid in cyan.

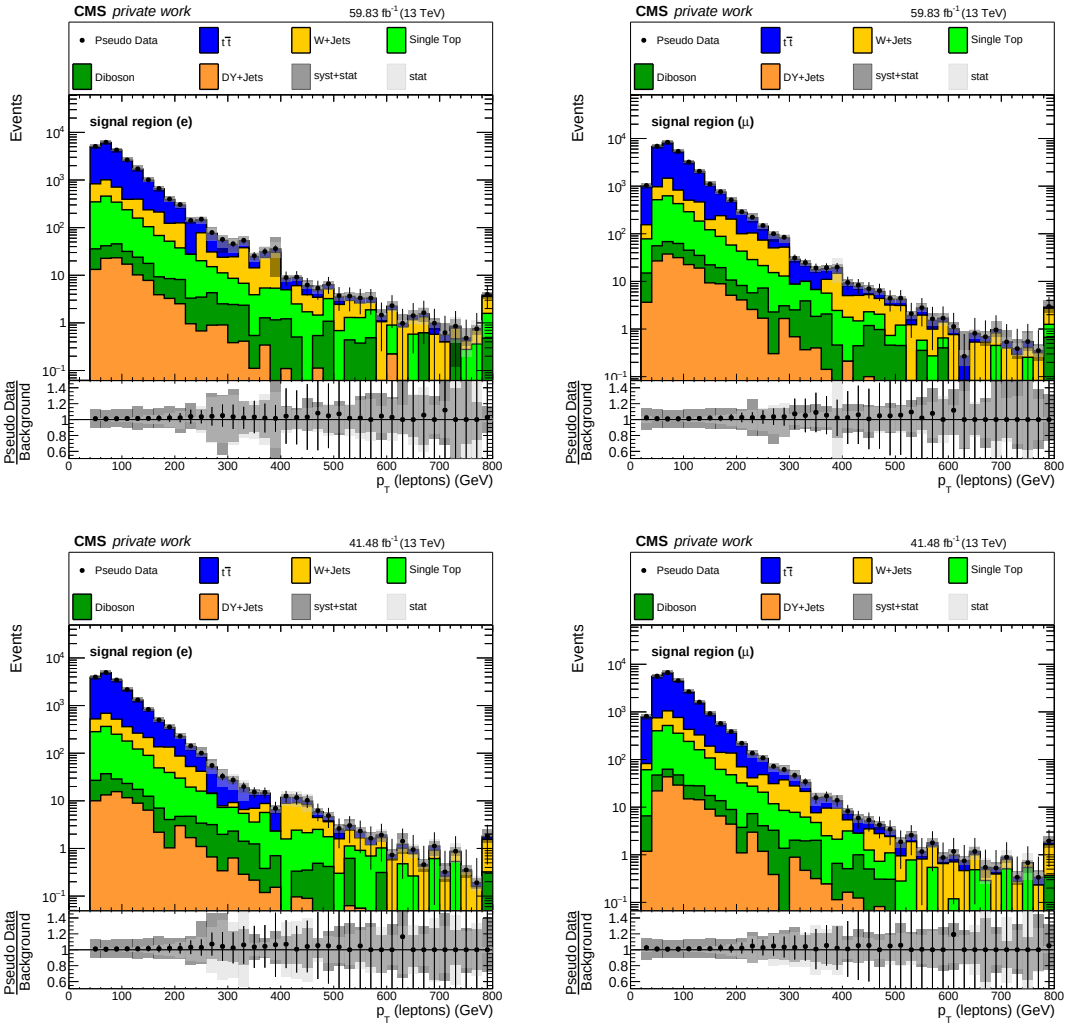

Figure E.6: Lepton p_{T} in the SRs of the leptonic mono-top analysis for the 2017 (top) and 2018 (bottom) data-taking eras. The left-hand side shows the electron channel, whereas the right-hand side corresponds to the muon channel. A signal-plus-background pseudo dataset in black points is compared to the background prediction from simulation as colored stacked histograms for different processes. The lower pad in each plot shows the ratio of a signal-plus-background pseudo dataset to the total background prediction. An exemplary signal prediction with a mediator mass of 1000 GeV and DM candidate mass of 150 GeV scaled to the total sum of expected backgrounds is overlaid in cyan.

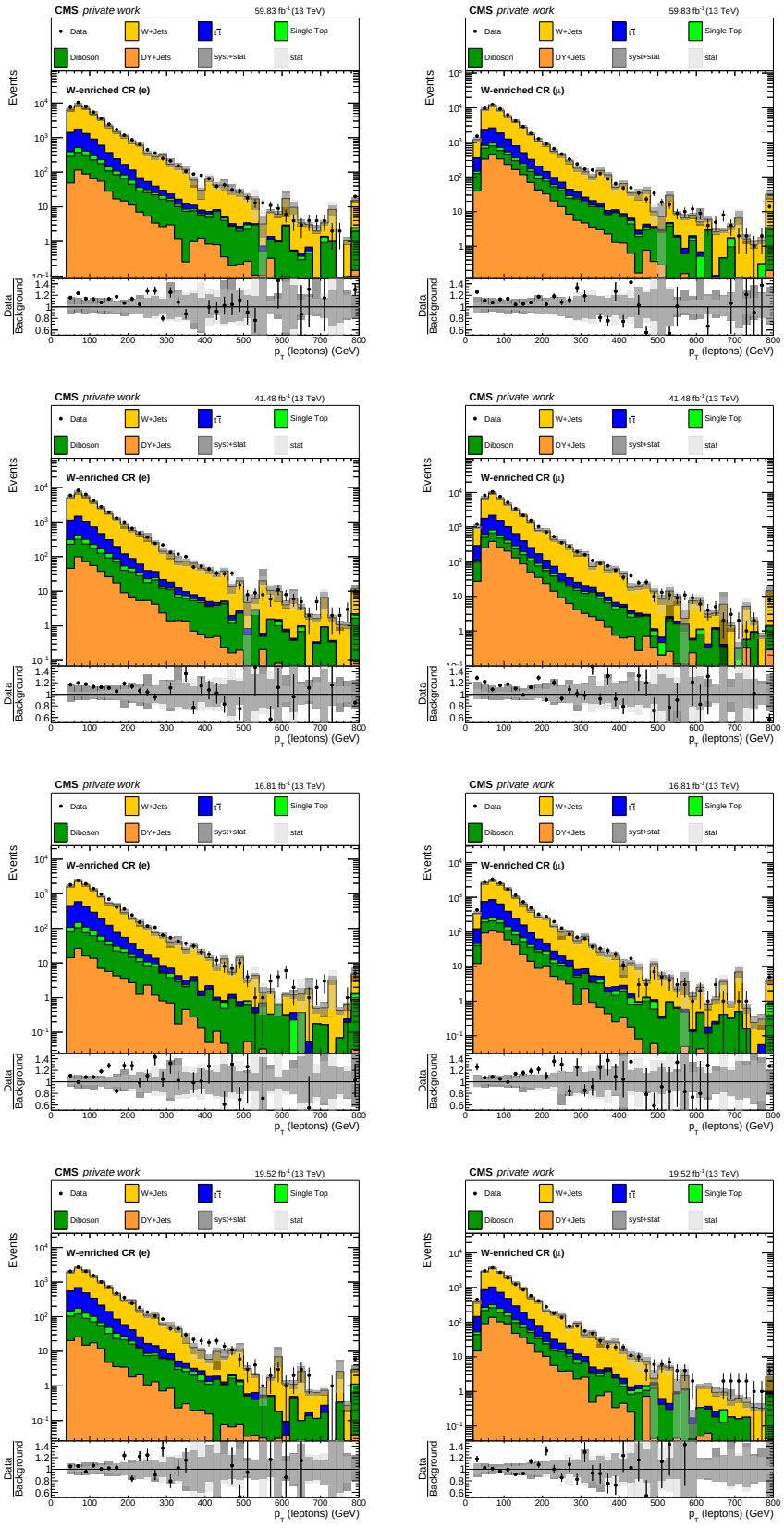

Figure E.7: Lepton p_T in the W boson CRs of the leptonic mono-top analysis for all four data-taking eras. The 2018, 2017, 2016postVFP, 2016preVFP data-taking eras are shown from top to bottom. The left-hand side shows the electron channel, whereas the right-hand side corresponds to the muon channel. The measured data in black points are compared to the background prediction from simulation as colored stacked histograms for different processes. The lower pad in each plot shows the ratio of data to the total background prediction.

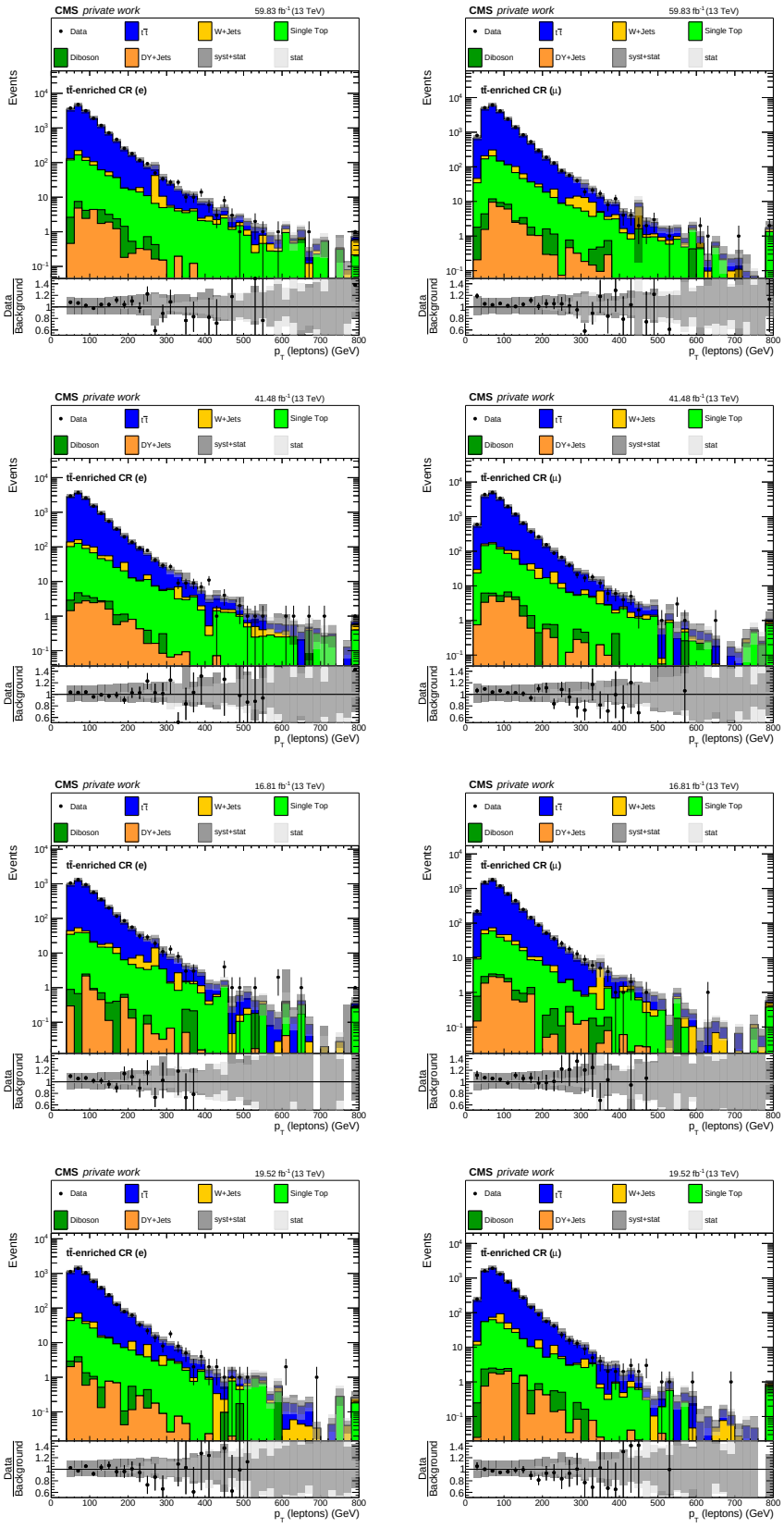

Figure E.8: Lepton p_T in the $t\bar{t}$ CRs of the leptonic mono-top analysis for all four data-taking eras. The 2018, 2017, 2016postVFP, 2016preVFP data-taking eras are shown from top to bottom. The left-hand side shows the electron channel, whereas the right-hand side corresponds to the muon channel. The measured data in black points are compared to the background prediction from simulation as colored stacked histograms for different processes. The lower pad in each plot shows the ratio of data to the total background prediction.

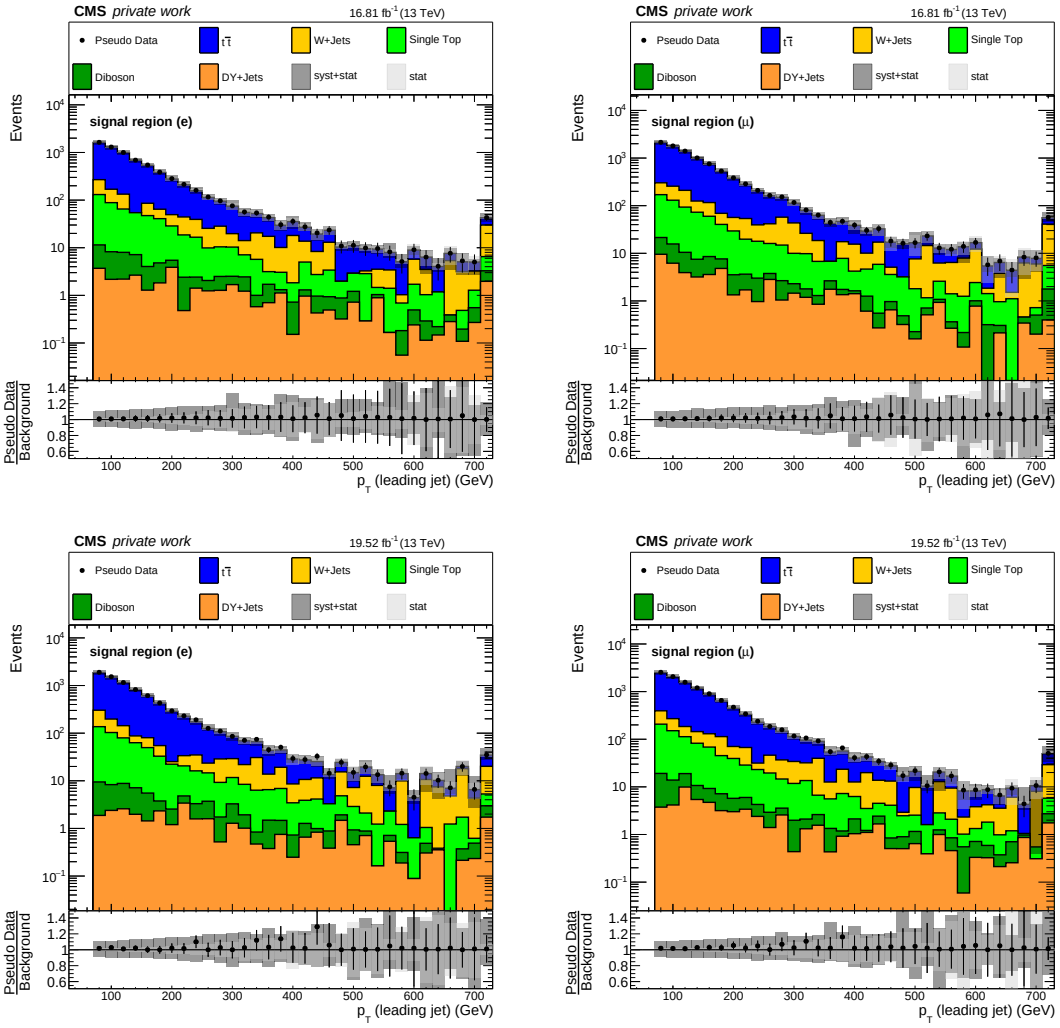

Figure E.9: Leading AK4 jet p_{T} in the SRs of the leptonic mono-top analysis for the 2016 data-taking eras. The 2016postVFP and 2016preVFP data-taking eras are shown from top to bottom. The left-hand side shows the electron channel, whereas the right-hand side corresponds to the muon channel. A signal-plus-background pseudo dataset in black points is compared to the background prediction from simulation as colored stacked histograms for different processes. The lower pad in each plot shows the ratio of a signal-plus-background pseudo dataset to the total background prediction. An exemplary signal prediction with a mediator mass of 1000 GeV and DM candidate mass of 150 GeV scaled to the total sum of expected backgrounds is overlaid in cyan.

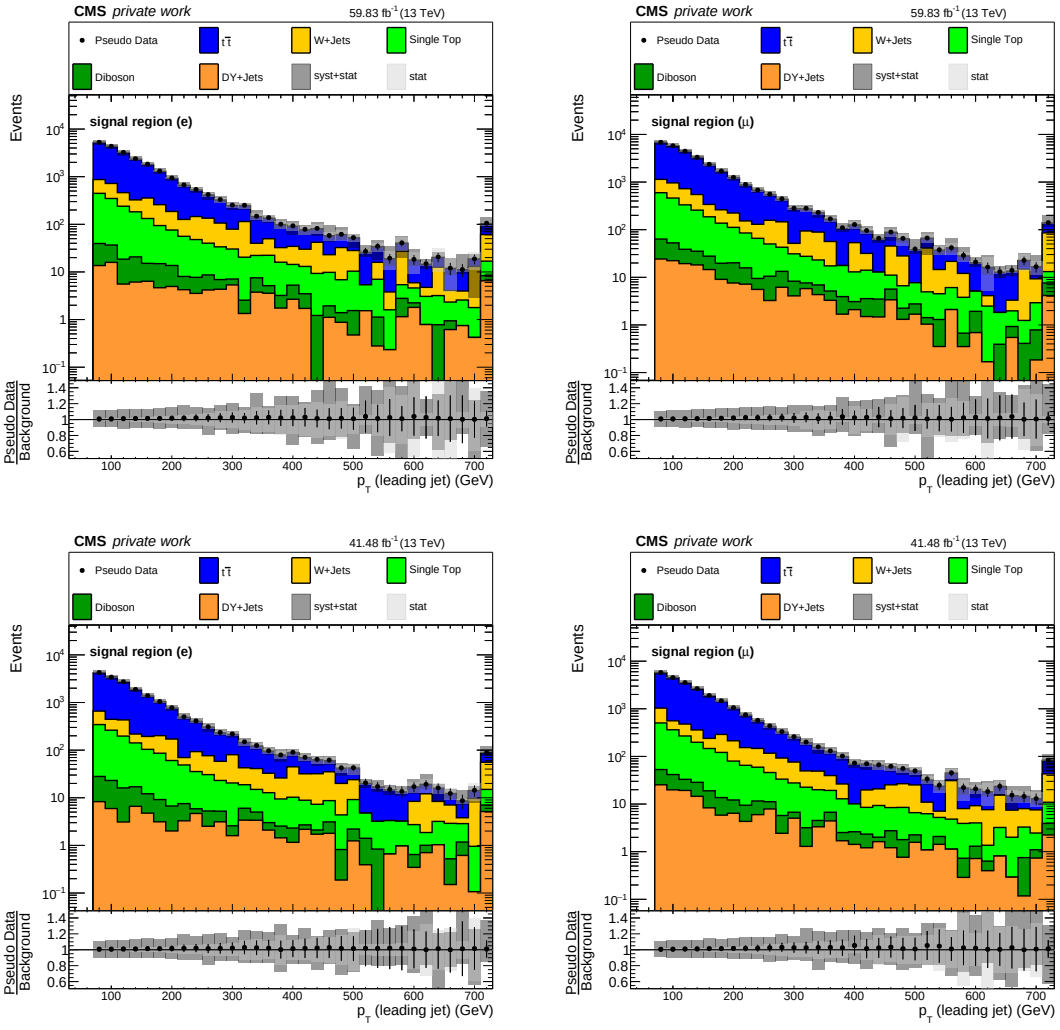

Figure E.10: Leading AK4 jet p_{T} in the SRs of the leptonic mono-top analysis for the 2017 (top) and 2018 (bottom) data-taking eras. The left-hand side shows the electron channel, whereas the right-hand side corresponds to the muon channel. A signal-plus-background pseudo dataset in black points is compared to the background prediction from simulation as colored stacked histograms for different processes. The lower pad in each plot shows the ratio of a signal-plus-background pseudo dataset to the total background prediction. An exemplary signal prediction with a mediator mass of 1000 GeV and DM candidate mass of 150 GeV scaled to the total sum of expected backgrounds is overlaid in cyan.

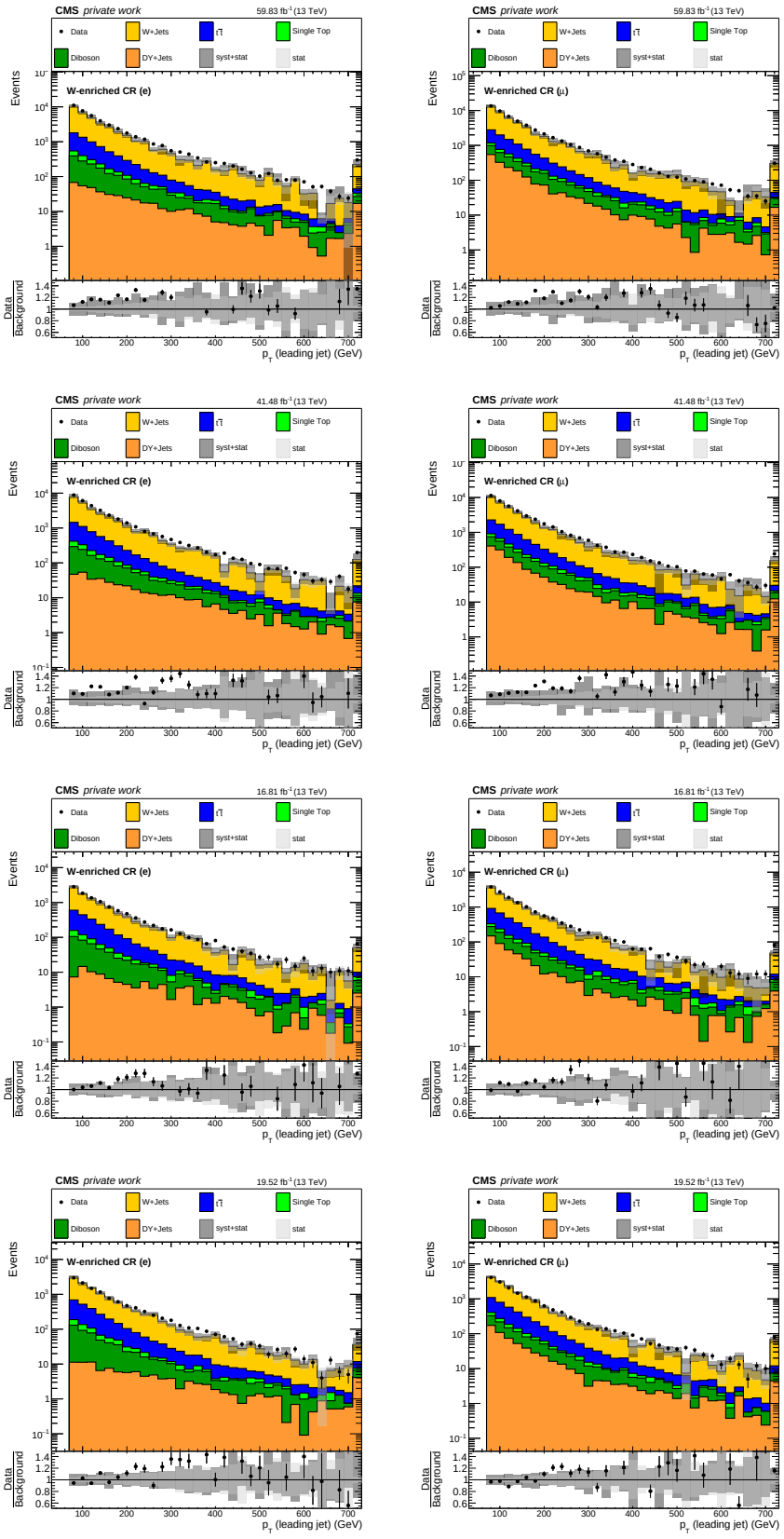

Figure E.11: Leading AK4 jet p_{T} in the W boson CRs of the leptonic mono-top analysis for all four data-taking eras. The 2018, 2017, 2016postVFP, 2016preVFP data-taking eras are shown from top to bottom. The left-hand side shows the electron channel, whereas the right-hand side corresponds to the muon channel. The measured data in black points are compared to the background prediction from simulation as colored stacked histograms for different processes. The lower pad in each plot shows the ratio of data to the total background prediction.

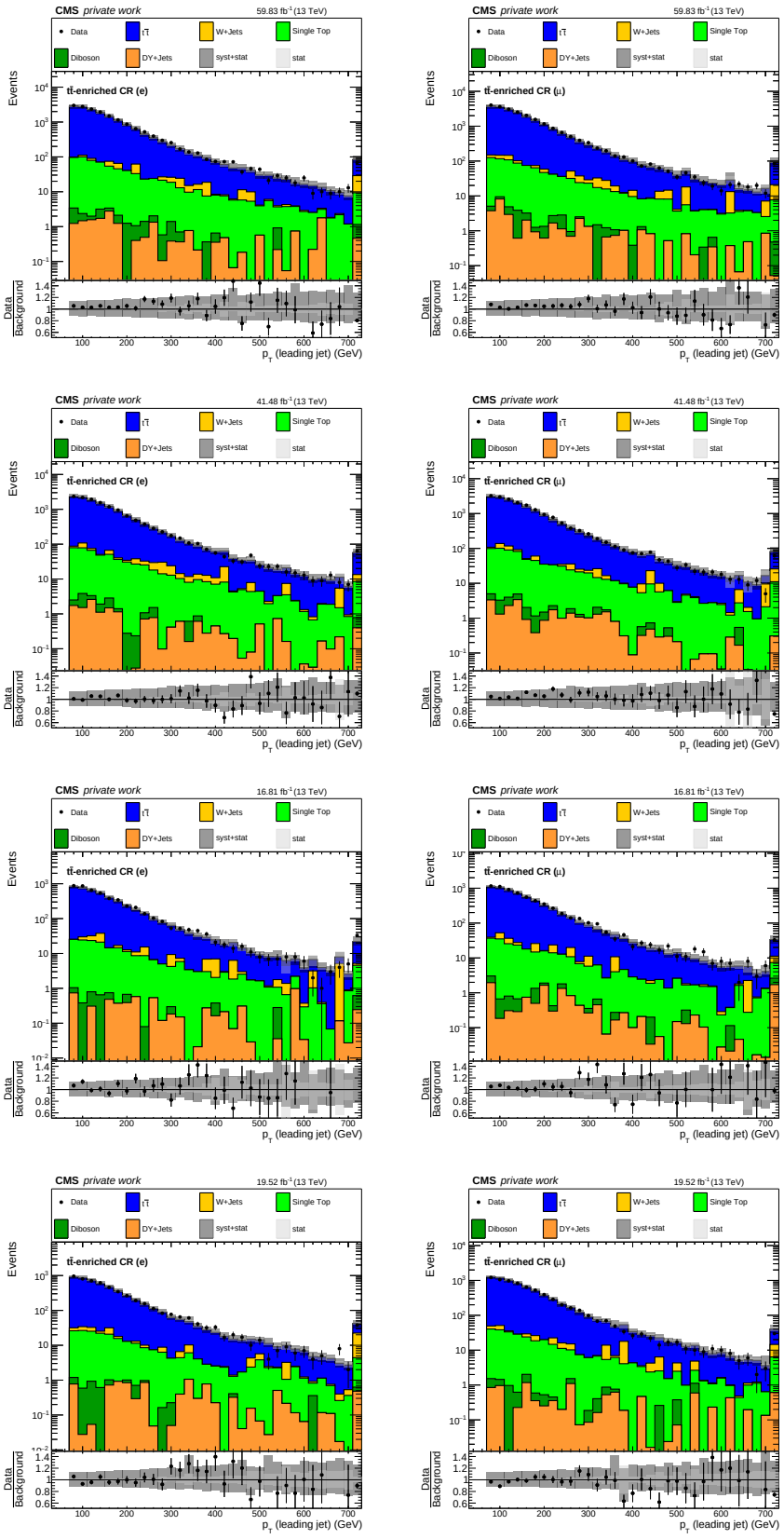

Figure E.12: Leading AK4 jet p_{T} in the $\mathrm{t\bar{t}}$ CRs of the leptonic mono-top analysis for all four data-taking eras. The 2018, 2017, 2016postVFP, 2016preVFP data-taking eras are shown from top to bottom. The left-hand side shows the electron channel, whereas the right-hand side corresponds to the muon channel. The measured data in black points are compared to the background prediction from simulation as colored stacked histograms for different processes. The lower pad in each plot shows the ratio of data to the total background prediction.

F Pulls in control region only fit in leptonic analysis

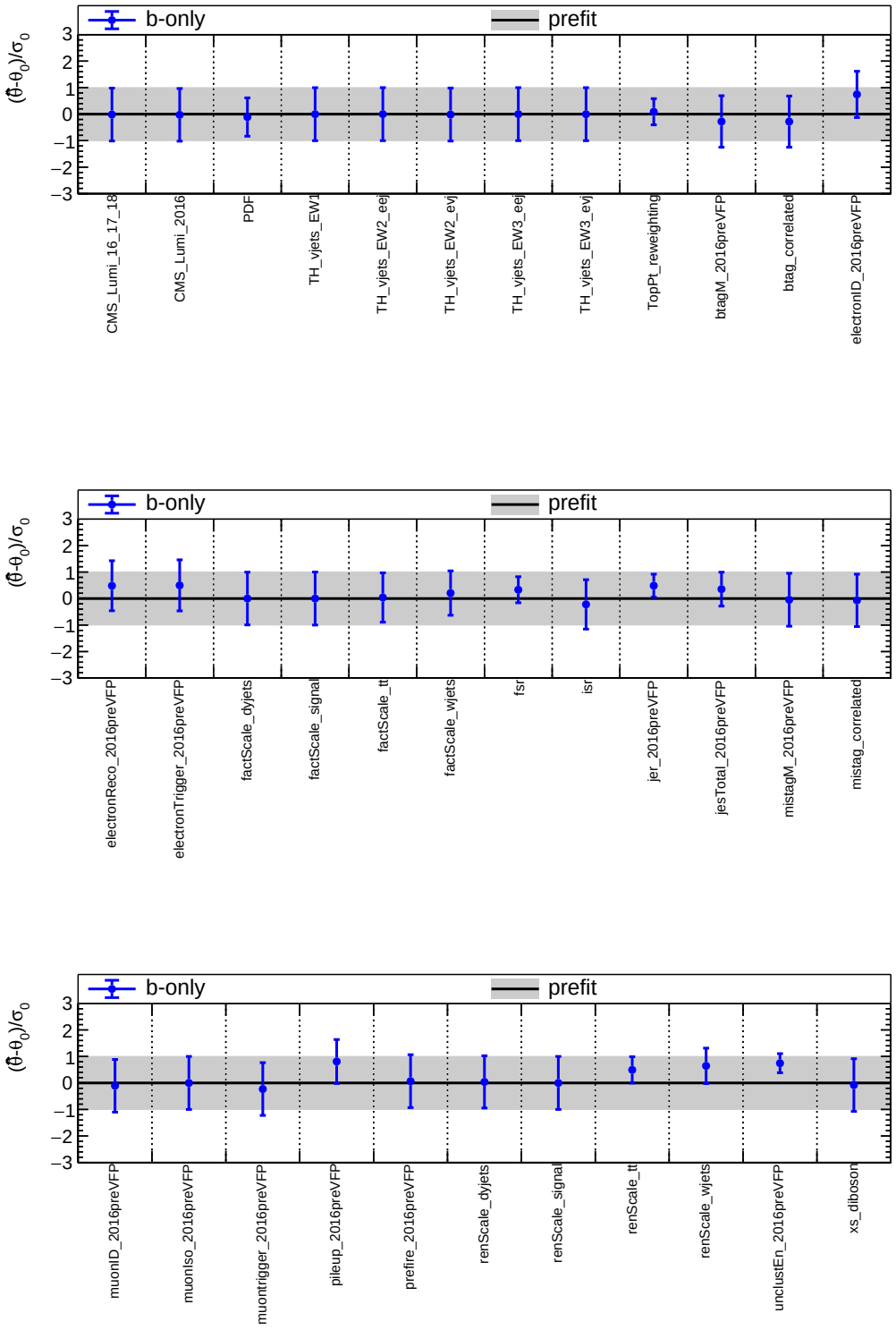

Figure F.1: Pulls of the nuisance parameters after performing the background-only fit in all CRs combined for 2016preVFP.

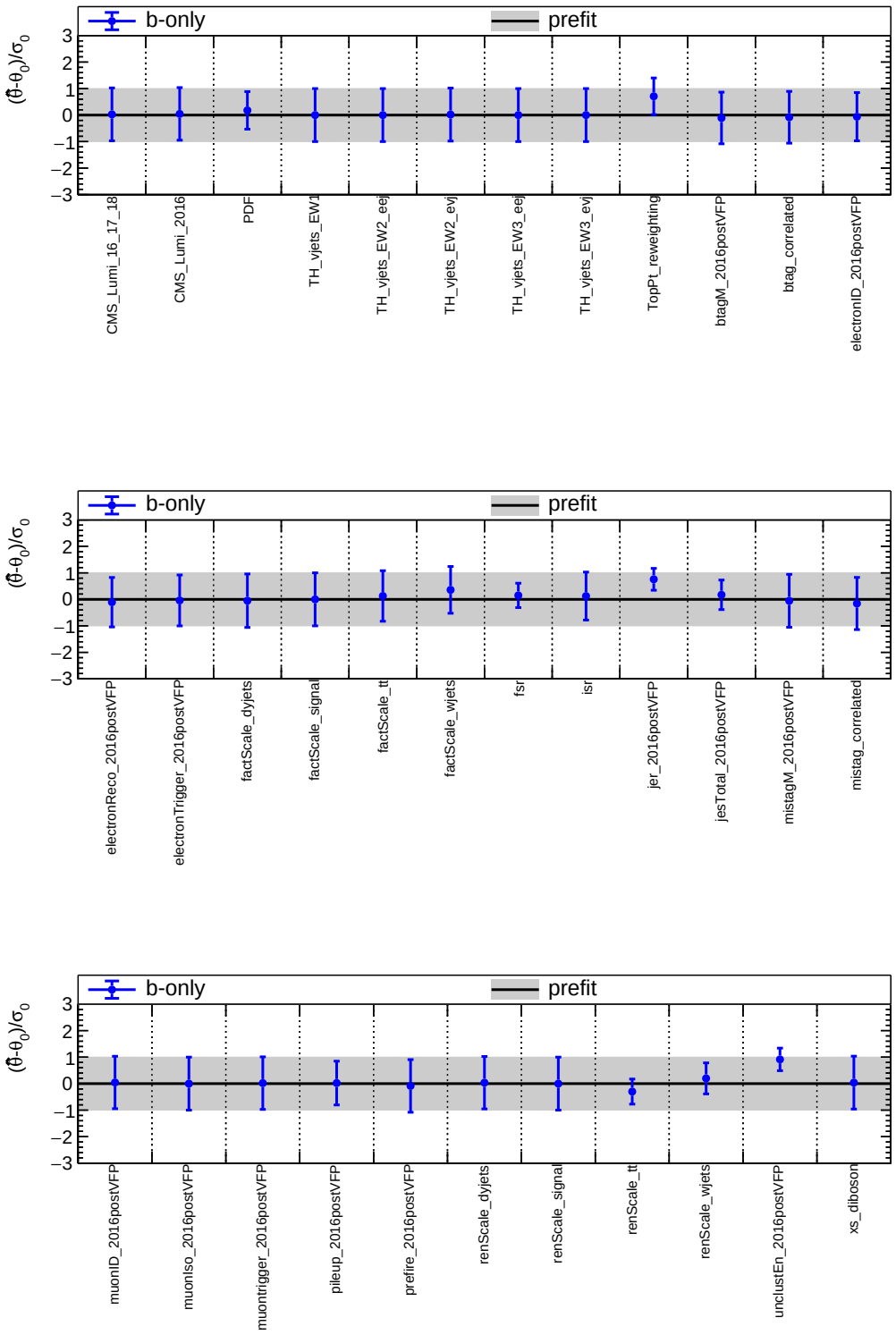

Figure F.2: Pulls of the nuisance parameters after performing the background-only fit in all CRs combined for 2016postVFP.

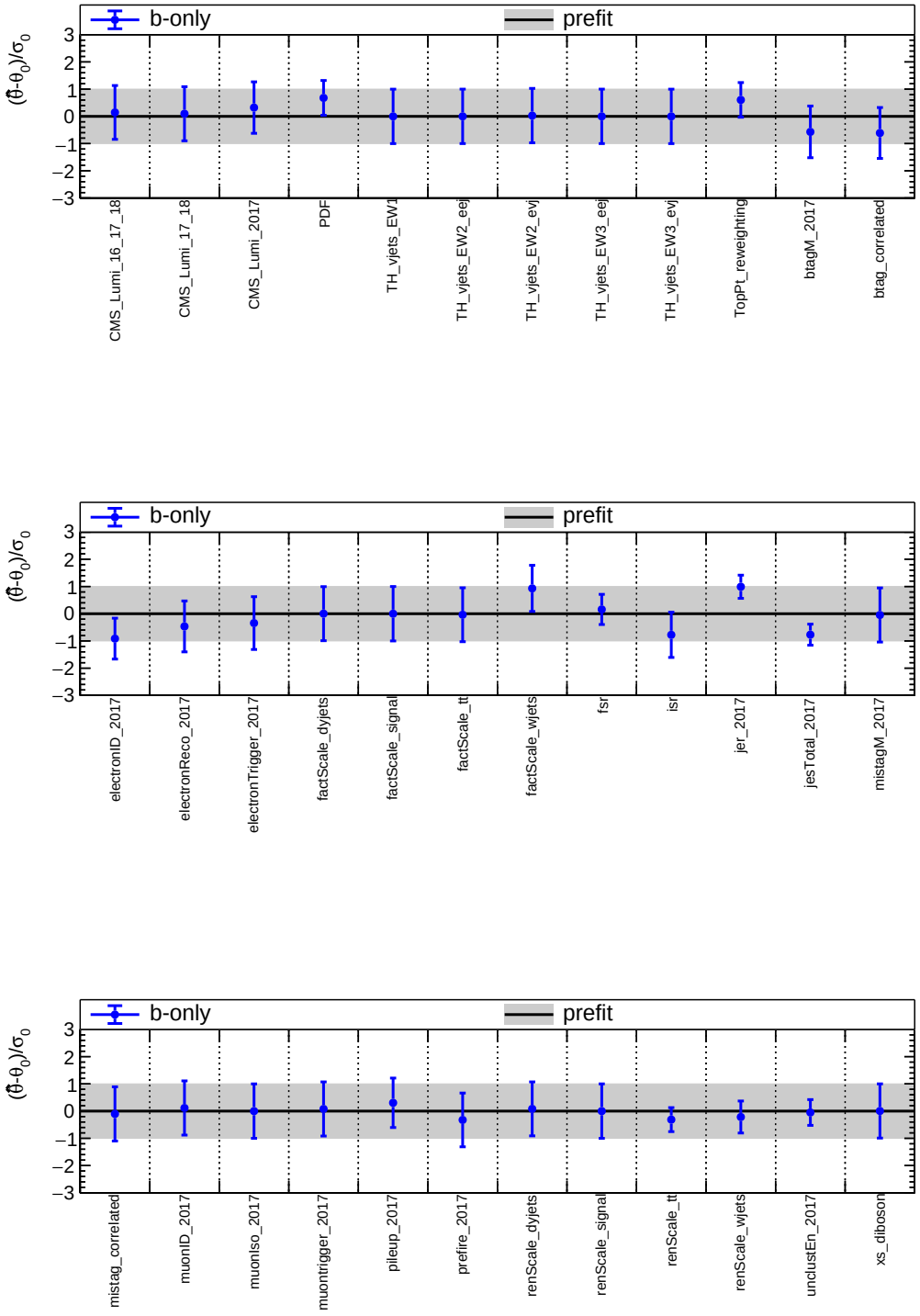

Figure F.3: Pulls of the nuisance parameters after performing the background-only fit in all CRs combined for 2017.

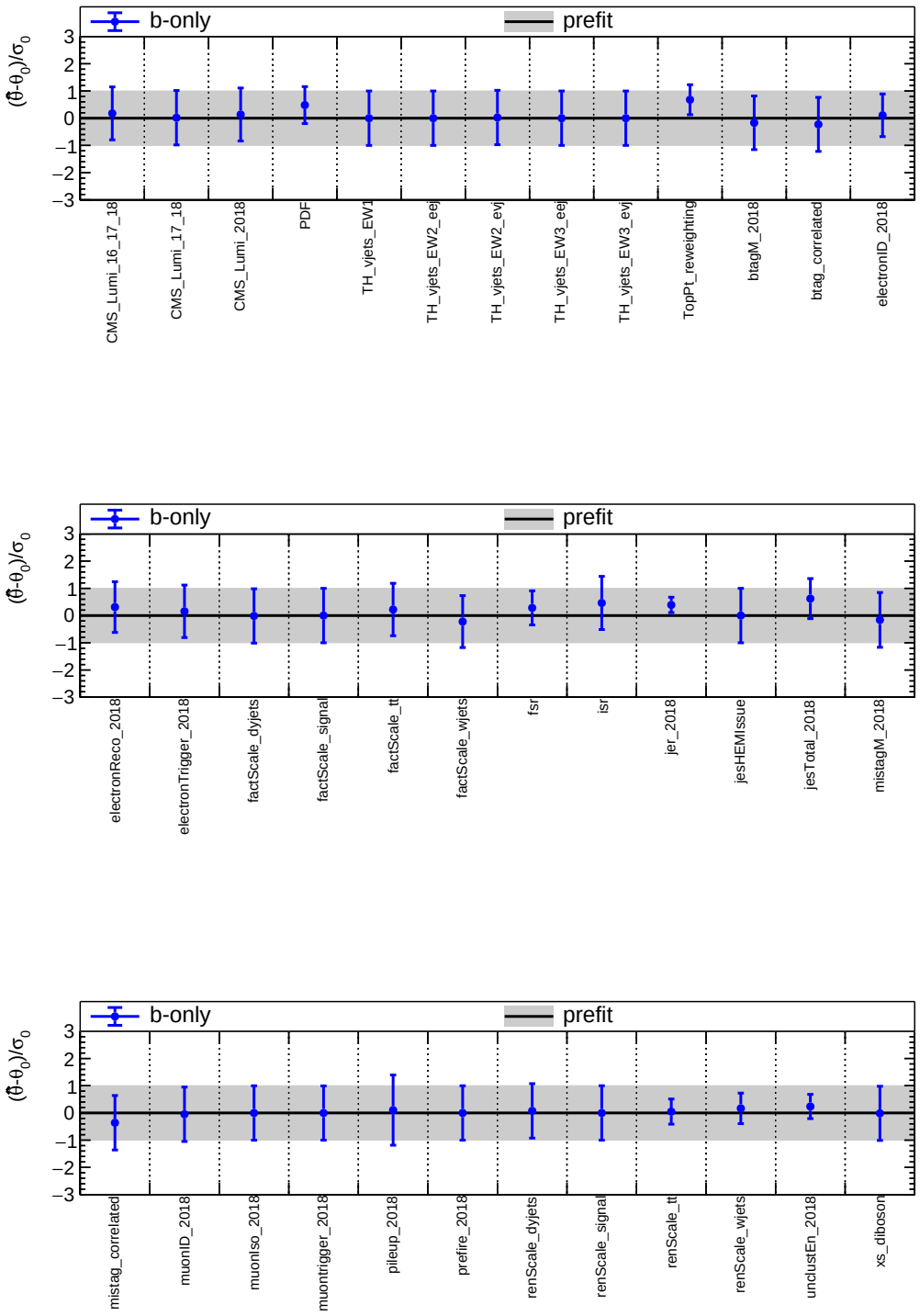

Figure F.4: Pulls of the nuisance parameters after performing the background-only fit in all CRs combined for 2018.

G Pulls and constraints in leptonic analysis

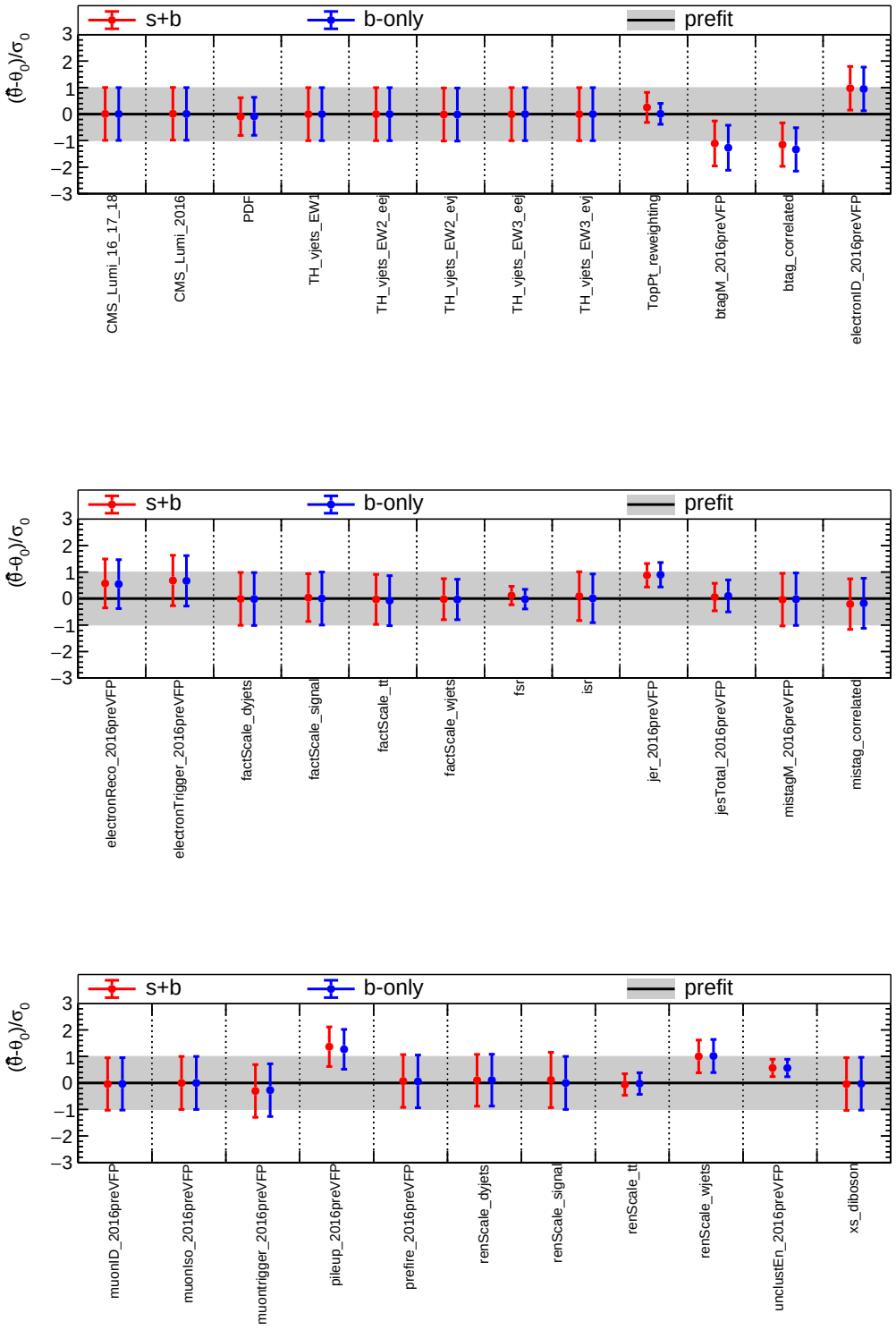

Figure G.1: Pulls of the nuisance parameters after performing a background-only and signal-plus-background fit in all analysis regions combined for 2016preVFP in blue and red, respectively.

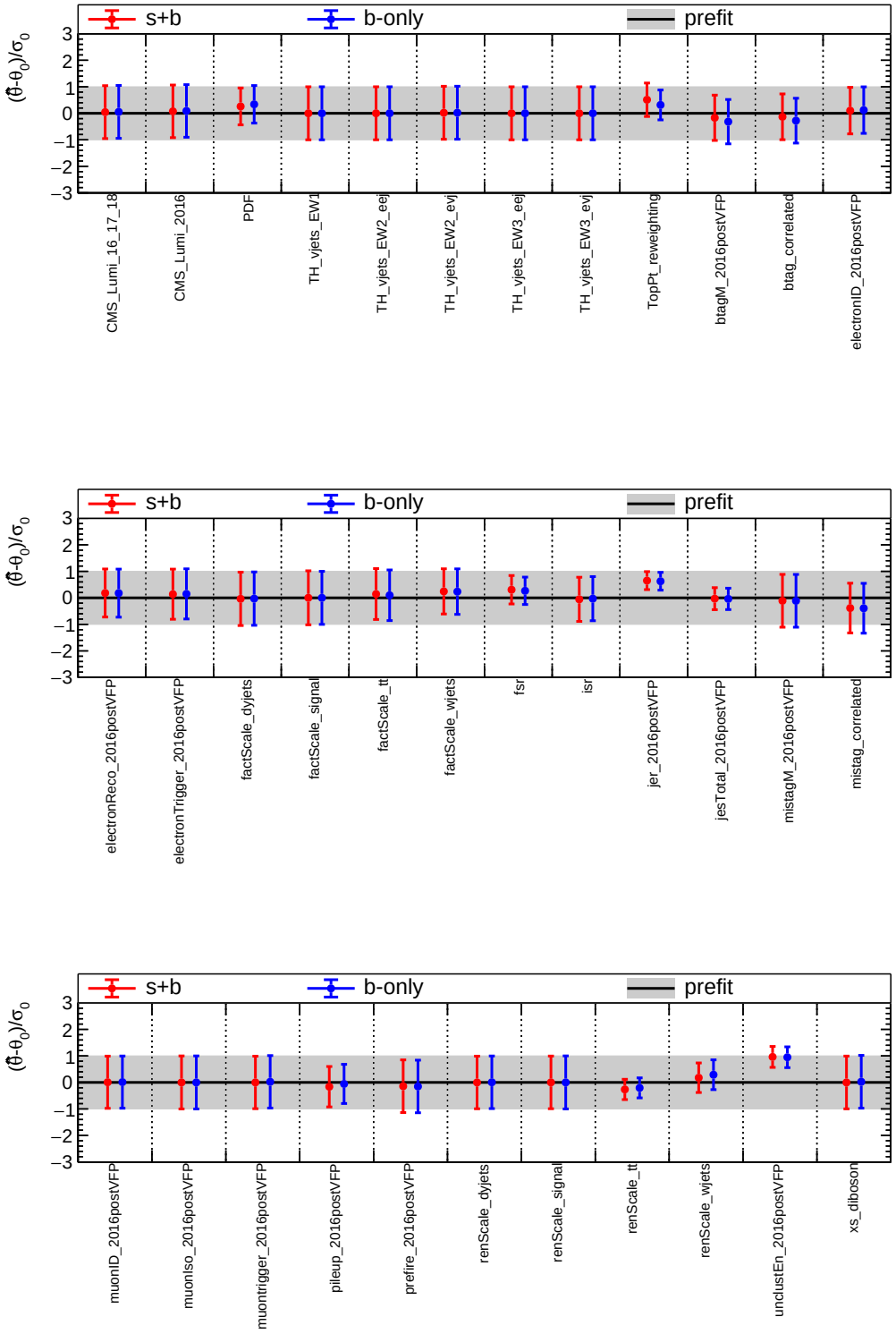

Figure G.2: Pulls of the nuisance parameters after performing a background-only and signal-plus-background fit in all analysis regions combined for 2016postVFP in blue and red, respectively.

H A-posteriori distributions in the leptonic analysis channel

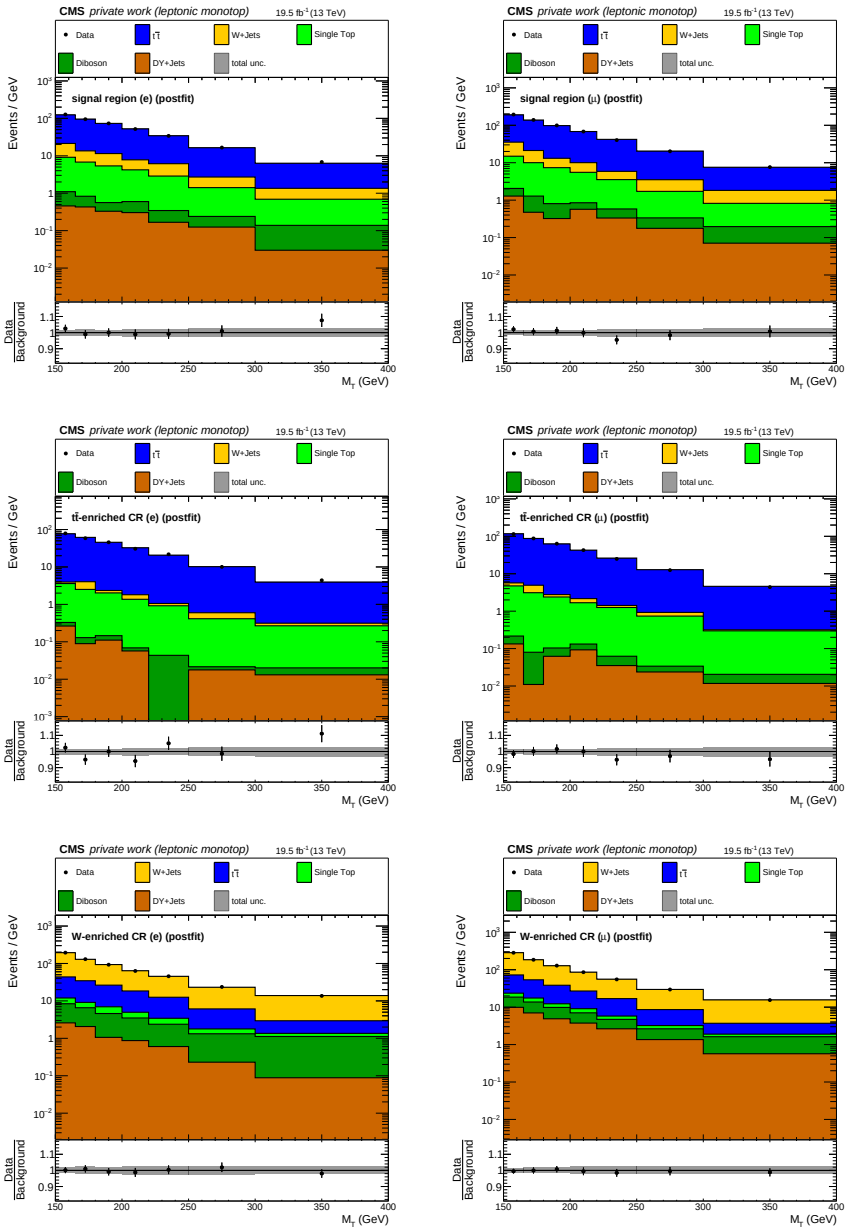

Figure H.1: Transverse mass distributions in the leptonic mono-top analysis for the 2016pre-VFP data-taking era after performing a background-only fit to the full Run 2 data. Shown are the signal regions as well as the $t\bar{t}$ and $W+$jets enriched control regions from top to bottom. The electron channels are shown on the left-hand side, whereas the muonic regions are depicted on the right-hand side. The measured data in black points are compared to the background prediction from the simulation as colored stacked histograms for different processes. The lower pad in each plot shows the ratio of data to the total background prediction. The dark grey shaded area illustrates the one standard deviation uncertainty band.

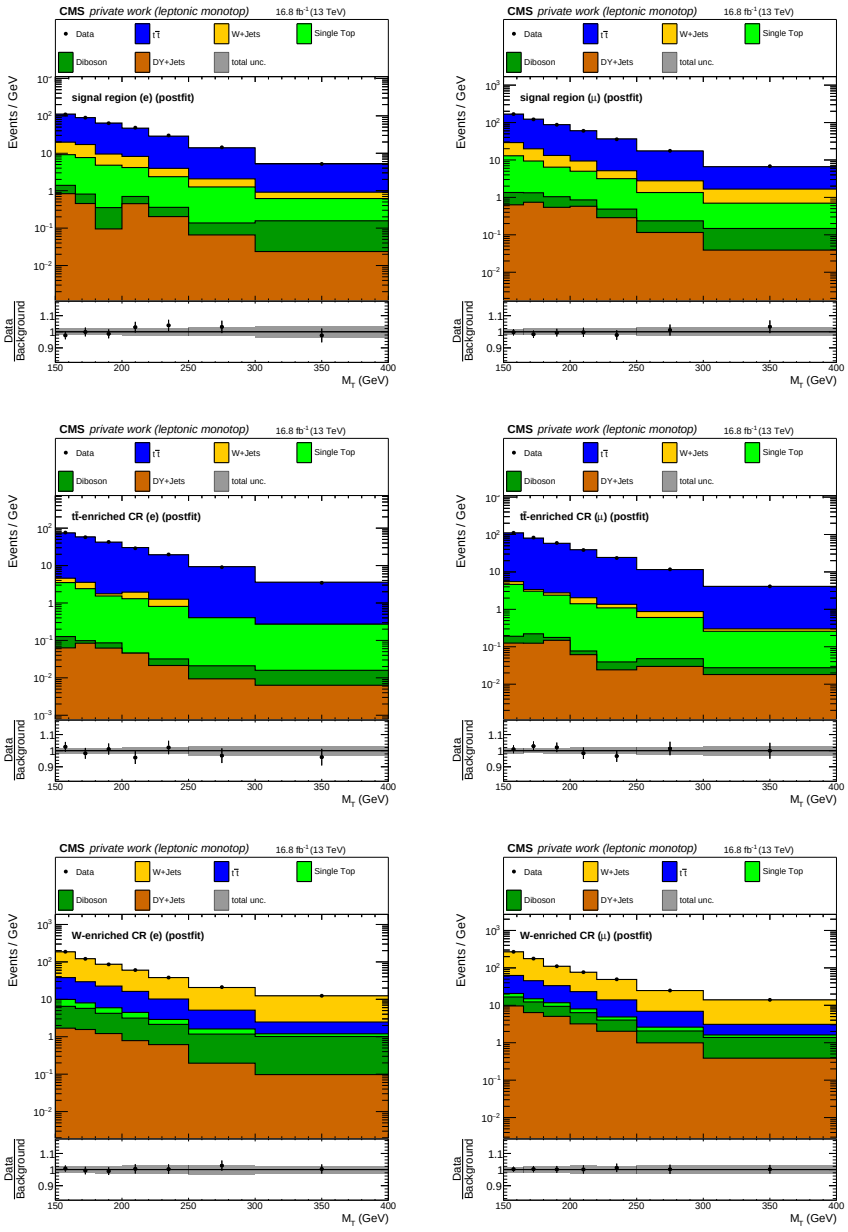

Figure H.2: Transverse mass distributions in the leptonic mono-top analysis for the 2016postVFP data-taking era after performing a background-only fit to the full Run 2 data. Shown are the signal regions as well as the $t\bar{t}$ and $W+$jets enriched control regions from top to bottom. The electron channels are shown on the left-hand side, whereas the muonic regions are depicted on the right-hand side. The measured data in black points are compared to the background prediction from the simulation as colored stacked histograms for different processes. The lower pad in each plot shows the ratio of data to the total background prediction. The dark grey shaded area illustrates the one standard deviation uncertainty band.

I Expected exclusion limits for leptonic analysis

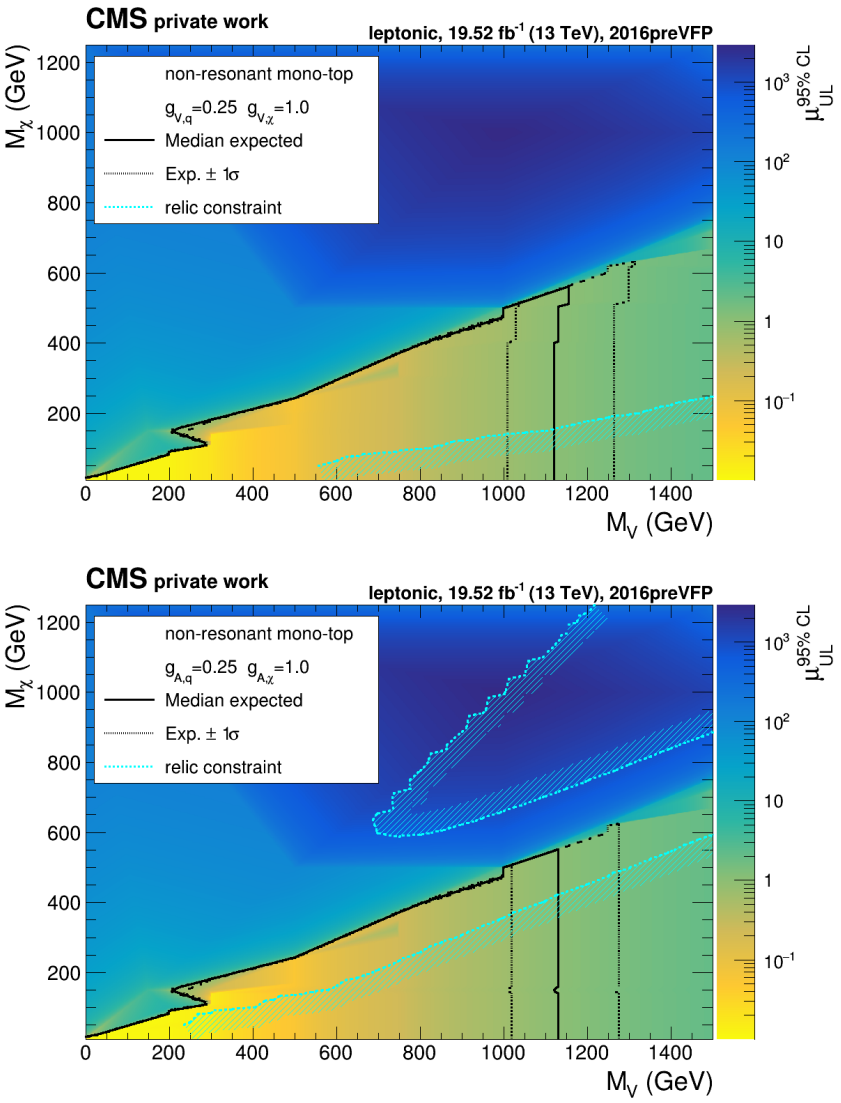

Figure I.1: Expected upper limits on the signal strength modifier μ at a confidence level of 95 % for the vector mono-top model for the 2016preVFP data-taking era in the plane of mediator and DM candidate masses M_V and M_χ. The solid black line indicates the contour for which the median, upper exclusion limit is equal to unity. The 68 % confidence interval on this contour is shown as a dashed black line. The area enclosed by the solid black line is parameter space expected to be excluded for the given mono-top model. The cyan, dashed exclusion line indicates a constraint on allowed masses in order to explain the measured DM relic density by the Planck Collaboration [30]. The upper exclusion plot corresponds to a pure vector coupling scenario, whereas the lower figure shows the exclusion limits for a pure axial-vector coupling scenario.

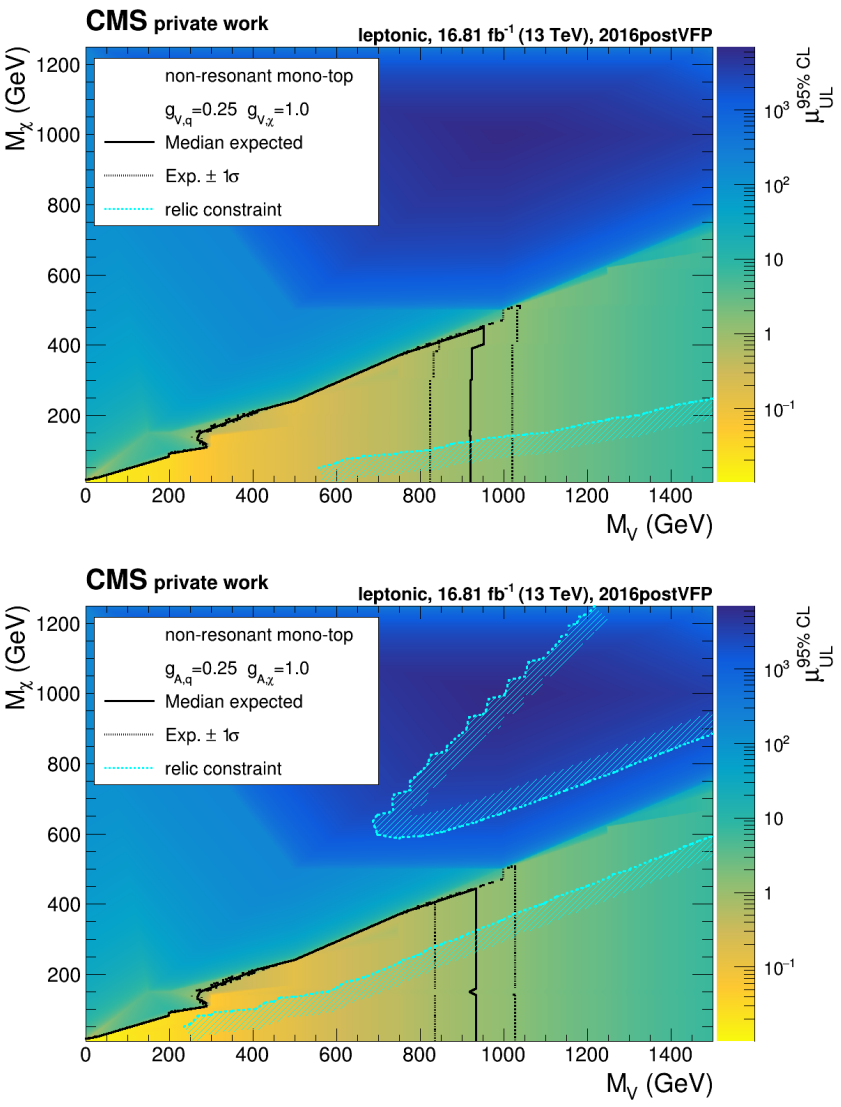

Figure I.2: Expected upper limits on the signal strength modifier μ at a confidence level of 95 % for the vector mono-top model for the 2016postVFP data-taking era in the plane of mediator and DM candidate masses M_V and M_χ. The solid black line indicates the contour for which the median, upper exclusion limit is equal to unity. The 68 % confidence interval on this contour is shown as a dashed black line. The area enclosed by the solid black line is parameter space expected to be excluded for the given mono-top model. The cyan, dashed exclusion line indicates a constraint on allowed masses in order to explain the measured DM relic density by the Planck Collaboration [30]. The upper exclusion plot corresponds to a pure vector coupling scenario, whereas the lower figure shows the exclusion limits for a pure axial-vector coupling scenario.

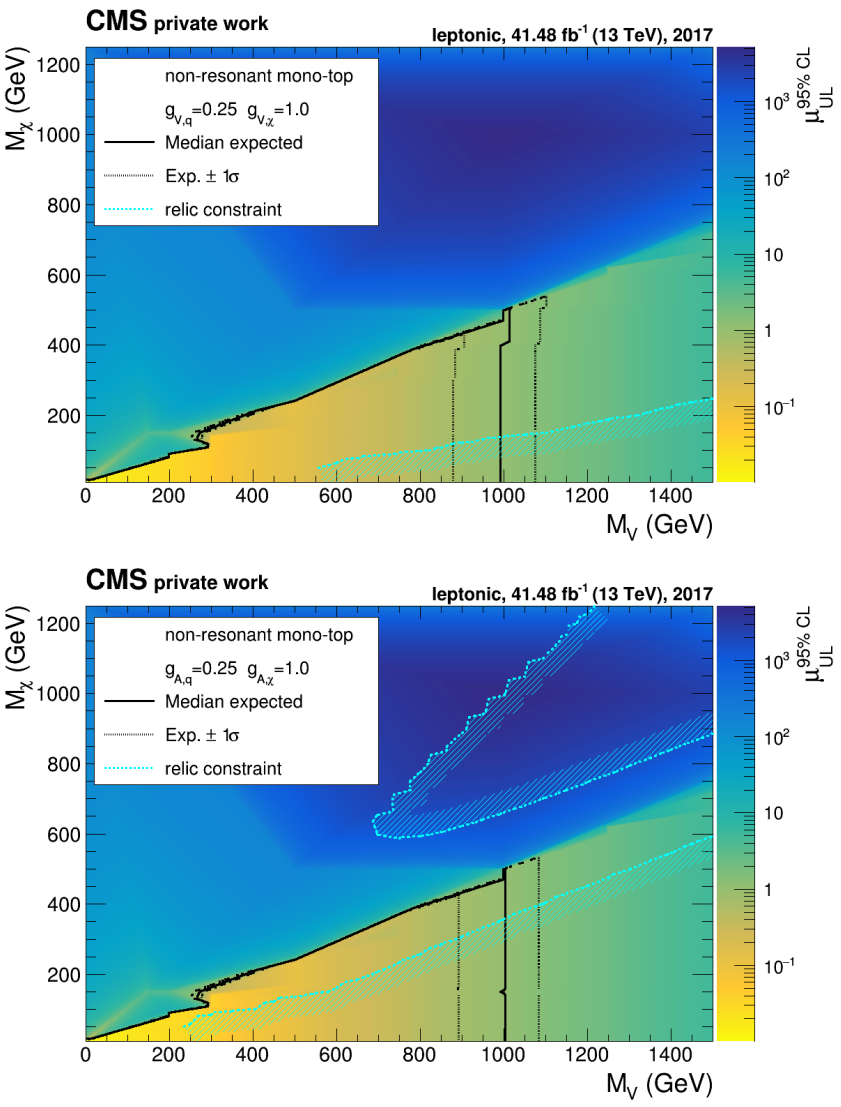

Figure I.3: Expected upper limits on the signal strength modifier μ at a confidence level of 95 % for the vector mono-top model for the 2017 data-taking era in the plane of mediator and DM candidate masses M_V and M_χ. The solid black line indicates the contour for which the median, upper exclusion limit is equal to unity. The 68 % confidence interval on this contour is shown as a dashed black line. The area enclosed by the solid black line is parameter space expected to be excluded for the given mono-top model. The cyan, dashed exclusion line indicates a constraint on allowed masses in order to explain the measured DM relic density by the Planck Collaboration [30]. The upper exclusion plot corresponds to a pure vector coupling scenario, whereas the lower figure shows the exclusion limits for a pure axial-vector coupling scenario.

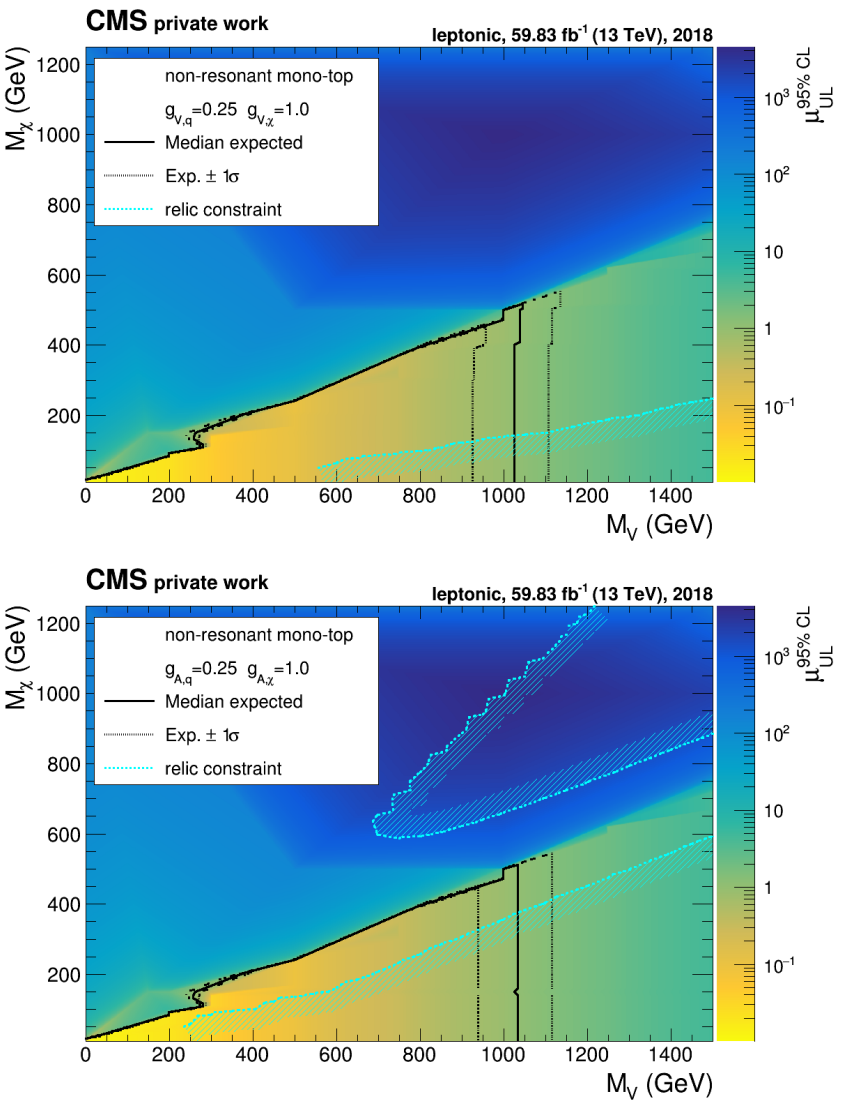

Figure I.4: Expected upper limits on the signal strength modifier μ at a confidence level of 95 % for the vector mono-top model for the 2018 data-taking era in the plane of mediator and DM candidate masses M_V and M_χ. The solid black line indicates the contour for which the median, upper exclusion limit is equal to unity. The 68 % confidence interval on this contour is shown as a dashed black line. The area enclosed by the solid black line is parameter space expected to be excluded for the given mono-top model. The cyan, dashed exclusion line indicates a constraint on allowed masses in order to explain the measured DM relic density by the Planck Collaboration [30]. The upper exclusion plot corresponds to a pure vector coupling scenario, whereas the lower figure shows the exclusion limits for a pure axial-vector coupling scenario.

J Observed exclusion limits for leptonic analysis

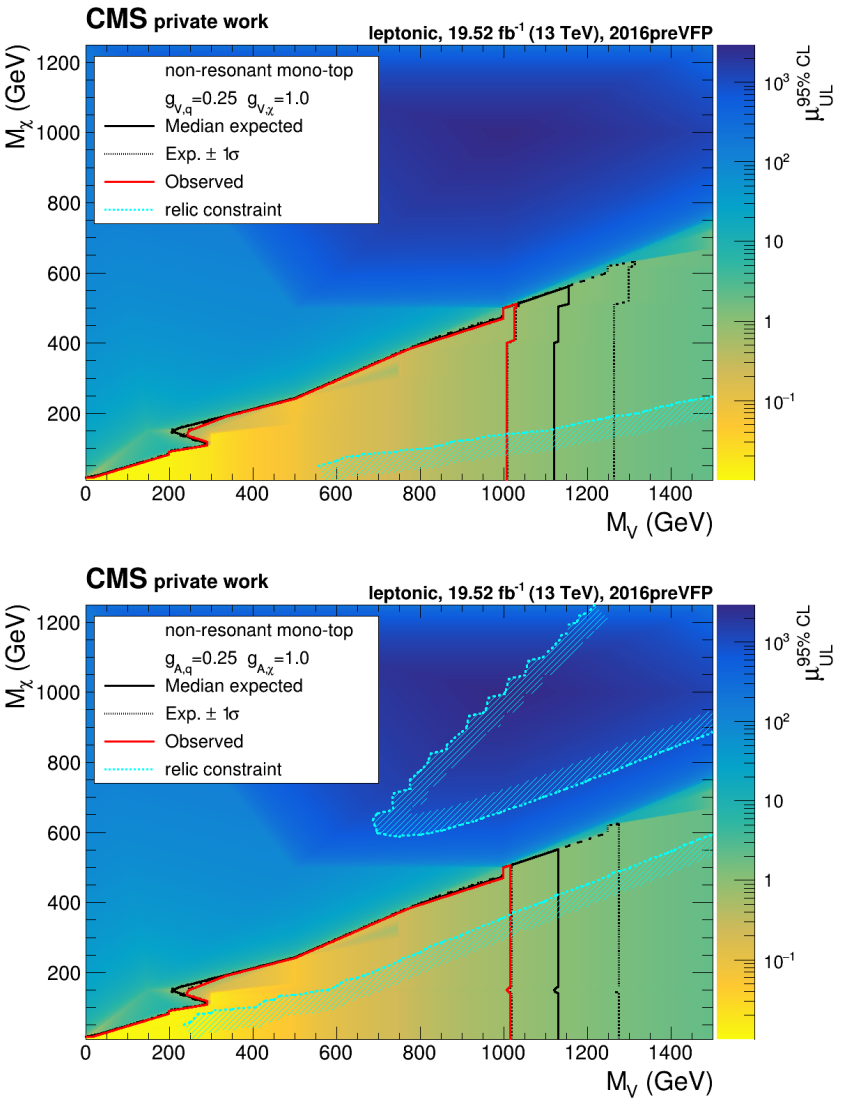

Figure J.5: Upper limits on the signal strength modifier μ at a confidence level of 95 % for the vector mono-top model for the 2016preVFP data-taking era in the plane of mediator and DM candidate masses M_V and M_χ. The solid black line indicates the contour for which the median, upper exclusion limit is equal to unity. The 68 % confidence interval on this contour is shown as a dashed black line. The area enclosed by the solid black line is parameter space expected to be excluded for the given mono-top model. The red line indicates the contour, where the observed upper limit equals unity, excluding the enclosed parameter space. The cyan, dashed exclusion line indicates a constraint on allowed masses in order to explain the measured DM relic density by the Planck Collaboration [30]. The upper exclusion plot corresponds to a pure vector coupling scenario, whereas the lower figure shows the exclusion limits for a pure axial-vector coupling scenario.

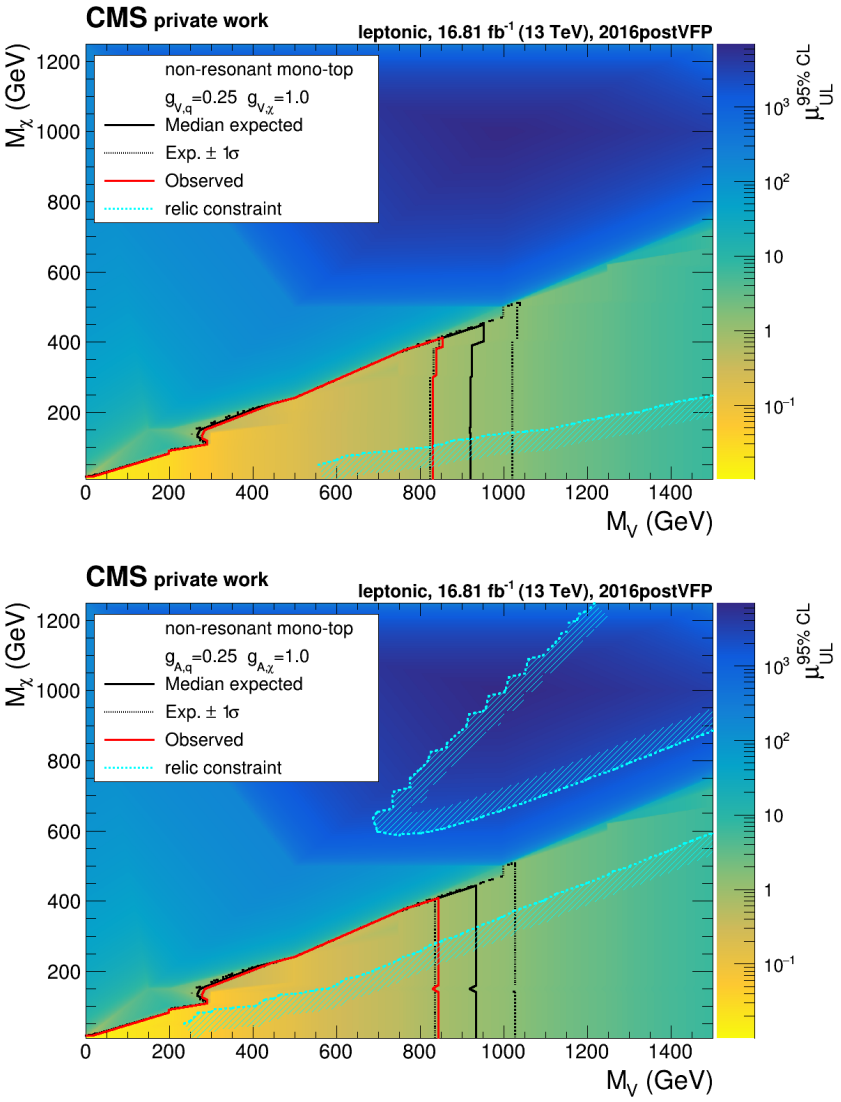

Figure J.6: Upper limits on the signal strength modifier μ at a confidence level of 95 % for the vector mono-top model for the 2016postVFP data-taking era in the plane of mediator and DM candidate masses M_V and M_χ. The solid black line indicates the contour for which the median, upper exclusion limit is equal to unity. The 68 % confidence interval on this contour is shown as a dashed black line. The area enclosed by the solid black line is parameter space expected to be excluded for the given mono-top model. The red line indicates the contour, where the observed upper limit equals unity, excluding the enclosed parameter space. The cyan, dashed exclusion line indicates a constraint on allowed masses in order to explain the measured DM relic density by the Planck Collaboration [30]. The upper exclusion plot corresponds to a pure vector coupling scenario, whereas the lower figure shows the exclusion limits for a pure axial-vector coupling scenario.

K Control distribution in the hadronic analysis channel without top-tagging requirements

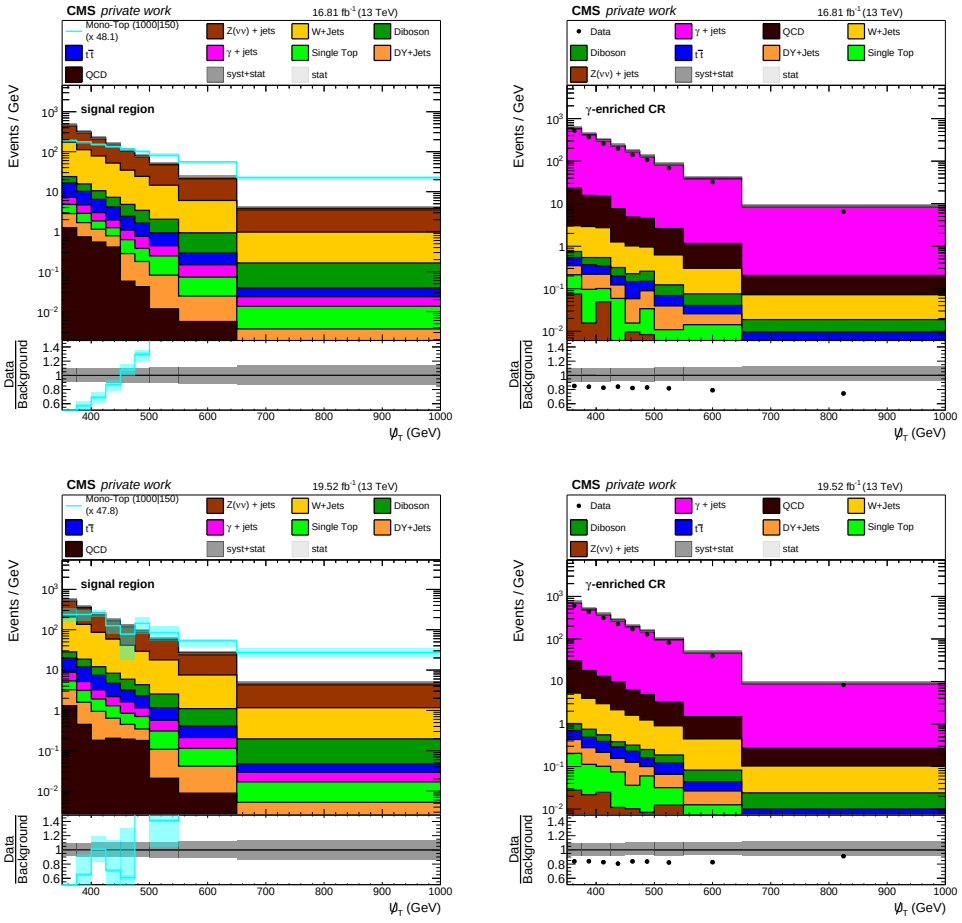

Figure K.1: Hadronic recoil p_T of the hadronic mono-top analysis selection with no top-tagging requirements applied for the 2016 data-taking eras. The 2016postVFP, 2016preVFP data-taking eras are shown from top to bottom. The left-hand side shows the SR, whereas the right-hand side corresponds to the photon CR. The measured data in black points are compared to the background prediction from simulation as colored stacked histograms for different processes. The lower pad in each plot shows the ratio of data to the total background prediction. The data points are hidden in the SR to not introduce a bias towards a possible signal contribution. For the signal regions, an exemplary signal prediction with a mediator mass of 1000 GeV and DM candidate mass of 150 GeV scaled to the total sum of expected backgrounds is overlaid in cyan.

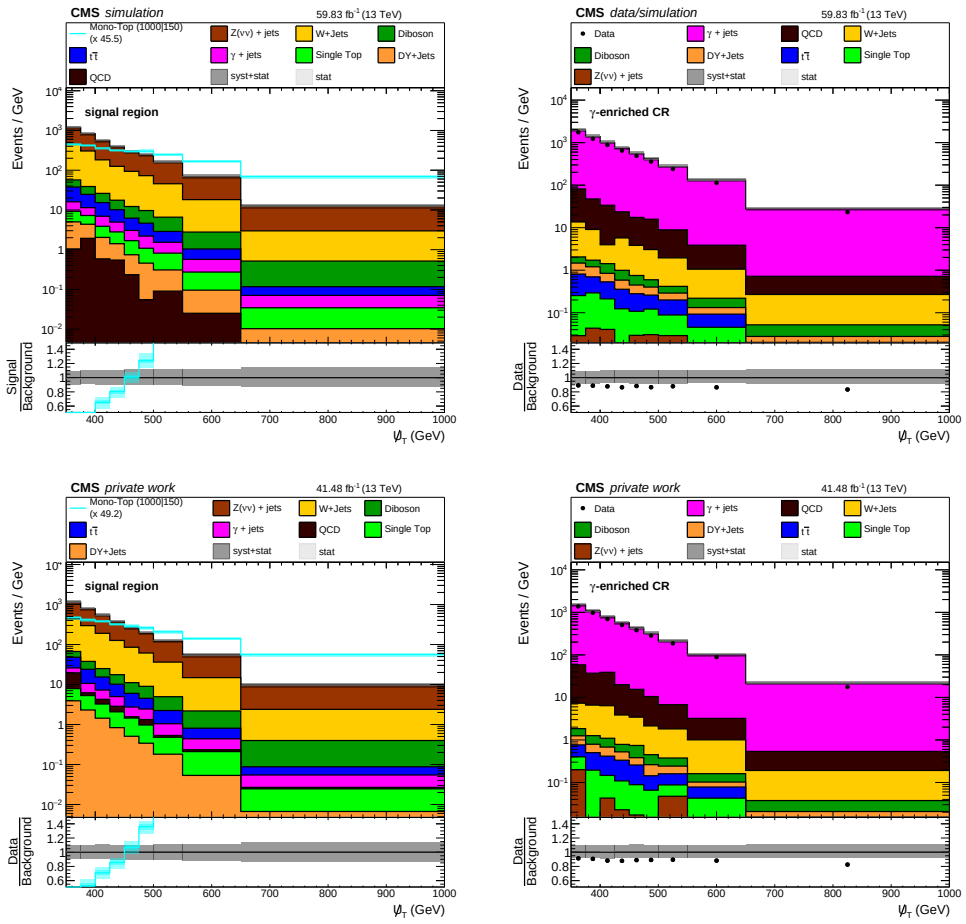

Figure K.2: Hadronic recoil p_{T} of the hadronic mono-top analysis selection with no top-tagging requirements applied for the 2017 (top) and 2018 (bottom) data-taking eras. The left-hand side shows the SR, whereas the right-hand side corresponds to the photon CR. The measured data in black points are compared to the background prediction from simulation as colored stacked histograms for different processes. The lower pad in each plot shows the ratio of data to the total background prediction. The data points are hidden in the SR to not introduce a bias towards a possible signal contribution. For the signal regions, an exemplary signal prediction with a mediator mass of 1000 GeV and DM candidate mass of 150 GeV scaled to the total sum of expected backgrounds is overlaid in cyan.

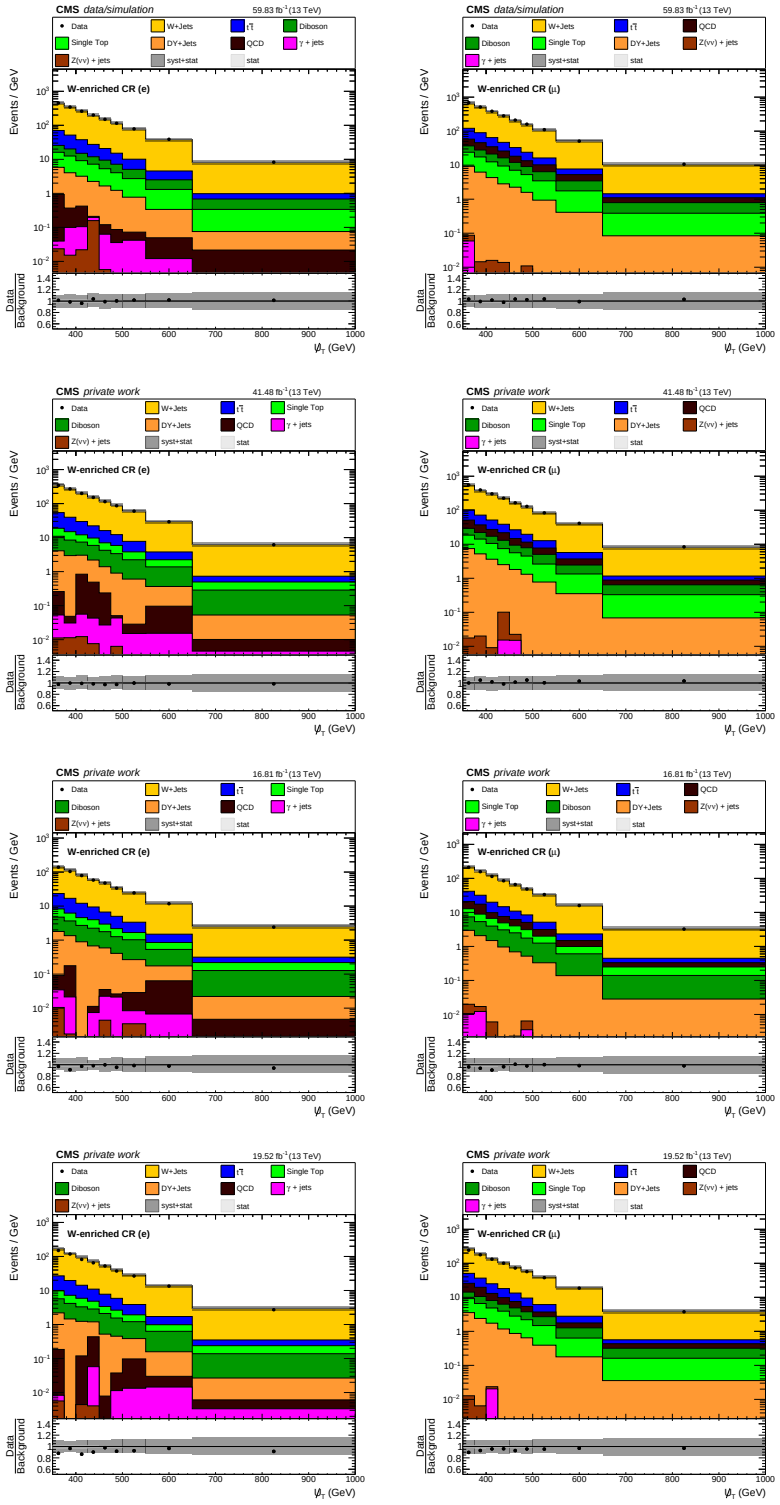

Figure K.3: Hadronic recoil p_{T} of the hadronic mono-top analysis selection with no top-tagging requirements applied for all four data-taking eras. The 2018, 2017, 2016postVFP, 2016preVFP data-taking eras are shown from top to bottom. Shown are the W boson CRs, where the left-hand side corresponds to the muon and the right-hand side to the electron channel. The measured data in black points are compared to the background prediction from simulation as colored stacked histograms for different processes. The lower pad in each plot shows the ratio of data to the total background prediction.

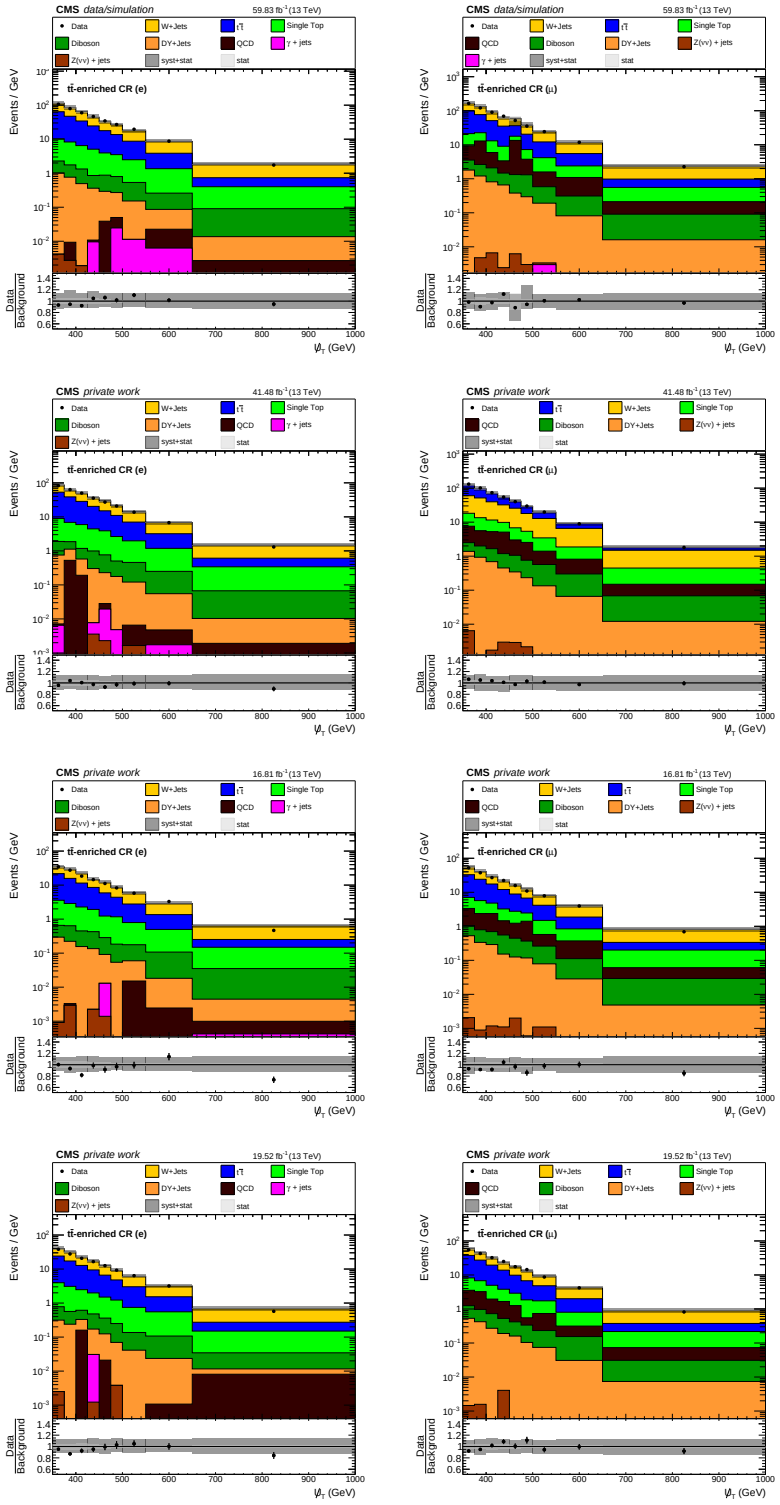

Figure K.4: Hadronic recoil p_{T} of the hadronic mono-top analysis selection with no top-tagging requirements applied for all four data-taking eras. The 2018, 2017, 2016postVFP, 2016preVFP data-taking eras are shown from top to bottom. Shown are the $\mathrm{t\bar{t}}$ CRs, where the left-hand side corresponds to the muon and the right-hand side to the electron channel. The measured data in black points are compared to the background prediction from simulation as colored stacked histograms for different processes. The lower pad in each plot shows the ratio of data to the total background prediction.

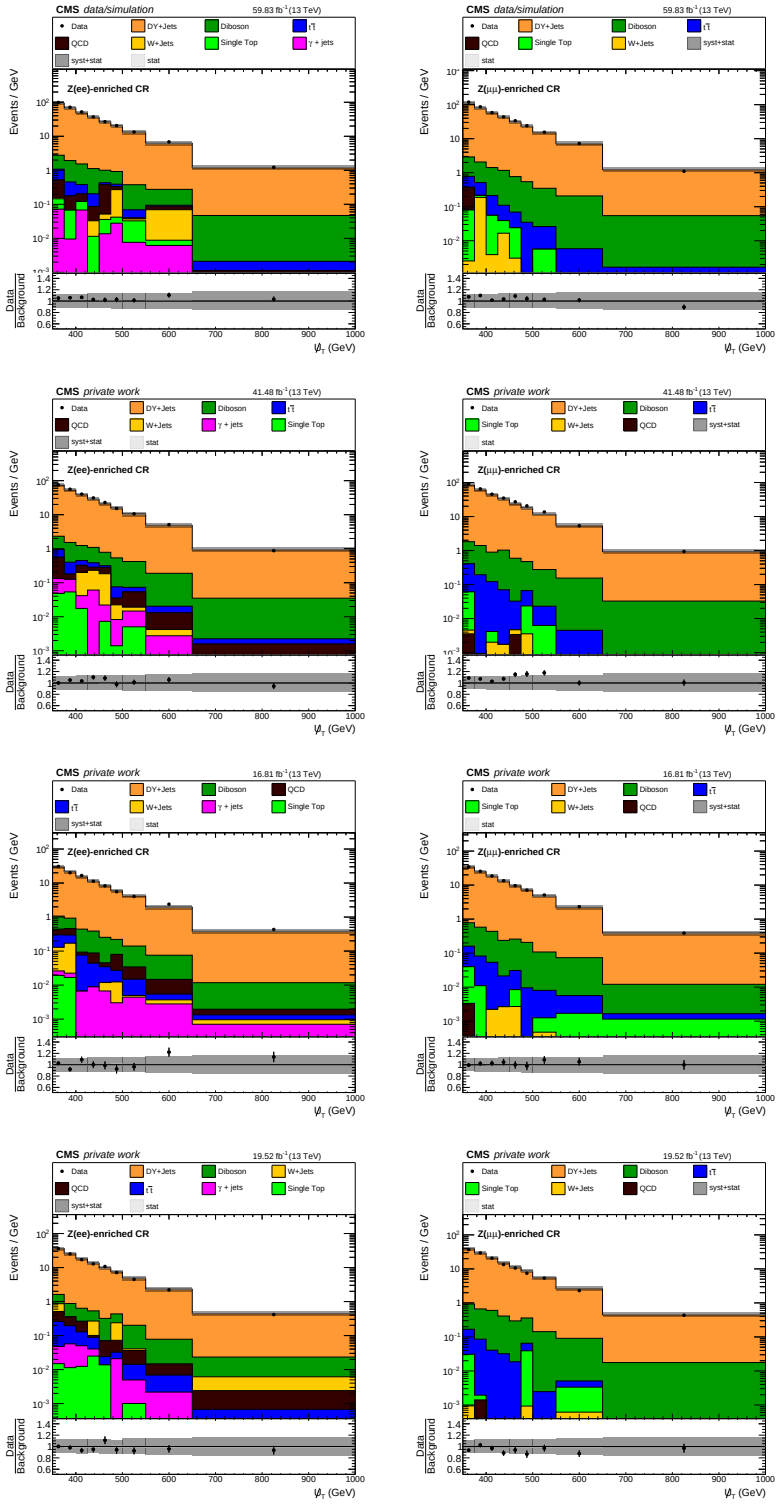

Figure K.5: Hadronic recoil p_{T} of the hadronic mono-top analysis selection with no top-tagging requirements applied for all four data-taking eras. The 2018, 2017, 2016postVFP, 2016preVFP data-taking eras are shown from top to bottom. Shown are the Z boson CRs, where the left-hand side corresponds to the muon and the right-hand side to the electron channel. The measured data in black points are compared to the background prediction from simulation as colored stacked histograms for different processes. The lower pad in each plot shows the ratio of data to the total background prediction.

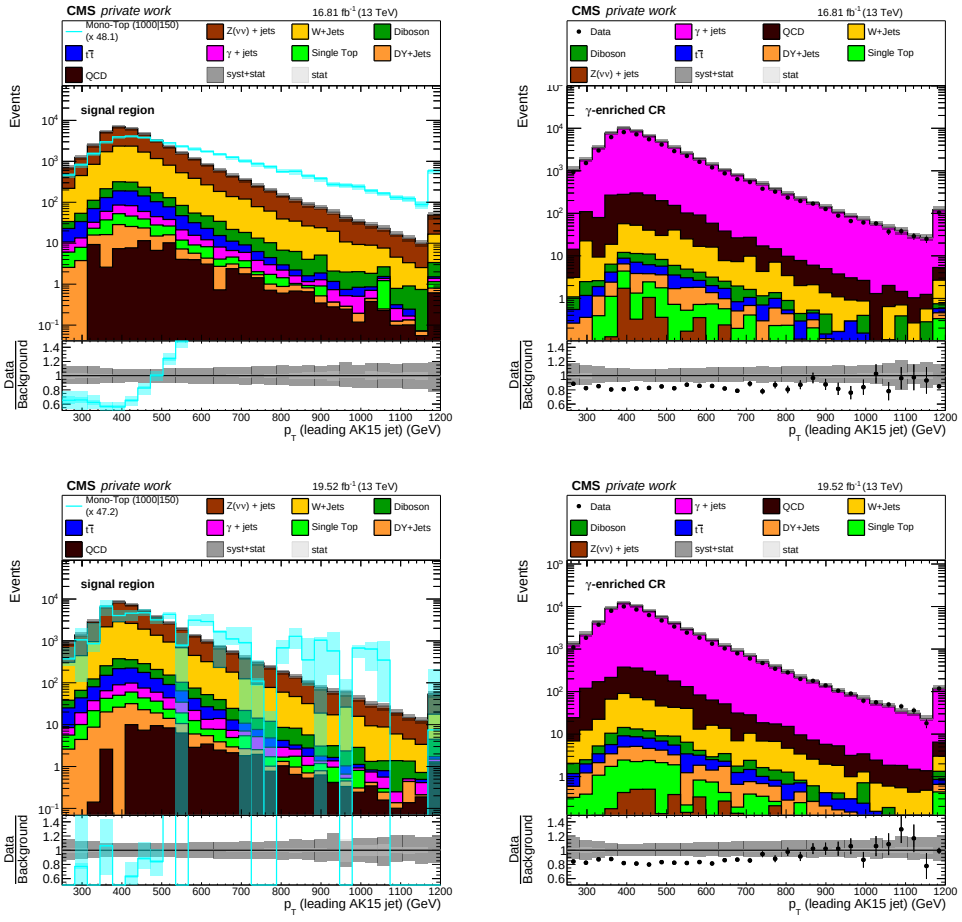

Figure K.6: Leading AK15 jet p_{T} of the hadronic mono-top analysis selection with no top-tagging requirements applied for the 2016 data-taking eras. The 2016postVFP, 2016preVFP data-taking eras are shown from top to bottom. The left-hand side shows the SR, whereas the right-hand side corresponds to the photon CR. The measured data in black points are compared to the background prediction from simulation as colored stacked histograms for different processes. The lower pad in each plot shows the ratio of data to the total background prediction. The data points are hidden in the SR to not introduce a bias towards a possible signal contribution. For the signal regions, an exemplary signal prediction with a mediator mass of 1000 GeV and DM candidate mass of 150 GeV scaled to the total sum of expected backgrounds is overlaid in cyan.

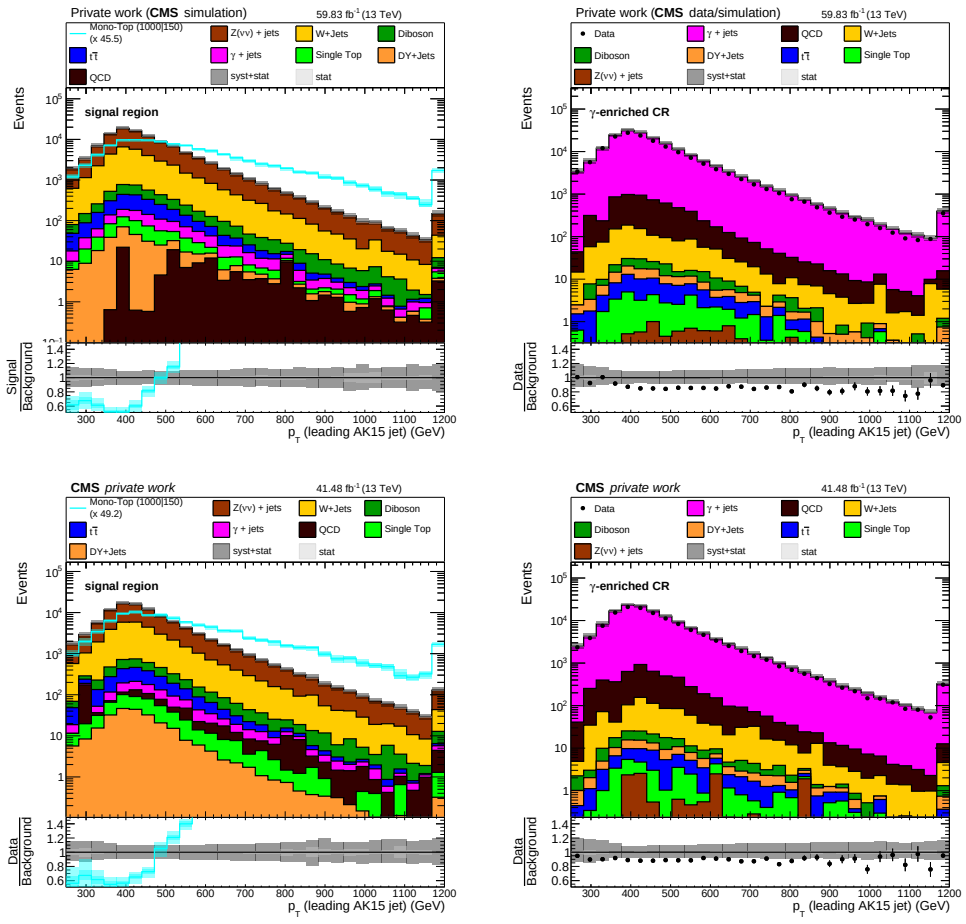

Figure K.7: Leading AK15 jet p_{T} of the hadronic mono-top analysis selection with no top-tagging requirements applied for the 2017 (top) and 2018 (bottom) data-taking eras. The left-hand side shows the SR, whereas the right-hand side corresponds to the photon CR. The measured data in black points are compared to the background prediction from simulation as colored stacked histograms for different processes. The lower pad in each plot shows the ratio of data to the total background prediction. The data points are hidden in the SR to not introduce a bias towards a possible signal contribution. For the signal regions, an exemplary signal prediction with a mediator mass of 1000 GeV and DM candidate mass of 150 GeV scaled to the total sum of expected backgrounds is overlaid in cyan.

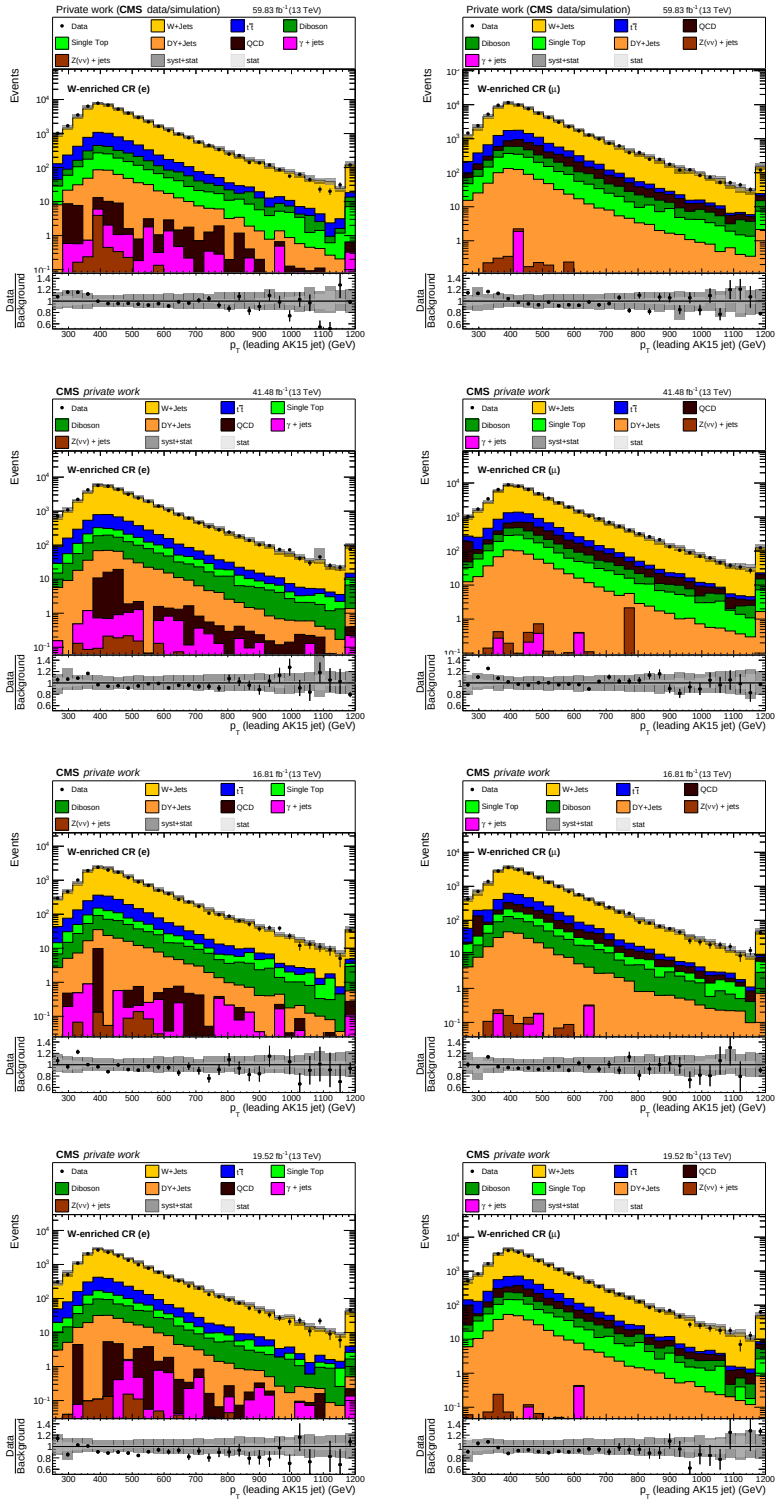

Figure K.8: Leading AK15 jet p_{T} of the hadronic mono-top analysis selection with no top-tagging requirements applied for all four data-taking eras. The 2018, 2017, 2016postVFP, 2016preVFP data-taking eras are shown from top to bottom. Shown are the W boson CRs, where the left-hand side corresponds to the muon and the right-hand side to the electron channel. The measured data in black points are compared to the background prediction from simulation as colored stacked histograms for different processes. The lower pad in each plot shows the ratio of data to the total background prediction.

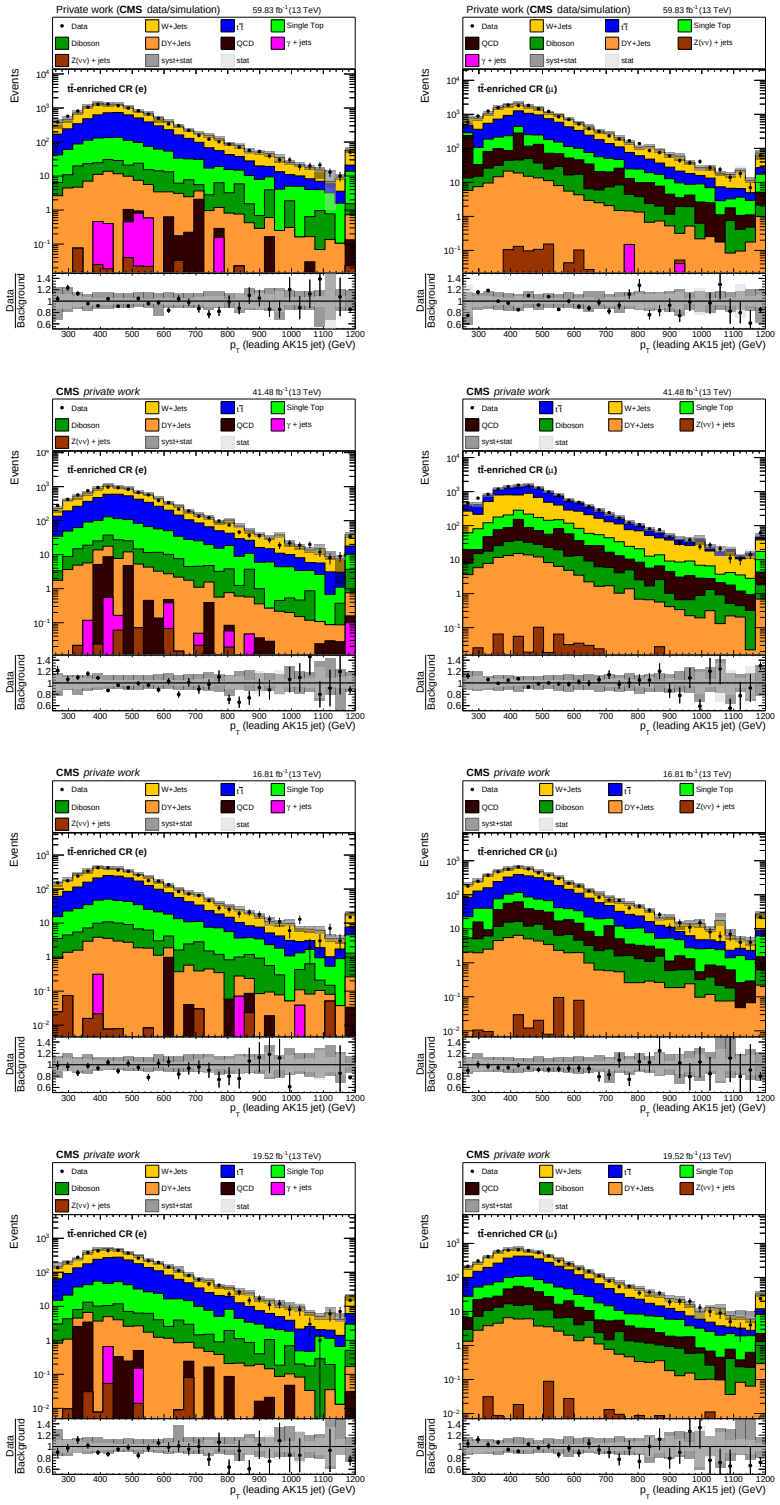

Figure K.9: Leading AK15 jet p_{T} of the hadronic mono-top analysis selection with no top-tagging requirements applied for all four data-taking eras. The 2018, 2017, 2016postVFP, 2016preVFP data-taking eras are shown from top to bottom. Shown are the $t\bar{t}$ CRs, where the left-hand side corresponds to the muon and the right-hand side to the electron channel. The measured data in black points are compared to the background prediction from simulation as colored stacked histograms for different processes. The lower pad in each plot shows the ratio of data to the total background prediction.

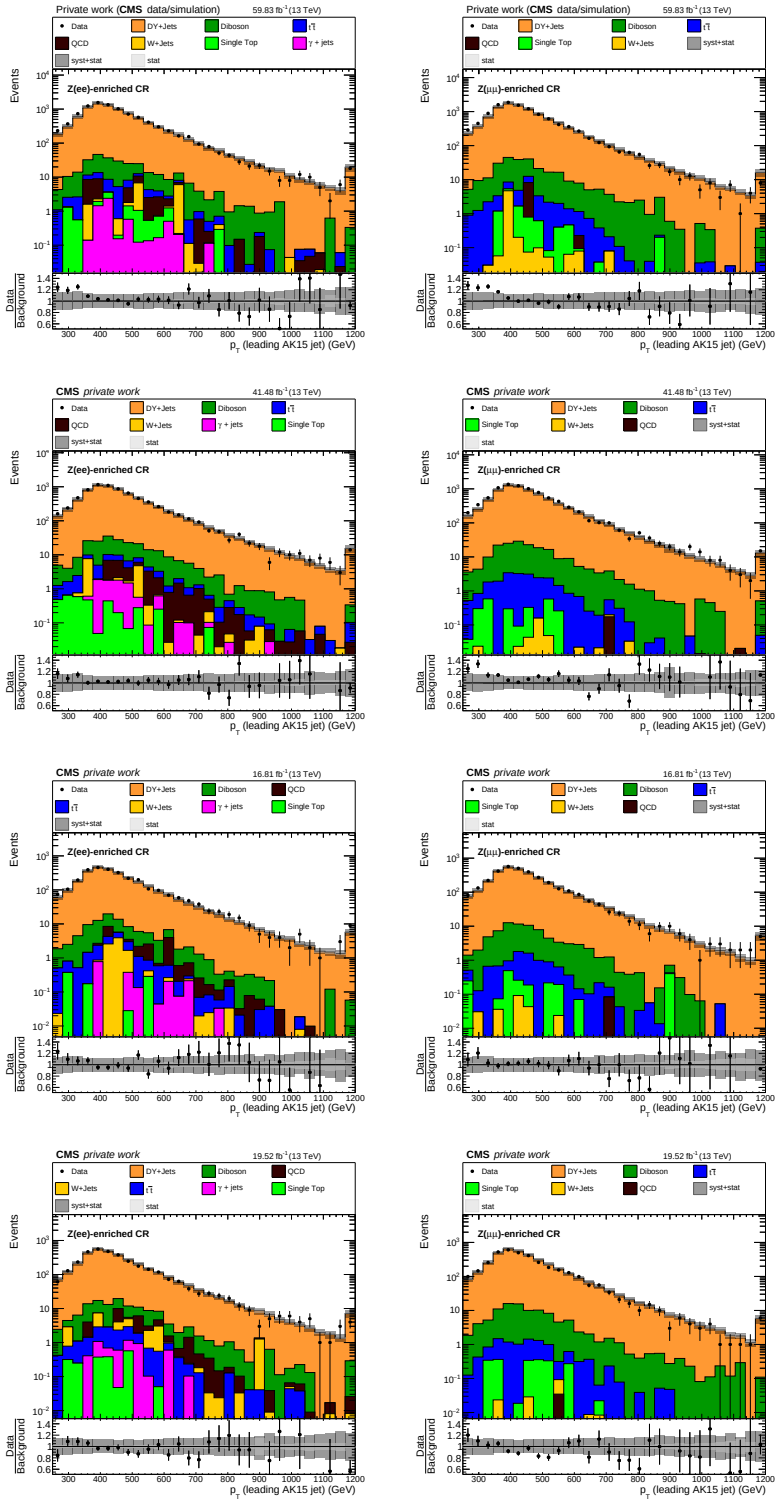

Figure K.10: Leading AK15 jet p_{T} of the hadronic mono-top analysis selection with no top-tagging requirements applied for all four data-taking eras. The 2018, 2017, 2016postVFP, 2016preVFP data-taking eras are shown from top to bottom. Shown are the Z boson CRs, where the left-hand side corresponds to the muon and the right-hand side to the electron channel. The measured data in black points are compared to the background prediction from simulation as colored stacked histograms for different processes. The lower pad in each plot shows the ratio of data to the total background prediction.

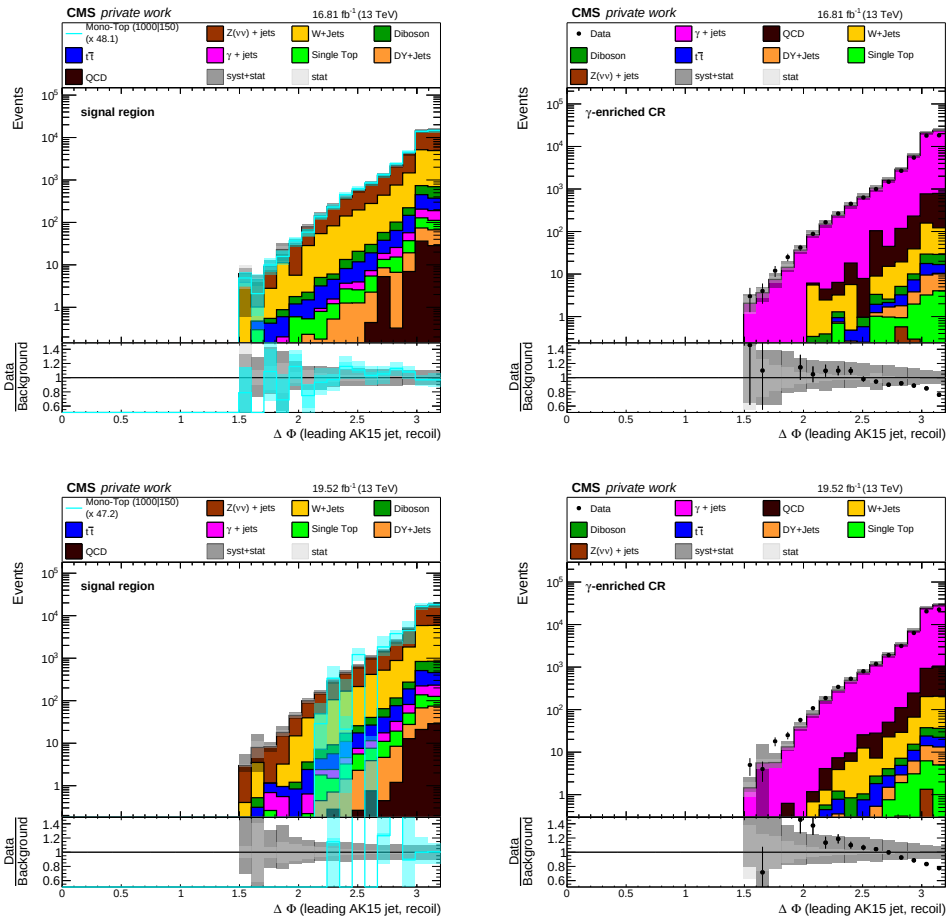

Figure K.11: Opening angle between leading AK15 jet and $\vec{\not{p}}_{\mathrm{T}}$ of the hadronic mono-top analysis selection with no top-tagging requirements applied for the 2016 data-taking eras. The 2016postVFP, 2016preVFP data-taking eras are shown from top to bottom. The left-hand side shows the SR, whereas the right-hand side corresponds to the photon CR. The measured data in black points are compared to the background prediction from simulation as colored stacked histograms for different processes. The lower pad in each plot shows the ratio of data to the total background prediction. The data points are hidden in the SR to not introduce a bias towards a possible signal contribution. For the signal regions, an exemplary signal prediction with a mediator mass of 1000 GeV and DM candidate mass of 150 GeV scaled to the total sum of expected backgrounds is overlaid in cyan.

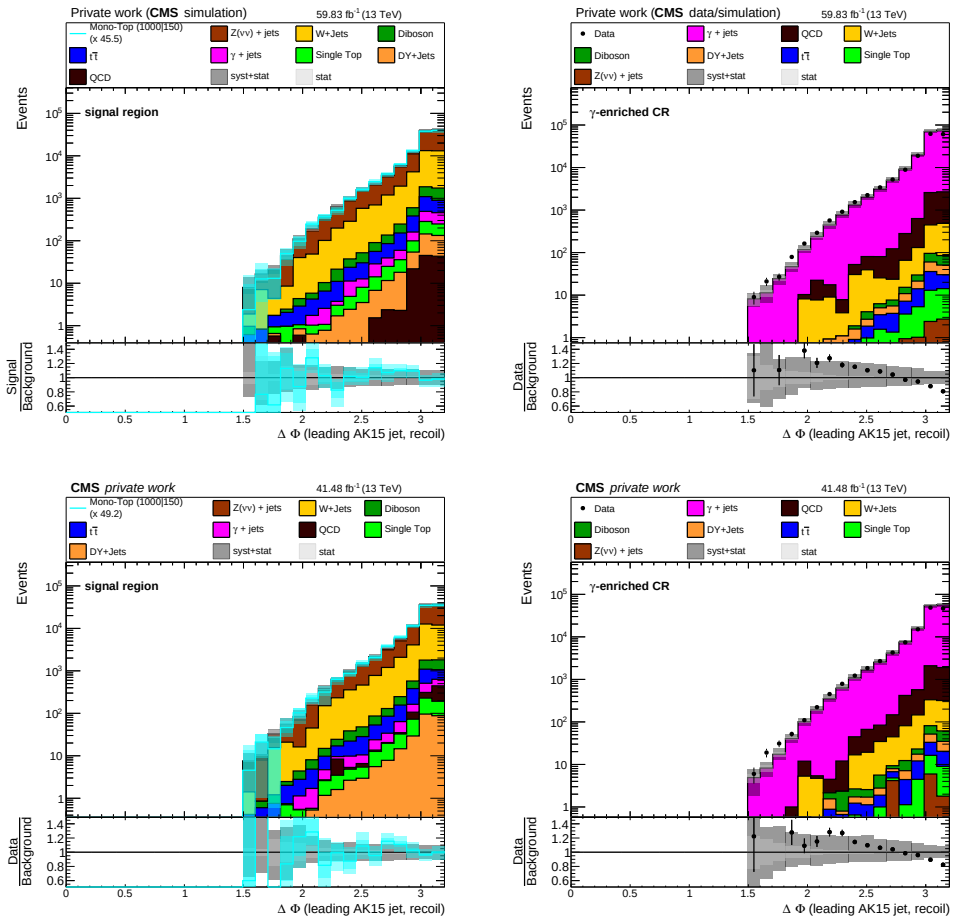

Figure K.12: Opening angle between leading AK15 jet and $\vec{\not{p}}_{\mathrm{T}}$ of the hadronic mono-top analysis selection with no top-tagging requirements applied for the 2017 (top) and 2018 (bottom) data-taking eras. The left-hand side shows the SR, whereas the right-hand side corresponds to the photon CR. The measured data in black points are compared to the background prediction from simulation as colored stacked histograms for different processes. The lower pad in each plot shows the ratio of data to the total background prediction. The data points are hidden in the SR to not introduce a bias towards a possible signal contribution. For the signal regions, an exemplary signal prediction with a mediator mass of 1000 GeV and DM candidate mass of 150 GeV scaled to the total sum of expected backgrounds is overlaid in cyan.

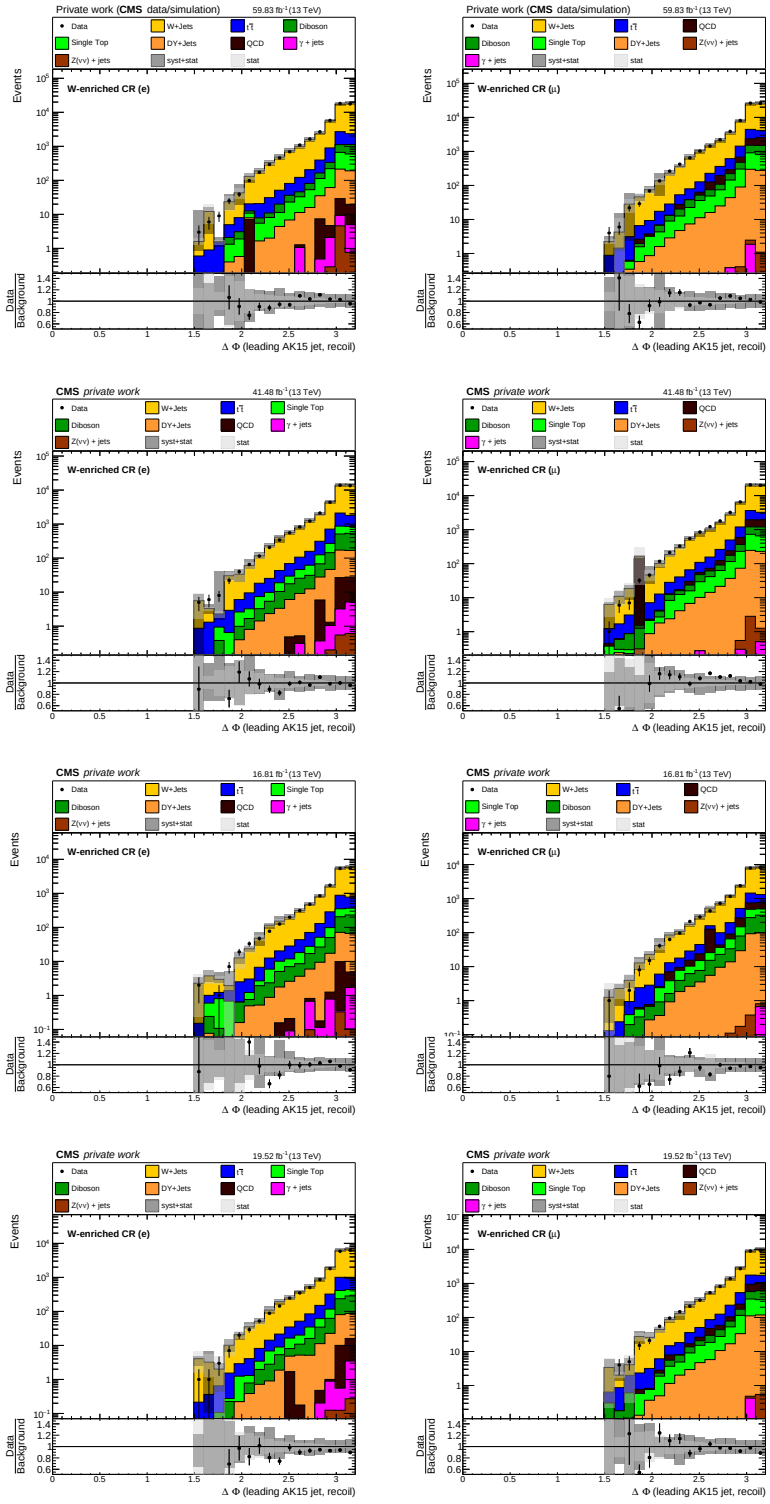

Figure K.13: Opening angle between leading AK15 jet and and $\vec{\not{U}}_{\mathrm{T}}$ of the hadronic mono-top analysis selection with no top-tagging requirements applied for all four data-taking eras. The 2018, 2017, 2016postVFP, 2016preVFP data-taking eras are shown from top to bottom. Shown are the W boson CRs, where the left-hand side corresponds to the muon and the right-hand side to the electron channel. The measured data in black points are compared to the background prediction from simulation as colored stacked histograms for different processes. The lower pad in each plot shows the ratio of data to the total background prediction.

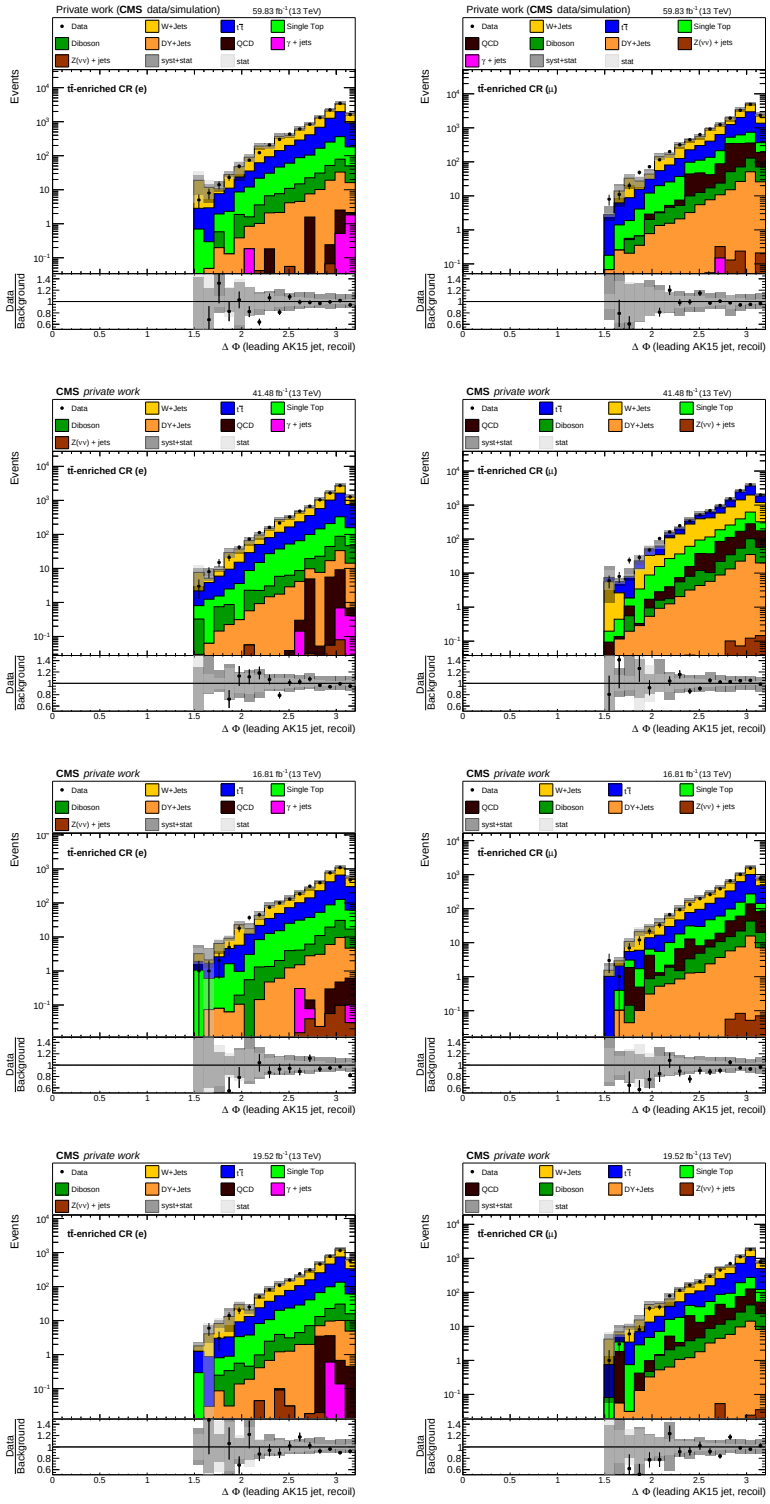

Figure K.14: Opening angle between leading AK15 jet and and $\vec{\not{U}}_{\mathrm{T}}$ of the hadronic mono-top analysis selection with no top-tagging requirements applied for all four data-taking eras. The 2018, 2017, 2016postVFP, 2016preVFP data-taking eras are shown from top to bottom. Shown are the $t\bar{t}$ CRs, where the left-hand side corresponds to the muon and the right-hand side to the electron channel. The measured data in black points are compared to the background prediction from simulation as colored stacked histograms for different processes. The lower pad in each plot shows the ratio of data to the total background prediction.

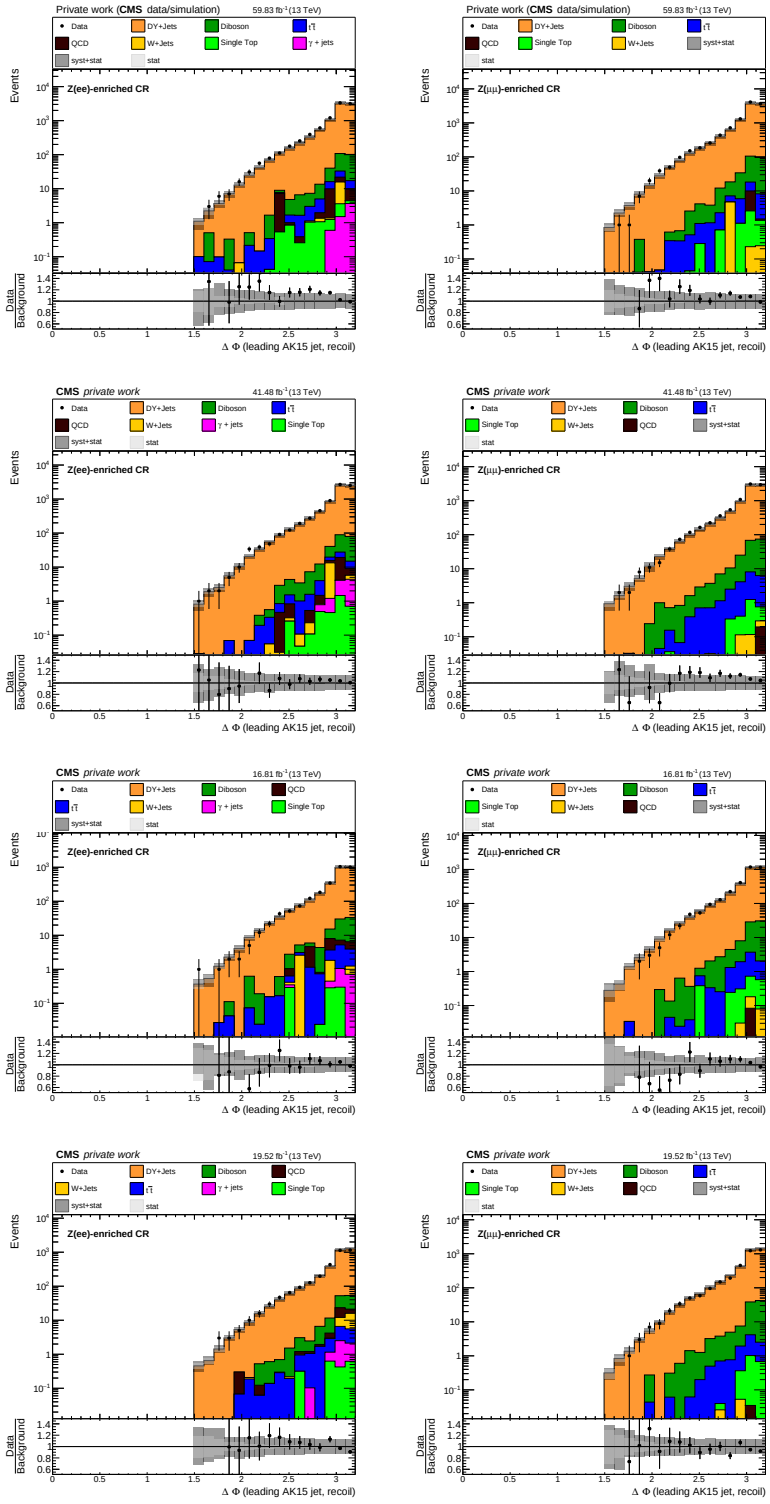

Figure K.15: Opening angle between leading AK15 jet and and $\vec{\not{U}}_{\mathrm{T}}$ of the hadronic mono-top analysis selection with no top-tagging requirements applied for all four data-taking eras. The 2018, 2017, 2016postVFP, 2016preVFP data-taking eras are shown from top to bottom. Shown are the Z boson CRs, where the left-hand side corresponds to the muon and the right-hand side to the electron channel. The measured data in black points are compared to the background prediction from simulation as colored stacked histograms for different processes. The lower pad in each plot shows the ratio of data to the total background prediction.

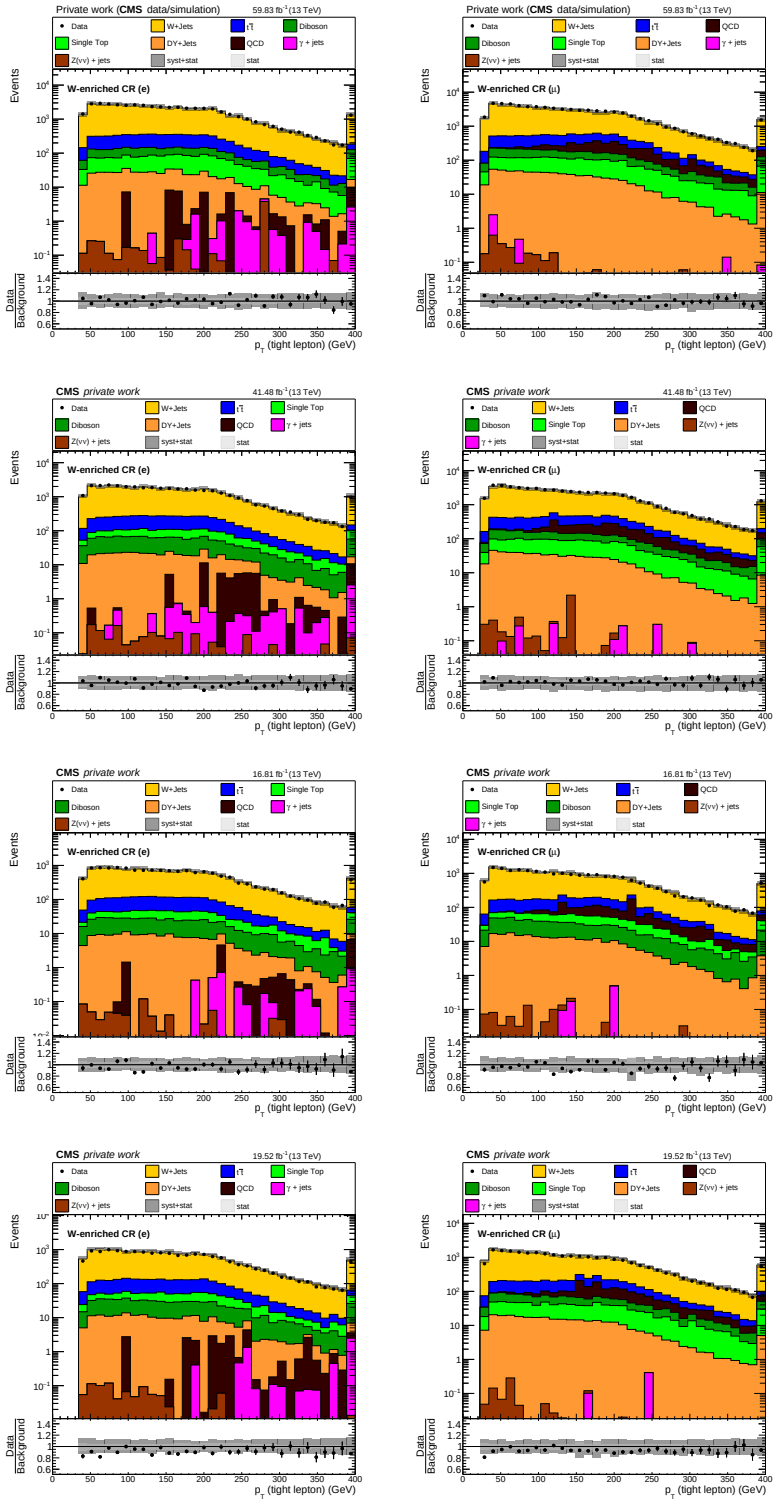

Figure K.16: Lepton p_{T} of the hadronic mono-top analysis selection with no top-tagging requirements applied for all four data-taking eras. The 2018, 2017, 2016postVFP, 2016preVFP data-taking eras are shown from top to bottom. Shown are the W boson CRs, where the left-hand side corresponds to the muon and the right-hand side to the electron channel. The measured data in black points are compared to the background prediction from simulation as colored stacked histograms for different processes. The lower pad in each plot shows the ratio of data to the total background prediction.

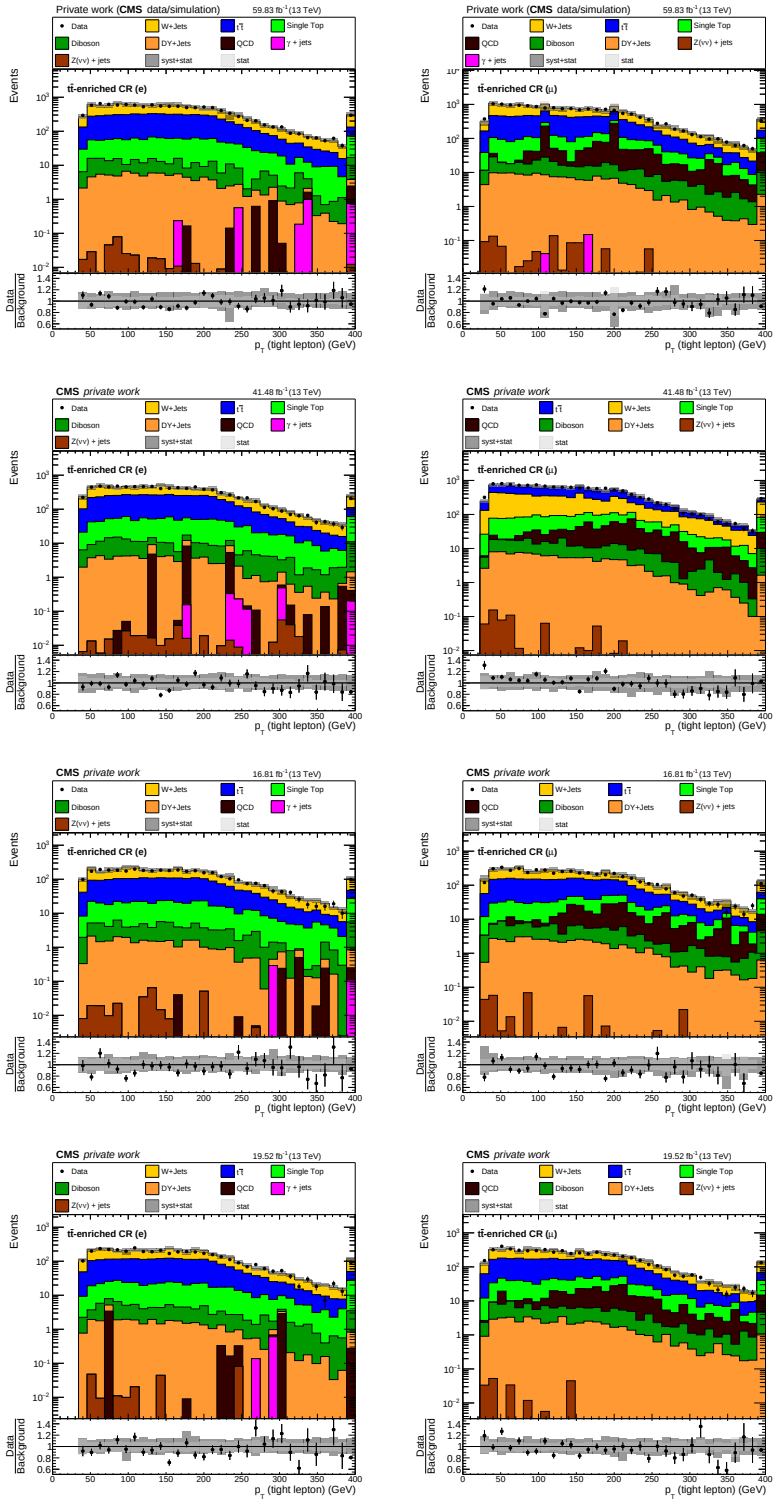

Figure K.17: Lepton p_{T} of the hadronic mono-top analysis selection with no top-tagging requirements applied for all four data-taking eras. The 2018, 2017, 2016postVFP, 2016preVFP data-taking eras are shown from top to bottom. Shown are the $t\bar{t}$ CRs, where the left-hand side corresponds to the muon and the right-hand side to the electron channel. The measured data in black points are compared to the background prediction from simulation as colored stacked histograms for different processes. The lower pad in each plot shows the ratio of data to the total background prediction.

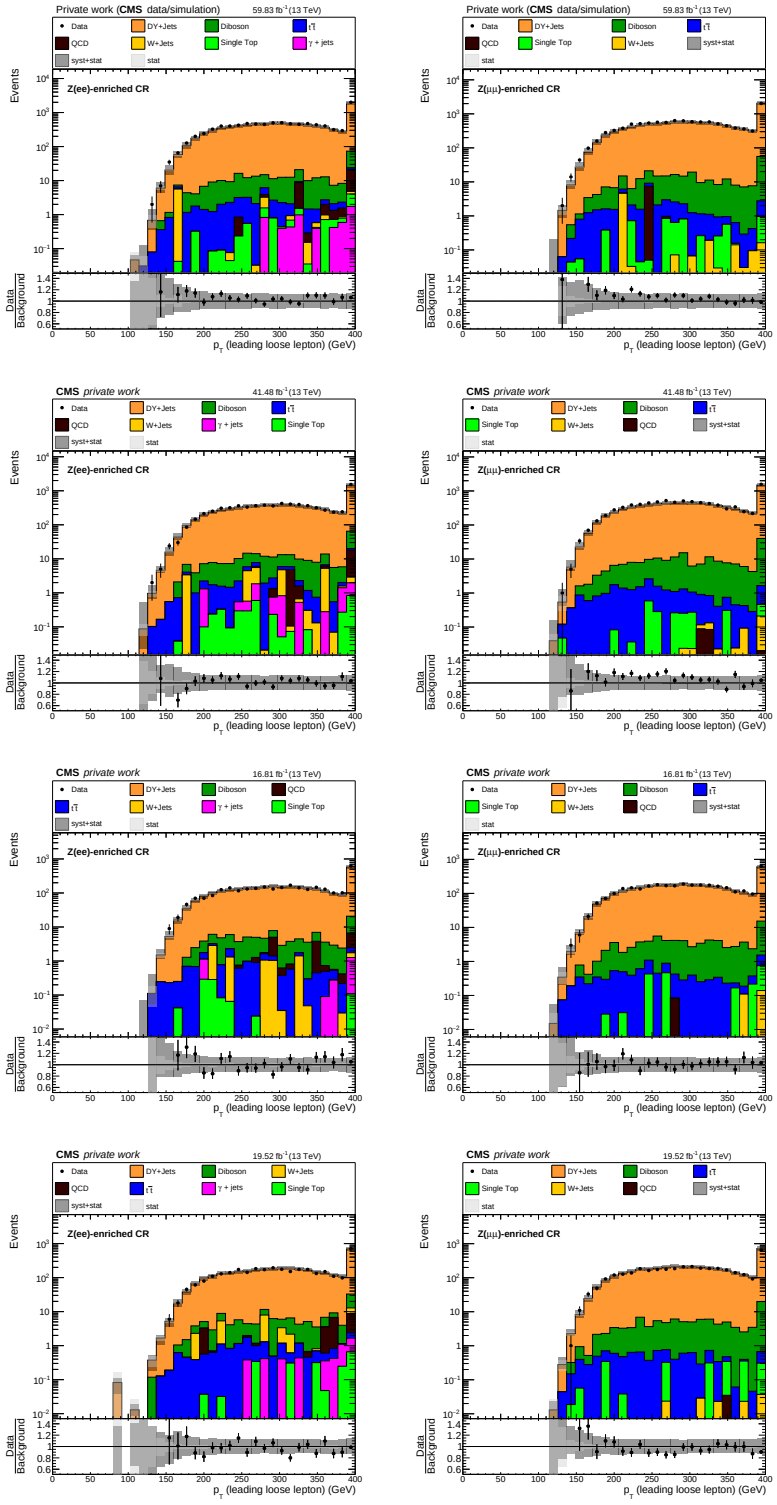

Figure K.18: Leading lepton p_{T} of the hadronic mono-top analysis selection with no top-tagging requirements applied for all four data-taking eras. The 2018, 2017, 2016postVFP, 2016preVFP data-taking eras are shown from top to bottom. Shown are the Z boson CRs, where the left-hand side corresponds to the muon and the right-hand side to the electron channel. The measured data in black points are compared to the background prediction from simulation as colored stacked histograms for different processes. The lower pad in each plot shows the ratio of data to the total background prediction.

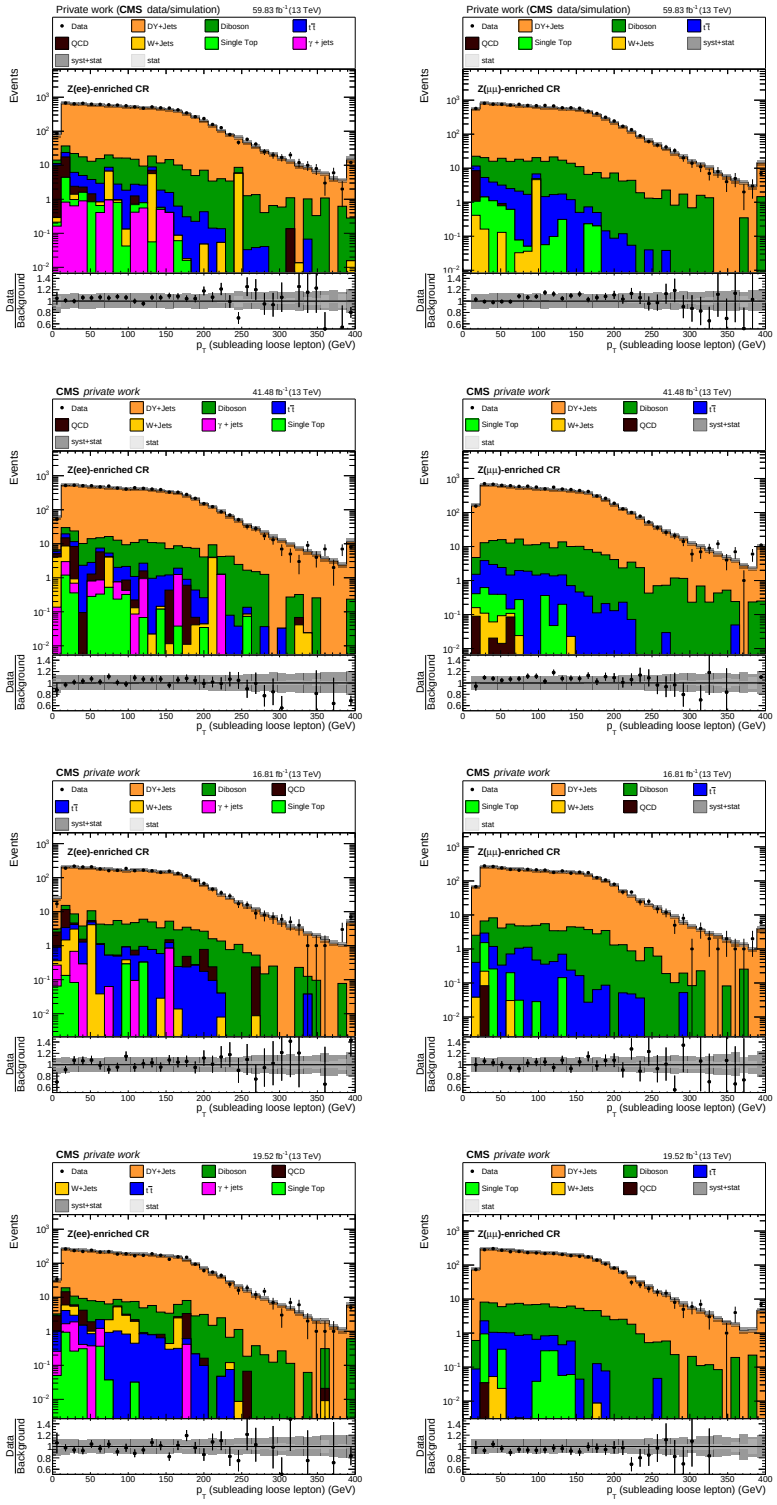

Figure K.19: Sub-leading lepton p_{T} of the hadronic mono-top analysis selection with no top-tagging requirements applied for all four data-taking eras. The 2018, 2017, 2016postVFP, 2016preVFP data-taking eras are shown from top to bottom. Shown are the Z boson CRs, where the left-hand side corresponds to the muon and the right-hand side to the electron channel. The measured data in black points are compared to the background prediction from simulation as colored stacked histograms for different processes. The lower pad in each plot shows the ratio of data to the total background prediction.

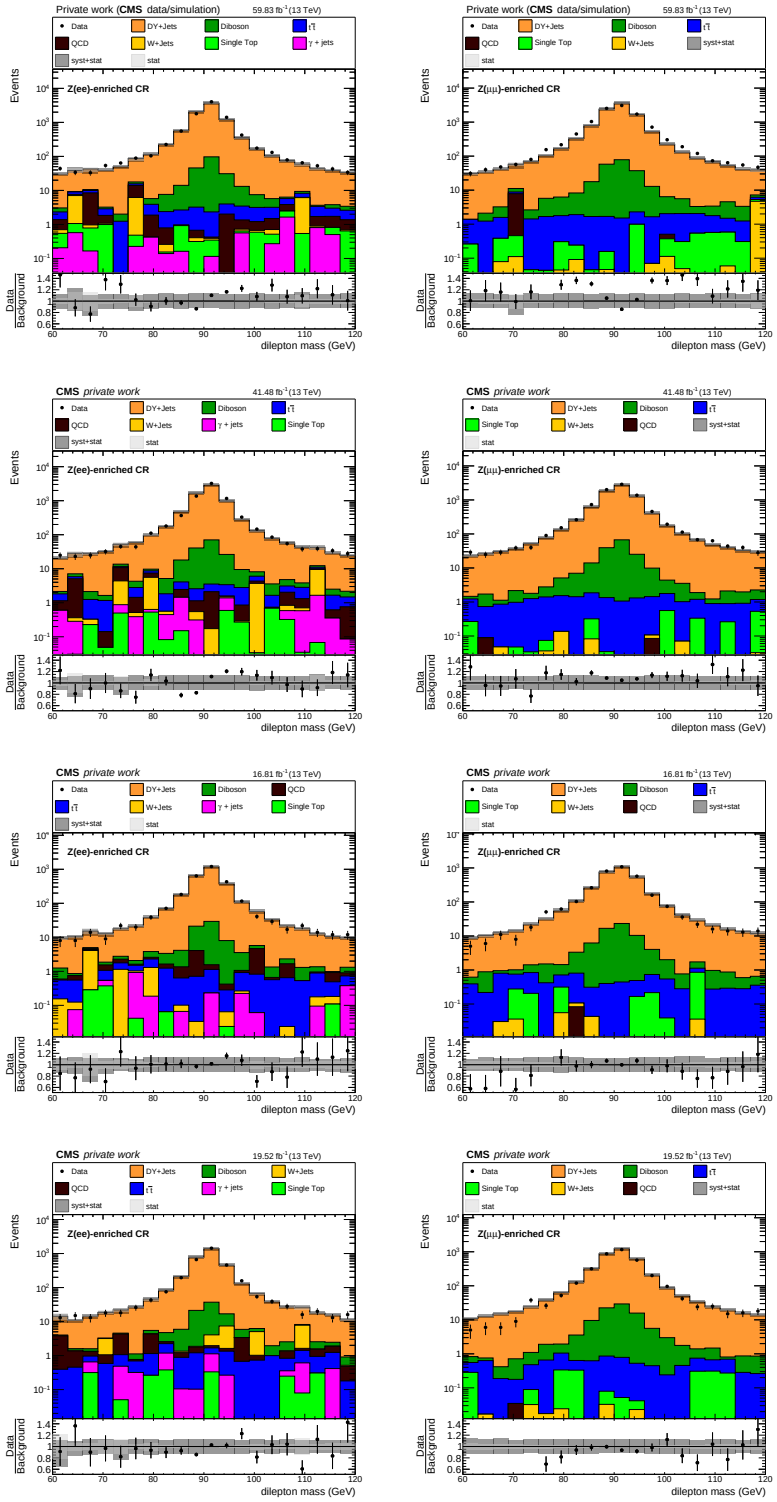

Figure K.20: Invariant mass of the dilepton system of the hadronic mono-top analysis selection with no top-tagging requirements applied for all four data-taking eras. The 2018, 2017, 2016postVFP, 2016preVFP data-taking eras are shown from top to bottom. Shown are the Z boson CRs, where the left-hand side corresponds to the muon and the right-hand side to the electron channel. The measured data in black points are compared to the background prediction from simulation as colored stacked histograms for different processes. The lower pad in each plot shows the ratio of data to the total background prediction.

L Hadronic recoil p_T in the hadronic analysis channel with the top-tagging requirement applied

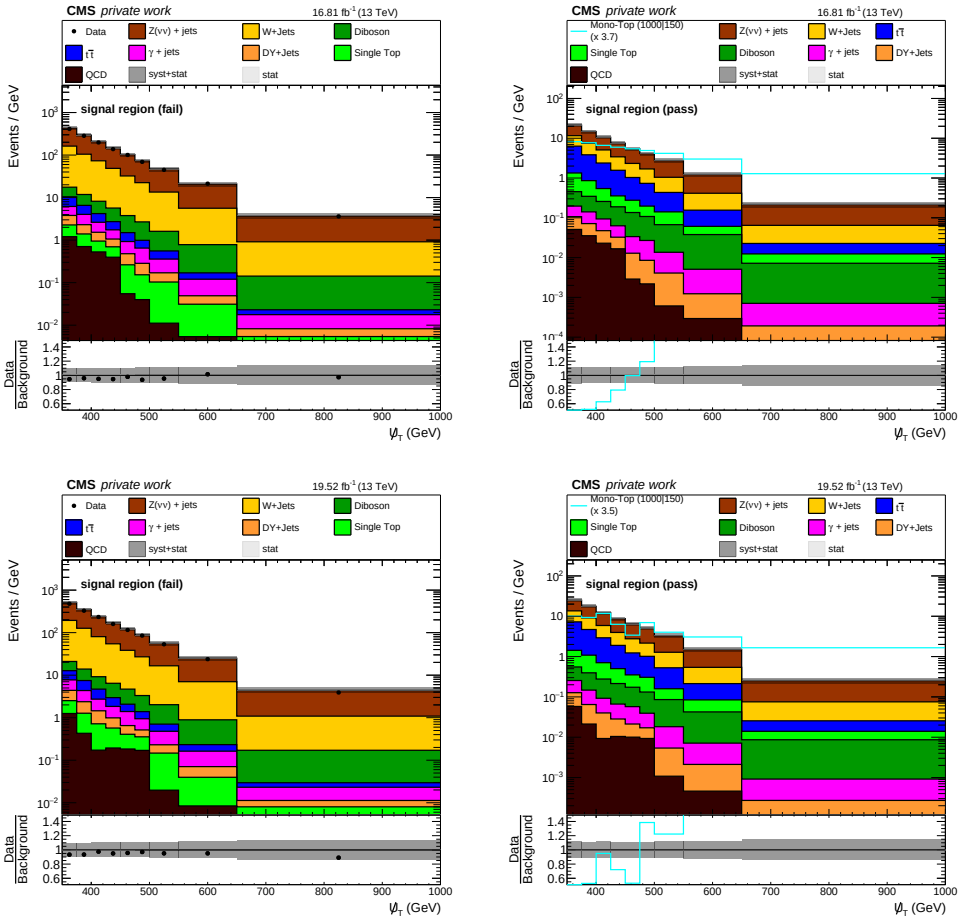

Figure L.1: Hadronic recoil p_T of the hadronic mono-top analysis for the 2016 data-taking eras. The 2016postVFP, 2016preVFP data-taking eras are shown from top to bottom. Shown is the SR, where the left-hand side corresponds to the pass region, whereas the right-hand side shows the fail region. The data points are hidden for the pass region to not introduce a bias towards a possible signal contribution.

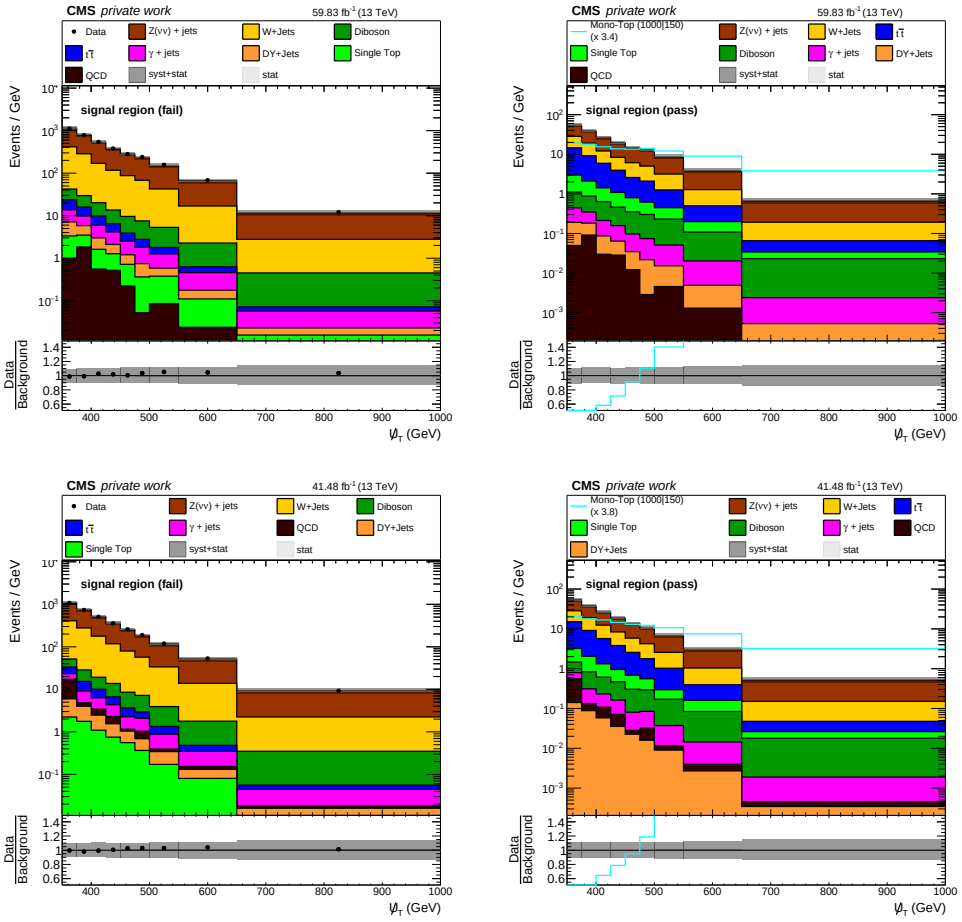

Figure L.2: Hadronic recoil p_{T} of the hadronic mono-top analysis for the 2017 (top) and 2018 (bottom) data-taking eras. Shown is the SR, where the left-hand side corresponds to the pass region, whereas the right-hand side shows the fail region. The data points are hidden for the pass region to not introduce a bias towards a possible signal contribution.

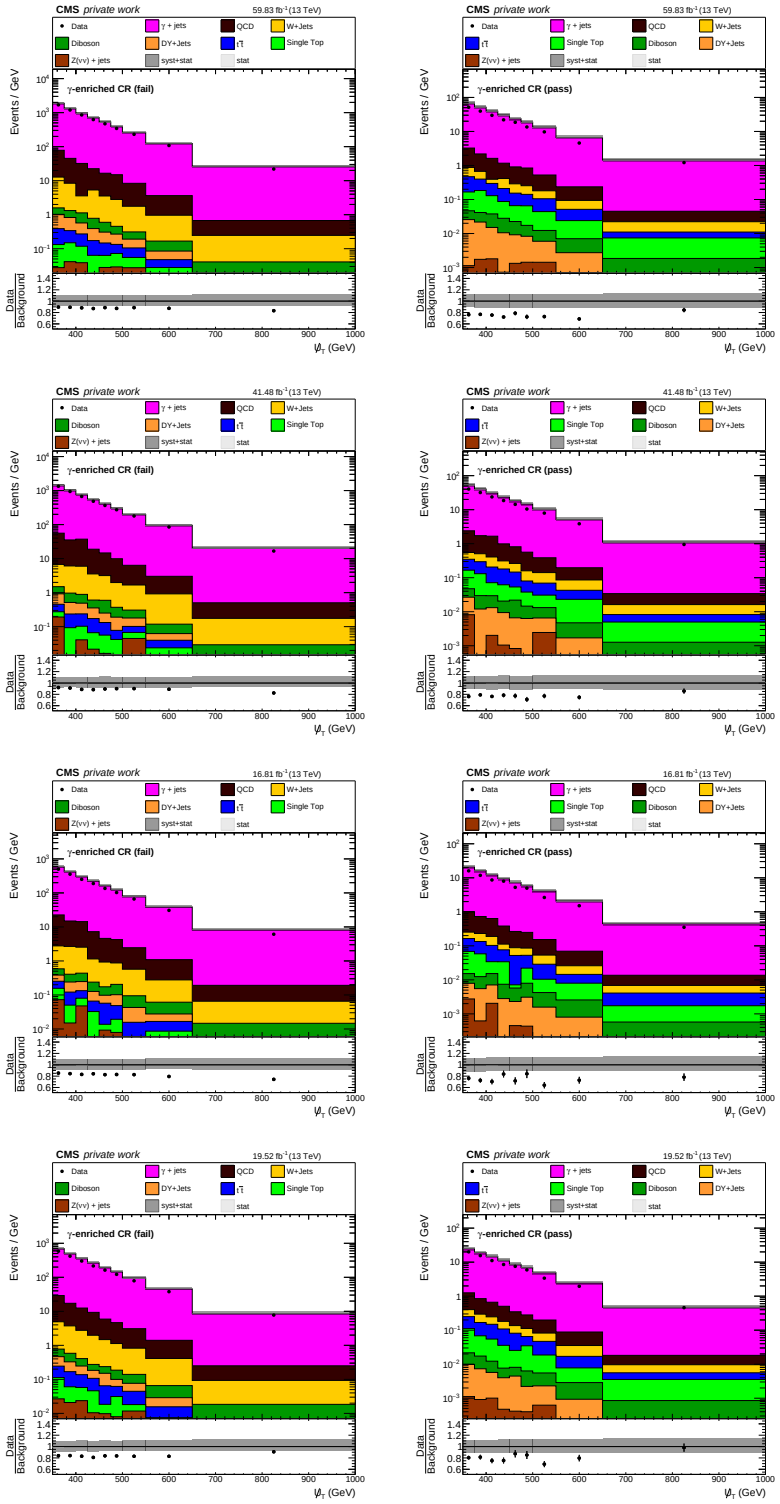

Figure L.3: Hadronic recoil p_{T} of the hadronic mono-top analysis for all four data-taking eras. The 2018, 2017, 2016postVFP, 2016preVFP data-taking eras are shown from top to bottom. Shown is the photon CR, where the left-hand side corresponds to the pass region, whereas the right-hand side shows the fail region.

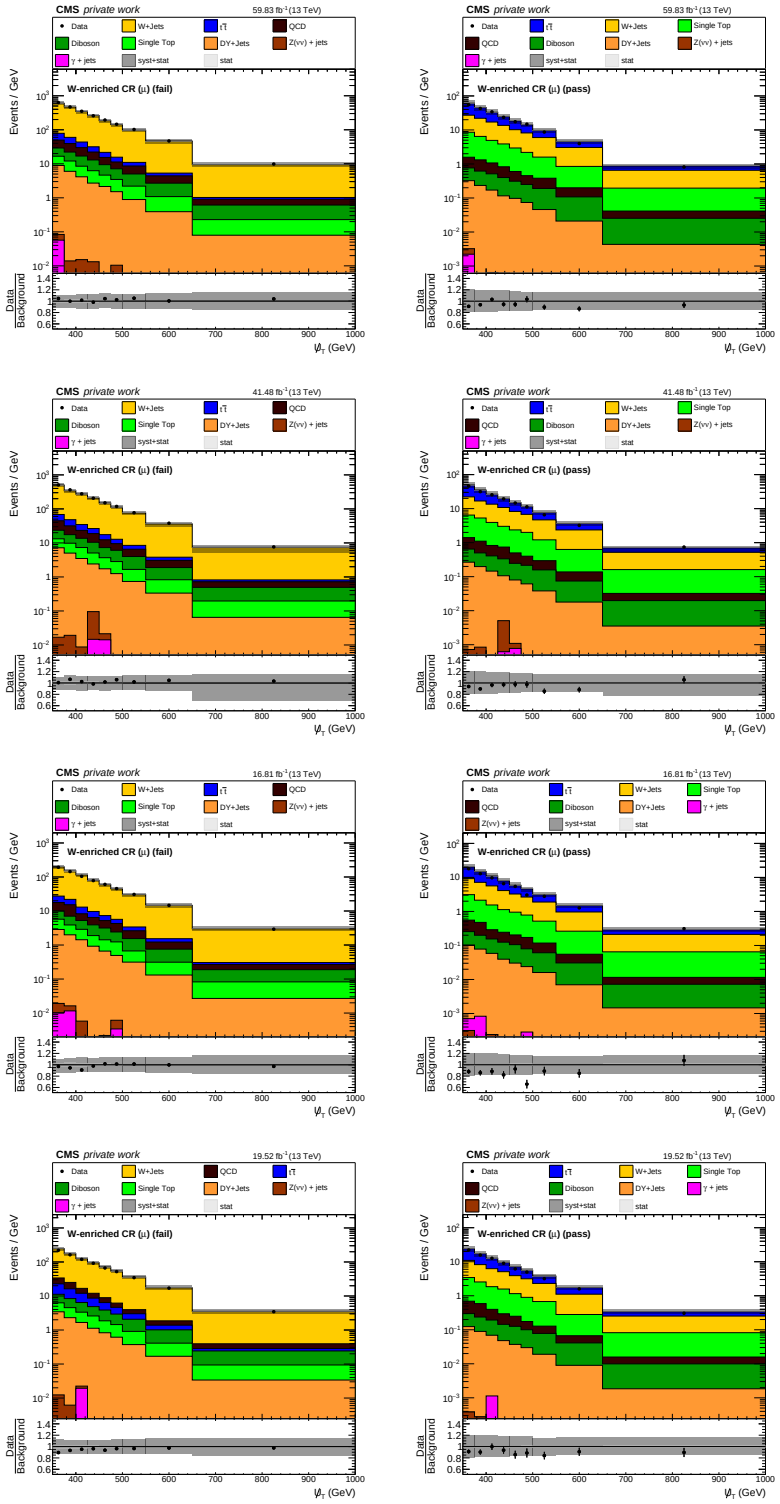

Figure L.4: Hadronic recoil p_{T} of the hadronic mono-top analysis for all four data-taking eras. The 2018, 2017, 2016postVFP, 2016preVFP data-taking eras are shown from top to bottom. Shown is the muon W boson CR, where the left-hand side corresponds to the pass region, whereas the right-hand side shows the fail region.

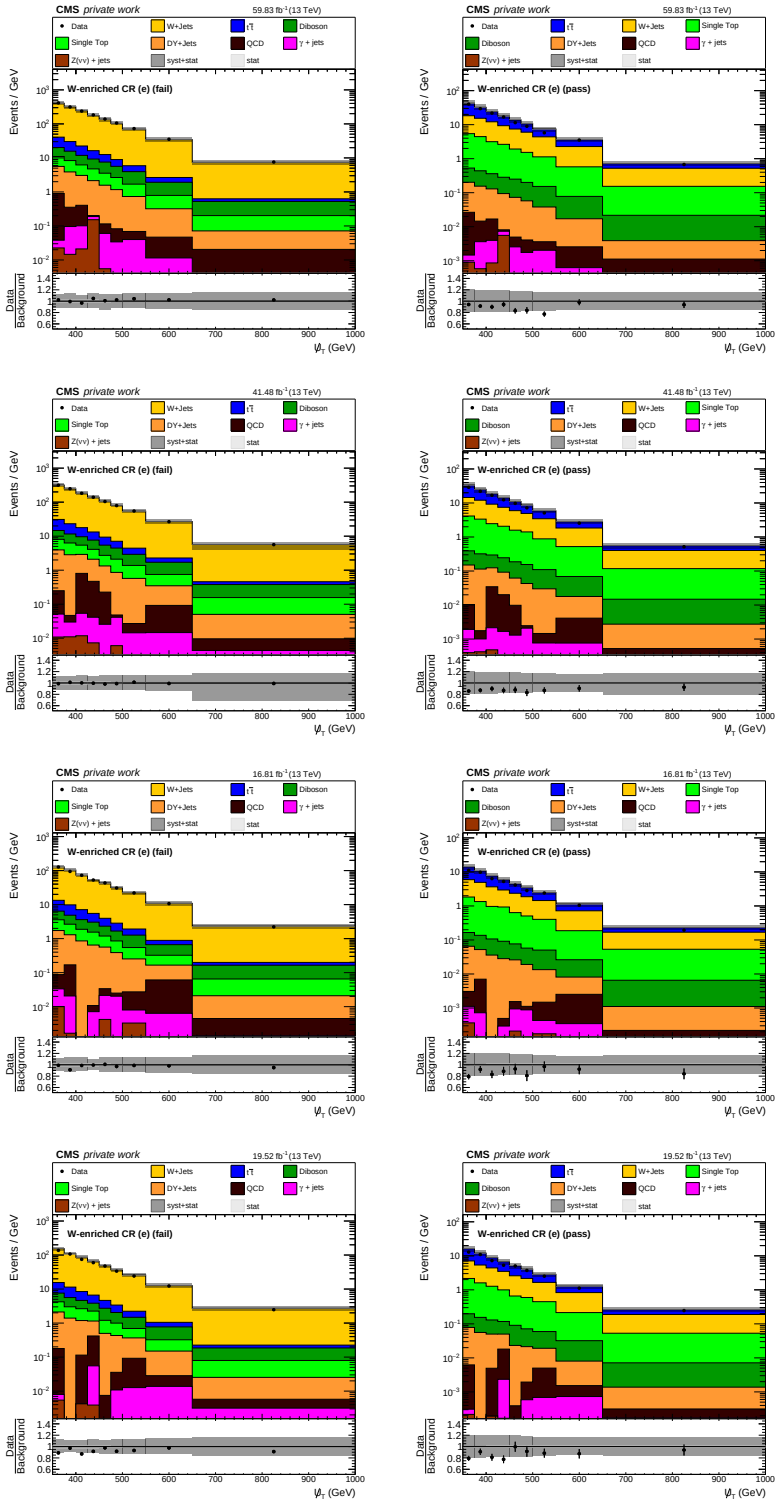

Figure L.5: Hadronic recoil p_{T} of the hadronic mono-top analysis for all four data-taking eras. The 2018, 2017, 2016postVFP, 2016preVFP data-taking eras are shown from top to bottom. Shown is the electron W boson CR, where the left-hand side corresponds to the pass region, whereas the right-hand side shows the fail region.

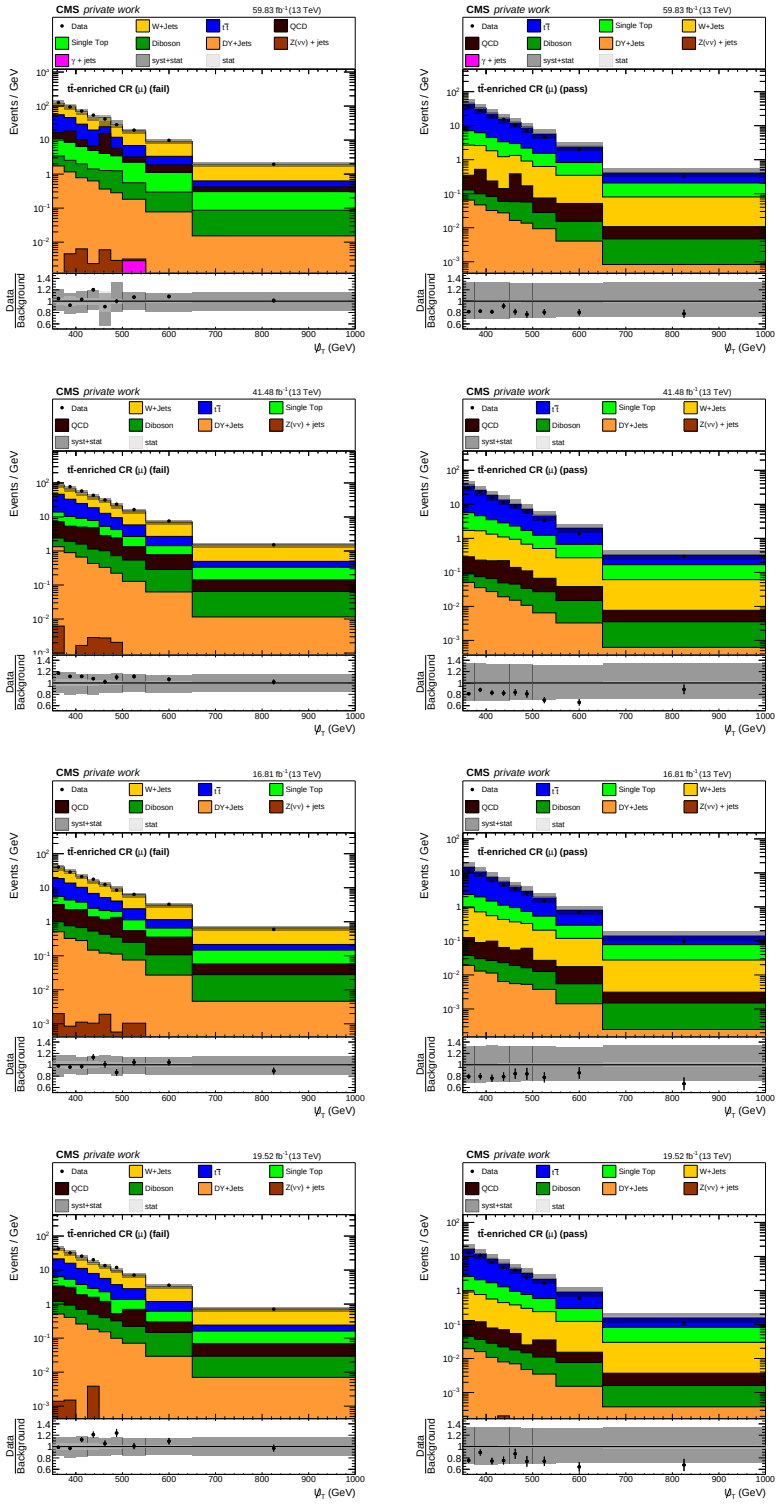

Figure L.6: Hadronic recoil p_{T} of the hadronic mono-top analysis for all four data-taking eras. The 2018, 2017, 2016postVFP, 2016preVFP data-taking eras are shown from top to bottom. Shown is the muon $\mathrm{t\bar{t}}$ CR, where the left-hand side corresponds to the pass region, whereas the right-hand side shows the fail region.

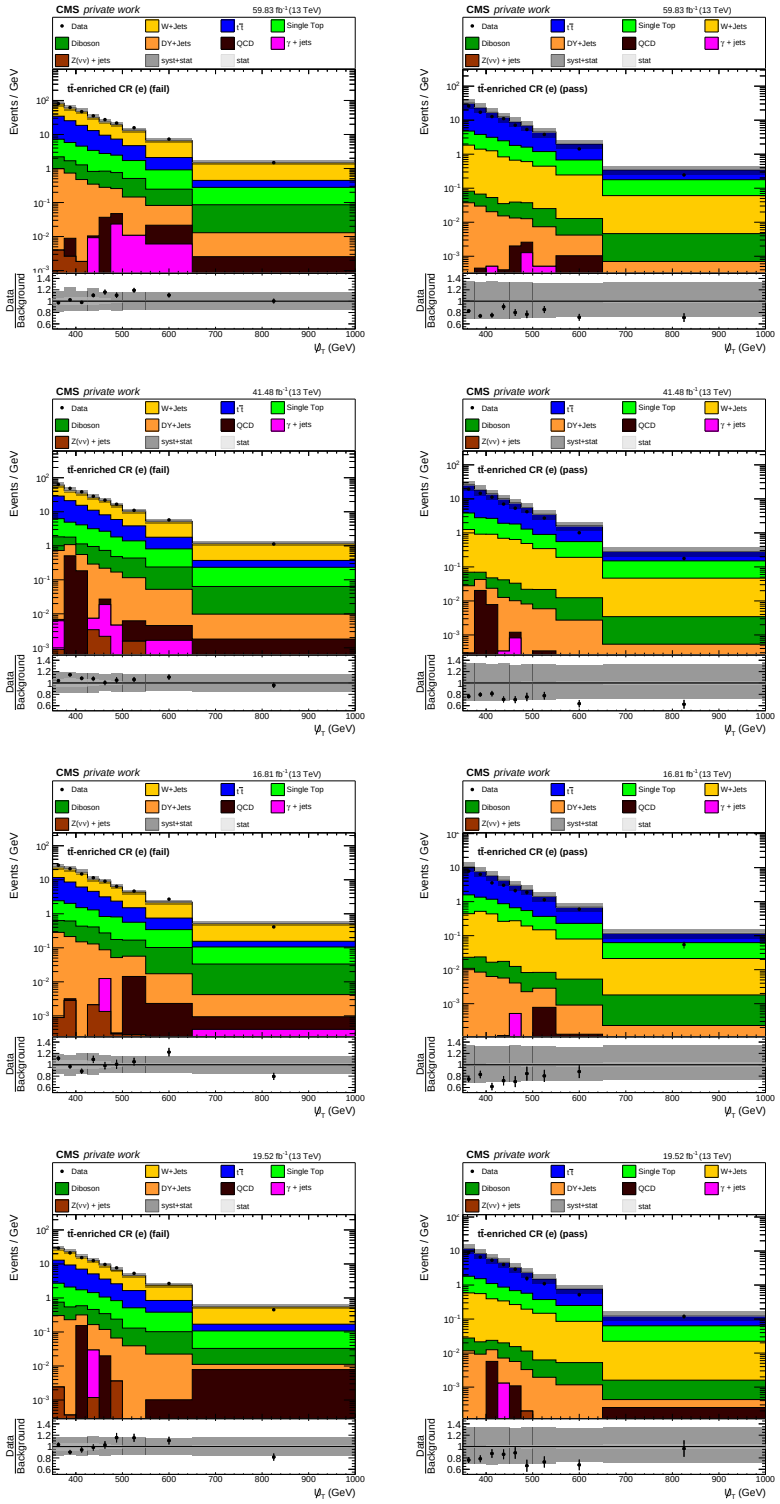

Figure L.7: Hadronic recoil p_{T} of the hadronic mono-top analysis for all four data-taking eras. The 2018, 2017, 2016postVFP, 2016preVFP data-taking eras are shown from top to bottom. Shown is the electron $t\bar{t}$ CR, where the left-hand side corresponds to the pass region, whereas the right-hand side shows the fail region.

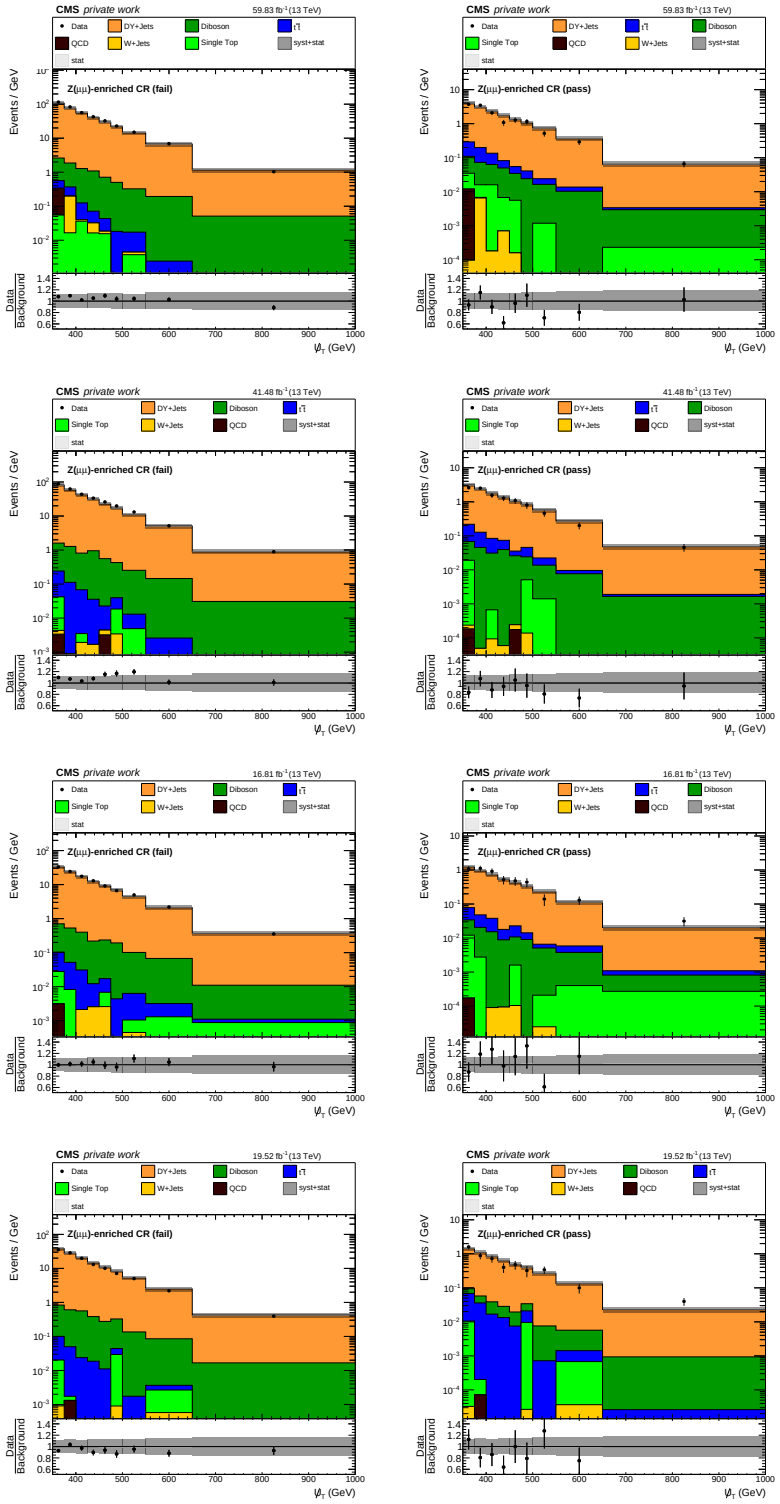

Figure L.8: Hadronic recoil p_{T} of the hadronic mono-top analysis for all four data-taking eras. The 2018, 2017, 2016postVFP, 2016preVFP data-taking eras are shown from top to bottom. Shown are the muon Z boson CRs, where the left-hand side corresponds to the pass region, whereas the right-hand side shows the fail region.

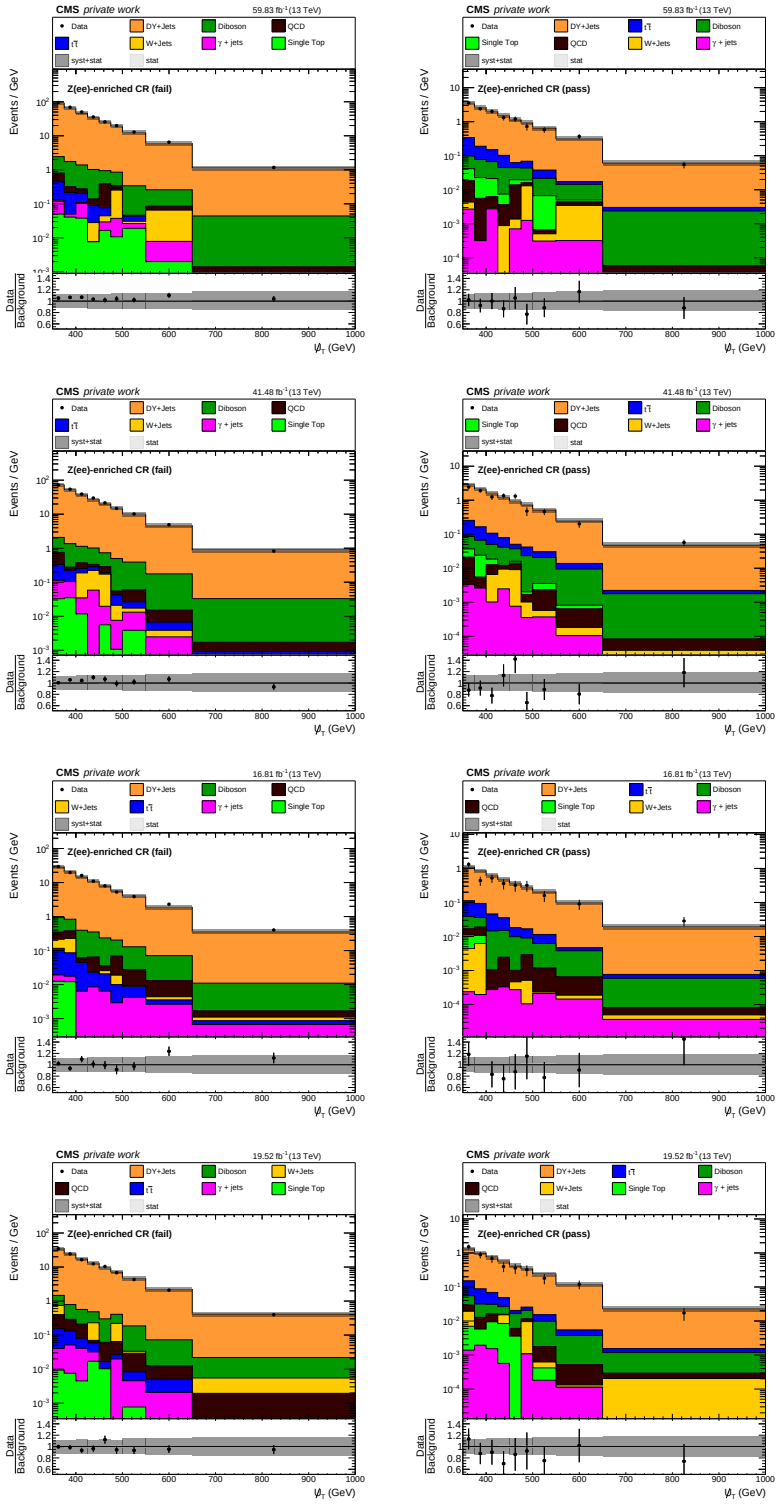

Figure L.9: Hadronic recoil p_{T} of the hadronic mono-top analysis for all four data-taking eras. The 2018, 2017, 2016postVFP, 2016preVFP data-taking eras are shown from top to bottom. Shown are the electron Z boson CRs, where the left-hand side corresponds to the pass region, whereas the right-hand side shows the fail region.

M Transfer factors in the hadronic analysis channel

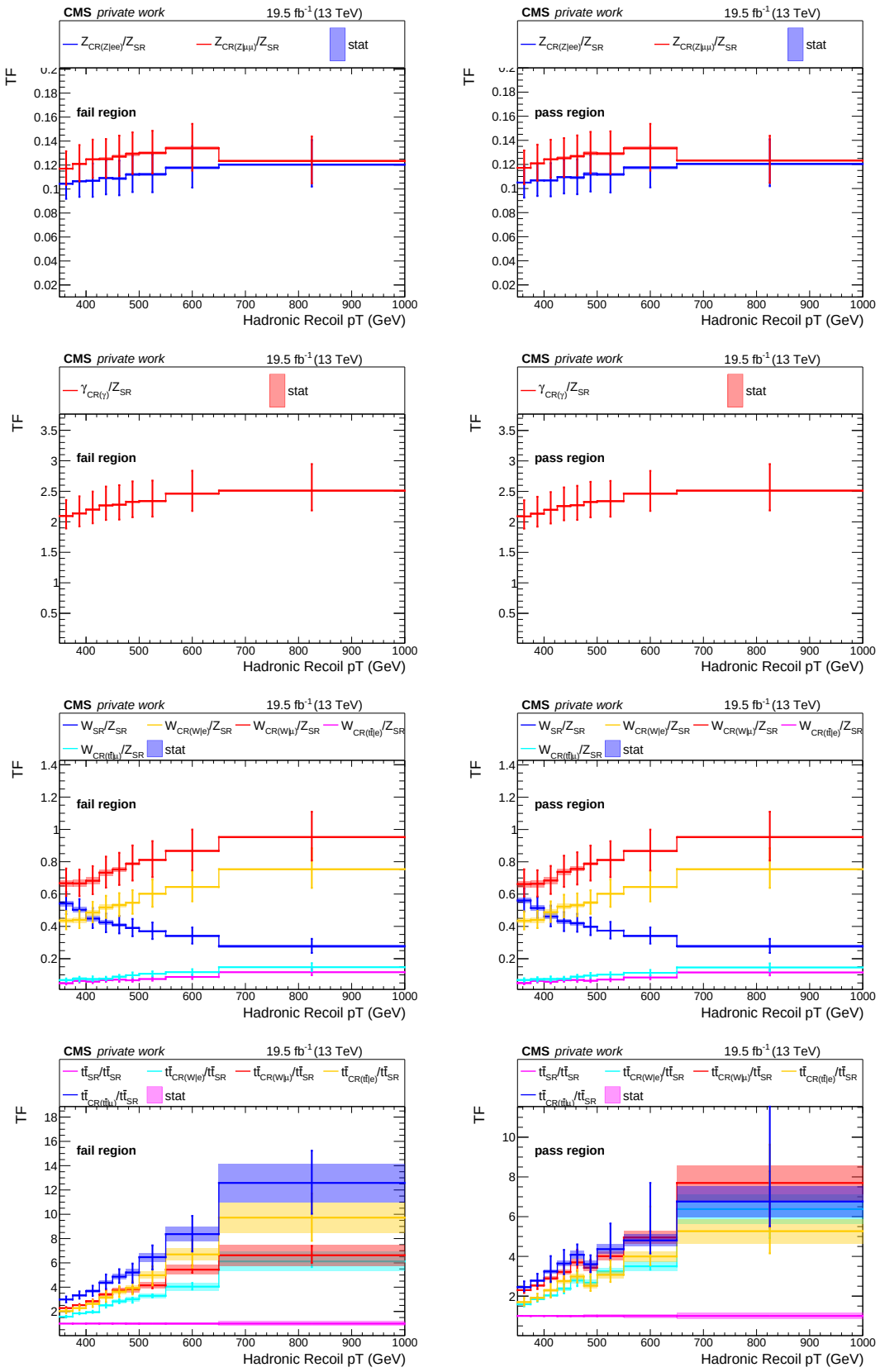

Figure M.1: Transfer factors in the fail region of the 2016preVFP data-taking era as a function of the hadronic recoil p_{T}. The left-hand side shows the fail region, whereas the right-hand side corresponds to the pass region. The error bars represent the total uncertainty, whereas the shaded area corresponds to the uncertainty due to the limited MC-simulated sample size.

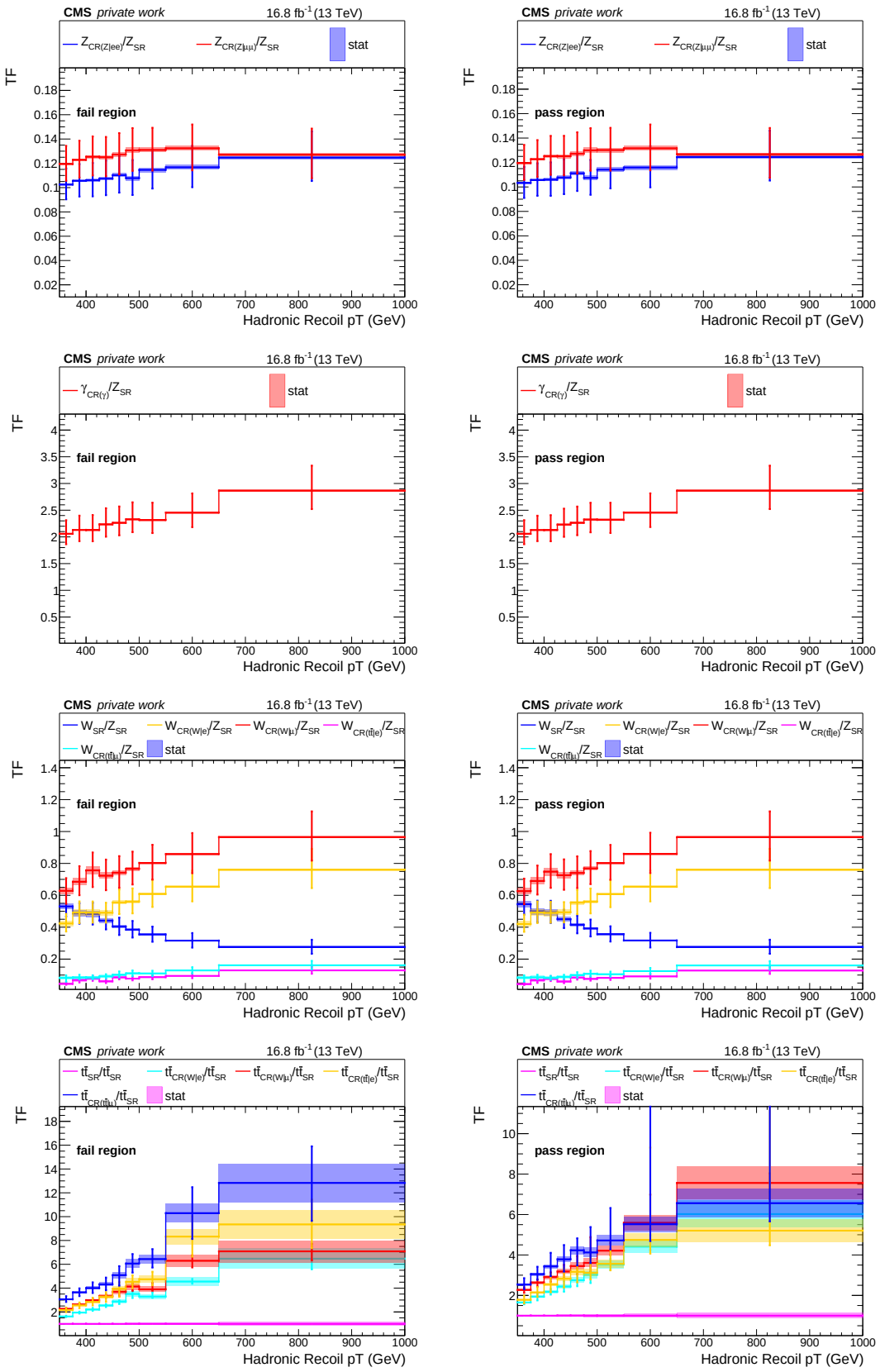

Figure M.2: Transfer factors in the fail region of the 2016postVFP data-taking era as a function of the hadronic recoil p_{T}. The left-hand side shows the fail region, whereas the right-hand side corresponds to the pass region. The error bars represent the total uncertainty, whereas the shaded area corresponds to the uncertainty due to the limited MC-simulated sample size.

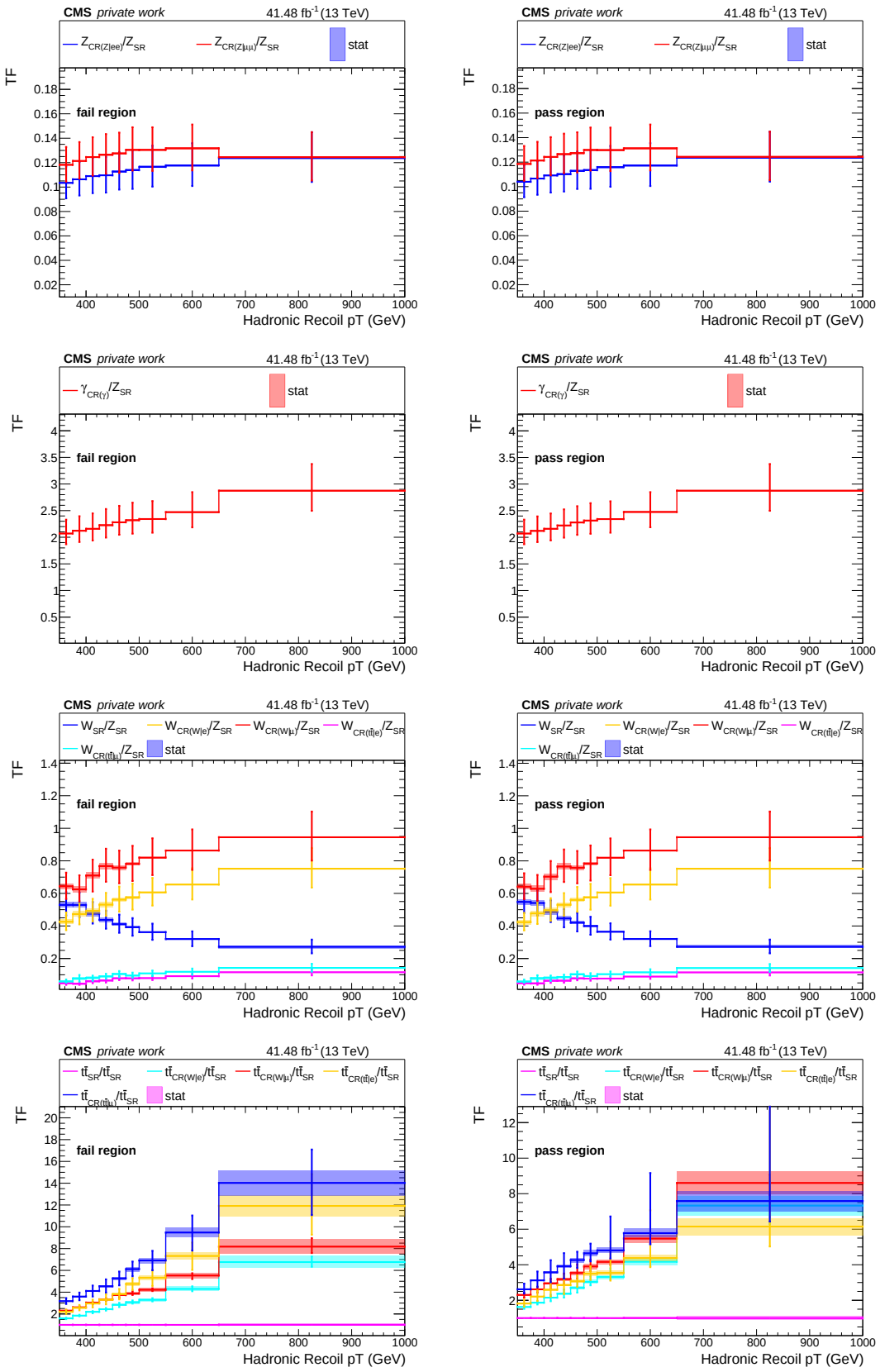

Figure M.3: Transfer factors in the fail region of the 2017 data-taking era as a function of the hadronic recoil p_{T}. The left-hand side shows the fail region, whereas the right-hand side corresponds to the pass region. The error bars represent the total uncertainty, whereas the shaded area corresponds to the uncertainty due to the limited MC-simulated sample size.

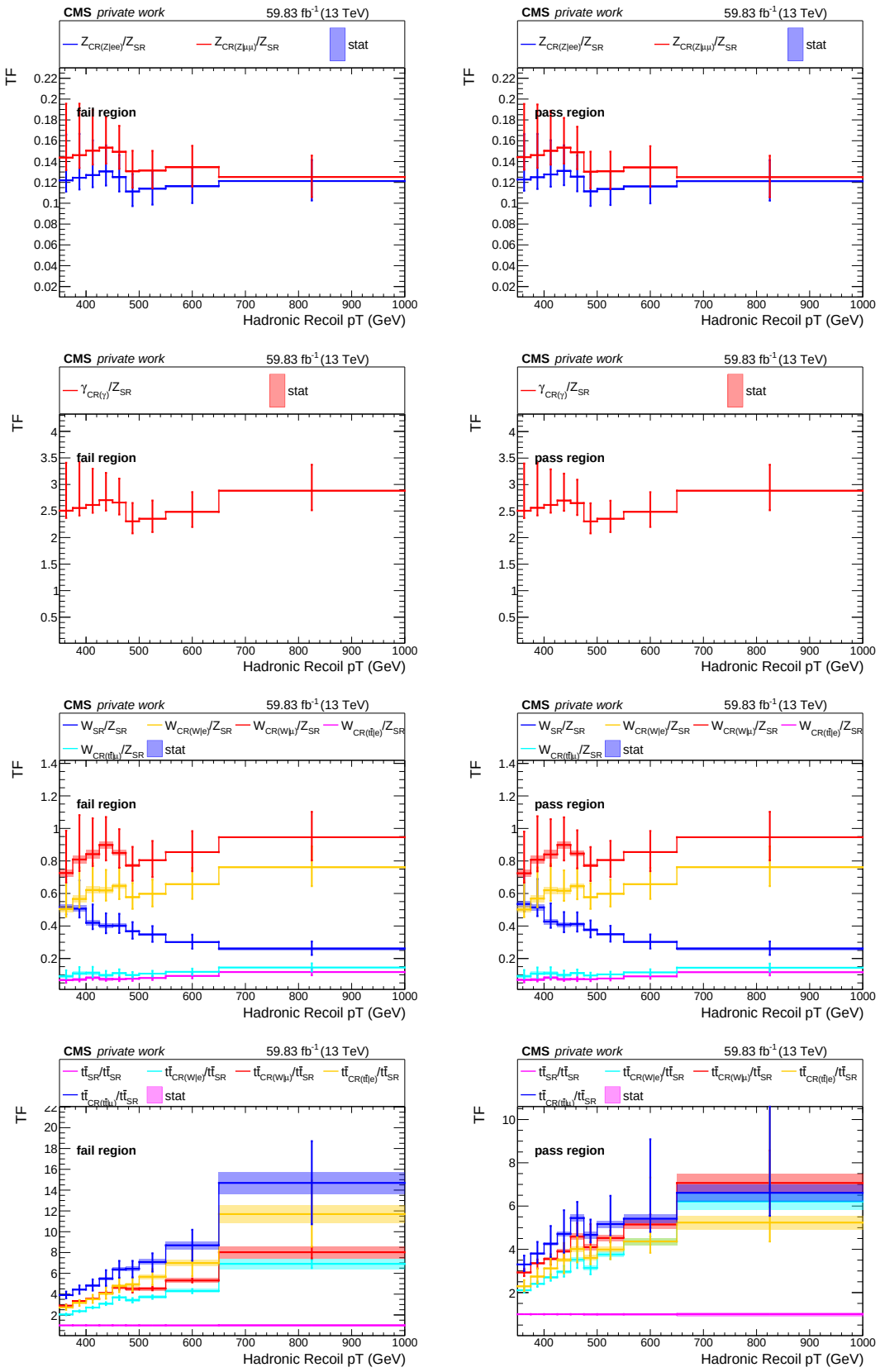

Figure M.4: Transfer factors in the fail region of the 2018 data-taking era as a function of the hadronic recoil p_{T}. The left-hand side shows the fail region, whereas the right-hand side corresponds to the pass region. The error bars represent the total uncertainty, whereas the shaded area corresponds to the uncertainty due to the limited MC-simulated sample size.

N A-posteriori distributions in the hadronic analysis channel

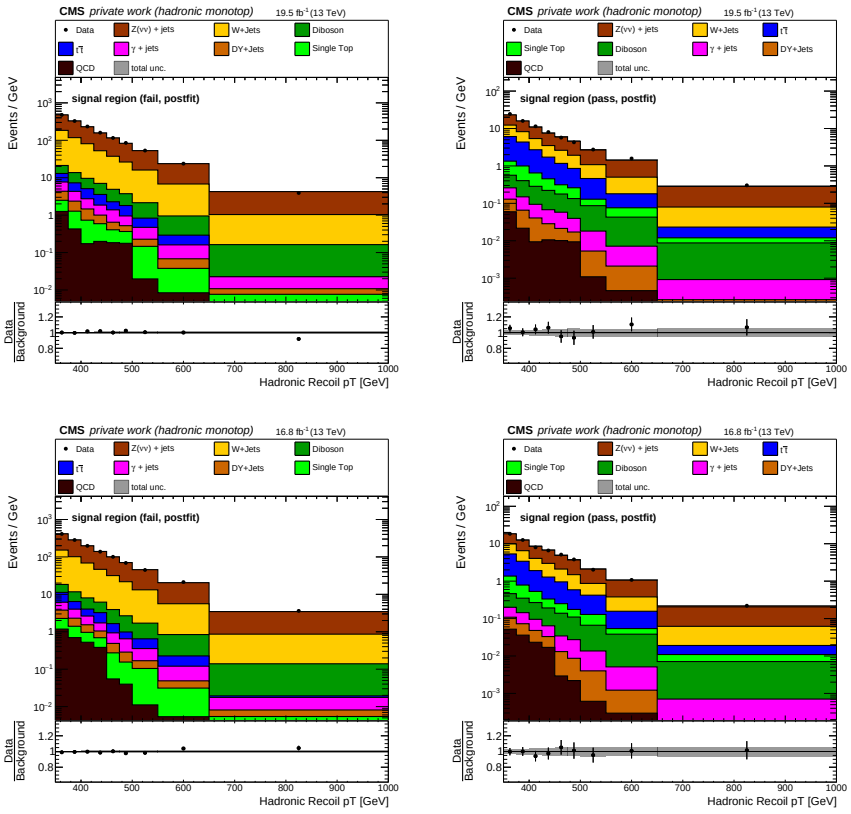

Figure N.1: Hadronic recoil p_{T} of the hadronic mono-top analysis for 2016preVFP (top) and 2016postVFP (bottom) data-taking eras after performing the maximum likelihood fit to the combined 2016 dataset. Shown is the SR, where the left-hand side corresponds to the fail region, whereas the right-hand side shows the pass region.

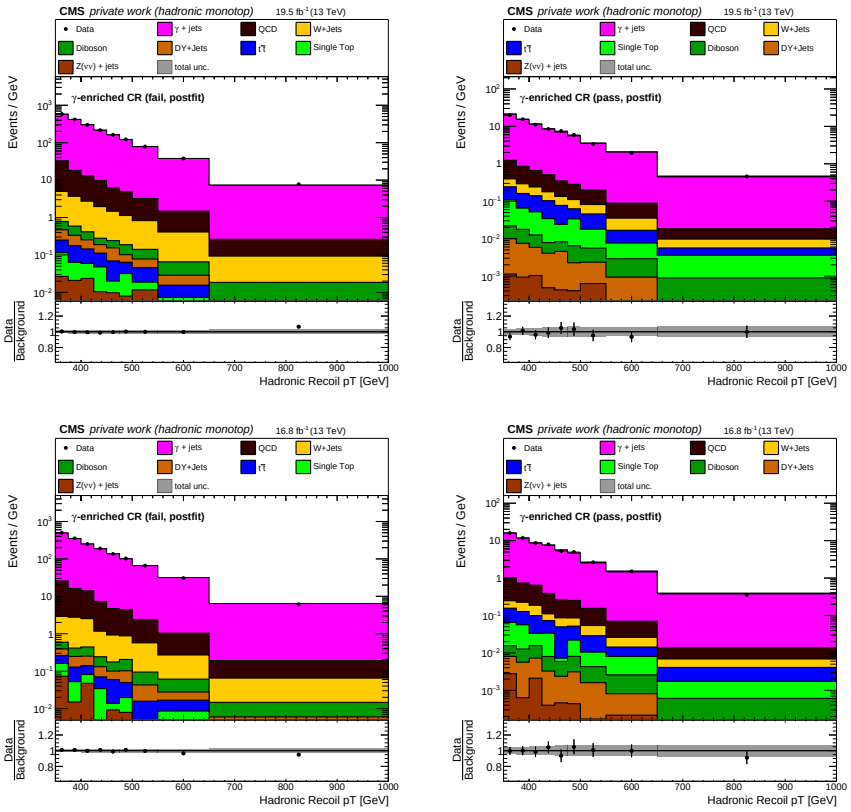

Figure N.2: Hadronic recoil p_{T} of the hadronic mono-top analysis for 2016preVFP (top) and 2016postVFP (bottom) data-taking eras after performing the maximum likelihood fit to the combined 2016 dataset. Shown is the photon CR, where the left-hand side corresponds to the fail region, whereas the right-hand side shows the pass region.

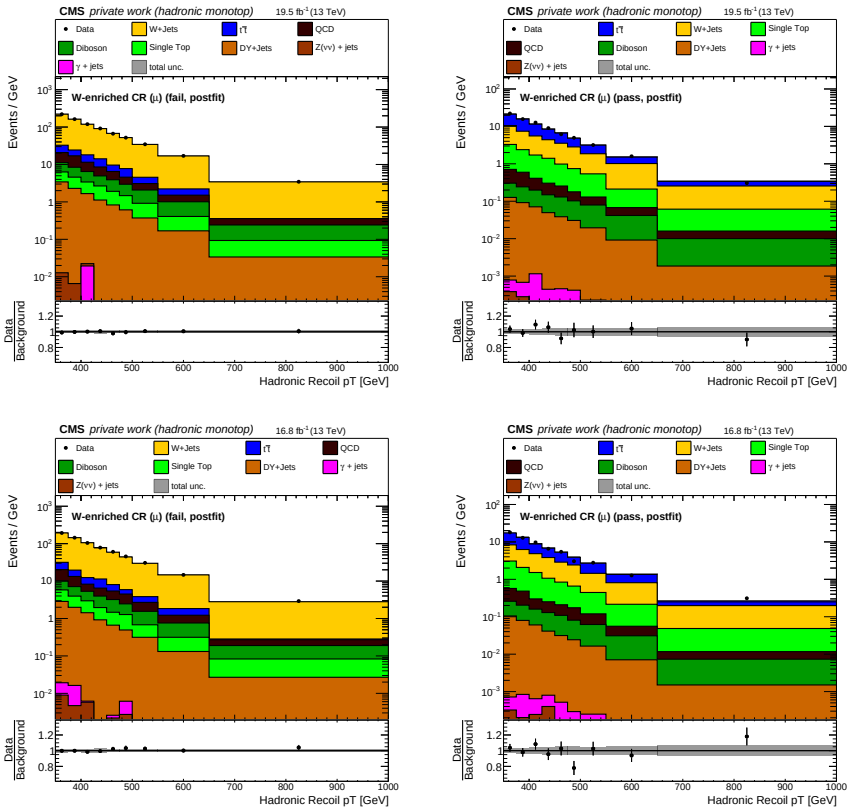

Figure N.3: Hadronic recoil p_{T} of the hadronic mono-top analysis for 2016preVFP (top) and 2016postVFP (bottom) data-taking eras after performing the maximum likelihood fit to the combined 2016 dataset. Shown is the muon W boson CR, where the left-hand side corresponds to the fail region, whereas the right-hand side shows the pass region.

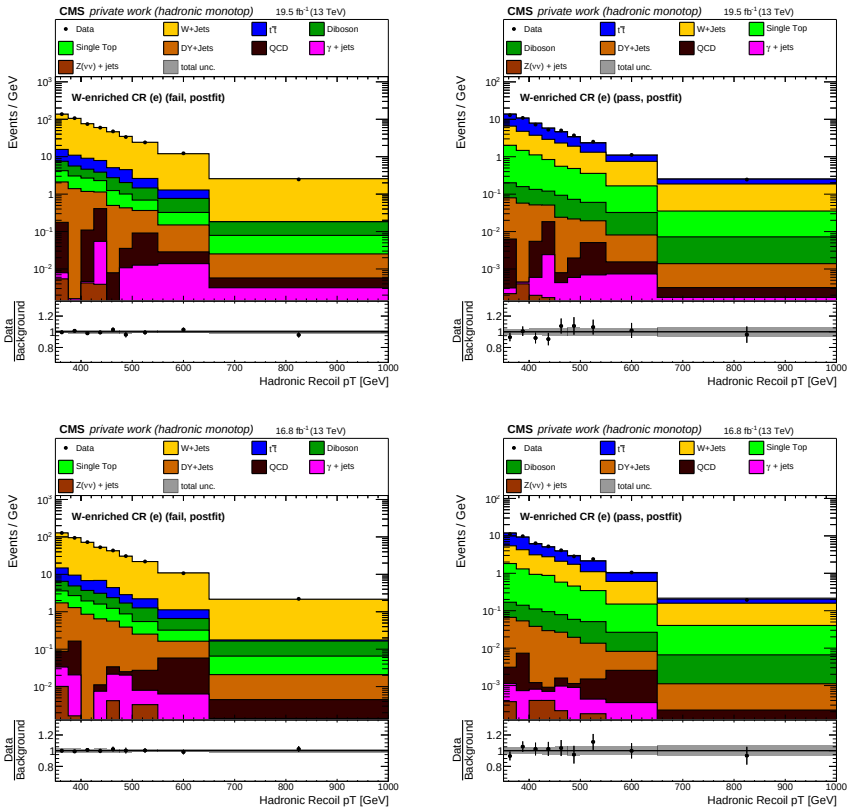

Figure N.4: Hadronic recoil p_{T} of the hadronic mono-top analysis for 2016preVFP (top) and 2016postVFP (bottom) data-taking eras after performing the maximum likelihood fit to the combined 2016 dataset. Shown is the electron W boson CR, where the left-hand side corresponds to the fail region, whereas the right-hand side shows the pass region.

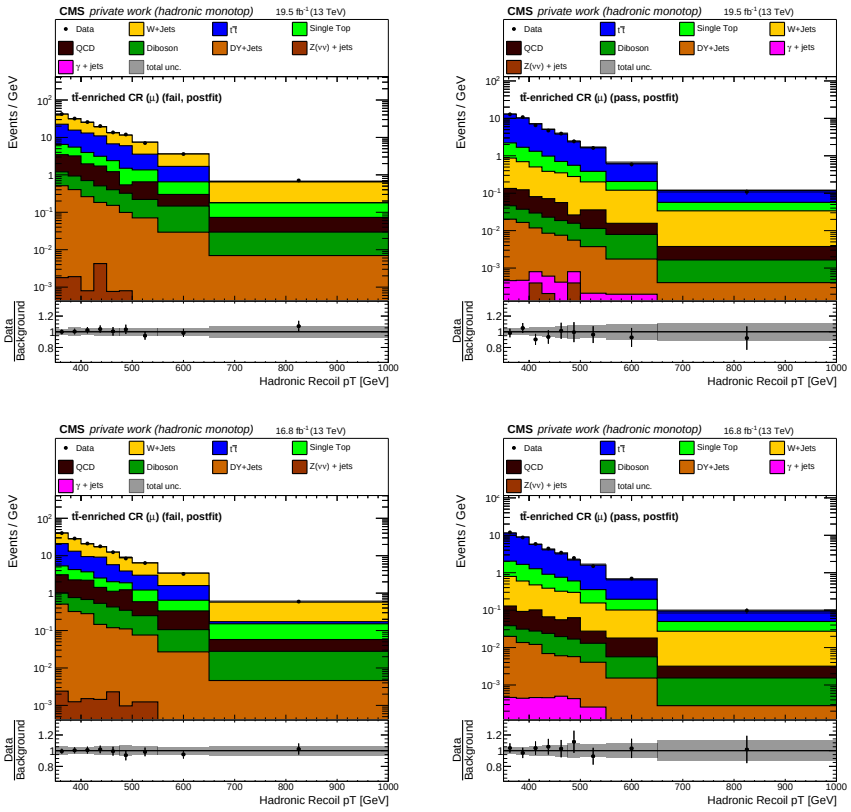

Figure N.5: Hadronic recoil p_{T} of the hadronic mono-top analysis for 2016preVFP (top) and 2016postVFP (bottom) data-taking eras after performing the maximum likelihood fit to the combined 2016 dataset. Shown is the muon $\mathrm{t\bar{t}}$ CR, where the left-hand side corresponds to the fail region, whereas the right-hand side shows the pass region.

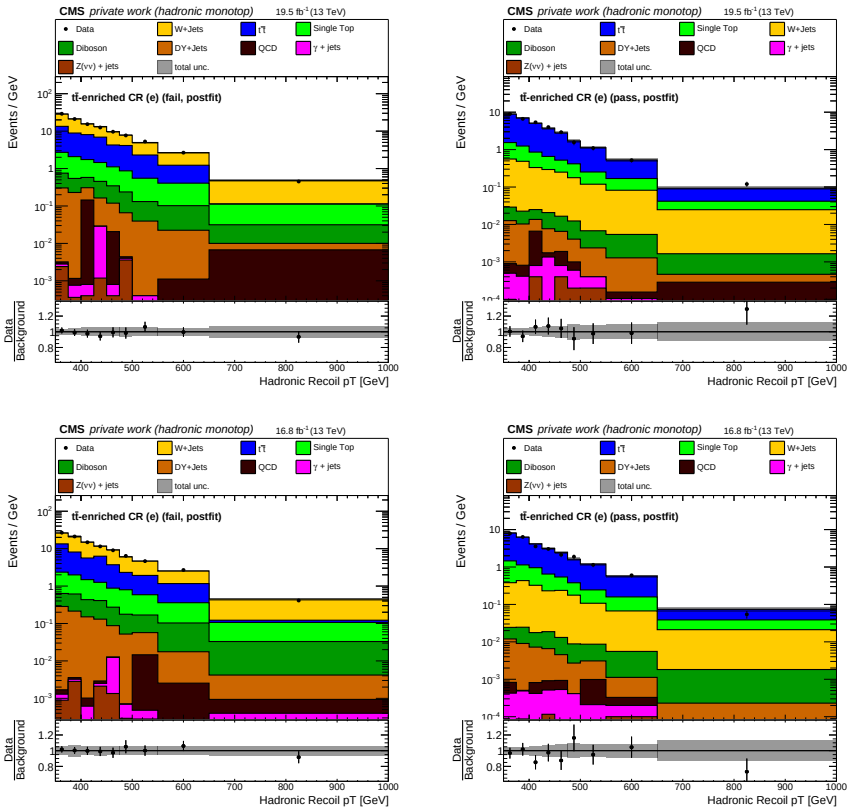

Figure N.6: Hadronic recoil p_{T} of the hadronic mono-top analysis for 2016preVFP (top) and 2016postVFP (bottom) data-taking eras after performing the maximum likelihood fit to the combined 2016 dataset. Shown is the electron $\mathrm{t\bar{t}}$ CR, where the left-hand side corresponds to the fail region, whereas the right-hand side shows the pass region.

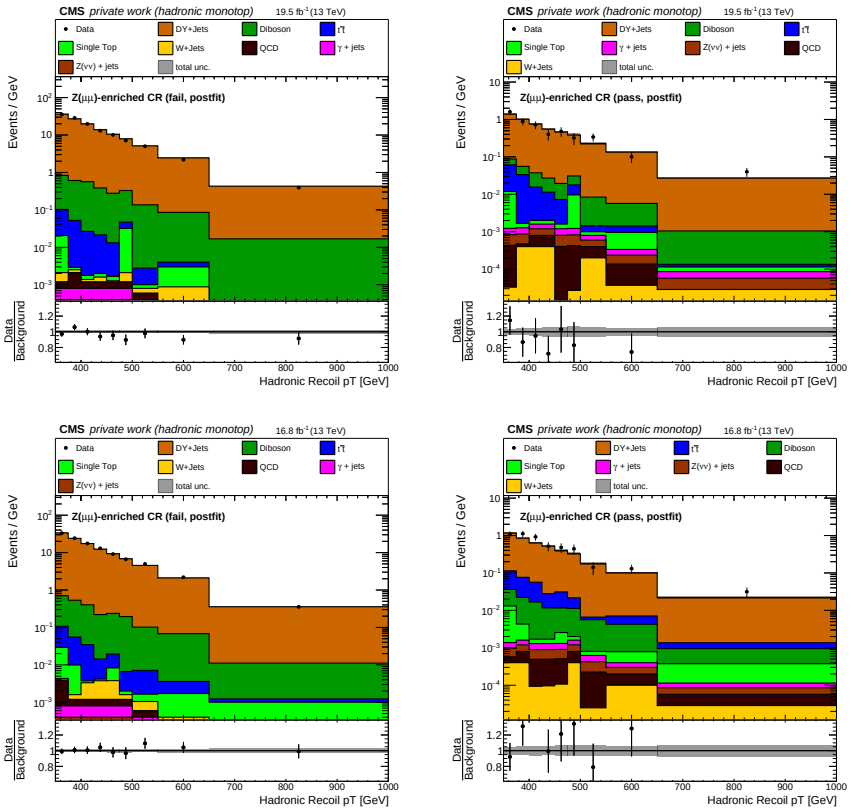

Figure N.7: Hadronic recoil p_{T} of the hadronic mono-top analysis for 2016preVFP (top) and 2016postVFP (bottom) data-taking eras after performing the maximum likelihood fit to the combined 2016 dataset. Shown are the muon Z boson CRs, where the left-hand side corresponds to the fail region, whereas the right-hand side shows the pass region.

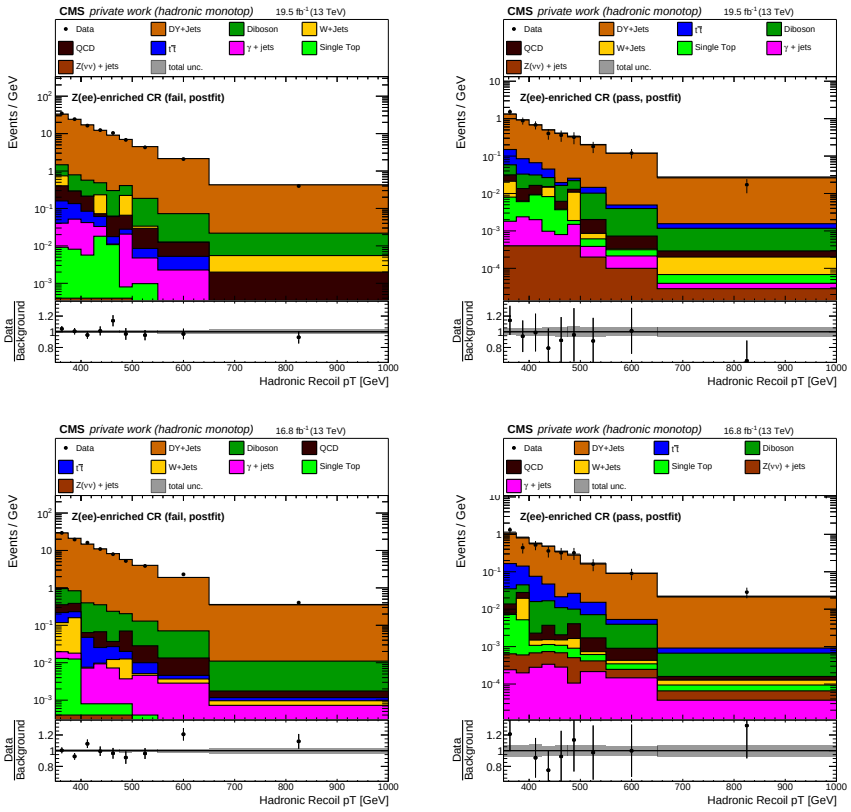

Figure N.8: Hadronic recoil p_{T} of the hadronic mono-top analysis for 2016preVFP (top) and 2016postVFP (bottom) data-taking eras after performing the maximum likelihood fit to the combined 2016 dataset. Shown are the electron Z boson CRs, where the left-hand side corresponds to the fail region, whereas the right-hand side shows the pass region.

O Expected exclusion limits for hadronic analysis

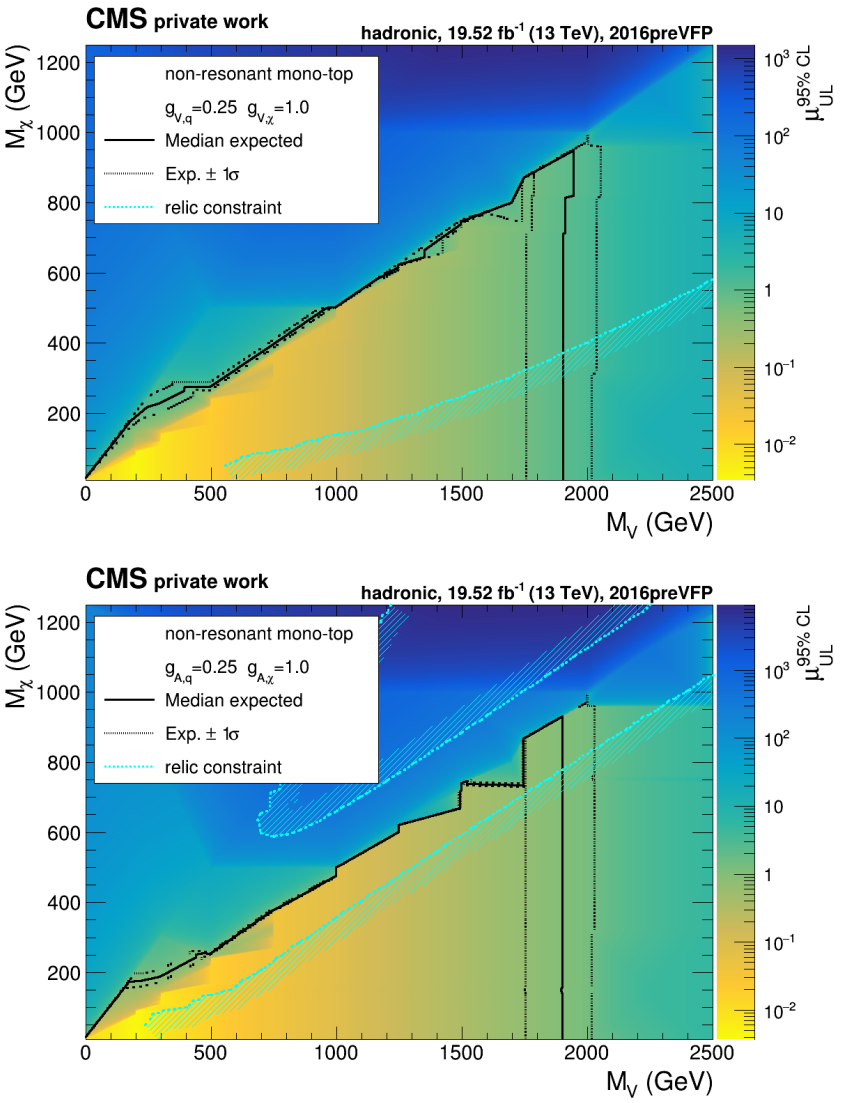

Figure O.9: Upper limits on the signal strength modifier μ at a confidence level of 95 % for the vector mono-top model for the 2016preVFP data-taking era in the plane of mediator and DM candidate masses M_V and M_χ. The solid black line indicates the contour for which the median, upper exclusion limit is equal to unity. The 68 % confidence interval on this contour is shown as a dashed black line. The area enclosed by the solid black line is parameter space expected to be excluded for the given mono-top model. The cyan, dashed exclusion line indicates a constraint on allowed masses in order to explain the measured DM relic density by the Planck Collaboration [30]. The upper exclusion plot corresponds to a pure vector coupling scenario, whereas the lower figure shows the exclusion limits for a pure axial-vector coupling scenario.

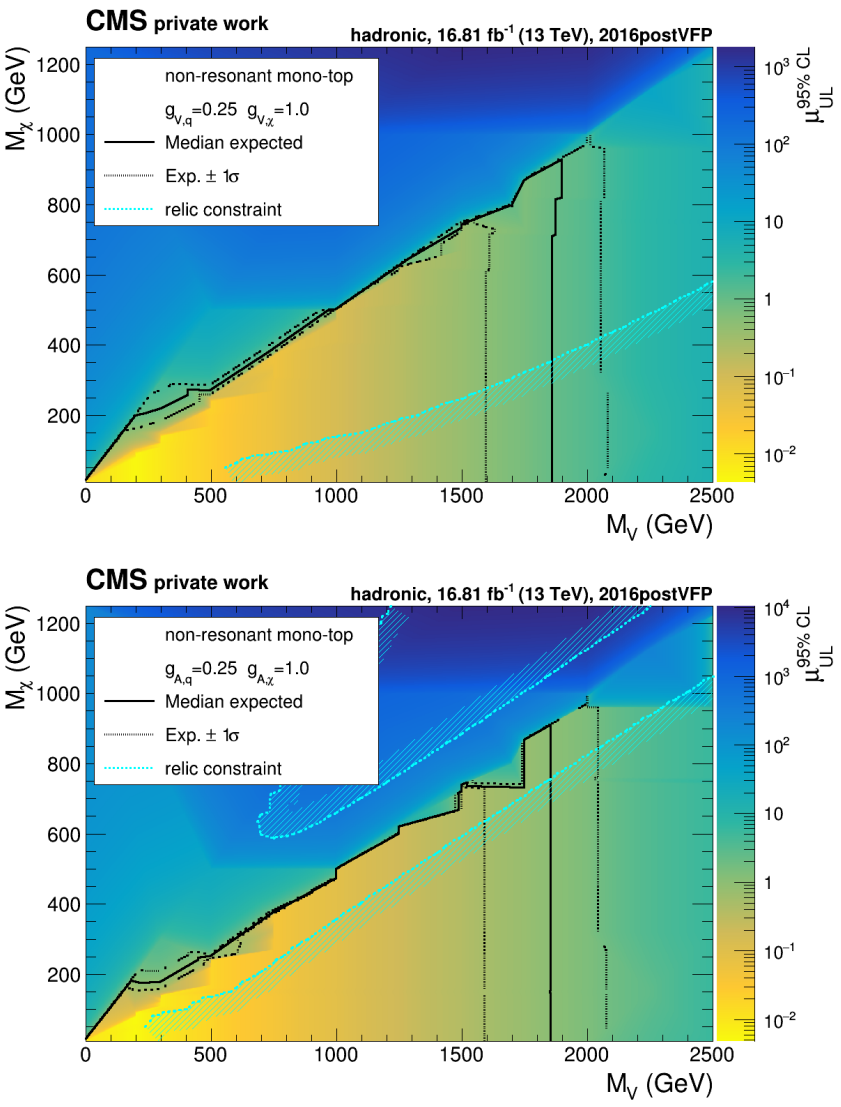

Figure O.10: Upper limits on the signal strength modifier μ at a confidence level of 95 % for the vector mono-top model for the 2016postVFP data-taking era in the plane of mediator and DM candidate masses M_V and M_χ. The solid black line indicates the contour for which the median, upper exclusion limit is equal to unity. The 68 % confidence interval on this contour is shown as a dashed black line. The area enclosed by the solid black line is parameter space expected to be excluded for the given mono-top model. The cyan, dashed exclusion line indicates a constraint on allowed masses in order to explain the measured DM relic density by the Planck Collaboration [30]. The upper exclusion plot corresponds to a pure vector coupling scenario, whereas the lower figure shows the exclusion limits for a pure axial-vector coupling scenario.

P Observed exclusion limits for hadronic analysis

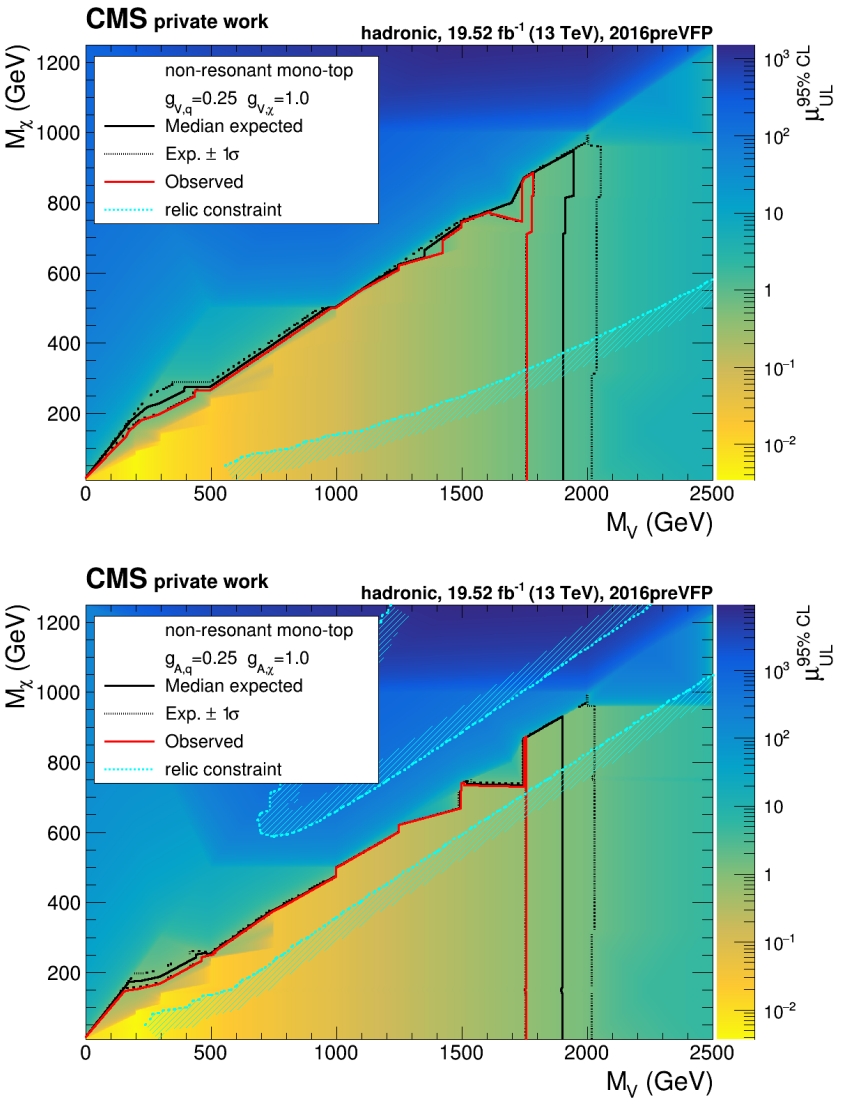

Figure P.1: Upper limits on the signal strength modifier μ at a confidence level of 95 % for the vector mono-top model for the 2016preVFP data-taking era in the plane of mediator and DM candidate masses M_V and M_χ. The solid black line indicates the contour, where the median, upper exclusion limit is equal to unity. The 68 % confidence interval on this contour is shown as a dashed black line. The area enclosed by the solid black line is parameter space expected to be excluded for the given mono-top model. The red line indicates the contour for which the observed upper limit is equal to unity, excluding the enclosed parameter space. The cyan, dashed exclusion line indicates a constraint on allowed masses in order to explain the measured DM relic density by the Planck Collaboration [30]. The upper exclusion plot corresponds to a pure vector coupling scenario, whereas the lower figure shows the exclusion limits for a pure axial-vector coupling scenario.

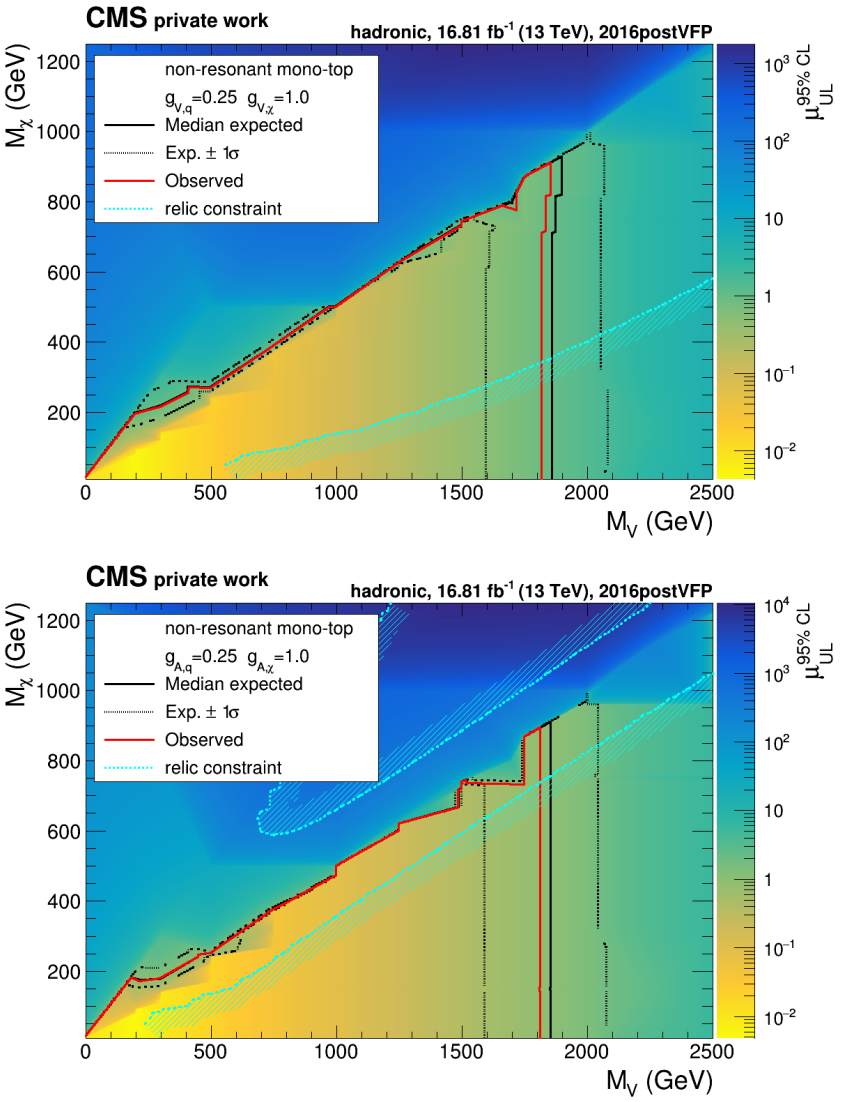

Figure P.2: Upper limits on the signal strength modifier μ at a confidence level of 95 % for the vector mono-top model for the 2016postVFP data-taking era in the plane of mediator and DM candidate masses M_V and M_χ. The solid black line indicates the contour, where the median, upper exclusion limit is equal to unity. The 68 % confidence interval on this contour is shown as a dashed black line. The area enclosed by the solid black line is parameter space expected to be excluded for the given mono-top model. The red line indicates the contour for which the observed upper limit is equal to unity, excluding the enclosed parameter space. The cyan, dashed exclusion line indicates a constraint on allowed masses in order to explain the measured DM relic density by the Planck Collaboration [30]. The upper exclusion plot corresponds to a pure vector coupling scenario, whereas the lower figure shows the exclusion limits for a pure axial-vector coupling scenario.

Acknowledgements

Zum Abschluss dieser Arbeit möchte ich noch einigen Personen meinen persönlichen Dank aussprechen. Ohne die gebotene Unterstützung wäre es mir nicht möglich gewesen, diese Arbeit durchzuführen.

Zunächste bedanke ich mich bei Prof. Dr. Ulrich Husemann, der mir bereits seit 2016 die Möglichkeit gab in seiner Arbeitsgruppe tätig zu sein und bei der Durchführung aller meiner Abschlussarbeiten unterstützt hat. Die Arbeit in seiner Gruppe war stets von einer offenen und freundlichen Atmosphäre geprägt, die es mir ermöglichte, mich in der Forschung zu entfalten und mich persönlich weiterzuentwickeln.

Ich möchte mich auch bei Prof. Dr. Günter Quast für die Übernahme der Korreferentenrolle bedanken.

An dieser Stelle möchte ich mich auch recht herzlich beim gesamten ETP, dem Graduiertenkolleg GRK 1694 und KSETA für die wissenschaftliche sowie finanzielle Unterstützung bedanken.

Ein besonderer Dank gilt auch meinem Betreuer Dr. Michael Waßmer, der mir schon seit der Masterarbeit zur Seite stand und mich in allen Fragen der wissenschaftlichen Arbeit unterstützt hat und dadurch maßgeblich dazu beigetragen hat diese Arbeit durchzuführen. Danke Michael! Ebenso gilt ein besonderer Dank Jan van der Linden und Dr. Philip Keicher für die grandiose Zeit zusammen. Es ist einfach toll, nicht nur mit Kollegen, sondern auch mit Freunden zu arbeiten. R418 wird mit stets positiv in Erinnerung bleiben.

Auch für die allgemeine Positivität und Unterstützung innerhalb der gesamten Arbeitsgruppe möchte ich mich bedanken.

Der letzte sehr große Dank gilt meiner Familie. An erster Stelle möchte ich mich bei meiner wundervollen Frau Isabel bedanken, die mir stets den Rücken freigehalten hat und auch in schweren Momenten immer an meiner Seite war und mich aufgebaut und ermutigt hat die Arbeit zu schaffen. Auch mein Sohn Max sei an dieser Stelle erwähnt. Dein Frohsinn, deine Neugier und dein Lächeln haben mich stets wieder aufgebaut. Danke für Alles!

Zu guter Letzt bedanke ich mich auch noch bei meiner restlichen Familie und Freunden, die immer mit einem offenen Ohr für mich da waren und mich stets unterstützt haben.